Photo- or photoelectro-catalytic glycerol valorization and simultaneous hydrogen production

Jie Yu

▶ **To cite this version:**

Jie Yu. Photo- or photoelectro-catalytic glycerol valorization and simultaneous hydrogen production. Catalysis. Université de Lyon, 2022. English. NNT : 2022LYSE1145 . tel-04719167

HAL Id: tel-04719167

https://theses.hal.science/tel-04719167v1

Submitted on 3 Oct 2024

HAL is a multi-disciplinary open access archive for the deposit and dissemination of scientific research documents, whether they are published or not. The documents may come from teaching and research institutions in France or abroad, or from public or private research centers.

L'archive ouverte pluridisciplinaire **HAL**, est destinée au dépôt et à la diffusion de documents scientifiques de niveau recherche, publiés ou non, émanant des établissements d'enseignement et de recherche français ou étrangers, des laboratoires publics ou privés.

N°d'ordre NNT : 2022LYSE1145

THESE de DOCTORAT DE L'UNIVERSITE DE LYON
opérée au sein de
l'Université Claude Bernard Lyon 1

Ecole Doctorale N° accréditation
(Chimie : Chimie, Procédés, Environnement)

Spécialité de doctorat : CHIMIE
Discipline : PHOTO-ELECTROCATALYSE

Soutenue publiquement le 20/07/2022, par :
Jie YU

Photo- or photoelectro-catalytic glycerol valorization and simultaneous hydrogen production

---

Devant le jury composé de :

Giroir-Fendler, Anne	Professeure / Université de Lyon	Présidente
Herlin Boime, Nathalie	Directeur de Recherche / Université Paris-Saclay	Rapporteur
Napporn, Têko	Chargé de Recherche / Université de Poitiers	Rapporteur
Marinas, Alberto	Professeur / University of Cordoba	Examinateur
Guillard, Chantal	Directeur de Recherche / CNRS Lyon	Directeur de thèse
Caravaca, Angel	Chargé de Recherche / CNRS Lyon	Co-directeur de thèse
Vernoux, Philippe	Directeur de Recherche / CNRS Lyon	Invité

Université Claude Bernard – LYON 1

Président de l'Université	M. Frédéric FLEURY
Président du Conseil Académique	M. Hamda BEN HADID
Vice-Président du Conseil d'Administration	M. Didier REVEL
Vice-Président du Conseil des Etudes et de la Vie Universitaire	M. Philippe CHEVALLIER
Vice-Président de la Commission de Recherche	M. Petru MIRONESCU
Directeur Général des Services	M. Pierre ROLLAND

COMPOSANTES SANTE

Département de Formation et Centre de Recherche en Biologie Humaine	Directrice : Mme Anne-Marie SCHOTT
Faculté d'Odontologie	Doyenne : Mme Dominique SEUX
Faculté de Médecine et Maïeutique Lyon Sud - Charles Mérieux	Doyenne : Mme Carole BURILLON
Faculté de Médecine Lyon-Est	Doyen : M. Gilles RODE
Institut des Sciences et Techniques de la Réadaptation (ISTR)	Directeur : M. Xavier PERROT
Institut des Sciences Pharmaceutiques et Biologiques (ISBP)	Directrice : Mme Christine VINCIGUERRA

COMPOSANTES & DEPARTEMENTS DE SCIENCES & TECHNOLOGIE

Département Génie Electrique et des Procédés (GEP)	Directrice : Mme Rosaria FERRIGNO
Département Informatique	Directeur : M. Behzad SHARIAT
Département Mécanique	Directeur M. Marc BUFFAT
Ecole Supérieure de Chimie, Physique, Electronique (CPE Lyon)	Directeur : Gérard PIGNAULT
Institut de Science Financière et d'Assurances (ISFA)	Directeur : M. Nicolas LEBOISNE
Institut National du Professorat et de l'Education	Administrateur Provisoire : M. Pierre CHAREYRON
Institut Universitaire de Technologie de Lyon 1	Directeur : M. Christophe VITON
Observatoire de Lyon	Directrice : Mme Isabelle DANIEL
Polytechnique Lyon	Directeur : Emmanuel PERRIN
UFR Biosciences	Administratrice provisoire : Mme Kathrin GIESELER
UFR des Sciences et Techniques des Activités Physiques et Sportives (STAPS)	Directeur : M. Yannick VANPOULLE
UFR Faculté des Sciences	Directeur : M. Bruno ANDRIOLETTI

Acknowledgments

First of all, I would like to thank my supervisor, Dr. Chantal Guillard, as the research director at CNRS, who is a hard-working, efficient, strong, brave person and good at communication. Since the first day we met, she has given me tremendous support, meticulously discussed every detail of my projects with me and respected my ideas with a kind attitude full of smiles. Besides, she supported me to attend academic conferences to expand my scientific vision and shared with me her understanding both academically and in life. I have learned her excellent qualities in guiding and supporting her students as a supervisor and a positive attitude towards life as a strong person.

Secondly, I would like to thank my co-supervisor Dr. Angel Caravaca, who gave me very detailed guidance in the field of electrocatalysis and taught me a rigorous scientific research attitude and a life-work balance. I enjoy every communication with him because he always gives positive affirmations saying "Alice, YOU ARE THE BEST", which gives me the strength to face all the difficulties in the research process. I always keep his teaching in mind: "Write honestly what you have verified, not what others want", whether in scientific research or life, he taught me to be a straightforward person.

Then, I would like to thank our engineer Dr. Frederic Dappozze, who is a hero to our group members, always helping us solve many problems during the experiments. He taught me meticulously about the use of HPLC, helped me establish the reaction setups, and aided me to deal with many documents. He always gives me positive feedback at the first time, efficiently supports my experiments, and cares about people's emotions and their lives. He is humorous, kind, and talkative, and lets me understand many aspects of French history, culture, social life, humanities, and natural landscapes.

Furthermore, I would like to thank Dr. Philippe Vernoux, the head of the research group, who participated in all my research projects, from data analysis, graph discussion, and paper writing, he did his best to support and provided a lot of valuable constructive comments. He cares about the safety of his students and always inspects the lab meticulously. I feel pleasure and blessed to work in the supportive, cohesive, and friendly team that he leads. Our team members, Dr. Jesus González-Cobos meticulously revised and discussed my paper, Nicolas gave me a lot of help in the construction of the photoelectrocatalytic device, and Brenda is my French study and essay writing partner. Besides, Antoinette, Essyllt, Christian, Matthieu, Clement, Weidong, Bomin, Xinke, Dandan, Feng, Xiaolong, Marwa, Insaf, Nouha, Ziba, Eya, Eddy *etc.*, all of them have given me aid during these three years.

Additionally, I would also like to thank my master's supervisors Prof. Juying Lei, Prof. Yongdi Liu and Prof. Jinlong Zhang, they care about my study and life in France even though they are thousands of miles far from me. When the epidemic was in the worst situation, Prof. Lei mailed me precious masks; on the traditional Chinese festival Mid-Autumn Festival, Prof. Liu sent me blessings; when I applied for a postdoctoral program, Prof. Zhang gave me great support.

In particular, I would like to thank the China Scholarship Council for its funding support, the director of IRCELYON Dr. Catherine Pinel for welcoming me to her laboratory, the scientific service center and the Spanish team from the University of Córdoba, for providing the detailed characterization of catalysts, as well as engineers at the workshop for reactor design and repairing!

Finally, I would like to thank my beloved family. Thanks to my father, Mr. Yu, who is always proud of his girls and pursuits of truth and knowledge. Thanks to my mother, Ms. Zhang, who always respects my decisions and supports all my choices with an optimistic attitude. Thanks to my little sister Lin Qing, who is one of the most powerful motivations in my study and life. She bravely took on family responsibilities when I was unable to return home to take care of my family due to the epidemic of Covid 19. Thanks for their love and concern for surrounding me, fulfilling my heart, and making me become a brave and kind person! Besides, I would like to thank my good friends, Liao Baoxin, Lei Libin, Yang Jiarui, Zhou Xinwen, Peng Yulan, Wang Huan, Chen Cuirong and Zeng Ximei for giving me a lot of spiritual support during my Ph.D.

All in all, thanks to everyone who has appeared in my life and participated in completing the thesis in the past three years! I am so grateful to meet you and you are my fondest memory of this beautiful city of Lyon.

Abstract

Our thesis presents the photocatalytic (PC) and photoelectrocatalytic (PEC) oxidation of glycerol into high value-added products via WO_3 catalysts synthesized by a hydrothermal process (with and without calcination), and compares its performance with commercial materials TiO_2 anatase (A), rutile (R), A/R and A/5% WO_3. By photocatalysis, the acidity of WO_3 promotes the formation of glyceraldehyde by selectively activating C-O bonds and facilitating its desorption into the liquid phase. Selectivity towards glyceraldehyde around 30% was obtained with WO_3-based catalysts, while TiO_2-based materials favoured the undesired mineralization of glycerol. The PEC study in the traditional single-chamber three-electrode cell showed an enhancement of glyceraldehyde and dihydroxyacetone (DHA) production to 4.5 and 11.5 times, respectively, at 1.5 V vs. Ag/AgCl, with a stable faradaic efficiency greater than 50%. Finally, an advanced dual-compartment cell (allowing temperature control) with a proton exchange membrane (PEM) and a WO_3-based photoanode was designed and developed in order to generate H_2 on the cathode side and valorize glycerol on the anode side. Glyceraldehyde and DHA production rates of 11.1 and 5.2 mmol m^{-2} h^{-1} at 60 ºC and 1.2 V of cell voltage, together with a production of 44 mmol H_2 m^{-2} h^{-1} were achieved, respectively.

Résumé

Nos travaux de thèse présente l'oxydation photocatalytique (PC) et photoélectrocatalytique (PEC) du glycérol en produits à haute valeur ajoutée en présence de catalyseurs WO_3 synthétisés par procédé hydrothermal (avec et sans calcination) et comparent leurs performances avec des matériaux commerciaux TiO_2 anatase (A), rutile (R), A/R et A/5% WO_3. Par photocatalyse, l'acidité de WO_3 favorise la formation du glycéraldéhyde en activant sélectivement les liaisons C-O et en facilitant sa désorption en phase liquide. Des sélectivités d'environ 30% sont obtenues avec les matériaux à base de WO_3. Les catalyseurs purement TiO_2 favorisent quant à eux la minéralisation du glycérol. L'étude PEC dans la cellule traditionnelle à trois électrodes a permis de montrer une augmentation du rendement en glycéraldéhyde et dihydroxyacétone (DHA) d'un facteur de 4,5 et 11,5 respectivement en présence de 1,5 V vs. Ag/AgCl avec une efficacité faradique stable supérieure à 50%. Finalement une cellule à double compartiments avec une membrane échangeuse de protons (PEM) et une photoanode WO_3 permettant le control de la température a été conçue afin de générer H_2 du côté cathodique et valoriser le glycérol du côté anodique. Des vitesses de production de glycéraldéhyde et DHA de 11,1 ; 5,2 mmol m^{-2} h^{-1} simultanément avec la production de 44 mmol m^{-2} h^{-1} d' hydrogène à 60 ºC avec une tension de cellule de 1,2 V sont respectivement obtenues.

Abbreviations

NMR	Nuclear magnetic resonance spectroscopy
A	Anatase
BET	Brunauer−Emmett−Teller
BJH	Barrett-Joyner-Halenda
CB	Conduction band
CO_2RR	CO_2 reduction reaction
CV	Cyclic voltammetry
DHA	Dihyroxyacetone
DRIFTS	Diffuse reflectance infrared Fourier transform spectroscopy
DRS	Diffuse reflectance spectroscopy
DSSC	Dye-sensitized solar cell
EC	Electrocatalysis
EPR	Electron paramagnetic resonance
ESI	Electronic supplementary information
FE	Faradaic efficiency
FTIR	Fourier-transform infrared spectroscopy
HER	Hydrogen evolution reaction
HOMO	Highest occupied molecular orbital
HPLC	High-performance liquid chromatography
HRTEM	High- resolution transmission electron microscopy
IPCE	Incident photon to current efficiency (IPCE)
IR	Infrared radiation
ITO	Indium-tin- oxide
LSV	Linear sweep voltammetry
LUMO	Lowest unoccupied molecular orbital
MEA	Membrane electrode assembly
NRR	N_2 reduction reaction
OER	Oxygen evolution reaction
ORR	Oxygen reduction reaction
PC	Photocatalysis
PEC	Photoelectrocatalysis

PEM	Proton exchange membrane
R	Rutile
RHE	Reversible Hydrogen Electrode
RID	Refractive index detector
ROS	Reactive oxidation species
SEM	Scanning electron microscopy
TC	Thermal catalysis
TOC	Total organic carbon
UV	Ultraviolet
Vis	Visible
VB	Valance band
WOR	Water oxidation reaction
XPS	X-ray photoelectron spectra
XRD	X-ray diffraction

Table of Contents

General Introduction

The generation of high-value-added chemical energy from sustainable sources by the means of an efficient and cheap process is a huge challenge for the replacement of petroleum products. Biomass, one of the most considerable renewable sources of carbon available in large quantities in nature, is regarded as a carbon-neutral sustainable resource for bioenergy and bio-material fabrication. In particular, biodiesel, an attractive alternative to fossil fuels, is generated more and more from biomass, of which production increases year by year and is forecasted to remain at a high level. However, glycerol is a considerable byproduct of biodiesel formation. For each 1 ton of biodiesel produced, approximately 100 kg of glycerol is generated. So how to well utilize glycerol to avoid waste of resources, air pollution, and CO_2 emission caused by simply burning or unselective oxidation of glycerol is of great significance.

Glycerol oxidation products are various, such as dihydroxyacetone (DHA), glyceraldehyde, glyceric acid, tartronic acid, formic acid, *etc*. Among them, C_3 products like glyceraldehyde and DHA are more valuable than other C_1 products like formic acid. To selectively oxidize glycerol to C_3 products rather than other C_2/C_1 products and limit CO_2 emissions has been the research hotspot.

A lot of research via catalytic processes is performed to generate valuable products from glycerol. However, the extensive functionalization of the glycerol molecule with hydroxy groups of similar reactivity renders its selective conversion particularly difficult, costly and non-environmentally friendly.

Photocatalysis (PC) could be an interesting process to elaborate valuable products from glycerol. Actually, photocatalysis allows redox reactions at room temperature, and atmospheric pressure by using a semiconductor activated with energy equal to or higher than its bandgap. This technology has already shown its potential in the treatment of toxic refractory organic

pollutants by completely oxidizing the organic pollutants. However, few publications deal with photocatalytic glycerol oxidation and most of them use only pristine TiO_2 as photocatalysts with the main objectives, the investigation of the reactional pathways for glycerol mineralization rather than optimizing the photocatalyst and the experimental conditions to generate valuable products with good selectivity. In addition, WO_3 with well-known acidity could be a good option to valorize glycerol due to the fact that acidity plays an important role in the selective oxidation of organics. Hence, it is of necessity and feasibility to investigate the valorization of glycerol into high-added-value products by photocatalysis over WO_3-based materials.

As we know, photocatalytic efficiency is generally hindered by the fast recombination of photo-induced carriers. Photoelectrocatalysis (PEC) which combines electrochemistry technology to provide an external bias to accelerate the directional movement of electrons to further separate photo-generated charges has emerged as a promising way for biomass conversion with simultaneous hydrogen production. However, very few PEC studies have successfully produced value-added oxidation products such as glyceraldehyde or DHA, especially under near-neutral conditions. Furthermore, most of the studies performed in 3-electrode cells only focused on one of the half-reactions, using anodes containing noble metals, or strongly acidic or basic media, which entails a lack of overall efficiency and chemical separation. Therefore, in this study we proposed, for the very first time, to systematically perform the PC or PEC oxidation of glycerol towards added-value products with WO_3-based materials.

In Part I, the homemade WO_3 and commercial WO_3/TiO_2 (DTW5) were compared with state-of-the-art TiO_2-based photocatalysts (Anatase, Rutile, and P25) on their performance of PC glycerol valorization. It is found that TiO_2 favours the mineralization of glycerol to undesired gas product CO_2, while WO_3-based materials exhibit an outstanding selectivity towards one of

the most valuable oxidation products: glyceraldehyde. It was attributed to their enhanced acidity, which selectively activates C-O bonds in glycerol and facilitates the further desorption of glyceraldehyde to the liquid phase. Due to the good crystallinity and electronic properties, the commercial DTW5 possesses superior kinetics and considerable glyceraldehyde selectivity. Thus, this work establishes a new starting point toward the development of advanced WO_3-based materials for an efficient valorization of glycerol.

In Part II, a monoclinic defect-engineered WO_3 catalyst was synthesized by a simple hydrothermal and post-calcination method for the selective PEC glycerol oxidation for the generation of these C_3 chemicals in a 3-electrode cell under natural conditions. Its outstanding PEC activity and stability were observed compared to the commercial catalyst DTW5. Among all liquid products, the joint selectivity of glyceraldehyde and DHA remained above 87% in the potential range of 0.5-2.0 V vs. RHE. Additionally, the effect of the electric polarization on the PEC glycerol valorization has been investigated. We found that glyceraldehyde and DHA synthesis was enhanced up to 4.5 and 11.5 times, respectively, by means of the external bias with a stable faradaic efficiency above 50% of the additional holes hypothetically generated, in the whole studied potential range. Furthermore, by comparison with DTW5, the influence of the applied potential and the catalyst activity for water oxidation in the glycerol reaction mechanism are discussed, as well as the key role of the sub-stoichiometric tungsten oxide content and the corresponding catalyst oxygen vacancies along with suitable acid sites, which together confer unpreceded properties to WO_3-based materials for the selective PEC valorization of glycerol.

In Part III, a pioneering dual-compartment PEC cell with a proton-exchange membrane (PEM) and a WO_3 photoanode under near-neutral conditions to address all mentioned bottlenecks of traditional PEC cell at once for PEC valorization of glycerol to generate hydrogen and value-added organics. The influence of light irradiation, external bias and cell

temperature has been studied, leading to maximum glyceraldehyde and DHA production rates of 11.1 and 5.2 mmol m^{-2} h^{-1} at 60 ºC and 1.2 V at the anodic side, along with the production of 44.0 mmol H_2 m^{-2} h^{-1} at the cathodic side. Besides, the long-term stability of the PEC cell has been evaluated and the results have been discussed by disclosing the PC, electrocatalytic (EC) and thermocatalytic (TC) effects on the overall performance of solar to chemical energy conversion. PEC has proved to be the most promising among the explored technologies, opening significant prospective for developing biomass valorization processes with simultaneous H_2 generation.

Chapter 1

Basic Comprehension and Future Trends in Photoelectrocatalysis: a mini-review

Jie Yu, Jesús González-Cobos, Frederic Dappozze, Philippe Vernoux, Angel Caravaca,* Chantal Guillard *

Univ Lyon, Université Claude Bernard Lyon 1, CNRS, IRCELYON, F-69626, Villeurbanne, France

E-mail: angel.caravaca@ircelyon.univ-lyon1.fr, chantal.guillard@ircelyon.univ-lyon1.fr

1. Introduction

Photocatalysis (PC) technology has attracted the attention of scientists since it was discovered by Fujishima and Honda in 1972, aiming to produce O_2 and H_2. [1] Under the irradiation of light, semiconductor materials could harvest the light energy to activate electrons that transited from the valance band (VB) to the conduction band (CB) and accordingly generate positive charge carriers (holes) in the VB. The photogenerated electrons and holes could react with oxidants (e.g., O_2 in air conditions) and reductants (e. g., H_2O or organics), respectively, to produce free radicals and together conduct redox reactions. Up to now, PC technology has been widely used in many fields such as pollutant degradation, [2,3] chemicals photosynthesis, [4,5] energy production, [6,7] and sterilization, [8–10] among others. Its efficiency depends on many parameters: physicochemical properties of materials, light source, environmental conditions such as temperature, humidity, pH, *etc*. Among them, the physicochemical properties of the semiconductors is the key point. To this date, the physical design of these materials and their chemical modifications have been widely developed, mainly in order to enhance the lifetime of the photogenerated charge carriers (electrons and holes), and the light response of the photocatalysts.

Regarding the physical design, introducing special structures like 1-dimensional (1D) quantum dots, [11–13] 2-dimensional (2D) nanowires, [14,15] 3-dimensional (3D) photonic crystals, [16,17], *etc*. are common approaches. As for the chemical modifications, a wide variety of different approaches have been already reported, [18] including the loading of metals onto the

surface of the semiconductors. [19] These modifications generally lead to the change in the surface area, bandgap, crystallinity and particle size, defects, acidity or basicity, *etc*., which could significantly affect the PC performance.

On the other hand, in recent decades, except for these two traditional methods (physical and chemical modifications), photoelectrocatalysis (PEC) technology has emerged to function as an extremely efficient tactic to considerably improve the PC performance. It utilizes an electric field to foster the electrons shifting directionally for the purpose of hindering the recombination of the photo-generated carriers [20,21] The PEC approach exhibits the following significant advantages: i) environmentally friendly; ii) high-efficiency; iii) it could be used for a wide variety of applications. [22,23] First of all, it uses clean energy (potentially sunlight) to drive the reactions based on the principles of PC. Secondly, the combination of electrochemical methods via applying an external bias, together with the traditional modification procedures of photocatalysts, can drastically improve the overall catalytic efficiency. Thirdly, its applications could cover all applications of PC like water splitting [24–34] and artificial photosynthesis [35] and extend to multiple functions based on oxidation half-reactions such as organic pollutant removal, [36,37] water oxidation, [38,39] biomass valorization [40,41] or reduction half-reactions like hydrogen generation, [42–46] CO_2 reduction, [47–49] N_2 fixation. [50–52] Although lots of surveys of PEC have been reviewed, most of them focused on a selected application [24–27,30,32,33,35,46,53], the sole modification of photoelectrodes [20,22,54–57], or on the use of a wide variety of photocatalytic materials like WO_3, [58] CuO, [59] ZnO, [60,61] ZrO_2, [62] g-C_3N_4, [10,63,64] TiO_2, [65] Au-TiO_2, [66] $BiVO_4$, [67,68] rGO/$BiVO_4$, [69] Bi_2O_3/Ni-Bi_2O_3, [70] FeO, [71] hematite, [72] polyoxometalate, [73] ternary metal oxides, [74], *etc*. To the best of our knowledge, none of these studies review a systematic appraisal of the whole PEC process: from principles, experimental setups and materials, towards their applications. Thus, in this review, a comprehensive and brief discussion is presented to assist the readers to apprehend the fundamental aspects of this emerging technology, and to provide an effectual reference and inspiration for green solar-to-chemical conversion.

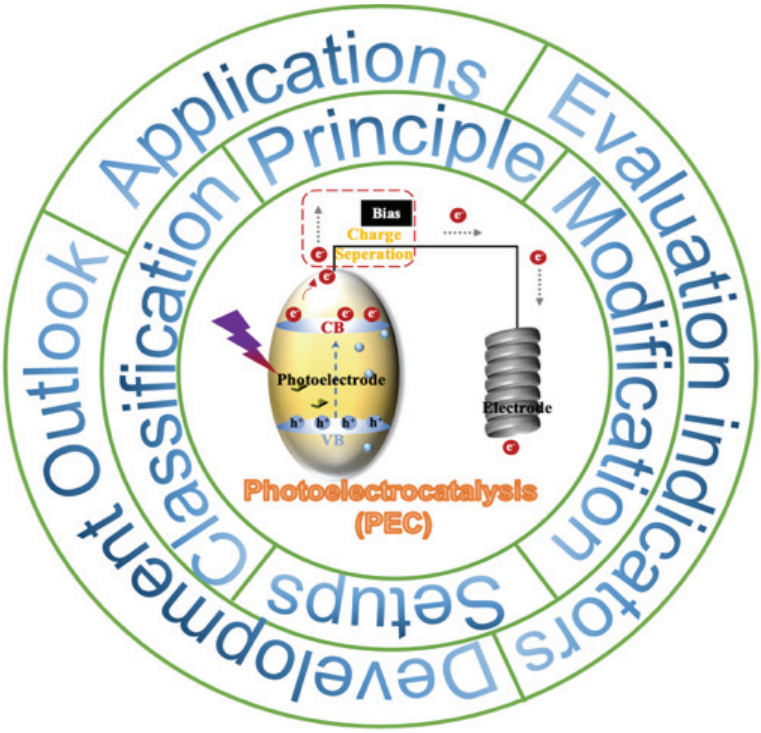

Fig. 1. 1. A brief description of the whole content of this review on the photoelectrocatalysis (PEC) system.

1. 1 Technology principle

PEC reactions operate based on the same principle of photo-generated interfacial charge transfer as PC. Under light irradiation (as long as the light energy ⩾ Semiconductors' bandgap energy), photo-generated electrons and holes are formed in the bulk of the semiconductor material used as a photocatalyst, and then separated and shift to the surface of photocatalysts to participate in redox reactions. Up to here, there is no difference between PEC and conventional PC. However, due to the external voltage, the directional movement of the charges is promoted, with a subsequent better separation rate in the PEC system, where at least two electrodes are required to be immersed into an electrolyte solution, and be connected to an external bias to close the electrical circuit, similar with electrocatalysis but exposed to the light irradiation. Therefore, the main difference between PC and PEC is that reactants and photocatalysts in the PC process are mixed in the same reactional environment, while PEC could be divided into two half-reactions (oxidation and reduction). Such reactions could happen separately in an anodic and a cathodic media, where the photocatalysts act as photoelectrodes (photoanode or photocathode).

The semiconductor that constitutes the photoelectrode is commonly the focus of research. It can be classified into two types: n-type semiconductor and p-type semiconductor. The

difference between them is that the electrons in n-type semiconductors undergo transitions and move directionally under photoexcitation. On the other hand, p-type semiconductors exhibit the movement of photogenerated holes due to the lack of free electrons. Therefore, the direction of the current generated by the two will be diametrically opposite (Fig. 1. 2). [75] Thus, generally, n-type semiconductors are served as photoanodes, whereas p-type semiconductors are applied as photocathodes. [27] Owing to the limited availability of p-type materials, at present, the most investigated photoelectrodes are n-type semiconductor materials, *e.g.*, TiO_2, WO_3, $BiVO_4$ and Fe_2O_3. Therefore, a common PEC system generally consists of an n-type semiconductor photoanode and a metallic cathode.

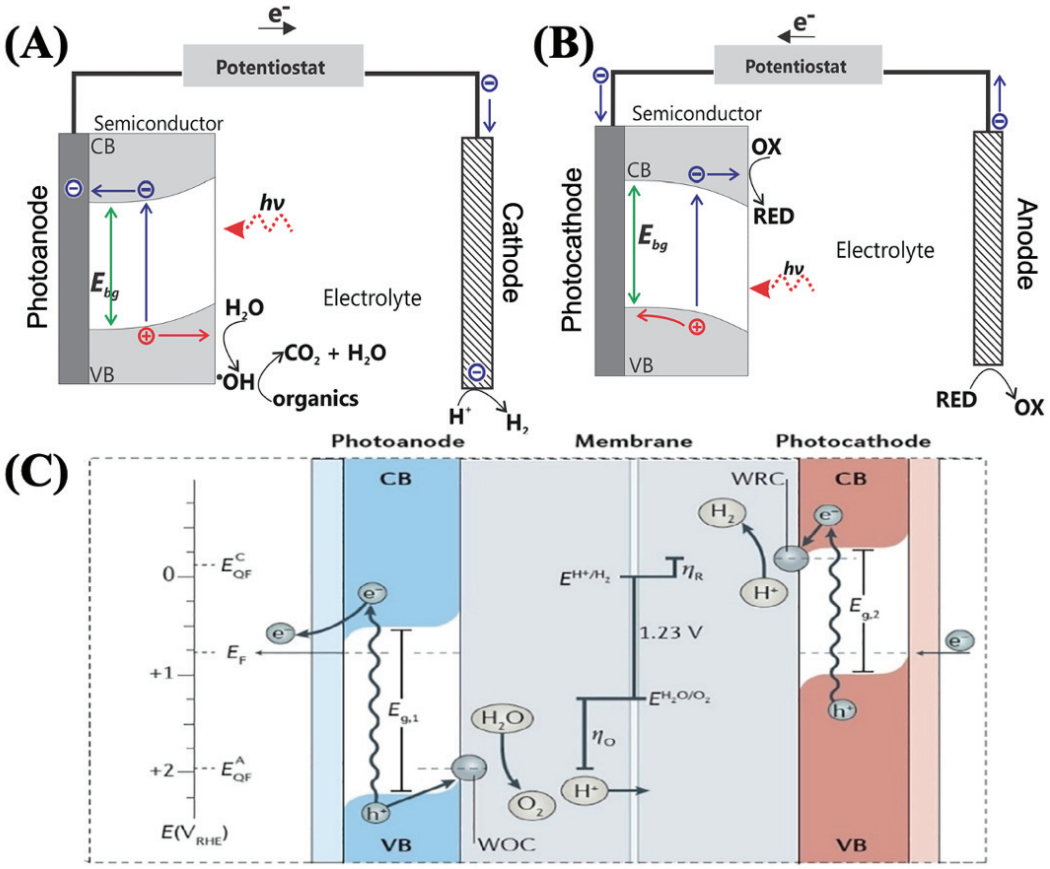

Fig. 1. 2. Mechanism of PEC for (a) n-type semiconductor, (b) p-type semiconductor from ref. [75] and the roles of these two types of materials in the PEC cell from ref. [27]

In a typical PEC system, oxidation reactions occur on the anodic photoelectrode (photoanode), where for instance, organic compounds are consumed to produce target chemical substances or mineralization of pollutants; on the cathode photoelectrode (photocathode), reduction reactions take place to generate molecules like H_2, CH_3OH or NH_3. Owing to the same

principle basis of PC, the PEC process also involves three vital steps: i) the light-harvesting, ii) separation and migration of photogenerated carriers and iii) the reactions between substrates and photo-electrons/holes as well as their derived radicals. Thus, PEC setups and experimental parameters consist of the light source, photoelectrocatalysts as electrodes and reactional chambers, *etc*., which will be discussed in the sections 1.2 and 1.3.

1. 2 Setups

PEC technology combines PC and electrochemistry. Although its principle is similar to that of PC, regarding the experimental setups, they are similar to those used for electrocatalysis purposes (EC). As opposed to the photovoltaics+eletrolyzers technology, with significant energy loss and complexity, PEC setups are more cost-efficient, and relatively simple. Conventional PEC tests are conducted in a three-electrode electrochemical setup including the working electrode (usually the anode/photoanode), the reference electrode such as a calomel electrode or an Ag/AgCl electrode, and the counter electrode (usually the cathode/photocathode), typically a Pt electrode with a large surface area, all of them submerged in an electrolyte solution to provide ionic conductivity. With these traditional reactors, research is mainly focused on the development of photoelectrocatalysts. To this date, the traditional three-electrode reactor has been unable to meet the needs of practical applications due to the fact that cathodic and anodic reactions occur in the same space. In other words, the reaction products obtained at the two electrodes are mixed in the same environment. Therefore, functional assemblies and separation of oxidation and reduction reactions by separators have been gradually developed.

In summary, PEC cells can be divided into four configurations: wired dual or single compartment(s), and wireless dual or single compartment(s), as shown in Fig. 1. 3a, named Conf. 1-4, respectively. Some details of those configurations are summarized on Table 1. 1. Among them, we consider that Conf. 1, i.e., wired-dual compartments is the most promising PEC cell, owing to the following merits on account of the presence of an external electrical circuit, and two separated compartments: i) ability to apply and measure (photo)currents and potentials, as well as to separately analyze the reaction products of both electrode compartments; ii) large electron pathlength; iii) electrode placement is flexible; iv) redox reactions are molecularly and spatially separated (Table 1. 1). [76] In this sense, both the H-cell and the proton exchange membrane (PEM) PEC cells are the most representative wired dual-compartment configurations. The former utilizes a fritted-glass to eliminate/reduce the

crossover of bubbles and the products recombination, while the latter uses a polymeric membrane with ability to conduct H^+ ions, in order to favor the ionic exchange, and to separate anodic and cathodic reactions. Due to the remarkable ohmic losses resulting from the typical larger distances between the electrodes of the H-cell, the PEM PEC cell is considered a more advanced and promising cell, in which the ionic transport distance is much shorter, on account of the so-called membrane electrode assembly (MEA) (Fig. 1. 3b).

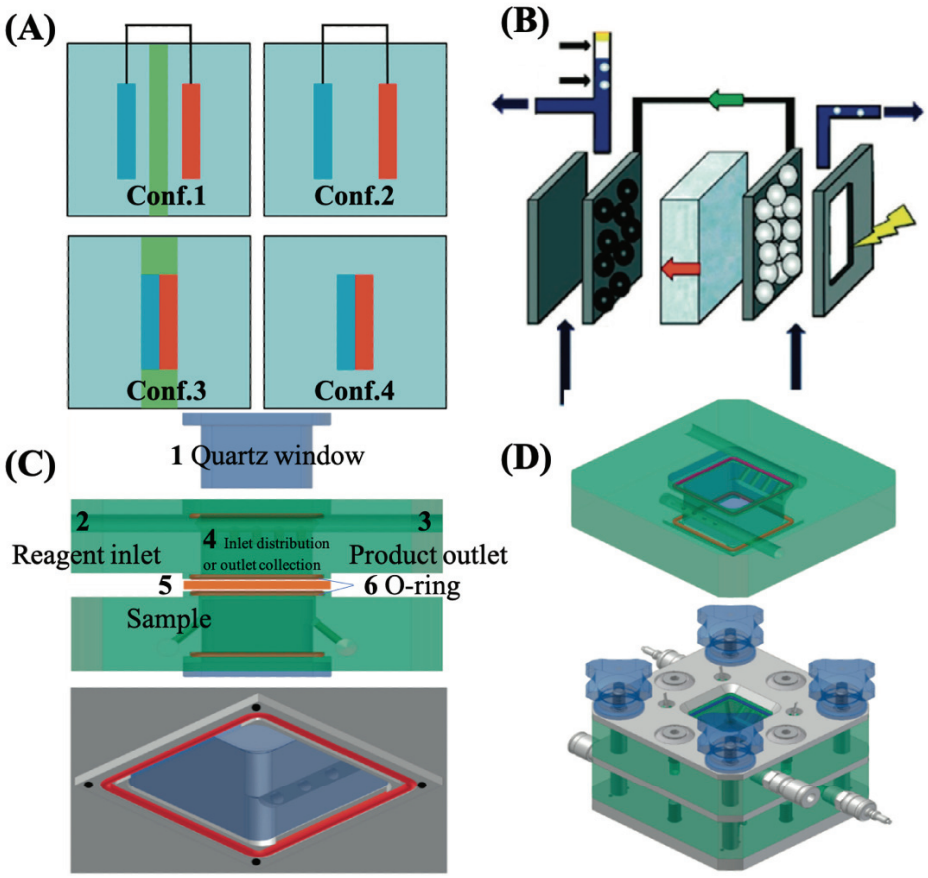

Fig. 1. 3. (a) Schematic representation of Conf. 1-4 as well as electrodes and molecular separators in PEC cells. Anode, cathode and separator is marked in Red, blue and green, respectively; (b) a typical Conf. 1 PEC cell; (c) side and top view of Conf. 1 PEC cell and (d) Assembled PEC cell from ref. [76]

A PEM PEC setup is typically composed of i) a translucent glass such as Pyrex® and quartz to allow visible and UV-light illumination irradiating onto the photoelectrode; ii) Chemically inert joints made of polymer materials such as Teflon® (or PolyEther Ether Ketone) to separate the two modular half-cells; iii) O-rings to seal the window; v) metal-based connectors to link the electrodes to a potentiostat-galvanostat (Fig. 1. 3c, d). As for the MEA, it generally consists of a H^+ conducting Nafion® membrane sandwiched between the anode and cathode. Usually,

a few drops of Nafion® suspension are added on each side, acting as an adhesive and enhancing at the same time the overall ionic conductivity at the electrode/membrane interface. To prepare the MEA, the elements are placed between two chemically inert plates and pressed at a certain pressure (at least 1 ton) and relatively high temperature (~120 ºC) to achieve the vitreous transition of the membrane material, leading to the fusion of the electrodes with the membrane. [77,78]

Table 1. 1. Comparison of 4 configurations of PEC cell

Configurations	Characteristic	Advantage	Disadvantage
Conf. 1	Wired dual compartments With separator	i) Able to measure (photo)currents and potentials ii) Large electron pathlength iii) Electrode placement is flexible iv) Redox reactions are molecularly and spatially separated	Assembly is relatively complicated
Conf. 2	Wired single compartment Without separator	i-iii) Same with 1st-4th merits of Conf.1 iv) Easy to assemble	Redox reactions, cathodic and anodic reaction products are mixed
Conf. 3	Wireless dual compartments With separator	i) Redox reactions are molecularly and spatially separated	i) Electron pathlength is minimized while the ionic pathlength is enhanced ii) Unable to measure (photo)currents and potentials （Characterization is limited to product analysis）

Configurations	Characteristic	Advantage	Disadvantage
			iii) Monolithic structure requires relatively complicated assembly
Conf. 4	Wireless single compartment Without separator	i) The overall structure is relatively simple	i-iii) Same with 1st-3rd drawbacks of Conf.3 iv) Redox reactions, cathodic and anodic reaction products are mixed

1. 3 Key parameters of PEC operation

A PEC system combines light absorption, generation and separation of electron-hole pairs, transport of charge carriers, together with ionic and molecular reactions. Once a PEC device is selected, together with the choice of the photoelectrocatalyst, the reaction conditions become the main factor affecting PEC performances. Typically, experimental parameters include irradiation wavelength and intensity, electrolyte composition (concentration and pH), reactant flow rates, applied potentials and environmental factors (temperature and pressure). It is unneglectable for researchers to optimize the reaction system according to the different study/production goals combined with the environmental and economic efficiency to achieve the best activities with the lowest possible energy consumption.

Firstly, regarding the semiconductor materials for the photoelectrodes, they respond to different ranges of light according to their bandgap (Fig. 1. 4). [79] For example, TiO_2 electrode just absorbs UV light due to the wide bandgap of ~3.2 eV, while WO_3 semiconductor could expand light responding range to visible light because of its narrow bandgap (~2.6 eV). Generally speaking, the same-composition light source with higher intensity induces more photo-induced h^+ and e^-, resulting in better PEC performances. A more profound review of photocatalytic materials will be explained in section 2.

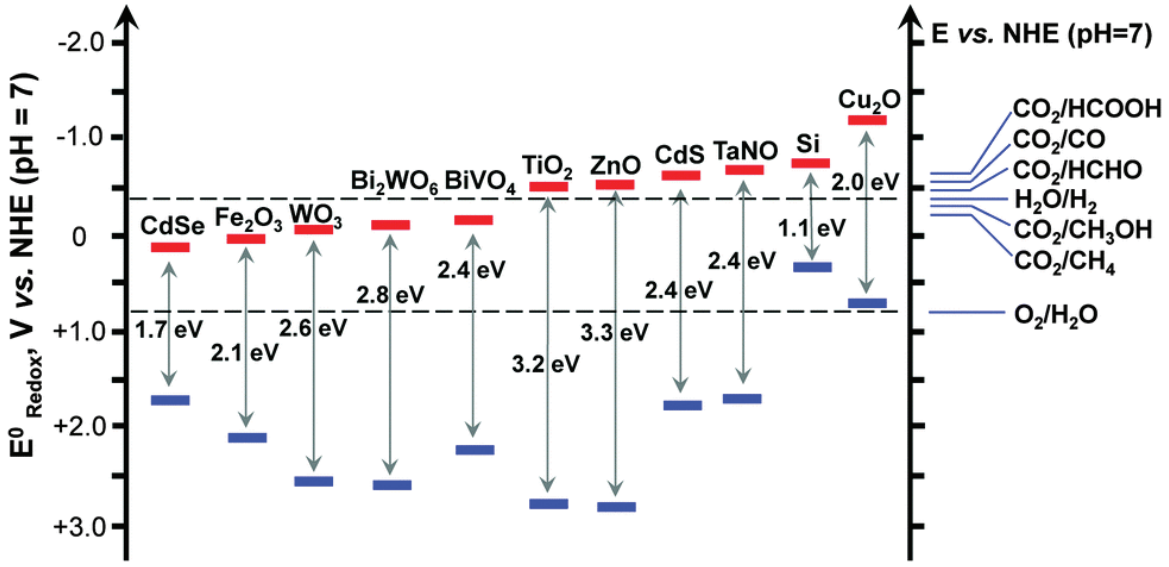

Fig. 1. 4. Band-edge positions of typical semiconductors relative to the energy levels of the redox couples where NHE stands for normal hydrogen electrode from ref. [79]

Secondly, the electrolyte plays a vital role in the exchange of the ionic species involved in the PEC system. Except for membrane-based electrolytes (*e.g.*, Nafion in PEM, which is doped with H_2SO_4 to favor H^+ conductivity), most liquid electrolytes are acid (*e.g.*, H_2SO_4, H_3PO_4) or alkaline solutions (*e.g.*, KOH, NaOH), which shift the system pH, and it could eventually affect the stability of the photoanode. In this sense, for instance, WO_3 is not stable in alkaline media, while $BiVO_4$ stability is favored in it. Also, it has been reported that strong acidic conditions with abundant H^+ ions may enhance the hydrogen production at the cathode (Hydrogen Evolution Reaction, HER) and generate additional super-oxidants (*e.g.*, H_2O_2, depicted in equations (2-3) in section 3. 1. 2), hence generally benefiting, for instance, the oxidation of organic species. [80] However, the use of strong acids or bases increases the safety risks of storage and transportation in view of the further industrialization of the PEC technology. Regarding reactant flow rates, a higher flow improves the mass transfer and eventually enhances the kinetics for the redox reactions. However, an excessively high reactant flow rate leads to the catalyst-drag from the (photo)electrodes, eventually decreasing the PEC performances.

Thirdly, the applied potential is of great significance to the PEC process. Given any external applied potential, the electrocatalytic (EC) activity, proportional to the obtained electrical current, could be remarkably improved upon irradiation. Likewise, the PC performance is enforced by the enhanced separation rate of photo-generated charge carriers. For traditional three-electrode PEC cells, the applied voltage needs to be modified and calculated based on

the pH and the used reference electrode, according to the Nernst function, to be compared with the Reversible Hydrogen Electrode (RHE), commonly used as a reference state. For instance, if an Ag/AgCl reference electrode is used:

$$E\ (RHE) = E_{Ag/AgCl} + 0.059\ pH + E^{0}_{Ag/AgCl} \quad (1)$$

Where $E^{0}_{Ag/AgCl} = 0.1976$ V at 25 °C and $E_{Ag/AgCl}$ is the applied potential.

However, for two-electrode PEM PEC cells (where the reference electrode is removed), the applied potential in the reaction system (anode vs cathode) is an absolute cell voltage. It should be pointed out that the application of high external potentials (as well as high temperature) may cause the water electrolysis reaction (thermodynamically possible from cell potentials higher than 1.23 V at room temperature, as shown in Fig. 1. 5).

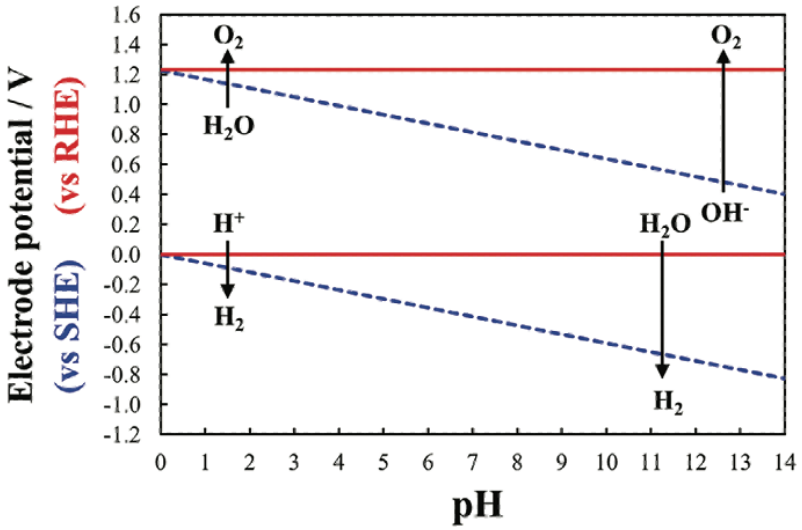

Fig. 1. 5. Pourbaix diagram of two half-reactions in the water splitting under standard conditions. SHE stands for the standard hydrogen electrode and RHE stands for the reversible hydrogen electrode from ref. [80]

Similarly, the selection and optimization of parameters such as temperature, pressure and the concentration of dissolved oxygen need to be carried out according to the type of PEC application. High pressure enhance gas molecule concentration per unit volume and thus enhance its transfer and contact with the photoelectrocatalysts, increasing therefore the kinetics of PEC gas-phase reactions, such as N_2 fixation and CO_2 reduction. On the other hand, an increase of the reaction temperature may accelerate the charge recombination of the PC process, which could be generally counterproductive for the overall PEC performance. Also, high temperature generally decreases the solubility of the reactant gases in the solvent and consequently hinders the production rate of target products. [81] Dissolved oxygen is beneficial for the generation of $\cdot O_2^-$, which are proved to be essential to decompose antibiotics in PEC

processes, [82] but O_2, as a scavenger of photo-induced electrons, consumes H^+ during reduction consequently competing with HER. [83]

In summary, many factors can remarkably affect both EC, PC and PEC processes with respect to redox efficiency, operational cost, system complexity and practical safety. Reasonable optimization of parameters to meet actual needs is a crucial part of PEC research.

2. Catalysts

The current research on PEC is mainly focused on the design and modifications of the photoelectroatalysts, which are the core of the PEC system. According to the composition, we will classify the photocatalytic materials as single-component catalysts, binary hybrid cocatalysts, and multi-component cocatalysts. Table 1. 2 shows a selection of photocatalyst representatives for PEC systems. Their classification, applicability and modification methods will be discussed in this section.

2. 1 Single-component catalysts

In this family of Single-component catalysts we will include the supported noble metal catalysts, metal oxide catalysts and non-metal-based catalysts. Generally speaking, upon the activation of light, the transition of electrons occurs, resulting in the generation of free radicals and/or promoting the occurrence of redox reactions. However, photogenerated electrons and holes are prone to recombine, and the recombination rate affects in a significant manner the performance of PEC. Supported noble metal-based catalysts, such as gold (Au), silver (Ag), platinum (Pt), palladium (Pd), rhodium (Rh), ruthenium (Ru), *etc*., due to the existence of localized surface plasmon resonance (LSPR), possess high PEC performance (superior kinetics and selectivity). [84] LSPR is an optical phenomenon that the light excites conductive nanoparticles to form collective electron charge oscillations, that is to say, the deposited electric field from light can collectively excite electrons of a conduction band to form coherent localized plasmon oscillations with a resonant frequency, resulting in enhanced optical properties: i.e., improved the electric field intensity, light scattering and absorption, as well as surface-enhanced scattering from adsorbed molecules. [85][86] Usually, the interaction between the nano-scale noble metal particles and the support enhances the catalysts' surface properties, including geometry and surface electrons, thus exhibiting high (photoelectro)catalytic activity. However, the expensive prices and limited reserves of noble metal catalysts force researchers to shift attention to other non-precious metal catalysts.

TiO_2, a classic metal oxide photocatalyst, has been used since the initial attempts of PEC, aiming for the photolysis of water, in 1972. [1] Due to the mature, simple and non-toxic preparation procedures, it has become the most extensively developed catalyst in the fields of

PC and PEC. In addition, other metal oxides such as WO_3, ZnO, SnO_2, Fe_2O_3, Cu_2O and CuO are also widely used as photoeletrocatalysts (Table 1. 2). [87–93] Due to their different bandgap and band-edge positions (Fig. 1. 4), the corresponding photo-response ranges and capabilities of redox reactions are also very large. Therefore, a suitable selection of catalysts to meet the requirements of a given practical application is a vital step for the construction of a satisfactory PEC system. For instance, WO_3 is good for oxygen production due to the suitable VB position while Cu_2O is used for CO_2 reduction thanks to its adequately negative CB position.

Besides, binary oxides single-component semiconductors, such as $BiVO_4$, [94,95] $CuWO_4$, [96,97] $CaFe_2O_4$, [98,99] $CuFeO_2$, [100,101] $CuNbO_3$, [102,103] $LaFeO_3$, [104,105] Fe_2TiO_5, [106,107] and Bi_2WO_6 [108,109] are emerging to overcome the drawback of high price of noble metal catalysts and high recombination rate of photo-induced charges of metal oxides like TiO_2 or WO_3. Most of them could be used as photocathodes for PEC reduction reactions. [27] Among them, $BiVO_4$ is the most successful catalyst which could achieve 90% of solar-to-current capability. [110]

As for non-metallic catalysts, the carbon family, such as graphene, [111,112] C nanotubes, [113] *etc*. are the most popular materials. Additionally, N [114,115] and P [116,117] series catalysts also attract more and more attention.

The morphology and composition of these materials are highly related to light-harvesting, charge transfer and separation, and the surface reaction kinetics, thus affecting the photon-to-product (or current) conversion efficiency of the photoelectrode. [118,119] Therefore, as discussed in the introduction section, many strategies including physical and chemical modification methods have been taken to adjust the morphology (thickness, size, shape, *etc*.) and compositions (bandgap range, bandgap position, *etc*.), which deeply influence carrier-diffusion length, adsorption/desorption of chemicals, light response range, light path and its capability of passing reaction energy barriers. For instance, when the thickness and dimensions of catalysts have the same range as their carrier-diffusion length, the charge collection efficiency would be favorable.

The composition-tuning, including doping, defect engineering and crystal engineering, is proven to improve the physicochemical properties and the low charge carrier mobility of catalysts. Suitable dopants would benefit PEC reactions via enhancing their electrical and optical properties. Take $BiVO_4$ as an example, Gd^{3+} is introduced to substitute Bi^{3+} in $BiVO_4$ photoelectrode, ~2-fold photocurrent intensity for water splitting was achieved due to the enhanced carrier separation without affecting its catalytic and optical properties, since the charge carriers mobility of $BiVO_4$ is increased by 50 % (measured by time-resolved microwave

conductivity). It results from a higher degree of monoclinic lattice distortion of Gd-doped $BiVO_4$ (Fig. 1. 6a-b). [120] Additionally, partially replacing Bi^{3+} in $BiVO_4$ is in favor of PEC performance, as reported by Zhou *et al.*. 7% In^{3+}-doped $BiVO_4$ photoelectrode shows the optimal photoelectrochemical performance of water oxidation at 1.23 V vs. RHE, and a photocurrent density of 1.56 mA cm^{-2} was obtained over this catalyst, which is more than ~2 folds compared to the undoped $BiVO_4$ (Fig. 1. 6c). [121]

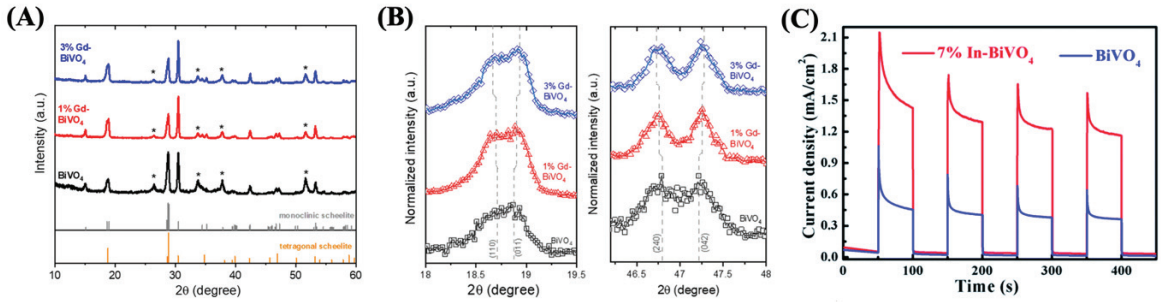

Fig. 1. 6. (a) X-ray diffractograms for undoped $BiVO_4$ and Gd doped $BiVO_4$ films on FTO substrates where the FTO peaks are marked with a star (*); (b) $2\theta = 18°$-$19.5°$ and $2\theta = 46°$-$48°$ range of the characteristic peak splitting of monoclinic scheelite from ref. [120]; (c) current density with time for pure $BiVO_4$ and 7% In^{3+} doped $BiVO_4$ films from ref. [121]

Except for substituting the elements of a single-component catalyst, the introduction of oxygen vacancies as well as porous structure, and the adjustment of crystal facets are also efficient strategies. [122] Take WO_3 as an example, Can Li's group fabricate WO_3 photoanodes with surface oxygen vacancies via a two-step flame heating approach (Fig. 1. 7a). Tuning the surface and bulk oxygen vacancies improved both the conductivity and trapping state density, thus resulting in 10 times increase in photoelectrochemical performance of WO_3 for water oxidation. [123] Morphology modification is a physical way to improve the PEC performance of photoelectrode, which generally results in a high surface area and enhanced capabilities regarding light-harvesting, charge separation and transfer. The common nanostructures include quantum dots, nanowires, nanotubes, nanosheets, nanospheres, mesoporous structures, photonic crystals and so on. [11–18] Chandra *et al.* prepared mesoporous structure WO_3 by an in-situ surfactant-thermal-carbonization method. The varied alkyl chain length of 2-(alkylaminomethyl)pyridine surfactant templates results in different size mesoporous structures of WO_3, as presented in Fig. 1. 7b. All modified WO_3 photoanodes obtained 5-7 times higher incident photon to current efficiency (IPCE) (24%-36%) than that (5%) of WO_3 without the introduction of porous structures. [124] Also, crystal engineering, which adjusts the exposure of certain crystal facets of catalysts shows the superiority of high selectivity and

yield rate of PEC redox reactions. Wang *et al.* combined the strategy of physical structure control with facet crystal engineering to fabricate (200) and (002) facets enriched WO_3 nanoplate arrays (Fig. 1. 7c) and obtained a remarkably high photocurrent density of 3.7 mA cm^{-2} at 1.23 V vs. RHE.

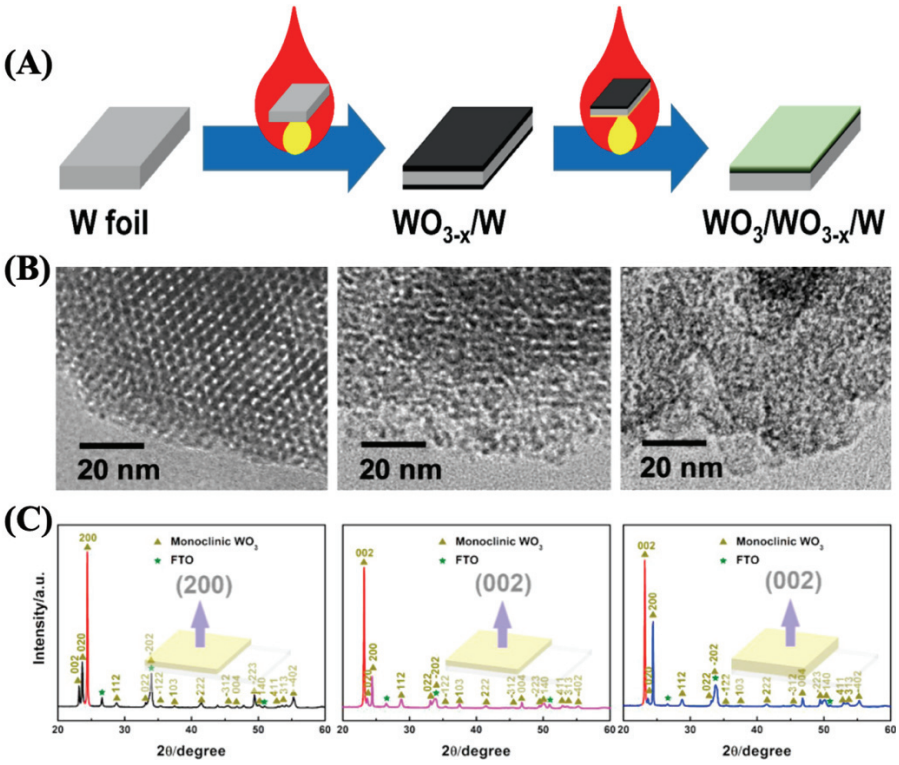

Fig. 1. 7. (a) Schematic illustration of the fabrication of defect engineered WO_3 via a two-step flame heating method; [123] (b) TEM images of as-prepared crystalline WO_3 with tunable mesoporous structure; [124] (c) XRD patterns and scheme of crystal facet exposure of crystal facet engineered WO_3 photoanode. The left sample is obtained via one-step hydrothermal treatment at180 ^oC for 16 h, the middle sample is via one-step hydrothermal treatment at 180 ^oC for 8 h, and the right sample is via two-step hydrothermal treatment at 180 ^oC for 8 h twice [125]

Although a single-component catalyst system seems strategically convenient regarding the synthesis and development point of view, it couldn't simultaneously provide suitable band edge positions, broad solar responding range and efficient charge separation and transport, thus requiring further improvement. In addition to the physical modification, one of the important strategies is to combine several strategic materials by chemical means, i.e., to couple a photocatalyst with a cocatalyst to form binary hybrid cocatalysts or multi-component

cocatalysts. The introduced component(s) participate in the catalytic reactions in some situations or just function to trap photo-induced charge carriers. In the latter situation, the co-catalytic components have two categories: reduction cocatalysts which trap electrons and provide active sites for the reduction half-reactions, and oxidation cocatalysts which can accept holes and supply reaction sites for oxidation half-reactions. [126]

2. 2 Binary hybrid cocatalysts

Noble metals are the most widely used and most effective reduction cocatalysts due to their excellent electron trapping capability, low overpotential for surface reaction, outstanding conductivity, and high durability. For instance, Esposito *et al.* modified WO_3 surface via the electrodeposition of Pt particles and applied this photoanode to the Methanol oxidation PEC process (aiming for the production of H_2). A significant increase in H_2 production rate (62 μmol h^{-1} cm^{-2}) was obtained at 0.8 V vs. RHE by Pt-WO_3, compared to pure WO_3 photoanode (21 μmol h^{-1} cm^{-2}) as shown in Fig. 1. 8a. [127] In addition, noble-metal-based alloys also have proved to be excellent reduction cocatalysts. For example, PtCu alloy with (730) facets was loaded on C_3N_4 nanosheets to improve the PC activity and selectivity of CO_2 reduction to CH_4. [128] In this case, (730) high-index facet possesses more low-coordinated metal active sites which increase the adsorption and activation of CO_2, while the introduction of Cu to Pt results in the synergistic effects between these two metals for high selectivity towards CH_4 (Fig. 1. 8b). However, as mentioned in the previous section, noble metals are scarce and expensive and suffer from the loss of stability in long-term reactions. Thus, low-cost and earth-abundant transition metals have already attracted researcher's attention to act as cocatalysts for reduction reactions. Mo, Ni, and Co-based photoelectrodes are good for HER. [129] Cobalt phosphide with hollow spheres was combined with silicon nanowire (SiNW) to obtain a binary hybrid SiNW/Co-P, which takes the advantages of morphology modification and composition-tuning. It leads to an enhanced performance of solar-driven H_2 evolution, presented by 18.2 mA cm^{-2} at 0 V vs. RHE, 91 times higher than that of the bare SiNW. [130]

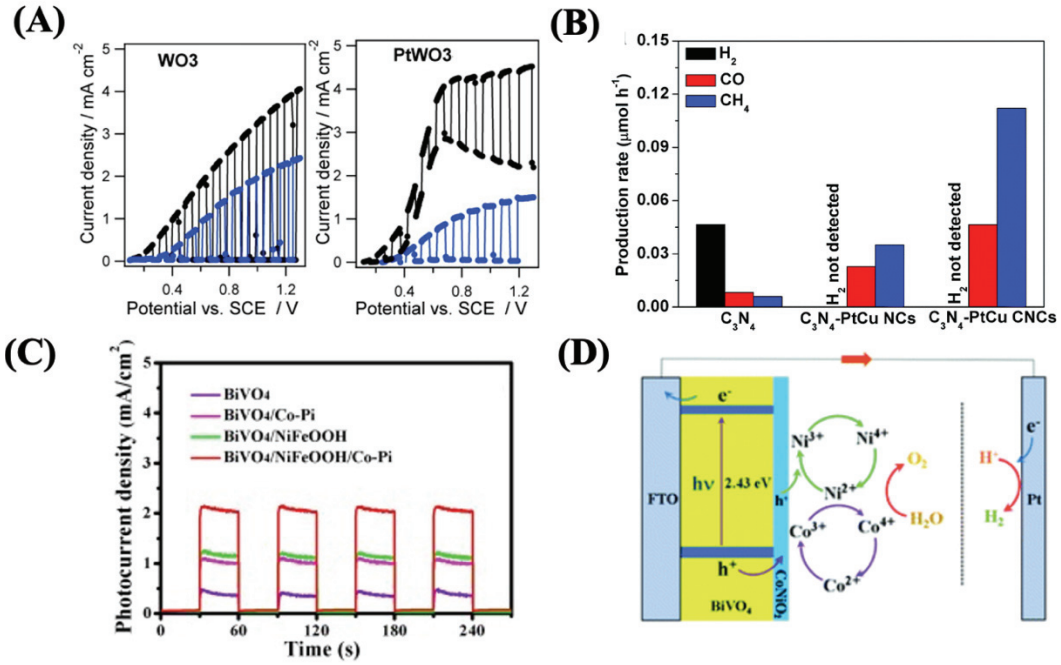

Fig. 1. 8. (a) Linear sweep voltammograms measured in 0.33 M H_2SO_4 (blue curves) and 1.0 M CH_3OH/0.33 M H_2SO_4 (black curves) over pure WO_3 and reduction cocatalyst Pt-WO_3. The non-zero dark current observed for the Pt-WO_3 in the CH_3OH-containing solutions is due to methanol oxidation under the simulated solar light source from ref. [127]; (b) Photocatalytic H_2, CO, and CH_4 evolution rates with C_3N_4, C_3N_4-PtCu NCs and C_3N_4-PtCu CNCs in the CO_2 reduction reaction under visible light irradiation from ref. [128]; (c) Photocurrent density of oxidation cocatalyst of $BiVO_4$/Co-Pi, $BiVO_4$/NiFeOOH, $BiVO_4$/NiFeOOH/Co-Pi, compared to pure $BiVO_4$ photoelectrode from ref. [131]; (d) the oxidation cocatalyst function of $CoNiO_2$-$BiVO_4$ for enhancing PEC water splitting performance from ref. [132]

Cobalt phosphates exhibit great performance for PEC oxidation reactions, where Co^{2+}/Co^{3+} of Co-Pi can be oxidized to a higher valence state of Co^{4+} after accepting holes, and then the obtained Co^{4+} could be further reduced to Co^{2+}/Co^{3+} quickly after participating in the PEC water/organic molecules oxidation reactions. Thus, PEC oxidation reactions could be improved by this redox cycle. [133] It was proven by Fang *et al.*'s research that the Co-Pi layer consumed the holes efficiently for the water oxidation in a binary hybrid $BiVO_4$/Co-Pi photoelectrode. Its activity was two times as high as that of pure $BiVO_4$, although the obtained photocurrent density (1.05 mA cm^{-2}) by this binary hybrid cocatalyst is not as good as the ternary multicomponent cocatalysts $BiVO_4$/NiFeOOH/Co-Pi (2.03 mA cm^{-2}) at 1.23 V vs. RHE (Fig. 1. 8c). [131] In addition, Fang *et al.* also investigated the functions of cocatalyst $CoNiO_2$ for enhancing PEC water splitting performance on $BiVO_4$ photoelectrode, proving that the novel

system allows: i) decreasing photo-induced hole-electron recombination centers; ii) acting as trapping sites to enhance charge separation; iii) improving the stability of the PEC system; iv) increasing active sites for reactions, and v) providing a lower overpotential of hydrogen generation (Fig. 1. 8d). Via this strategy of cocatalyst modification, a higher photocurrent density of 1.16 mA cm^{-2} at 1.23 V vs. RHE and a lower onset potential of ~0.06 V vs. RHE were observed over $BiVO_4/CoNiO_2$ photoanode, showing the superiority of the binary hybrid cocatalysts compared to the single-component catalysts $BiVO_4$ of which photocurrent density is 0.5 mA cm^{-2} at 1.23 V vs. RHE and onset potential is ~0.24 V vs. RHE. [132]

2. 3 Multi-component cocatalysts

Depending on the applications, the fundamental limitations of single-component or binary-hybrid catalysts related to bandgap energy, stability, and charge separation/transport, accelerate researchers to systemize ternary even multi-component hybrid cocatalysts to ensure efficient and stable PEC performances. [134] Some examples were already mentioned in the previous section. Additional conductive components could serve as strong binders to noble metals for enhanced catalytic stability and prevent the undesirable cation exchange between the semiconductors and noble metals. For instance, $ZnO/Ag/Ag_2WO_4$ was prepared via a successive ionic layer adsorption and reaction (SILAR) method by Nur *et al.*, where Ag/Ag_2WO_4 was deposited on the ZnO nanorods. [135] In this case, both the semiconductors absorb light and the well-constructed heterostructure of Ag_2WO_4/ZnO ensures the photo-induced electrons in the VB migrate to a higher potential of Ag_2WO_4 (-0.07 eV) from ZnO (-0.34 eV) where Ag_0 nanoparticles in the three-component cocatalyst acts as a bridge via the surface plasmon resonance (SPR) effect to achieve the effective charge separation and transfer (Fig. 1. 9a).

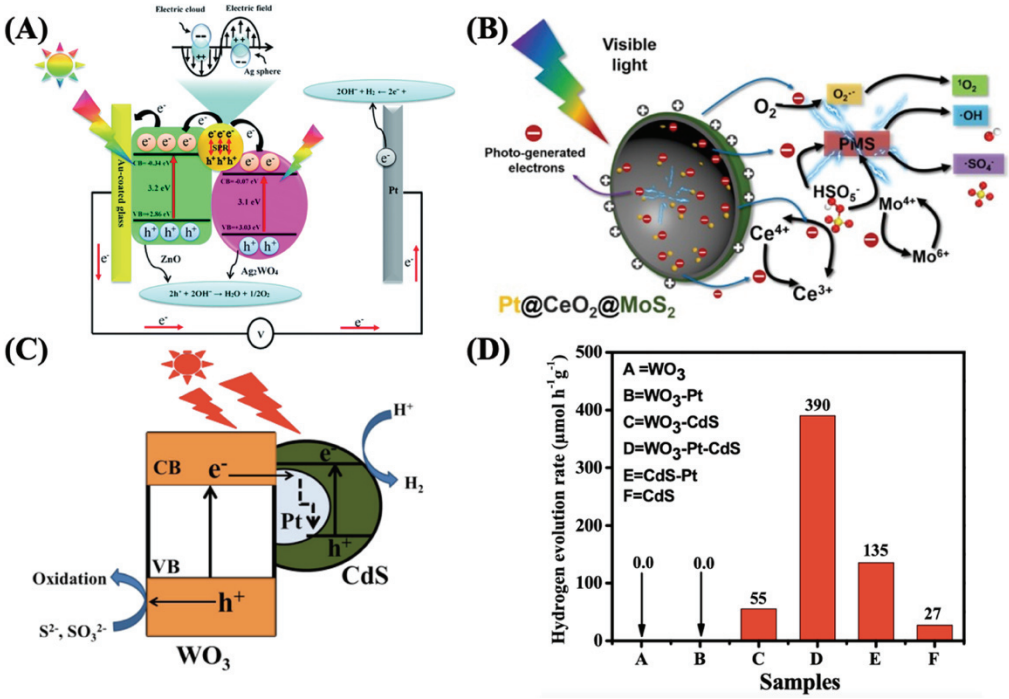

Fig. 1. 9. (a) ZnO/Ag/Ag_2WO_4 system; [135] (b) photo-electrocatalysis-assisted PEC/PMS system Pt@CeO_2@MoS_2 from ref. [136]; (c) the charge transportation in WO_3-Pt-CdS composite (d) comparison of hydrogen evolution rate between single component/binary cocatalysts and the trinary cocatalyst from ref. [137]

On the other hand, combined with morphology modifications and a reasonable reactional system design, a hollow-structured Pt@CeO_2@MoS_2 was fabricated by Dong *et al.* and applied in a photo-electrocatalysis-assisted peroxymonosulfate (PEC/PMS) system. [136] Pt was selected due to its excellent conductivity and good accumulation of photo-generated electrons in PEC process. The change of surface valence states (Ce^{3+} to Ce^{4+}) of Ce element and (Mo^{4+} to Mo^{6+}) of Mo element in this ternary catalyst contribute to enhancing the PEC performances of degrading pharmaceuticals and personal care products (PPCPs) by promoting the PMS activation. Besides it is found that photogenerated radicals as $O_2{\cdot}^-$, $SO_4{\cdot}^-$ and ·OH play dominant roles in the reactions (Fig. 1. 9b). In addition, a ternary WO_3-Pt-CdS composite was synthesized by Akple *et al.* where a Z-scheme was constructed due to the well-matched bandgaps of WO_3/CdS. Meanwhile, Pt acted as a bridge to accelerate the charge transportation between WO_3 and CdS (Fig. 1. 9c), resulting in higher hydrogen generation rate (390 μmol h^{-1} g^{-1}) than that of a single catalyst CdS (27 μmol h^{-1} g^{-1}), as well as binary cocatalysts WO_3-CdS (55 μmol h^{-1} g^{-1}) and CdS-Pt (135 μmol h^{-1} g^{-1}) (Fig. 1. 9d). [137]

Table 1. 2. Selected single-component or modified photoelectrocatalysts for PEC electrode

Photoelectro -catalyts	Roles	Classifications	Modifications	PEC applications	Ref.
TiO_2	Photoanode	Single-component	/	Water splitting	[1]
TiO_2 nanotube	Photoanode	Single-component	Physical	Water treatment & H_2O_2 production	[138]
g-C_3N_4/TiO_2 Nanotubes	Photoanode	Binary hybrid	Physical & Chemical	Water treatment	[139]
Pt-TiO_2 nanotubes Pt-rGO	Photoanode Photocathode	Binary hybrid Binary hybrid	Physical & Chemical Chemical	Artificial photosynthesis	[140]
N doped WO_3 WOx	Photoanode	Binary hybrid Single-component	Chemical	Water splitting	[87] [123]
TiO_2/WO_3	Photoanode	Binary hybrid	Chemical	Air treatment	[88]
ZnO	Photoanode	Single-component	/	Water splitting	[89]
CuO/ZnO	Photoanode	Binary hybrid	Physical & Chemical	Water splitting	[90]
Cu/Cu_2O/-$Cd(OH)_2$	Photocathode	Multi-component	Chemical	Hydrogen generation	[91]
SnO_2-TiO_2/QD	Photoanode	Binary hybrid	Physical & Chemical	Hydrogen generation	[92]
$BiVO_4$	Photoanode	Single-component	/	Water treatment	[141]
$BiVO_4$	Photoanode	Single-component	Physical	Biomass valorization & HER	[40]
FeCoOx/-$BiVO_4$	Photoanode	Binary hybrid	Chemical	Water splitting	[142]

Photoelectro-catalyts	Roles	Classifications	Modifications	PEC applications	Ref.
α-Fe_2O_3/-NiOOH	Photoanode	Binary hybrid	Chemical	Water oxidation	[93]
SnS_2-Pt Nanoplates	Photoanode	Binary hybrid	Physical & Chemical	Water oxidation	[143]
RuO_2/-$NaTaO_3$	Photocathode	Binary hybrid	Chemical	Hydrogen generation	[144]
Au/CeO_2-TiO_2	Photocathode	Multi-component	Chemical	Biomass valorization	[145]
Bi_2WO_6/-BiOCl	Photocathode	Binary hybrid	Chemical	CO_2 reduction	[146]
$CuBi_2O_4$/-TiO_2	Photocathode	Binary hybrid	Chemical	CO_2 reduction	[147]
Graphene-carbon nanotube/-Fe_2O_3	Photoanode	Multi-component	Physical & Chemical	Water oxidation	[148]
Ag/Ni-MOF/Cu_2O	Photocathode	Multi-component	Physical & Chemical	N_2 fixation	[149]
MoS_2/CdSe/-NiO	Photocathode	Multi-component	Chemical	Hydrogen generation	[150]
Pd/TiO_2 nanotubes	Photoanode	Binary hybrid	Physical & Chemical	Water treatment	[151]
CoNiFe/-Ta_3N_5 nanotubes	Photoanode	Binary hybrid	Physical & Chemical	Biomass valorization & HER	[152]
NiPi/Pi/-Fe_2O_3	Photoanode	Binary hybrid	Chemical	Biomass valorization & HER	[153]
$ZnFe_2O_4$/CdS/ZnO nanorods	Photoanode	Multi-component	Physical & Chemical	Hydrogen generation	[154]

Photoelectro-catalyts	Roles	Classifications	Modifications	PEC applications	Ref.
TiO_2-Cu_2O/Ru	Photoanode	Multi-component	Chemical	Water treatment & N_2 fixation	[155]

3. Applications

In this section, several applications of the PEC technology will be highlighted. Considering that oxidation and reduction reactions occur separately, the PEC applications will be classified according to the aim of the process. This way, in sections 3.1 and 3.2 we will discuss the features of some applications focusing either on oxidation and reduction processes, respectively, while section 3.3 deals with applications where both, oxidation and reduction reactions are efficiently valorized.

3. 1 PEC focused on oxidation reactions

3. 1. 1 Water or Air treatment

PEC water or air treatment is used to efficiently oxidize organic pollutants (e.g. antibiotics, dyes, *etc.*), aiming for their total mineralization into CO_2. The target oxidation process takes place in the anode of the PEC system, as depicted in Fig. 1. 10. In 1993, a pioneer study of PEC technology for organic pollutant treatment was published. The research results dealt with the efficient degradation of 4-chlorophenol by TiO_2-based thin film electrodes under ultraviolet irradiation. [36] Afterwards, great progress on PEC water or air treatment has been achieved gradually. In these applications, it has been proved that reactive oxidation species (ROS) play a crucial role for pollutant removal. For instance, Dong *et al.* developed MoS_2 nanoflakes as photoelectrode to degrade rhodamine B, chlorpyrifos, 4-chlorophenol, and ciprofloxacin under visible-light irradiation in a three-electrode system with Pt foil as a cathode and Ag/AgCl as a reference, where hydroxyl radicals were the relevant ROS. Besides, a series of reaction parameters was studied, including the applied bias, the pH, dissolved oxygen concentration, molecular structure and properties of the pollutants, showing that acidic conditions are favored in most cases. [37] Cao *et al.* fabricated an Ag_3PO_4/$BiVO_4$ photoanode for PEC degradation of a typical antibiotic norfloxacin in a three-electrode cell where a Pt wire serves as the cathode and a saturated calomel electrode acts as the reference electrode. Under the irradiation of visible light, at low applied bias (0.5 V), the composite Ag_3PO_4/$BiVO_4$ totally oxidized Norfloxacin (C_0 = 5 mg/L) in 90 min through hydroxyl radicals and holes attacking the piperazine ring and causing the decarboxylation process. The further increased applied bias potential (0.75-1.0 V) showed relatively insignificant improvement for the degradation efficiency of norfloxacin,

most likely due to the competitive O_2 generation, favored at high applied potentials. [156] PEC air treatment requires a more complicated setup to introduce and separate gas. Thus, it's an emerging and challenging future trend of PEC applications. Liu *et al.* designed a flat-plate type device composed of Au interdigital electrode and printed TiO_2/WO_3 nanocomposite catalyst film used for organic gas degradation. This composite material could largely reduce the external bias needed compared to pure TiO_2 PEC process. Under UV light (365 nm) irradiation, at only 0.2 V bias, the PEC degradation rate of 300 ppm acetone gas was about 12.28×10^{-3} min^{-1}, which is 2.42 times as high as that of the PC process. [88]

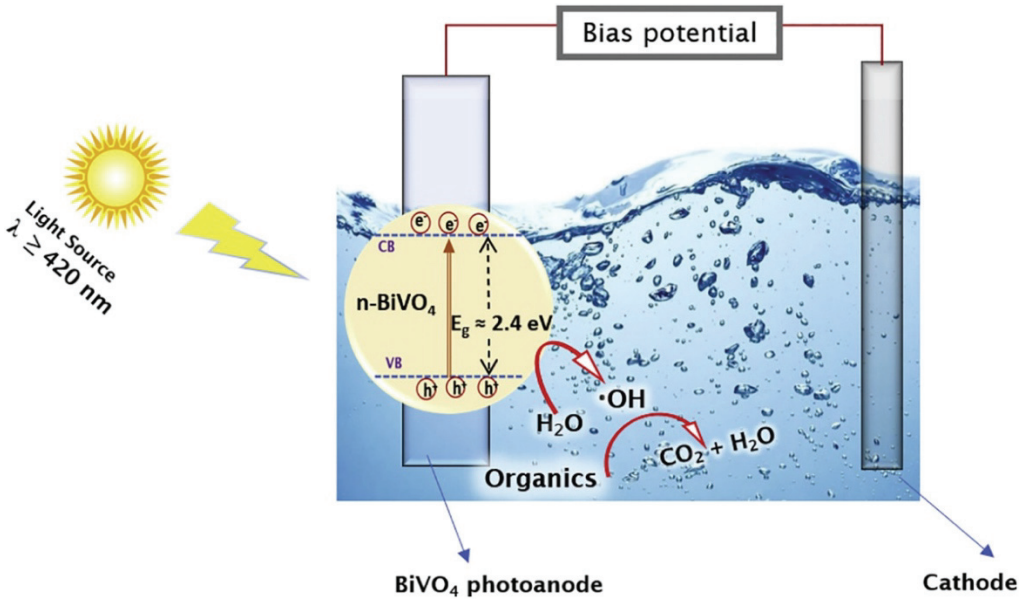

Fig. 1. 10. Scheme of water treatment involving reactive oxidation species (ROS) like hydroxyl radicals, from ref. [157]

3. 1. 2 Water oxidation

PEC water oxidation reaction (WOR) aims to oxidize water to generate oxygen (O_2) or hydrogen peroxide (H_2O_2). Their pathways involve either a 4-electron or 2-electron transfer, and of course, as an oxidation process, it happens at the anode. The former is called oxygen evolution reaction (OER): as part of the water splitting process (aiming to separately produce H_2 and O_2), it is the limiting step of the whole photoelectrochemical process. Thus it will be discussed together with the hydrogen evolution reaction (HER, the other half-reaction of water splitting) in section 3.3. Here we will focus on the latter PEC generation of H_2O_2, as depicted in Fig. 1. 11a, which could not only be used in the field of environment, like in advanced oxidation processes (AOPs) for wastewater treatment, but also in the domain of energy to serve as a liquid fuel in a fuel cell alternative to H_2 and O_2.

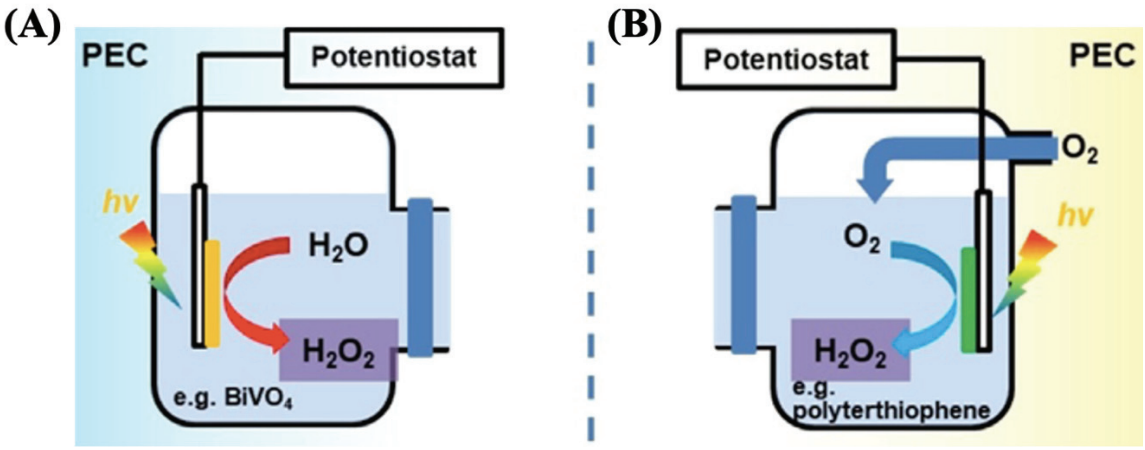

Fig. 1. 11. Scheme of the 2-electron water oxidation for H_2O_2 formation derived from (a) anodic water oxidation reaction (WOR) and cathodic oxygen reduction reaction (ORR) from ref. [158]

Anodic WOR or water oxidative H_2O_2 formation is based on equation 2, which requires a high positive potential (1.77 V vs. RHE). [159–161] A separated dual-compartment setup could protect the generated H_2O_2 from being reduced in the cathode. Low temperature is vital to prevent the thermal decomposition of H_2O_2 to H_2O and O_2. Fuku *et al.* designed a binary catalyst $WO_3/BiVO_4$ as a photoanode with an improved charge separation rate as well as a good visible light response. An excellent selectivity of H_2O_2 (ca. 54%) was obtained in a two-compartment cell at 5 °C. [162] Furthermore, Fuku and his co-workers introduced MeOx (Me = Si, Zr, Ti, Al, or Co) onto the $WO_3/BiVO_4$ surface to fabricate multi-component cocatalysts. [163] Al_2O_3 is proved to significantly facilitate the anodic H_2O_2 generation presented as unprecedented selectivity (ca. 80%) by inhibition of the oxidative degradation of the formed H_2O_2 whereas CoOx is the worst one among these five selected cocatalysts because of its high efficiency towards H_2O_2 decomposition or O_2 generation.

$$2H_2O \rightarrow 2H_2O_2 + 2H^+ + 2e^- \quad E(H_2O/H_2O_2)=+1.77 \text{ V vs. RHE} \qquad (2)$$

$$O_2 + 2H^+ + 2e^- \rightarrow H_2O_2 \quad E(O_2/H_2O_2)=+0.68 \text{ V vs. RHE} \qquad (3)$$

It should be noted that compared to anodic H_2O_2 generation, the OER is thermodynamically more inclined to occur due to the lower requirement of external potential (+1.23 vs. RHE). Besides, cathodic H_2O_2 generation by the oxygen reduction reaction (ORR) is more common based on equation 3, and is depicted in Fig. 1. 11b. [158] Thus the design of efficient and low-price photoelectrode or seeking alternative reactions of WOR is a critical issue considering the economic and social benefits.

3. 1. 3 Biomass valorization

Biomass valorization allows upgrading biomass-based products, like glycerol, lignin, and sugar, to some high value-added chemicals like glyceraldehyde, dihydroxyacetone, *etc.* (Fig. 1. 12, 13). [164] It differs from mineralizing organic compounds to CO_2 in the case of PEC water or air treatment, and requires a thermodynamically lower applied potential than the above described OER to generate valuable chemicals. In other words, this technology could be translated into lower energy input to create a higher economic profile.

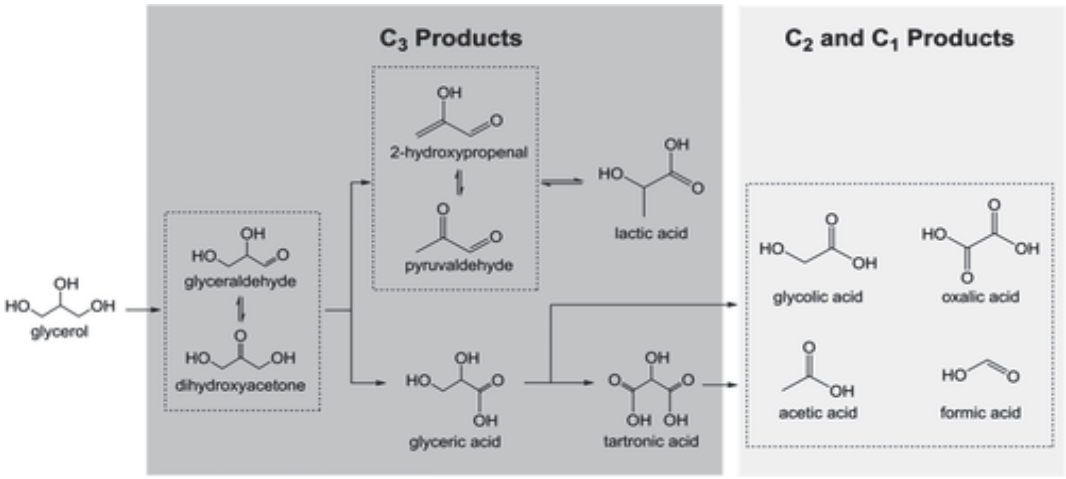

Fig. 1. 12. Simplified general glycerol PC/EC/PEC oxidation pathway from ref. [164]

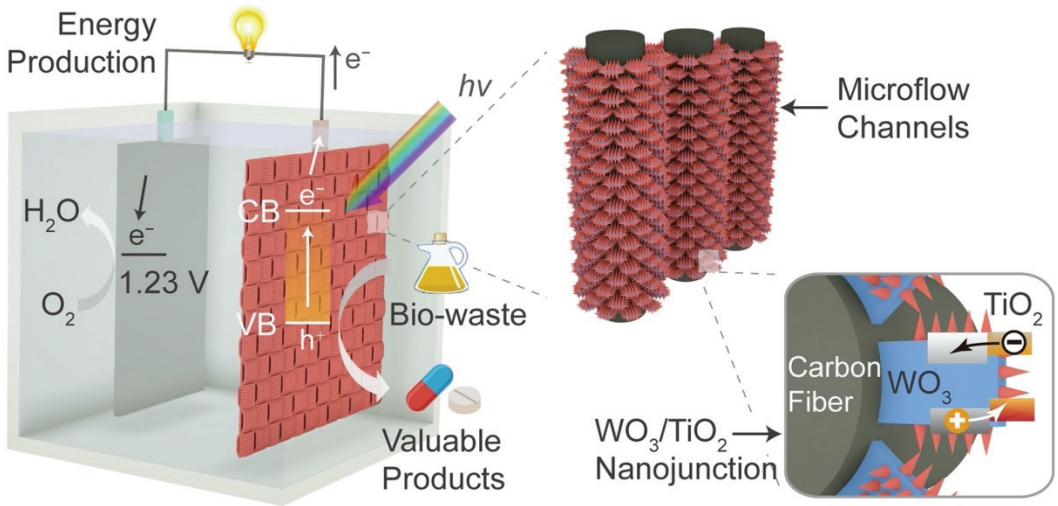

Fig. 1. 13. Scheme of PEC biomass valorization on photoanode (TiO_2/WO_3 binary hybrid cocatalyst in this case) from ref. [165]

The difficulties of this application lie in the identification of the products and the construction of a highly selective catalytic system. Here, we take glycerol PEC oxidation as an example. As the main byproduct of biodiesel which is the ideal alternative to fossil fuel and is forecasted to

stay at a high consumption level of ~50 billion L in the future decade, [166] glycerol is oversupplied in the market. Because 1 ton of biodiesel production generates around 100 kg of glycerol (~110 kg of crude glycerol). [167] Thus, the economic value of glycerol is seriously wasted because most of them are converted into thermal energy by simple combustion with a large amount of CO_2 emission rather than being used to produce more valuable chemical energy. Therefore, glycerol valorization which can not only increase huge economic benefits but also cater to the global low-carbon and energy-saving environmental protection needs, becomes a research hotspot. Its oxidation products include 3C products such as glyceraldehyde, dihydroxyacetone, glyceric acid, tartronic acid, 2C products like oxalic acid, lactic acid, glycolic acid, acetic acid and 1C liquid products formic acid as well as gas product CO_2 (Fig.13). [164] Of course, the economic values of those oxidation products are quite different. For example, the primary 3C products of glycerol oxidation, dihydroxyacetone and glyceraldehyde, which could be used in the fields of cosmetics and pharmaceuticals, have much higher commercial value than that of 1C product formic acid, which is industrialized as a commodity at a large scale. Thus, selectivity towards high value-added chemicals is one of the most important evaluation indicators for PEC biomass valorization. Gu *et al.* constructed a microfluidic platform using WO_3/TiO_2 as the photoanode for the oxidative upgrading of various chemicals: biomass-based glycerol, cyclohexane, and inorganic substrate HSO_4^-. As for glycerol oxidation, glyceraldehyde and 1,3-dihydroxyacetone were obtained as the main products, with a total selectivity of 85 %, together with a small amount of formic acid, glycolic acid, and CO_2 as gas by-products were observed at 1.2 V vs. RHE in a mixture solution of 0.1 M glycerol, 0.5 M Na_2SO_4, and 0.1 M borate buffer (pH = 6). [165] In Schichtl *et al.*'s study, AuPtBi-Ni as the anode was developed for crude glycerol oxidation to replace OER in the alkaline electrolyte of 2 M KOH. Although the oxidation products including glyceraldehyde, dihydroxyacetone, formic acid, *etc.* were well detected by proton nuclear magnetic resonance (1H NMR) spectroscopy, this study lacks of discussion regarding the selectivity of these valuable products. [168] It focused mainly on hydrogen generation, in a similar way to most research on PEC glycerol upgrading/reforming, [154,168–179]. This reveals, to some extent, one of the main difficulties for the glycerol upgrading towards value-added products: the analysis of the obtained products.

For other biomass resources, like lignocellulose, mainly composed of complex bio-polymers like cellulose (40–50 wt.%), hemicellulose (20–30 wt.%), and lignin (15–25 wt.%), their PEC valorization seem more complicated and requires more in-deep investigation of the reactions and mechanisms. [181] In summary, transformation of biomass to desired products with

considerably efficient yield, high selectivity, and mild reactional conditions are highly demanded in large-scale industrial production.

3. 2 PEC focused on reduction reactions

3. 2. 1 CO_2 reduction

Highly selective conversion of CO_2 into chemical fuels (CO, CH_4, CH_3OH, *etc*.) with added value by solar energy attracted a large number of scientific researchers in recent years due to the world consensus goal of carbon neutrality. CO_2 molecules are firstly adsorbed on a (photo)cathode and then, with the help of light irradiation and upon the application of an external potential, they are converted into $HCOO^-$ as well as other chemicals via the PEC process, as depicted in Fig. 1. 14. [182] Generally, the reduction of CO_2 demands a highly negative potential, i.e., -1.9 V vs. NHE at neutral pH. Therefore, the catalysts which possess low bandgap, high electron conductivity, and high CO_2 adsorption capacity (high surface area) are preferred for PEC CO_2 reduction. [183] For instance, Wang *et al.* synthesized a ternary composite Ag-g-C_3N_4/BN-C and used it for PC CO_2 reduction to CO. The doping of Ag helps the charge separation and increases the utilization of light energy *i.e.*, the SPR effect. Thus, a highly enhanced yield of 166.5 $\mu mol \cdot g^{-1}$ was obtained via the path of $CO_2 \rightarrow {}^*COOH \rightarrow {}^*CO \rightarrow CO$. [184]

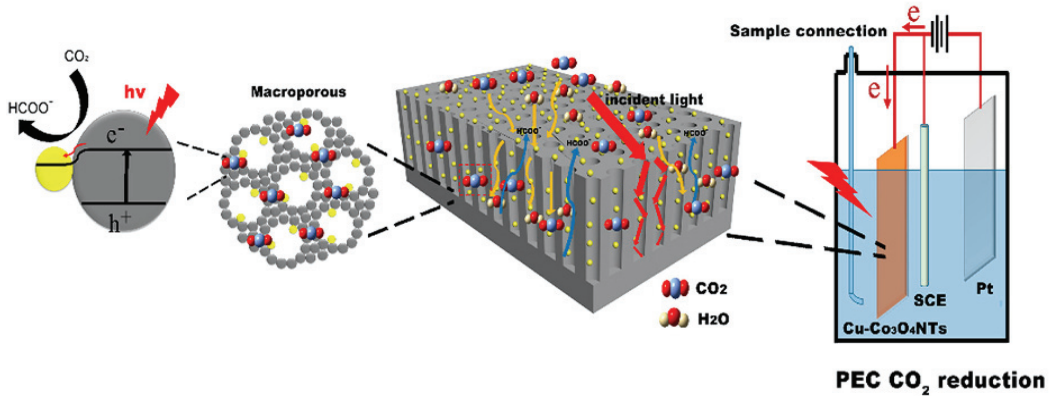

Fig. 1. 14. Scheme of PEC CO_2 reduction on photocathode (Cu-Co_3O_4 nanotubes binary hybrid cocatalyst in this case) from ref. [185]

Also, for PEC CO_2 reduction, p-type metal oxides such as Cu_2O are commonly applied as photocathodes. [48] Md. Maksudur RahmanKhan's group conducted PEC reduction of CO_2 to methanol over a p-type $CuFe_2O_4$ and hybrid photocatalyst 5% Polyaniline(PANI)@$CuFe_2O_4$ in the cathodic compartment. [186][49] $CuFe_2O_4$ acts mainly as a light harvester while PANI

possessing CO_2 binding capacity, electron conductivity and visible light sensitivity, contributes to CO_2 adsorption and serves as reduction sites for achieving a high rate (49.3 μmol g^{-1} h^{-1}) and high selectivity of methanol formation. The selection and optimization of catalysts are vital to this application. Shen *et al.* designed a metallic Cu decorated Co_3O_4 nanotubes photocathode used for CO_2 reduction where Co foil acts as the substrate. Co_3O_4 nanotubes were grown directly in the substrate via one-step anodization method, which minimizes the contact resistance between them. Nearly 100% of selectivity of formate and high yield up to 6.75 $mmol \cdot L^{-1} \cdot cm^{-2}$ was obtained in a homemade gastight chamber with 0.1 M Na_2SO_4 as the electrolyte after PEC reduction for 8 h. [185]

3. 2. 2 N_2 fixation

Due to the surge in the world's population, natural synthetic ammonia (NH_3) has been unable to meet the needs of the modern fertilizer industry, so the pursuit of industrial-grade ammonia synthesis technology is crucial. The high energy consumption and high pollution characteristics of industrial nitrogen fixation via the Haber-Bosch process under harsh reaction conditions (650-750 K, 150-350 bar) hinder the development of synthetic ammonia. [187] PEC has emerged as a promising solution to produce NH_3 by photo-generated electrons to activate and convert N_2 into NH_3 in the cathode, which is called PEC N_2 fixation, as depicted in Fig. 1. 15. [188] Altering hydrogenation pathways of PC/PEC N_2 fixation have been put forward and widely accepted as shown in Fig. 1. 16. [189][50] The difficulties of this PEC application lie in low activity and insufficient selectivity of NH_3 because of the high charge-carrier combination and the slow N_2 activation kinetics. To further explain the latter, nitrogen molecules possess the high bond energy of the triple bond (941 kJ mol^{-1}). [190] The addition of the first H atom to N_2 is endothermic (ΔH_0=37.6 kJ mol^{-1}), so N_2 fixation is thermodynamically unfavored. [191,192] Besides, the large energy gap (10.82 eV) between the highest occupied molecular orbital (HOMO) and the lowest unoccupied molecular orbital (LUMO) of N_2 is not conducive to the electron transfer process, which results in the thermodynamic constraints of the reaction intermediates.

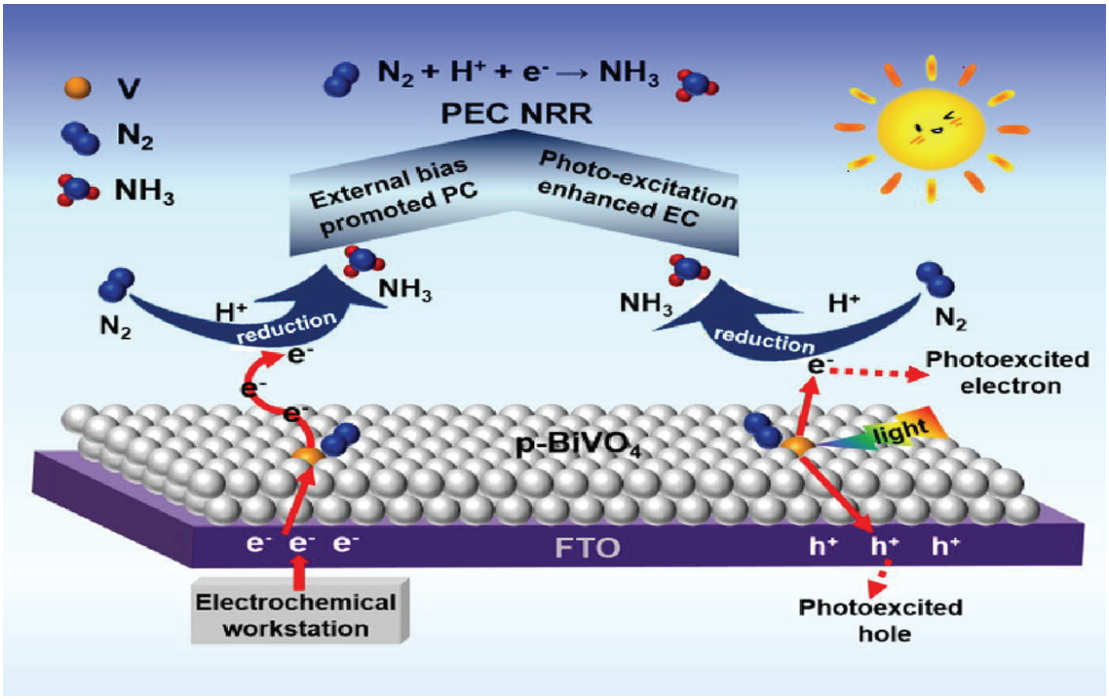

Fig. 1. 15. Scheme of PEC N_2 fixation on photocathode (single-component catalyst $BiVO_4$ in this case) from ref. [193]

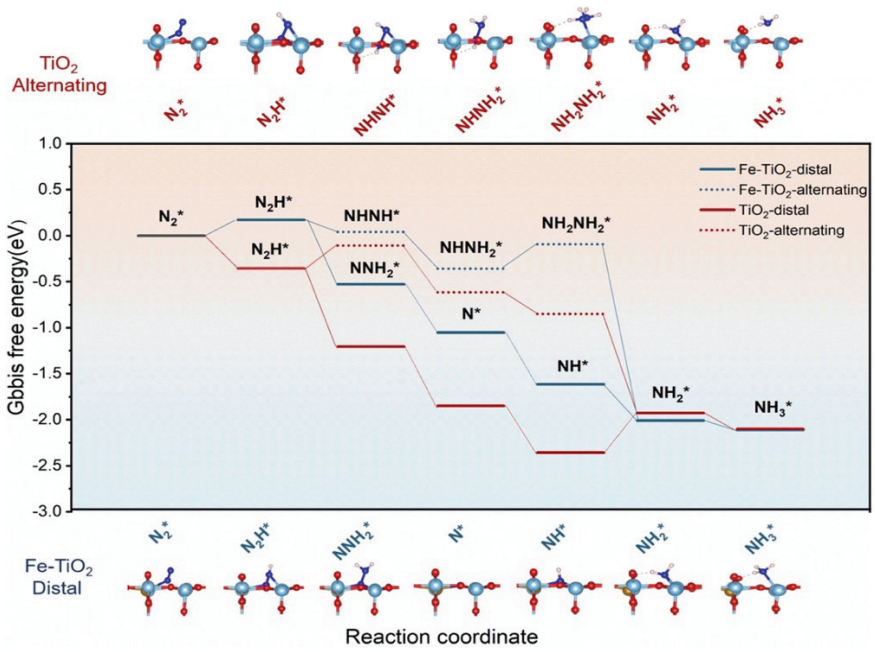

Fig. 1. 16. Associative distal and associative alternating pathways, corresponding Gibbs free energy profiles of NRR process at Ti-Ovs-Ti (red) and Fe-Ovs-Ti sites (blue), and the optimized geometric structure of intermediates adsorbed from ref. [189]

To the best of our knowledge, the optimal rate is about 100 μmol g^{-1} h^{-1}, and the PC conversion efficiency is only 0.1% at the highest. [194] The advantage of PEC is that the energy of

electrons can be changed by adjusting the external potential, which can break through the restriction of the redox potential of photocatalysts, which is determined by its bandgap and not easy to be tuned. PEC N_2 reduction reaction (NRR) usually exhibits remarkable performance due to the synergistic effect of PC and electrochemistry in NH_3 synthesis where photoelectrode design is key to this application. Thanks to the fact that vanadium nitrogenase could effectively inhibit HER, the rival of NRR, $BiVO_4$-based photoelectrocatalysts are favored by researchers. [193] Shi *et al.* developed a Z-scheme heterojunction of $BiVO_4$/PANI photocathode where the staggered band structure and perfect interface accelerated the separation and transfer of photogenerated carriers, resulting in an NH_3 yield rate of 0.93 μg h^{-1} cm^{-2} at -0.1 V vs. RHE. [51] Li *et al.* combined crystal facet engineering, defect engineering with morphology modification to fabricate BiOBr nanosheets with oxygen vacancies on the exposed (001) facets and transfer N_2 to NH_3 upon monochromatic light (420 nm) irradiation for 1 h under room temperature and atmospheric pressure via the PEC process. [52] Owing to the gas-liquid interface reaction, the experimental parameters such as temperature, pressure, and the photoreactor structure (photon flux, the maximum light absorption, the separation of products, *etc.*) need to be well considered to achieve an excellent rate of NH_3 synthesis with high selectivity. This field is still in its infancy at this stage.

3. 3 PEC focused on both, oxidation and reduction reactions

As previously discussed, most studies focused their attention to one of the half-reactions in the PEC system and neglect the other, which greatly reduces economic efficiency. With the development of PEC research, it is strongly beneficial to observe the trend to combine both side reactions to achieve a more completed and profitable PEC system. Except for the most intensively investigated water splitting, there are emerging technologies, including artificial photosynthesis, dual-functional environmental treatment with simultaneous energy production, biomass valorization and hydrogen generation, and so on.

3. 3 .1 Water splitting

PEC water splitting is a chemical reaction in which water is split into oxygen and hydrogen, including therefore the hydrogen evolution reaction (HER) at the cathode, and the oxygen evolution reaction (OER) at the anode, requiring a minimum applied thermodynamic voltage of 1.23V vs. RHE, as depicted in Fig. 1. 17. For water splitting, the separation of two half-reactions (HER and OER) has high concern on the safety risks, and the efficient semiconductors' design with proper bandgap for both reactions is the vital factor to improve

their limitation towards practical applications, which have been well discussed in several reviews. [33-43]

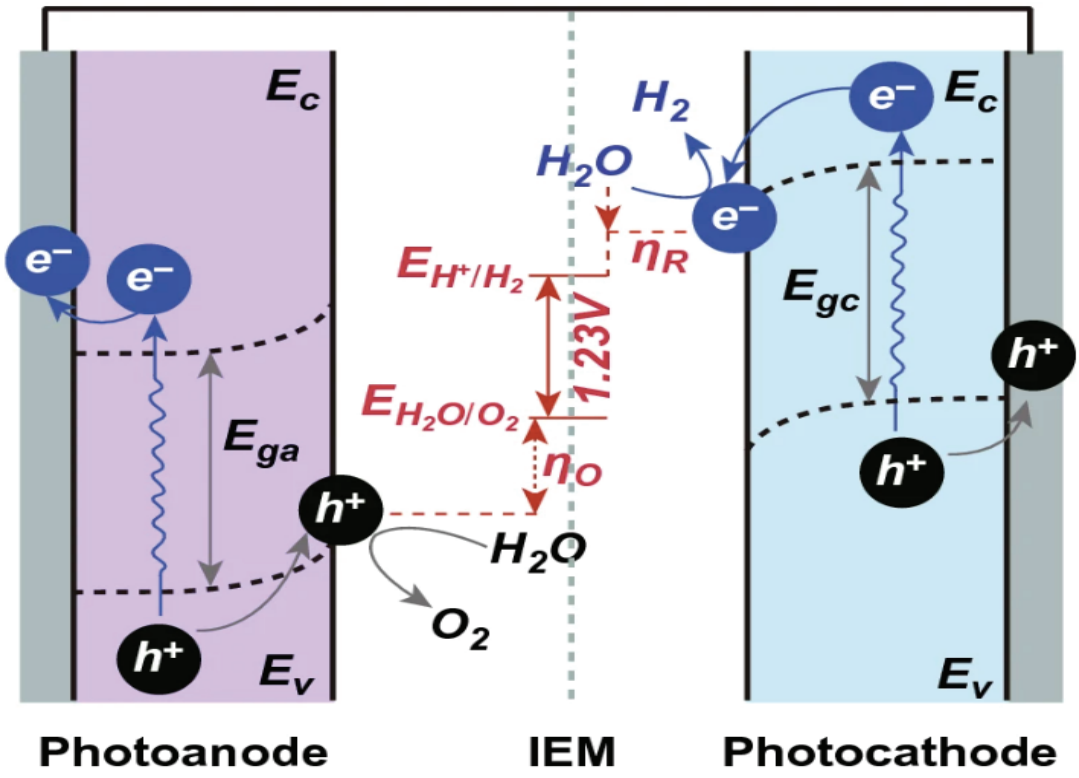

Fig. 1. 17. Scheme of PEC water splitting where oxygen evolution reaction (OER) happens on the anode and hydrogen evolution reaction (HER) happens on the cathode from ref. [113]

OER, as a oxidation reaction on the anode, involves four electrons in the process (equations 4 and 5) thus generally showing sluggish kinetics. [195]

Acid medium: $2H_2O \rightarrow O_2 + 4H^+ + 4e^-$ $E(H_2O/O_2)$=+1.23 V vs. RHE (4)

Alkaline medium: $4OH^- \rightarrow O_2 + 2H_2O + 4e^-$ $E(H_2O/O_2)$=+1.23 V vs. RHE (5)

Noble metal materials such as Ru/Ir-based catalysts are highly active for OER. A possible mechanism is that the active sites of catalysis (marked by catalyst*) react with a hydroxyl group (OH^-) to form a catalyst*OH intermediate (step 1, equation 6) followed by the generation of catalyst *O intermediate (step 2, equation 7), which further form a catalyst*OOH intermediate (step 3, equation 8) and eventually an oxygen molecule is produced (step 4, equation 9). [196]

Catalyst* + OH^- → Catalyst*OH + e^- (step 1) (6)

Catalyst*OH + OH^- → Catalyst*O + H_2O + e^- (step 2) (7)

Catalyst*O + OH^- → Catalyst*OOH + e^- (step 2) (8)

Catalyst*OOH + OH^-→ Catalyst* + O_2 + H_2O + e^- (step 4) (9)

Compared to the limitation OER of water splitting with an inferior economic value, HER, as a reduction reaction in the cathode, for high-value-added fuel H_2 generation is a research hotspot

in recent years due to the increasing demand for clean energy, which involves two electrons (equations 10 and 11). [197]

Acid medium: $2H^+ + 2e^- \rightarrow H_2$ $E(H_2O/H_2)$=+0.00 V vs. RHE (10)

Alkaline medium: $2H_2O + 2e^- \rightarrow H_2 + 2OH^-$ $E(H_2O/H_2)$=+0.00 V vs. RHE (11)

Noble metal Pt has excellent performances towards HER. Zong *et al.* [198] utilized an Ar-plasma etching technique and took the strategies of morphology modification and defect engineering to fabricate controllable surface oxygen vacancies onto three-dimensional (3D) nanoporous $BiVO_4$ photoanodes. They recorded a high photocurrent of 4.32 mA cm^{-2} at 1.23 V vs. RHE and obtained excellent Faraday efficiency (FE) of ~100%, solar-to-hydrogen (STH) efficiency of 1.8 % at 0.66 V vs. RHE in a neutral electrolyte under 1 sun illumination (1000 W m^{-2} and 25°C standard cell temperature), which is 7 times higher than that of the pristine $BiVO_4$ counterpart. Zhao *et al.* prepared WO_3 thin films with oxygen vacancies (chemical defects) by a simple post-annealing method at 450 °C for 1 h (heating rate: 5 °C min^{-1}) at different atmospheres (air, N_2 and O_2) and observed a promoted PEC efficiency of HER, contrast to the WO_3 photoanodes with physical defects (*e.g.,* microsized holes or cracks) obtained by atomic layer deposition (ALD) and a sputtering method. It is found that the WO_3 films (sputtered WO_3 and ALD WO_3) annealed in air show the highest photocurrent density (0.06 and 0.1 mA cm^2) than those obtained in N_2 (0.04 and 0.08 mA cm^2) and in O_2 (0.05 and 0.09) at 1.23 V vs. RHE in 0.5 M H_2SO_4 (pH ~ 0.3). [199] Yang *et al.* synthesized a Cu_2O/CuO bilayered composite via electrodeposition and subsequent thermal oxidation method and applied it as the photocathode for HER in a three-electrode PEC cell where a Pt sheet is the counter (anode) and a saturated calomel electrode is the reference. As-prepared Cu_2O/CuO photocathode possesses the extended utilization of solar energy red-shifted to ca. 900 nm, and enhanced electron-hole separation capability. Thus an excellent photocurrent density of 3.15 mA cm^{-2} was obtained at the applied potential of 0.40 V vs. RHE in 1.0 M KOH solution. [200] Besides the photoelectrocatalyst itself, the experimental operating conditions play a crucial role in the production of hydrogen. Acid electrolyte, high temperature, and dissolved oxygen-free environment are beneficial to obtaining an outstanding hydrogen generation rate. Take the acid environment as an example, Monfort *et al*. found that using H_2SO_4 solution (pH=2) instead of $NaHCO_3$ (pH=8.2) in the cathode compartment led to a boost in hydrogen production rate from 0.18 mmol h^{-1} to 0.27 mmol h^{-1} due to the fact that the availability of protons in the acidic environment facilitates hydrogen generation via H^+ reduction. [201]

3. 3. 2 Artificial photosynthesis

PEC artificial photosynthesis is a combination of water oxidation (OER or H_2O_2 generation) and CO_2 reduction reaction (CO_2RR), which mimics the behavior of natural plants, bacteria and algae capturing light and oxidizing water to generate O_2 in the anode meanwhile reducing CO_2 to produce hydrocarbons in the cathode (Fig. 1. 18). Selectivity and efficiency are the main handicaps in this study. Design of setups, modification of photoelectrodes, and optimization of experimental parameters are efficient strategies to overcome these difficulties. Nath *et al*. designed a PEC artificial photosynthesis system using WO_3/dye-sensitized solar cell (WO_3/DSSC) as the photoanode and Cu_xO wire arrays as the cathode. Under irradiation with simulated sunlight, the dual-absorber photoanode exhibits promising electrocatalytic activity presented as a gained potential of ~0.7 V, which makes CO_2 conversion to CO at cathode possible without an external power supply. OER simultaneously happens on photoanode WO_3 for O_2 generation. [202] Bharath *et al.* replaced anodic OER by the oxidation of furfural to 2-furoic acid and 5-hydroxyfuroic acid and constructed a novel PEC artificial photosynthesis system using Au/α-Fe_2O_3/rGO photocathode and Ru/rGO/Pt anode, separated by a proton exchange membrane (Nafion N-117). In the photocathode, CO_2 was converted to CH_3OH with high yield (63 μmol L^{-1} cm^{-1}) with a FE of 91 % at -0.6 V under the irradiation of visible light. In the anode, furfural oxidation with a FE conversion (82 %) to 2-furoic acid and 5-hydroxyfuroic acid were obtained. [203] Similar to water splitting, the two semi-reactions need to be well separated, and suitable semiconductors need to be selected to overcome the energy barriers. Also, as discussed in the first section of this review, the experimental conditions, including temperature and pressure, with significant effects on mass transfer and ionic conductivity of the PEC system need to be considered for a high efficient PEC artificial photosynthesis system.

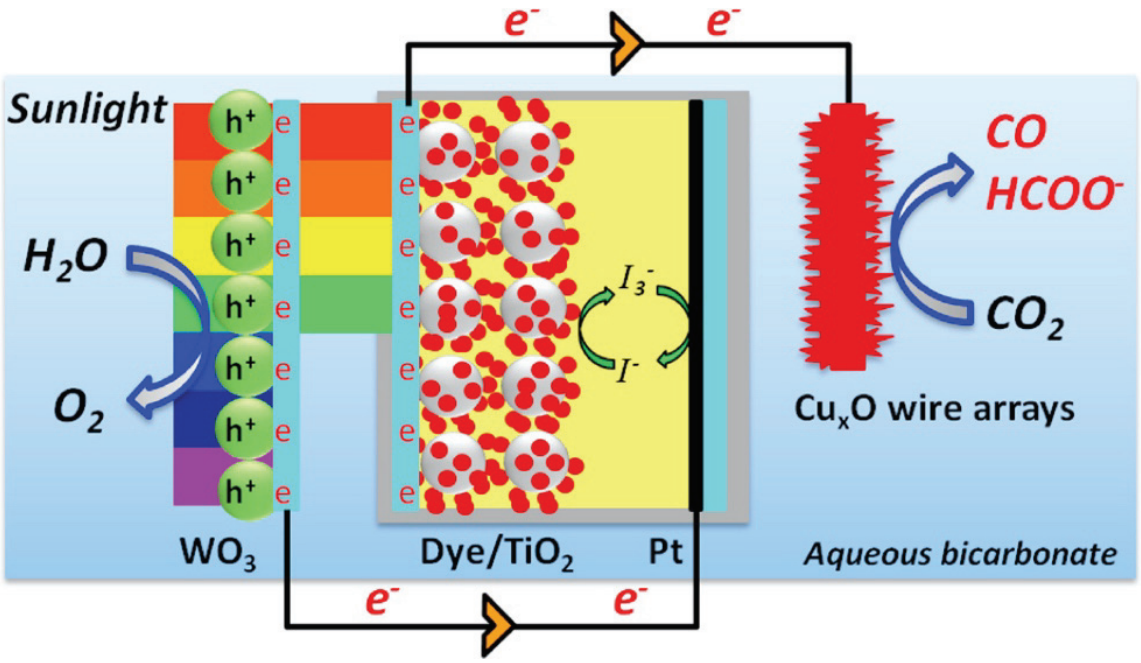

Fig. 1. 18. Schematic of artificial photosynthesis (photoanode: WO_3/dye-sensitized solar cell (WO_3/DSSC) and cathode single-component catalyst Cu_xO wire arrays in this case) from ref. [202]

3. 3. 3 Environmental treatment and hydrogen production

H_2 generation has the lowest requirement for the potential compared with other already discussed reduction reactions (CO_2 reduction and NH_3 synthesis). Therefore, it seems convenient to combine H_2 generation with other oxidation reactions like environmental pollutant removal. Although each application alone has been extensively investigated, the dual functional systems combined with water treatment and HER in spatial separation mode are still rare. As depicted in Fig. 1. 19, environmental treatment occurs in the anode and hydrogen production happens in the cathode. Generally, the water treatment part is driven by the hole oxidation power and the generation of reactive oxidation species (ROS), while the counterpart H_2 generation utilizes the electron reduction power based on the mechanism of multiple electron transfer. Lo *et al.* investigated the role of sulfate radicals, being the dominant species in the PEC degradation of benzophenone-3 over $BiVO_4$ upon visible light radiation. The addition of 1.5 mM of Na_2SO_3 greatly improved the PEC water treatment performance and hydrogen generation due to the strong oxidant radical $\cdot SO_4^-$ being formed and holes scavenged to generate H^+. [204] In Choi *et al.*'s study, PEC degradation of phenolic, acid contaminants and the inactivation of E. coli were remarkably improved by in situ reactive chlorine species (RCS) generated in PEC reactions using Pt as the counter electrode, Ag/AgCl as reference

electrode and WO_3 as the photoanode in a single-compartment 3-electrode reactor. In the contrast, the activities of the PC, as well as EC processes, were negligible. Besides, the efficiency and stability of the PEC chlorination system should be further improved to meet practical needs. [205]

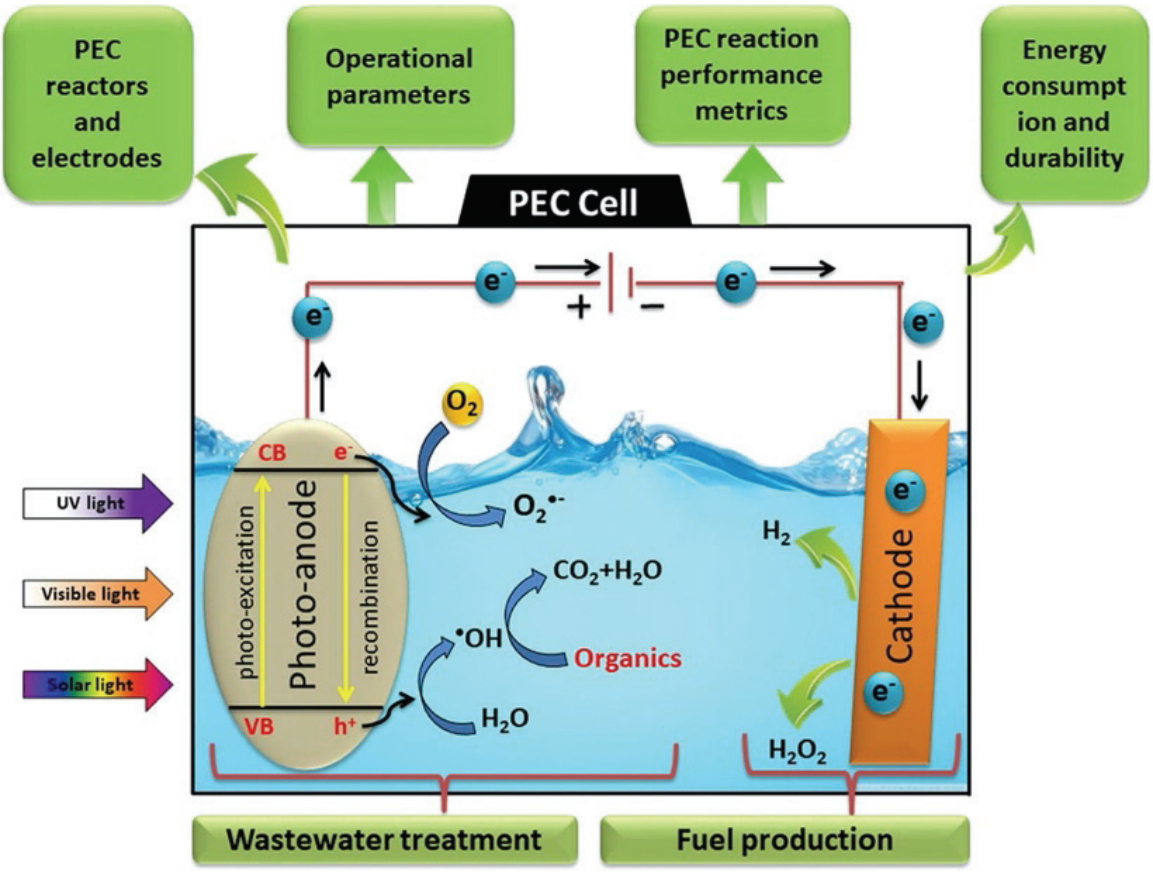

Fig. 1. 19. Schematic of dual-functional PEC system for environmental treatment and energy production from ref. [206]

As we discussed in section 3.1.1, ROS such as superoxide radical ion ($O_2^{\bullet-}$), hydrogen peroxide (H_2O_2), and hydroxyl radical (·OH) as well as photo-induced electrons and holes participate in water and air treatment. In this process, dissolved oxygen is required to act as the precursor of ROS and a reagent to conduct pollutant mineralization. However, O_2 is a scavenger of photo-induced electrons, which eventually might hinder the hydrogen production. In the PC process, several well-designed photocatalysts like F-TiO_2-Pt [207] and P-TiO_2-Pt [208] have been developed for dual-functional PC water treatment and simultaneous hydrogen production. In these materials, the noble metal Pt acts as surface electron trapping (enhancing the HER) while F or P anions decrease the concentration of the surface -OH group (the hole trapping) via ligand exchange, thus favouring more h^+ to increase the amount of free ·OH radicals to participate in pollutant destruction (in the absence of dissolved O_2). However, spatial separation of oxidation

and reduction reactions cannot be achieved in the pure PC process, thus it requires the additional procedures to recycle catalysts and collect gas/liquid substances. Therefore, the PEC process could be a promising solution where two reactions happened in the anode and cathode separately at the same time. [206,209] However, PEC cells applied in the above two cases are traditional 3-electrode cells that could not achieve real spatial redox reactions and separately meet the requirements for each half-reaction at the same time. Thus, the optimization of reactional conditions and a well-designed PEC system including the modifications of photoelectrocatalysts and the separation of reactions are essential due to the fact that single hole transfer for water treatment and multiple electrons transfer for H_2 generation should be enhanced simultaneously.

3. 3. 4 Biomass valorization and hydrogen generation

Replacing anodic OER reactions of water splitting by biomass valorization and keeping HER in the cathode to generate high value-added chemicals and clean energy H_2 is the objective of this technology, as depicted in Fig. 1. 20c. Although biomass valorization (via photoelectrooxidation) could be achieved with simultaneous H_2 production, to the best of our knowledge, just a few studies reported such concept. Huang et.al utilized the single-component catalyst $BiVO_4$ to replace the OER reaction for the oxidation of glycerol, one of the most important biomass derivatives, where formic acid (85%) and dihydroxyacetone (15%) are the main products (Fig. 1. 20a). In that study, a remarkable H_2 generation (Fig. 1. 20b) was observed in a three-electrode configuration with an alkaline solution of 0.1 M $Na_2B_4O_7$ (pH=9.4), resulting in an outstanding incident photon-to-current efficiency (IPCE) of 55%. [41] Liu *et al.* investigated the $BiVO_4$ photoelectrode for glycerol valorization to form the initially oxidized product dihydroxyacetone, and the acid environment was proven to contribute to the formation of this initial product. 3.7 mA cm^{-2} of photocurrent density was obtained at 1.2 V versus RHE at pH=2, showing the good capability of simultaneous hydrogen generation. [40] Two significant drawbacks for the above two cases are non-neutral reactional conditions and non-spatial-divided configuration. Luo *et al.* used a heterogeneous photoanode of Bi_2O_3/TiO_2 binary cocatalyst (Bi_2O_3 nanoparticles on TiO_2 nanorod arrays) for PEC oxidation of glycerol to DHA in a H-type quartz cell with 0.5 M Na_2SO_4 (pH = 2) containing 0.1 M glycerol. At 1.0 V vs RHE, a high selectivity of 75.4 % with a glycerol conversion of ~18 % was achieved in this photoanode under AM 1.5G illumination (an incident power of 1000 W m^{-2}) for 1 h. [210] PEM PEC cell (Conf. 1) which used solid electrolyte and possesses shorter electrode distance and separated compartments could be a good option for this dual-functional PEC application.

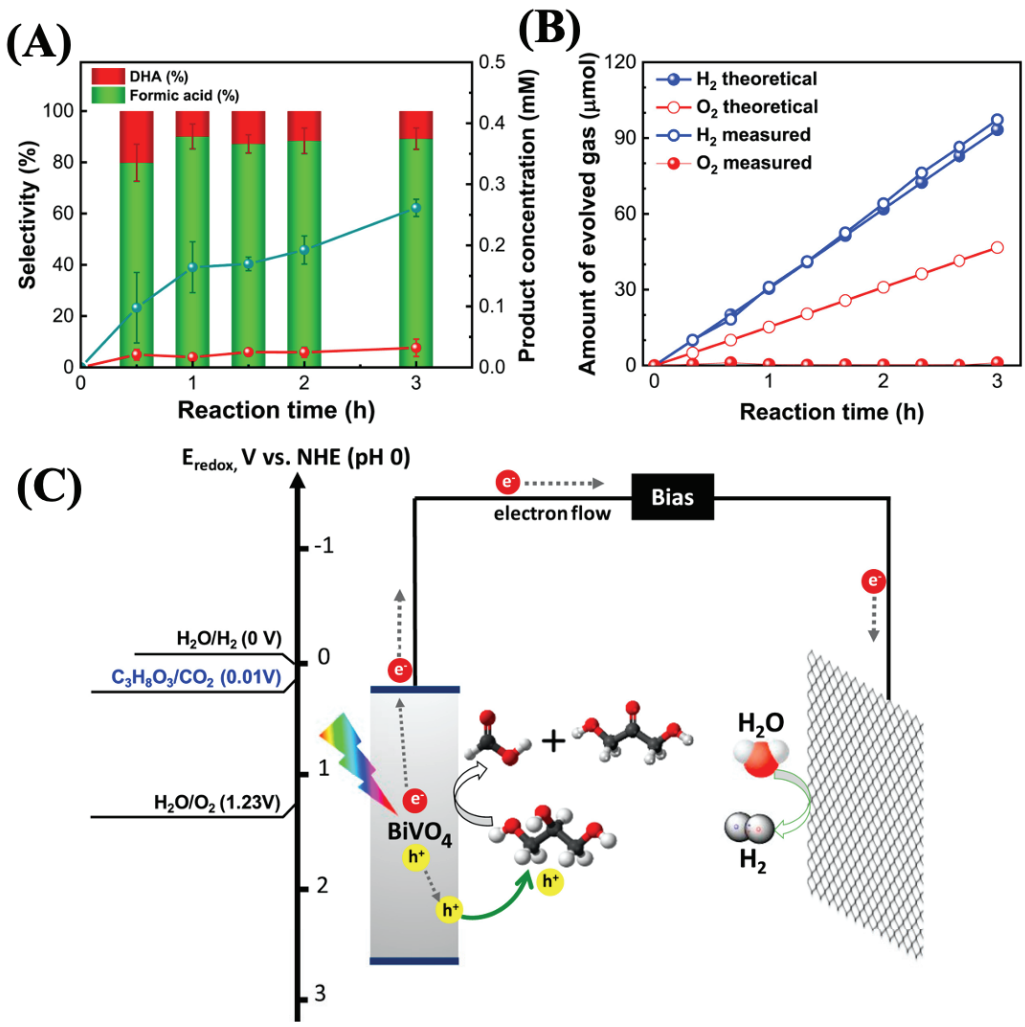

Fig. 1. 20. (a) Plot giving the concentration and selectivity of formic acid and dihydroxyacetone vs. time; (b) H_2 and O_2 obtained during the glycerol oxidation on $BiVO_4$ photoanode at 0.7 V vs. RHE; (c) Schematic representation of the dual-functional PEC process of biomass valorization and hydrogen generation from ref. [41]

Since the research on the reaction of cathodic H_2 production is well established, the biomass conversion and optimization of experimental parameters is the future research direction of this bifunctional system. The selection of efficient and stable photocatalysts, and the choice of reaction parameters to simultaneously produce high-value organics in the liquid phase and green energy hydrogen in the gas phase remain to be studied.

Table 1. 3. Summary of PEC applications based on oxidation and reduction reactions

Type of reaction	Applications	Reaction phase	Main products	Requirements
Oxidation	Water or Air treatment	Liquid or Gas	Mineralized products and CO_2	(Dissolved) O_2 to generate ROS
	Water oxidation for H_2O_2 or O_2 generation	Liquid or Liquid-Gas	H_2O_2 or O_2	Efficient catalysts
	Biomass valorization	Liquid (mostly)	Alcohols, aldehydes, acids, *etc*.	Selectivity to valuable products
Reduction	Hydrogen or H_2O_2 generation	Liquid-Gas or Liquid	H_2 or H_2O_2	Efficient catalysts
	CO_2 reduction	Liquid-Gas	CH_4, CH_3OH, HCHO, CO, HCOOH, *etc*.	Selectivity to valuable products, mass transfer
	N_2 Fixation	Liquid-Gas	NH_3	Selectivity to valuable products, mass transfer
Overall Redox	Water spliting	Liquid-Gas	Anode: O_2 Cathode: H_2	Efficient catalysts
	Artificial photosynthesis	Gas	Anode: O_2 Cathode: CH_4, CH_3OH, HCHO, CO, HCOOH, *etc*.	Selectivity to valuable products

Type of reaction	Applications	Reaction phase	Main products	Requirements
	Environmental treatment and energy production	Liquid-Gas	Anode: Mineralized products, CO_2 Cathode: H_2	High mineralization rate and H_2 generation rate
	Biomass valorization and energy production	Liquid-Gas	Anode: Alcohols, aldehydes, acids, *etc*. Cathode: H_2	Selectivity to valuable products

4. Summary and prospective

This review aims to provide a comprehensive and brief guide to PEC research including technology principles, setup developments, operational parameters, catalysts and their modifications, applications, and indicate the future research direction: bifunctional PEC appliance. According to the above discussion, it comes to the below conclusions.

Firstly, PEC technology is an intriguing technology that combines photocatalysis and electrochemistry. In order to obtain excellent performances to meet the requirements of experimental and practical industrialization, well-designed setups, optimized reactions and modified catalysts are of remarkable significance. In detail, four types of setups (wired or wireless and single compartment or dual compartment), show different complexity and applicability; reactional conditions including electrolytes, temperature, pressures, *etc*. significantly affect PEC activities; various catalysts suit for different redox reactions and electrodes due to diverse bandgaps and physicochemical properties which require further modifications via chemical or physical methods to shift material's band edges' position and enhance their activities; PEC applications are abundant but the research is limited to several ones such as water splitting and most of them just focus on one-half reactions, thus dual-functional applications should arise more attention;

Secondly, some insufficiency of PEC research needs to be overcome in the future. Most of the experimental setups used in nowadays' studies are still 3-electrode one compartment wired configurations, which could not separate spatially the two half-redox reactions and leads to the lack of deep investigation of both anodic and cathodic systems. Besides, how basic parameters, such as temperature, affect the PC, EC and PEC reactions separately and jointly is still not

clear, which needs to be surveyed more meticulously. Efficient and stable photoelectrodes with noble metal-free material are still rare, and the study on photocathodes is relatively less than on photoanode. In addition, newly-developed PEC applications such as biomass valorization, N_2 fixation and artificial photosynthesis with high selectivity toward chemical products and fuels are still not mature enough to be applied to real industrial markets, which call for more in-depth and precise research. Furthermore, to the best of the authors' knowledge, some electrocatalytic application such as urea synthesis [211] is also waiting for researchers in the field of PEC to explore.

Thirdly, we believe that constructing a cost-effective, efficient, easy-to-operate, mild PEC system could be a promising and environmentally-friendly strategy to solve the energy crisis and pollutant problem, which requires the collaboration of researchers from multiple fields including chemistry, environment, engineering, materials, *etc*. With the continuous progress stemming from a wide range of scientific research, the ideal PEC system with fully functional devices, efficient and durable photoelectrodes, as well as optimized working conditions, will gradually come out in the near future.

References

[1] A. Fujishima, K. Honda, Electrochemical photolysis of water at a semiconductor electrode, Nature. 238 (1972) 37–38.

[2] M.R.D. Khaki, M.S. Shafeeyan, A.A.A. Raman, W.M.A.W. Daud, Application of doped photocatalysts for organic pollutant degradation-A review, J. Environ. Manage. 198 (2017) 78–94.

[3] Z. Wei, J. Liu, W. Shangguan, A review on photocatalysis in antibiotic wastewater: Pollutant degradation and hydrogen production, Chinese J. Catal. 41 (2020) 1440–1450.

[4] T. Zhang, W. Lin, Metal--organic frameworks for artificial photosynthesis and photocatalysis, Chem. Soc. Rev. 43 (2014) 5982–5993.

[5] S. Chen, Y. Qi, C. Li, K. Domen, F. Zhang, Surface strategies for particulate photocatalysts toward artificial photosynthesis, Joule. 2 (2018) 2260–2288.

[6] T. Wu, X. Liu, Y. Liu, M. Cheng, Z. Liu, G. Zeng, B. Shao, Q. Liang, W. Zhang, Q. He, Application of QD-MOF composites for photocatalysis: Energy production and environmental remediation, Coord. Chem. Rev. 403 (2020) 213097.

[7] Y. Zhao, X. Jia, G.I.N. Waterhouse, L.-Z. Wu, C.-H. Tung, D. O'Hare, T. Zhang, Layered double hydroxide nanostructured photocatalysts for renewable energy production, Adv. Energy Mater. 6 (2016) 1501974.

[8] M. Gong, S. Xiao, X. Yu, C. Dong, J. Ji, D. Zhang, M. Xing, Research progress of

photocatalytic sterilization over semiconductors, RSC Adv. 9 (2019) 19278–19284.

[9] A. Upadhyaya, G. Rincón, others, Visible-Light-Active Noble-Metal Photocatalysts for Water Disinfection: A Review, J. Water Resour. Prot. 11 (2019) 1207.

[10] W. Wang, C. Zhou, Y. Yang, G. Zeng, C. Zhang, Y. Zhou, J. Yang, D. Huang, H. Wang, W. Xiong, others, Carbon nitride based photocatalysts for solar photocatalytic disinfection, can we go further? Chem. Eng. J. 404 (2021) 126540.

[11] X.-C. Dai, S. Hou, M.-H. Huang, Y.-B. Li, T. Li, F.-X. Xiao, Electrochemically anodized one-dimensional semiconductors: A fruitful platform for solar energy conversion, J. Phys. Energy. 1 (2019) 22002.

[12] H. Lu, Z. Huang, M.S. Martinez, J.C. Johnson, J.M. Luther, M.C. Beard, Transforming energy using quantum dots, Energy & Environ. Sci. 13 (2020) 1347–1376.

[13] D. Gogoi, R. Koyani, A.K. Golder, N.R. Peela, Enhanced photocatalytic hydrogen evolution using green carbon quantum dots modified 1-D CdS nanowires under visible light irradiation, Sol. Energy. 208 (2020) 966–977.

[14] H.-M. Xu, H.-C. Wang, Y. Shen, Y.-H. Lin, C.-W. Nan, Low-dimensional nanostructured photocatalysts, J. Adv. Ceram. 4 (2015) 159–182.

[15] Y. Liu, X. Zeng, X. Hu, J. Hu, X. Zhang, Two-dimensional nanomaterials for photocatalytic water disinfection: recent progress and future challenges, J. Chem. Technol. & Biotechnol. 94 (2019) 22–37.

[16] J.J. Pietron, P.A. DeSario, Review of roles for photonic crystals in solar fuels photocatalysis, J. Photonics Energy. 7 (2016) 12007.

[17] T. Raja-Mogan, B. Ohtani, E. Kowalska, Photonic crystals for plasmonic photocatalysis, Catalysts. 10 (2020) 827.

[18] J. Yu, J. Lei, L. Wang, J. Zhang, Y. Liu, TiO_2 inverse opal photonic crystals: Synthesis, modification, and applications - A review, J. Alloys Compd. 769 (2018) 740–757.

[19] J. Yang, D. Wang, H. Han, C.A.N. Li, Roles of cocatalysts in photocatalysis and photoelectrocatalysis, Acc. Chem. Res. 46 (2013) 1900–1909.

[20] Y. Han, J. Wu, Y. Li, X. Gu, T. He, Y. Zhao, H. Huang, Y. Liu, Z. Kang, Carbon dots enhance the interface electron transfer and photoelectrochemical kinetics in TiO_2 photoanode, Appl. Catal. B Environ. 304 (2022) 120983.

[21] J. Kegel, I.M. Povey, M.E. Pemble, Zinc oxide for solar water splitting: A brief review of the material's challenges and associated opportunities, Nano Energy. 54 (2018) 409–428.

[22] J. Lin, W. Wang, G. Li, Modulating Surface/Interface Structure of Emerging InGaN

Nanowires for Efficient Photoelectrochemical Water Splitting, Adv. Funct. Mater. 30 (2020) 2005677.

[23] S. Farhoosh, B. Eftekharinia, M. Tayebi, B.-K. Lee, N. Naseri, Newly designed ternary hematite-based heterojunction for PEC water splitting, Appl. Surf. Sci. 550 (2021) 149374.

[24] J. Ran, J. Zhang, J. Yu, M. Jaroniec, S.Z. Qiao, Earth-abundant cocatalysts for semiconductor-based photocatalytic water splitting, Chem. Soc. Rev. 43 (2014) 7787–7812.

[25] J. Joy, J. Mathew, S.C. George, Nanomaterials for photoelectrochemical water splitting--review, Int. J. Hydrogen Energy. 43 (2018) 4804–4817.

[26] S.-S. Yi, X.-B. Zhang, B.-R. Wulan, J.-M. Yan, Q. Jiang, Non-noble metals applied to solar water splitting, Energy & Environ. Sci. 11 (2018) 3128–3156.

[27] Y.J. Jang, J.S. Lee, Photoelectrochemical water splitting with p-type metal oxide semiconductor photocathodes, ChemSusChem. 12 (2019) 1835–1845.

[28] J.D. Desai, P.K. Baviskar, K.N. Hui, H.M. Pathan, Quadrivalently doped hematite thin films for solar water splitting, ES Energy & Environ. 2 (2018) 21–30.

[29] S. Singh, H. Chen, S. Shahrokhi, L.P. Wang, C.-H. Lin, L. Hu, X. Guan, A. Tricoli, Z.J. Xu, T. Wu, Hybrid organic--inorganic materials and composites for photoelectrochemical water splitting, ACS Energy Lett. 5 (2020) 1487–1497.

[30] Z. Luo, T. Wang, J. Gong, Single-crystal silicon-based electrodes for unbiased solar water splitting: current status and prospects, Chem. Soc. Rev. 48 (2019) 2158–2181.

[31] C. Ros, T. Andreu, J.R. Morante, Photoelectrochemical water splitting: a road from stable metal oxides to protected thin film solar cells, J. Mater. Chem. A. 8 (2020) 10625–10669.

[32] S.M. Thalluri, L. Bai, C. Lv, Z. Huang, X. Hu, L. Liu, Strategies for semiconductor/electrocatalyst coupling toward solar-driven water splitting, Adv. Sci. 7 (2020) 1902102.

[33] Z. Yang, C. Zhang, G. Zeng, X. Tan, D. Huang, J. Zhou, Q. Fang, K. Yang, H. Wang, J. Wei, others, State-of-the-art progress in the rational design of layered double hydroxide based photocatalysts for photocatalytic and photoelectrochemical H_2/O_2 production, Coord. Chem. Rev. 446 (2021) 214103.

[34] S. Chen, D. Huang, P. Xu, W. Xue, L. Lei, M. Cheng, R. Wang, X. Liu, R. Deng, Semiconductor-based photocatalysts for photocatalytic and photoelectrochemical water splitting: will we stop with photocorrosion? J. Mater. Chem. A. 8 (2020) 2286–2322.

[35] B. Qiu, M. Du, Y. Ma, Q. Zhu, M. Xing, J. Zhang, Integration of redox cocatalysts for artificial photosynthesis, Energy & Environ. Sci. (2021).

[36] K. Vinodgopal, S. Hotchandani, P. V Kamat, Electrochemically assisted photocatalysis: titania particulate film electrodes for photocatalytic degradation of 4-chlorophenol, J. Phys. Chem. 97 (1993) 9040–9044.

[37] Y. Zhou, X. Fan, G. Zhang, W. Dong, Fabricating MoS_2 nanoflakes photoanode with unprecedented high photoelectrochemical performance and multi-pollutants degradation test for water treatment, Chem. Eng. J. 356 (2019) 1003–1013.

[38] Y. Kuang, T. Yamada, K. Domen, Surface and interface engineering for photoelectrochemical water oxidation, Joule. 1 (2017) 290–305.

[39] X. Liang, X. Cao, W. Sun, Y. Ding, Recent progress in visible light driven water oxidation using semiconductors coupled with molecular catalysts, ChemCatChem. 11 (2019) 6190–6202.

[40] D. Liu, J.-C. Liu, W. Cai, J. Ma, H. Bin Yang, H. Xiao, J. Li, Y. Xiong, Y. Huang, B. Liu, Selective photoelectrochemical oxidation of glycerol to high value-added dihydroxyacetone, Nat. Commun. 10 (2019) 1–8.

[41] L.-W. Huang, T.-G. Vo, C.-Y. Chiang, Converting glycerol aqueous solution to hydrogen energy and dihydroxyacetone by the $BiVO_4$ photoelectrochemical cell, Electrochim. Acta. 322 (2019) 134725.

[42] M.B. Tahir, M.F. Malik, A. Ahmed, T. Nawaz, M. Ijaz, H.S. Min, S. Muhammad, S.M. Siddeeg, Semiconductor based nanomaterials for harvesting green hydrogen energy under solar light irradiation, Int. J. Environ. Anal. Chem. 101 (2021) 2255–2271.

[43] X.-H. Liu, F. Du, Q. Y. Chen, Y. H. Wang, An effective self-driven PFC-PEC hybrid system for hydrogen generation from organic substance, Electrochim. Acta. 245 (2017) 379–385.

[44] Y.-H. Chiu, T.-H. Lai, M.-Y. Kuo, P.-Y. Hsieh, Y.-J. Hsu, Photoelectrochemical cells for solar hydrogen production: Challenges and opportunities, APL Mater. 7 (2019) 80901.

[45] S.D. Tilley, Recent advances and emerging trends in photo-electrochemical solar energy conversion, Adv. Energy Mater. 9 (2019) 1802877.

[46] M. Ahmed, I. Dincer, A review on photoelectrochemical hydrogen production systems: Challenges and future directions, Int. J. Hydrogen Energy. 44 (2019) 2474–2507.

[47] X. Li, J. Yu, M. Jaroniec, X. Chen, Cocatalysts for selective photoreduction of CO_2 into solar fuels, Chem. Rev. 119 (2019) 3962–4179.

[48] Y. Chen, Y. Liu, F. Wang, X. Guan, L. Guo, Toward practical photoelectrochemical water splitting and CO_2 reduction using earth-abundant materials, J. Energy Chem. 61 (2021) 469–488.

[49] K.M.R. Karim, M. Tarek, S.M. Sarkar, R. Mouras, H.R. Ong, H. Abdullah, C.K. Cheng, M.M.R. Khan, Photoelectrocatalytic reduction of CO_2 to methanol over $CuFe_2O_4$@ PANI photocathode, Int. J. Hydrogen Energy. 46 (2021) 24709–24720.

[50] H. Li, C. Mao, H. Shang, Z. Yang, Z. Ai, L. Zhang, New opportunities for efficient N_2 fixation by nanosheet photocatalysts, Nanoscale. 10 (2018) 15429–15435.

[51] Y. Bai, H. Bai, Z. Fang, X. Li, W. Fan, W. Shi, Understanding the Z-scheme heterojunction of $BiVO_4$/PANI for photoelectrochemical nitrogen reduction, Chem. Commun. 57 (2021) 10568–10571.

[52] H. Li, J. Shang, Z. Ai, L. Zhang, Efficient visible light nitrogen fixation with BiOBr nanosheets of oxygen vacancies on the exposed {001} facets, J. Am. Chem. Soc. 137 (2015) 6393–6399.

[53] J. Feng, H. Huang, S. Yan, W. Luo, T. Yu, Z. Li, Z. Zou, Non-oxide semiconductors for artificial photosynthesis: progress on photoelectrochemical water splitting and carbon dioxide reduction, Nano Today. 30 (2020) 100830.

[54] Z. Zeng, S. Chen, T. T.Y. Tan, F. X. Xiao, Graphene quantum dots (GQDs) and its derivatives for multifarious photocatalysis and photoelectrocatalysis, Catal. Today. 315 (2018) 171–183.

[55] X. Tong, A.I. Channa, Y. You, P. Wei, X. Li, F. Lin, J. Wu, A. Vomiero, Z.M. Wang, Boosting the performance of eco-friendly quantum dots-based photoelectrochemical cells via effective surface passivation, Nano Energy. 76 (2020) 105062.

[56] J. Liang, D. Chen, X. Yao, K. Zhang, F. Qu, L. Qin, Y. Huang, J. Li, Recent progress and development in inorganic halide perovskite quantum dots for photoelectrochemical applications, Small. 16 (2020) 1903398.

[57] C. Li, Q. Cao, F. Wang, Y. Xiao, Y. Li, J.-J. Delaunay, H. Zhu, Engineering graphene and TMDs based van der Waals heterostructures for photovoltaic and photoelectrochemical solar energy conversion, Chem. Soc. Rev. 47 (2018) 4981–5037.

[58] T. Zhu, M.N. Chong, E.S. Chan, Nanostructured tungsten trioxide thin films synthesized for photoelectrocatalytic water oxidation: a review, ChemSusChem. 7 (2014) 2974–2997.

[59] L. Zhang, Y.-C. Zhu, Y.-Y. Liang, W.-W. Zhao, J.-J. Xu, H.-Y. Chen, Semiconducting CuO nanotubes: synthesis, characterization, and bifunctional photocathodic enzymatic

bioanalysis, Anal. Chem. 90 (2018) 5439–5444.

[60] L. Luo, X. Liu, S. Ma, L. Li, T. You, Quantification of zearalenone in mildewing cereal crops using an innovative photoelectrochemical aptamer sensing strategy based on ZnO-NGQDs composites, Food Chem. 322 (2020) 126778.

[61] A. Sreedhar, I.N. Reddy, Q.T.H. Ta, E. Cho, J.-S. Noh, Insight into anions and cations effect on charge carrier generation and transportation of flake-like Co-doped ZnO thin films for stable PEC water splitting activity, J. Electroanal. Chem. 855 (2019) 113583.

[62] C.V. Reddy, I.N. Reddy, K. Ravindranadh, K.R. Reddy, N.P. Shetti, D. Kim, J. Shim, T.M. Aminabhavi, Copper-doped ZrO_2 nanoparticles as high-performance catalysts for efficient removal of toxic organic pollutants and stable solar water oxidation, J. Environ. Manage. 260 (2020) 110088.

[63] L. Wang, Y. Tong, J. Feng, J. Hou, J. Li, X. Hou, J. Liang, G-C_3N_4-based films: A rising star for photoelectrochemical water splitting, Sustain. Mater. Technol. 19 (2019) 00089.

[64] W. Xiong, F. Huang, R.-Q. Zhang, Recent developments in carbon nitride based films for photoelectrochemical water splitting, Sustain. Energy & Fuels. 4 (2020) 485–503.

[65] R. Yalavarthi, A. Naldoni, Š. Kment, L. Mascaretti, H. Kmentová, O. Tomanec, P. Schmuki, R. Zbo\vril, Radiative and non-radiative recombination pathways in mixed-phase TiO_2 nanotubes for PEC water-splitting, Catalysts. 9 (2019) 204.

[66] R. Hernández, I. Olvera-Rodriguez, C. Guzmán, A. Medel, L. Escobar-Alarcón, E. Brillas, I. Sirés, K. Esquivel, Microwave-assisted sol-gel synthesis of an Au-TiO_2 photoanode for the advanced oxidation of paracetamol as model pharmaceutical pollutant, Electrochem. Commun. 96 (2018) 42–46.

[67] W. Zhang, R. Li, X. Zhao, Z. Chen, A.W.-K. Law, K. Zhou, A cobalt-based metal--organic framework as cocatalyst on $BiVO_4$ photoanode for enhanced photoelectrochemical water oxidation, ChemSusChem. 11 (2018) 2710–2716.

[68] S. Ju, H. Kang, J. Jun, S. Son, J. Park, W. Kim, H. Lee, Periodic Micropillar-Patterned FTO/$BiVO_4$ with Superior Light Absorption and Separation Efficiency for Efficient PEC Performance, Small. 17 (2021) 2006558.

[69] T. Soltani, A. Tayyebi, B.-K. Lee, Enhanced photoelectrochemical (PEC) and photocatalytic properties of visible-light reduced graphene-oxide/bismuth vanadate, Appl. Surf. Sci. 448 (2018) 465–473.

[70] S. Singh, R. Sharma, Bi_2O_3/Ni-Bi_2O_3 system obtained via Ni-doping for enhanced PEC and photocatalytic activity supported by DFT and experimental study, Sol. Energy Mater. Sol. Cells. 186 (2018) 208–216.

[71] Š. Kment, K. Sivula, A. Naldoni, S.P. Sarmah, H. Kmentová, M. Kulkarni, Y. Rambabu, P. Schmuki, R. Zbovril, FeO-based nanostructures and nanohybrids for photoelectrochemical water splitting, Prog. Mater. Sci. 110 (2020) 100632.

[72] P. Tang, J. Arbiol, Engineering surface states of hematite based photoanodes for boosting photoelectrochemical water splitting, Nanoscale Horizons. 4 (2019) 1256–1276.

[73] D. Jeon, H. Kim, C. Lee, Y. Han, M. Gu, B.-S. Kim, J. Ryu, Layer-by-layer assembly of polyoxometalates for photoelectrochemical (PEC) water splitting: toward modular PEC devices, ACS Appl. Mater. & Interfaces. 9 (2017) 40151–40161.

[74] H. He, A. Liao, W. Guo, W. Luo, Y. Zhou, Z. Zou, State-of-the-art progress in the use of ternary metal oxides as photoelectrode materials for water splitting and organic synthesis, Nano Today. 28 (2019) 100763.

[75] G.G. Bessegato, T.T. Guaraldo, J.F. de Brito, M.F. Brugnera, M.V.B. Zanoni, Achievements and trends in photoelectrocatalysis: from environmental to energy applications, Electrocatalysis. 6 (2015) 415–441.

[76] T. Bosserez, J. Rongé, J. Van Humbeeck, S. Haussener, J. Martens, Design of compact photoelectrochemical cells for water splitting, Oil & Gas Sci. Technol. D'IFP Energies Nouv. 70 (2015) 877–889.

[77] J. Rongé, D. Nijs, S. Kerkhofs, K. Masschaele, J.A. Martens, Chronoamperometric study of membrane electrode assembly operation in continuous flow photoelectrochemical water splitting, Phys. Chem. Chem. Phys. 15 (2013) 9315–9325.

[78] N. Grimaldos-Osorio, F. Sordello, M. Passananti, P. Vernoux, A. Caravaca, From plastic-waste to H_2: Electrolysis of a Poly (methyl methacrylate) model molecule on polymer electrolyte membrane reactors, J. Power Sources. 480 (2020) 228800.

[79] S. Xie, Q. Zhang, G. Liu, Y. Wang, Photocatalytic and photoelectrocatalytic reduction of CO_2 using heterogeneous catalysts with controlled nanostructures, Chem. Commun. 52 (2016) 35–59.

[80] B. Moss, O. Babacan, A. Kafizas, A. Hankin, A Review of Inorganic Photoelectrode Developments and Reactor Scale-Up Challenges for Solar Hydrogen Production, Adv. Energy Mater. 11 (2021) 2003286.

[81] A.U. Pawar, C.W. Kim, M.-T. Nguyen-Le, Y.S. Kang, General review on the components and parameters of photoelectrochemical system for CO_2 reduction with in situ analysis, ACS Sustain. Chem. & Eng. 7 (2019) 7431–7455.

[82] S. Wu, Y.H. Hu, A comprehensive review on catalysts for electrocatalytic and

photoelectrocatalytic degradation of antibiotics, Chem. Eng. J. 409 (2021) 127739.

[83] X. R. Li, X.-Z. Meng, Q. H. Zhang, H. R. Cai, Z. Z. Yan, L. K. Wu, F. H. Cao, In situ studies of hydrogen evolution kinetics on pure titanium surface: The effects of pre-reduction and dissolved oxygen, J. Phys. Chem. C. (2022).

[84] W. W. Zhao, C. Y. Tian, J. J. Xu, H. Y. Chen, The coupling of localized surface plasmon resonance-based photoelectrochemistry and nanoparticle size effect: towards novel plasmonic photoelectrochemical biosensing, Chem. Commun. 48 (2012) 895–897.

[85] A. Agrawal, S.H. Cho, O. Zandi, S. Ghosh, R.W. Johns, D.J. Milliron, Localized surface plasmon resonance in semiconductor nanocrystals, Chem. Rev. 118 (2018) 3121–3207.

[86] E. Petryayeva, U.J. Krull, Localized surface plasmon resonance: Nanostructures, bioassays and biosensing-A review, Anal. Chim. Acta. 706 (2011) 8–24.

[87] B. Cole, B. Marsen, E. Miller, Y. Yan, B. To, K. Jones, M. Al-Jassim, Evaluation of nitrogen doping of tungsten oxide for photoelectrochemical water splitting, J. Phys. Chem. C. 112 (2008) 5213–5220.

[88] Y. Liu, C. Xie, H. Li, H. Chen, Y. Liao, D. Zeng, Low bias photoelectrocatalytic (PEC) performance for organic vapour degradation using TiO_2/WO_3 nanocomposite, Appl. Catal. B Environ. 102 (2011) 157–162.

[89] A. Wolcott, W.A. Smith, T.R. Kuykendall, Y. Zhao, J.Z. Zhang, Photoelectrochemical study of nanostructured ZnO thin films for hydrogen generation from water splitting, Adv. Funct. Mater. 19 (2009) 1849–1856.

[90] A. Dhara, B. Show, A. Baral, S. Chabri, A. Sinha, N.R. Bandyopadhyay, N. Mukherjee, Core-shell CuO-ZnO pn heterojunction with high specific surface area for enhanced photoelectrochemical (PEC) energy conversion, Sol. Energy. 136 (2016) 327–332.

[91] S. Shyamal, A. Maity, A.K. Satpati, C. Bhattacharya, Amplification of PEC hydrogen production through synergistic modification of Cu_2O using cadmium as buffer layer and dopant, Appl. Catal. B Environ. 246 (2019) 111–119.

[92] K. Basu, H. Zhang, H. Zhao, S. Bhattacharya, F. Navarro-Pardo, P.K. Datta, L. Jin, S. Sun, F. Vetrone, F. Rosei, Highly stable photoelectrochemical cells for hydrogen production using a SnO_2-TiO_2/quantum dot heterostructured photoanode, Nanoscale. 10 (2018) 15273–15284.

[93] F. Malara, A. Minguzzi, M. Marelli, S. Morandi, R. Psaro, V. Dal Santo, A. Naldoni, α-Fe_2O_3/NiOOH: an effective heterostructure for photoelectrochemical water oxidation, ACS Catal. 5 (2015) 5292–5300.

[94] M. Tayebi, B.-K. Lee, Recent advances in $BiVO_4$ semiconductor materials for hydrogen

production using photoelectrochemical water splitting, Renew. Sustain. Energy Rev. 111 (2019) 332–343.

[95] J.H. Kim, J.S. Lee, $BiVO_4$-based heterostructured photocatalysts for solar water splitting: a review, Energy Environ. Focus. 3 (2014) 339–353.

[96] I. Rodriguez-Gutiérrez, E. Djatoubai, M. Rodriguez-Pérez, J. Su, G. Rodriguez-Gattorno, L. Vayssieres, G. Oskam, Photoelectrochemical water oxidation at FTO|WO_3@$CuWO_4$ and FTO|WO_3@$CuWO_4$|$BiVO_4$ heterojunction systems: an IMPS analysis, Electrochim. Acta. 308 (2019) 317–327.

[97] C.M. Tian, M. Jiang, D. Tang, L. Qiao, H.Y. Xiao, F.E. Oropeza, J.P. Hofmann, E.J.M. Hensen, A. Tadich, W. Li, others, Elucidating the electronic structure of $CuWO_4$ thin films for enhanced photoelectrochemical water splitting, J. Mater. Chem. A. 7 (2019) 11895–11907.

[98] H. Kenfoud, N. Nasrallah, D. Meziani, M. Trari, Photoelectrochemical study of the spinel $CaFe_2O_4$ nanostructure: Application to Basic Blue 41 oxidation under solar light, J. Solid State Electrochem. 25 (2021) 1815–1823.

[99] A. Bloesser, J. Timm, H. Kurz, W. Milius, S. Hayama, J. Breu, B. Weber, R. Marschall, A novel synthesis yielding macroporous $CaFe_2O_4$ sponges for solar energy conversion, Sol. RRL. 4 (2020) 1900570.

[100] C.G. Read, Y. Park, K.-S. Choi, Electrochemical synthesis of p-type $CuFeO_2$ electrodes for use in a photoelectrochemical cell, J. Phys. Chem. Lett. 3 (2012) 1872–1876.

[101] L. Mao, S. Mohan, S.K. Gupta, Y. Mao, Multifunctional delafossite CuFeO2 as water splitting catalyst and rhodamine B sensor, Mater. Chem. Phys. 278 (2022) 125643.

[102] K. Skorupska, P.A. Maggard, R. Eichberger, K. Schwarzburg, P. Shahbazi, B. Zoellner, B.A. Parkinson, Combinatorial investigations of high temperature CuNb oxide phases for photoelectrochemical water splitting, ACS Comb. Sci. 17 (2015) 742–751.

[103] C.T. Crespo, $CuNbO_3$ as a solar energy converter to fuel and electricity, Sol. Energy Mater. Sol. Cells. 179 (2018) 305–311.

[104] F. Andrei, V. Ion, R. Birjega, M. Dinescu, N. Enea, D. Pantelica, M.D. Mihai, V. A. Maraloiu, V.S. Teodorescu, I. C. Marcu, others, Thickness-dependent photoelectrochemical water splitting properties of self-assembled nanostructured $LaFeO_3$ perovskite thin films, Nanomaterials. 11 (2021) 1371.

[105] M.-K. Son, H. Seo, M. Watanabe, M. Shiratani, T. Ishihara, Characteristics of crystalline sputtered $LaFeO_3$ thin films as photoelectrochemical water splitting photocathodes, Nanoscale. 12 (2020) 9653–9660.

[106] Y. Gao, Y. Li, G. Yang, S. Li, N. Xiao, B. Xu, S. Liu, P. Qiu, S. Hao, L. Ge, Fe_2TiO_5 as an efficient co-catalyst to improve the photoelectrochemical water splitting performance of $BiVO_4$, ACS Appl. Mater. & Interfaces. 10 (2018) 39713–39722.

[107] P.S. Bassi, S.Y. Chiam, J. Barber, L.H. Wong, Hydrothermal grown nanoporous iron based titanate, Fe_2TiO_5 for light driven water splitting, ACS Appl. Mater. & Interfaces. 6 (2014) 22490–22495.

[108] L. Zhang, D. Bahnemann, Synthesis of nanovoid Bi_2WO_6 2D ordered arrays as photoanodes for photoelectrochemical water splitting, ChemSusChem. 6 (2013) 283–290.

[109] L. Zhang, C. Baumanis, L. Robben, T. Kandiel, D. Bahnemann, Bi_2WO_6 inverse opals: facile fabrication and efficient visible-light-driven photocatalytic and photoelectrochemical water-splitting activity, Small. 7 (2011) 2714–2720.

[110] Y. Pihosh, I. Turkevych, K. Mawatari, J. Uemura, Y. Kazoe, S. Kosar, K. Makita, T. Sugaya, T. Matsui, D. Fujita, others, Photocatalytic generation of hydrogen by core-shell $WO_3/BiVO_4$ nanorods with ultimate water splitting efficiency, Sci. Rep. 5 (2015) 1–10.

[111] A.R. Marlinda, N. Yusoff, S. Sagadevan, M.R. Johan, Recent developments in reduced graphene oxide nanocomposites for photoelectrochemical water-splitting applications, Int. J. Hydrogen Energy. 45 (2020) 11976–11994.

[112] G. Xie, K. Zhang, B. Guo, Q. Liu, L. Fang, J.R. Gong, Graphene-based materials for hydrogen generation from light-driven water splitting, Adv. Mater. 25 (2013) 3820–3839.

[113] J. Ke, F. He, H. Wu, S. Lyu, J. Liu, B. Yang, Z. Li, Q. Zhang, J. Chen, L. Lei, others, Nanocarbon-enhanced 2D photoelectrodes: a new paradigm in photoelectrochemical water splitting, Nano-Micro Lett. 13 (2021) 1–29.

[114] M. Volokh, G. Peng, J. Barrio, M. Shalom, Carbon nitride materials for water splitting photoelectrochemical cells, Angew. Chemie Int. Ed. 58 (2019) 6138–6151.

[115] C. Zhen, R. Chen, L. Wang, G. Liu, H.-M. Cheng, Tantalum (oxy) nitride based photoanodes for solar-driven water oxidation, J. Mater. Chem. A. 4 (2016) 2783–2800.

[116] S. Li, Y. Zhang, H. Huang, Black phosphorus-based heterostructures for photocatalysis and photoelectrochemical water splitting, J. Energy Chem. 67 (2022) 745–779.

[117] F. Liu, C. Huang, C.-X. Liu, R. Shi, Y. Chen, Black Phosphorus-Based Semiconductor Heterojunctions for Photocatalytic Water Splitting, Chem. Eur. J. 26 (2020) 4449–4460.

[118] S. Tang, W. Qiu, S. Xiao, Y. Tong, S. Yang, Harnessing hierarchical architectures to

trap light for efficient photoelectrochemical cells, Energy & Environ. Sci. 13 (2020) 660–684.

[119] W.-J. Yin, H. Tang, S.-H. Wei, M.M. Al-Jassim, J. Turner, Y. Yan, Band structure engineering of semiconductors for enhanced photoelectrochemical water splitting: the case of TiO_2, Phys. Rev. B. 82 (2010) 45106.

[120] S. Sriwichai, R. Irani, F. Xi, D. Friedrich, C. Höhn, I.Y. Ahmet, N. Wetchakun, F.F. Abdi, Role of Gd in Enhancing the Charge Carrier Mobility of Spray--Deposited $BiVO_4$ Photoanodes, Sol. RRL. 5 (2021) 2100268.

[121] X. Zhong, H. He, M. Yang, G. Ke, Z. Zhao, F. Dong, B. Wang, Y. Chen, X. Shi, Y. Zhou, In^{3+}-doped $BiVO_4$ photoanodes with passivated surface states for photoelectrochemical water oxidation, J. Mater. Chem. A. 6 (2018) 10456–10465.

[122] G. Wang, Y. Yang, D. Han, Y. Li, Oxygen defective metal oxides for energy conversion and storage, Nano Today. 13 (2017) 23–39.

[123] C. Shao, A.S. Malik, J. Han, D. Li, M. Dupuis, X. Zong, C. Li, Oxygen vacancy engineering with flame heating approach towards enhanced photoelectrochemical water oxidation on WO_3 photoanode, Nano Energy. 77 (2020) 105190.

[124] D. Chandra, K. Saito, T. Yui, M. Yagi, Tunable mesoporous structure of crystalline WO_3 photoanode toward efficient visible-light-driven water oxidation, ACS Sustain. Chem. & Eng. 6 (2018) 16838–16846.

[125] S. Wang, H. Chen, G. Gao, T. Butburee, M. Lyu, S. Thaweesak, J.-H. Yun, A. Du, G. Liu, L. Wang, Synergistic crystal facet engineering and structural control of WO_3 films exhibiting unprecedented photoelectrochemical performance, Nano Energy. 24 (2016) 94–102.

[126] S. Zhong, Y. Xi, S. Wu, Q. Liu, L. Zhao, S. Bai, Hybrid cocatalysts in semiconductor-based photocatalysis and photoelectrocatalysis, J. Mater. Chem. A. 8 (2020) 14863–14894.

[127] D. V Esposito, J.G. Chen, R.W. Birkmire, Y. Chang, N. Gaillard, Hydrogen production from photo-driven electrolysis of biomass-derived oxygenates: A case study on methanol using Pt-modified WO_3 thin film electrodes, Int. J. Hydrogen Energy. 36 (2011) 9632–9644.

[128] Q. Lang, Y. Yang, Y. Zhu, W. Hu, W. Jiang, S. Zhong, P. Gong, B. Teng, L. Zhao, S. Bai, High-index facet engineering of PtCu cocatalysts for superior photocatalytic reduction of CO_2 to CH_4, J. Mater. Chem. A. 5 (2017) 6686–6694.

[129] D. Li, J. Shi, C. Li, Transition-metal-based electrocatalysts as cocatalysts for

photoelectrochemical water splitting: a mini review, Small. 14 (2018) 1704179.

[130] X.-Q. Bao, M.F. Cerqueira, P. Alpuim, L. Liu, Silicon nanowire arrays coupled with cobalt phosphide spheres as low-cost photocathodes for efficient solar hydrogen evolution, Chem. Commun. 51 (2015) 10742–10745.

[131] G. Fang, Z. Liu, C. Han, Enhancing the PEC water splitting performance of $BiVO_4$ co-modifying with NiFeOOH and Co-Pi double layer cocatalysts, Appl. Surf. Sci. 515 (2020) 146095.

[132] G. Fang, Z. Liu, C. Han, X. Ma, H. Lv, C. Huang, Z. Cheng, Z. Tong, P. Wang, CoNiO 2 as a novel water oxidation cocatalyst to enhance PEC water splitting performance of $BiVO_4$, Chem. Commun. 56 (2020) 9158–9161.

[133] X.-T. Xu, L. Pan, X. Zhang, L. Wang, J.-J. Zou, Rational Design and Construction of Cocatalysts for Semiconductor-Based Photo-Electrochemical Oxygen Evolution: A Comprehensive Review, Adv. Sci. 6 (2019) 1801505.

[134] J. Jian, G. Jiang, R. van de Krol, B. Wei, H. Wang, Recent advances in rational engineering of multinary semiconductors for photoelectrochemical hydrogen generation, Nano Energy. 51 (2018) 457–480.

[135] R.E. Adam, M. Pirhashemi, S. Elhag, X. Liu, A. Habibi-Yangjeh, M. Willander, O. Nur, $ZnO/Ag/Ag_2WO_4$ photo-electrodes with plasmonic behavior for enhanced photoelectrochemical water oxidation, RSC Adv. 9 (2019) 8271–8279.

[136] C. Dong, Z. Zheng, M.A.H. Badsha, J. He, I.M.C. Lo, Visible-light-driven peroxymonosulfate activation in photo-electrocatalytic system using hollow-structured $Pt@CeO_2@$ MoS_2 photoanode for the degradation of pharmaceuticals and personal care products, Environ. Int. 154 (2021) 106572.

[137] M.S. Akple, S.P. Chimmikuttanda, A ternary Z-scheme WO_3-Pt-CdS composite for improved visible-light photocatalytic H2 production activity, J. Nanoparticle Res. 20 (2018) 1–16.

[138] T. Wang, F. Ye, S. Wu, S. Chen, H. Yu, X. Quan, Efficient Light-Driven Fuel Cell with Simultaneous Degradation of Pollutants on a TiO_2 Photoanode and Production of H_2O_2 on a Gas Diffusion Electrode Cathode, ACS ES&T Eng. 1 (2021) 1122–1130.

[139] L. Liu, G. Zhang, J.T.S. Irvine, Y. Wu, Organic Semiconductor g-C_3N_4 Modified TiO_2 Nanotube Arrays for Enhanced Photoelectrochemical Performance in Wastewater Treatment, Energy Technol. 3 (2015) 982–988.

[140] J. Cheng, M. Zhang, G. Wu, X. Wang, J. Zhou, K. Cen, Photoelectrocatalytic reduction of CO_2 into chemicals using Pt-modified reduced graphene oxide combined with Pt-

modified TiO_2 nanotubes, Environ. Sci. & Technol. 48 (2014) 7076–7084.

[141] X. Zhang, S. Chen, X. Quan, H. Zhao, Preparation and characterization of $BiVO_4$ film electrode and investigation of its photoelectrocatalytic (PEC) ability under visible light, Sep. Purif. Technol. 64 (2009) 309–313.

[142] S. Wang, T. He, J.-H. Yun, Y. Hu, M. Xiao, A. Du, L. Wang, New iron-cobalt oxide catalysts promoting BiVO4 films for photoelectrochemical water splitting, Adv. Funct. Mater. 28 (2018) 1802685.

[143] Y. Zuo, Y. Liu, J. Li, R. Du, X. Yu, C. Xing, T. Zhang, L. Yao, J. Arbiol, J. Llorca, others, Solution-processed ultrathin SnS_2--Pt nanoplates for photoelectrochemical water oxidation, ACS Appl. Mater. & Interfaces. 11 (2019) 6918–6926.

[144] C. Gómez-Solis, J.C. Ballesteros, L.M. Torres-Martinez, I. Juárez-Ramirez, RuO_2--$NaTaO_3$ heterostructure for its application in photoelectrochemical water splitting under simulated sunlight illumination, Fuel. 166 (2016) 36–41.

[145] Y. Zhang, G. Zhao, Y. Zhang, X. Huang, Highly efficient visible-light-driven photoelectro-catalytic selective aerobic oxidation of biomass alcohols to aldehydes, Green Chem. 16 (2014) 3860–3869.

[146] J. Wang, Y. Wei, B. Yang, B. Wang, J. Chen, H. Jing, In situ grown heterojunction of Bi_2WO_6/BiOCl for efficient photoelectrocatalytic CO_2 reduction, J. Catal. 377 (2019) 209–217.

[147] H. Cao, H. Yu, Y. Lu, H. Zhang, G. Hou, Y. Tang, G. Zheng, Photoelectrocatalytic Reduction of CO_2 over $CuBi_2O_4$/TiO_2-NTs under Simulated Solar Irradiation, ChemistrySelect. 5 (2020) 5137–5145.

[148] J.Y. Kim, J. W. Jang, D. H. Youn, J. Y. Kim, E.S. Kim, J. S. Lee, Graphene-carbon nanotube composite as an effective conducting scaffold to enhance the photoelectrochemical water oxidation activity of a hematite film, Rsc Adv. 2 (2012) 9415–9422.

[149] Y. Liu, J. Lu, Q. Zhang, Y. Bai, X. Pang, S. Wang, H. Bai, W. Fan, Charge-transfer dynamics at a Ag/Ni-MOF/Cu_2O heterostructure in photoelectrochemical NH_3 production, Chem. Commun. 57 (2021) 8031–8034.

[150] Y. Dong, Y. Chen, P. Jiang, G. Wang, X. Wu, R. Wu, C. Zhang, Efficient and stable MoS_2/CdSe/NiO photocathode for photoelectrochemical hydrogen generation from water, Chem. Asian J. 10 (2015) 1660–1667.

[151] Z. Zhang, Y. Yu, P. Wang, Hierarchical top-porous/bottom-tubular TiO_2 nanostructures decorated with Pd nanoparticles for efficient photoelectrocatalytic decomposition of

synergistic pollutants, ACS Appl. Mater. & Interfaces. 4 (2012) 990–996.

[152] Q. Wang, X. Ma, P. Wu, B. Li, L. Zhang, J. Shi, CoNiFe-LDHs decorated Ta_3N_5 nanotube array photoanode for remarkably enhanced photoelectrochemical glycerol conversion coupled with hydrogen generation, Nano Energy. 89 (2021) 106326.

[153] R. Chong, B. Wang, D. Li, Z. Chang, L. Zhang, Enhanced photoelectrochemical activity of Nickel-phosphate decorated phosphate-Fe_2O_3 photoanode for glycerol-based fuel cell, Sol. Energy Mater. Sol. Cells. 160 (2017) 287–293..

[154] S. Cao, X. Yan, Z. Kang, Q. Liang, X. Liao, Y. Zhang, Band alignment engineering for improved performance and stability of $ZnFe_2O_4$ modified CdS/ZnO nanostructured photoanode for PEC water splitting, Nano Energy. 24 (2016) 25–31.

[155] J. Zhang, G. Zhang, H. Lan, H. Liu, J. Qu, Sustainable nitrogen fixation over Ru single atoms decorated Cu_2O using electrons produced from photoelectrocatalytic organics degradation, Chem. Eng. J. 428 (2022) 130373.

[156] D. Cao, Y. Wang, M. Qiao, X. Zhao, Enhanced photoelectrocatalytic degradation of norfloxacin by an Ag_3PO_4/$BiVO_4$ electrode with low bias, J. Catal. 360 (2018) 240–249.

[157] B.O. Orimolade, O.A. Arotiba, Bismuth vanadate in photoelectrocatalytic water treatment systems for the degradation of organics: a review on recent trends, J. Electroanal. Chem. 878 (2020) 114724.

[158] Y. Xue, Y. Wang, Z. Pan, K. Sayama, Electrochemical and photoelectrochemical water oxidation for hydrogen peroxide production, Angew. Chemie Int. Ed. 60 (2021) 10469–10480.

[159] L. Wang, Y. Lu, N. Han, C. Dong, C. Lin, S. Lu, Y. Min, K. Zhang, Suppressing Water Dissociation via Control of Intrinsic Oxygen Defects for Awakening Solar H_2O-to-H_2O_2 Generation, Small. 17 (2021) 2100400.

[160] J. Liu, Y. Zou, B. Jin, K. Zhang, J.H. Park, Hydrogen peroxide production from solar water oxidation, ACS Energy Lett. 4 (2019) 3018–3027.

[161] K. Zhang, J. Liu, L. Wang, B. Jin, X. Yang, S. Zhang, J.H. Park, Near-complete suppression of oxygen evolution for photoelectrochemical H_2O oxidative H_2O_2 synthesis, J. Am. Chem. Soc. 142 (2020) 8641–8648.

[162] K. Fuku, K. Sayama, Efficient oxidative hydrogen peroxide production and accumulation in photoelectrochemical water splitting using a tungsten trioxide/bismuth vanadate photoanode, Chem. Commun. 52 (2016) 5406–5409.

[163] K. Fuku, Y. Miyase, Y. Miseki, T. Gunji, K. Sayama, WO_3/$BiVO_4$ photoanode coated with mesoporous Al_2O_3 layer for oxidative production of hydrogen peroxide from water

with high selectivity, RSC Adv. 7 (2017) 47619–47623.

[164] G. Dodekatos, S. Schünemann, H. Tüysüz, Recent Advances in Thermo-, Photo-, and Electrocatalytic Glycerol Oxidation, ACS Catal. 8 (2018) 6301–6333.

[165] Z. Gu, X. An, R. Liu, L. Xiong, J. Tang, C. Hu, H. Liu, J. Qu, Interface-modulated nanojunction and microfluidic platform for photoelectrocatalytic chemicals upgrading, Appl. Catal. B Environ. 282 (2021) 119541.

[166] O.P. Paris/FAO, OECD-FAO Agricultural Outlook 2020-2029, 2020.

[167] C. Santibáñez, M.T. Varnero, M. Bustamante, Residual glycerol from biodiesel manufacturing, waste or potential source of bioenergy: a review, Chil. J. Agric. Res. 71 (2011) 469–475.

[168] Z.G. Schichtl, S.K. Conlin, H. Mehrabi, A.C. Nielander, R.H. Coridan, Characterizing sustained solar-to-hydrogen electrocatalysis at low cell potentials enabled by crude glycerol oxidation, ACS Appl. Energy Mater. (2022).

[169] Y. Lee, S. Kim, S.Y. Jeong, S. Seo, C. Kim, H. Yoon, H.W. Jang, S. Lee, Surface-modified Co-doped ZnO photoanode for photoelectrochemical oxidation of glycerol, Catal. Today. 359 (2021) 43–49.

[170] F.J. Mancilla, S.F. Rojas, A.F. Gualdrón-Reyes, M.I. Carreño-Lizcano, L.J. Duarte, M.E. Niño-Gómez, Improving the photoelectrocatalytic performance of boron-modified TiO $_2$/Ti sol--gel-based electrodes for glycerol oxidation under visible illumination, RSC Adv. 6 (2016) 46668–46677.

[171] S.A.L. Bastos, P.A.L. Lopes, F.N. Santos, L.A. Silva, Experimental design as a tool to study the reaction parameters in hydrogen production from photoinduced reforming of glycerol over CdS photocatalyst, Int. J. Hydrogen Energy. 39 (2014) 14588–14595.

[172] M. Ibadurrohman, K. Hellgardt, Photoelectrochemical performance of graphene-modified TiO_2 photoanodes in the presence of glycerol as a hole scavenger, Int. J. Hydrogen Energy. 39 (2014) 18204–18215.

[173] J. Baltrusaitis, Y.-S. Hu, E.W. McFarland, A. Hellman, Photoelectrochemical Hydrogen Production on α-Fe_2O_3 (0001): Insights from Theory and Experiments, ChemSusChem. 7 (2014) 162–171.

[174] R. Bashiri, N.M. Mohamed, C.F. Kait, S. Sufian, M. Khatani, Enhanced hydrogen production over incorporated Cu and Ni into titania photocatalyst in glycerol-based photoelectrochemical cell: Effect of total metal loading and calcination temperature, Int. J. Hydrogen Energy. 42 (2017) 9553–9566.

[175] R. Bashiri, N.M. Mohamed, N.A. Suhaimi, M.U. Shahid, C.F. Kait, S. Sufian, M.

Khatani, A. Mumtaz, Photoelectrochemical water splitting with tailored $TiO_2/SrTiO_3$@ g-C_3N_4 heterostructure nanorod in photoelectrochemical cell, Diam. Relat. Mater. 85 (2018) 5–12.

[176] M. Antoniadou, P. Lianos, Near ultraviolet and visible light photoelectrochemical degradation of organic substances producing electricity and hydrogen, J. Photochem. Photobiol. A Chem. 204 (2009) 69–74.

[177] R. Bashiri, N.M. Mohamed, L.Y. Ling, N.A. Suhaimi, M.U. Shahid, S. Sufian, C.F. Kait, S.M. Saheed, Influence of seeding layer on photoelectrochemical hydrogen production over TiO_2 nanorod decorated with reduced graphene oxide, Diam. Relat. Mater. 94 (2019) 194–202.

[178] D. Raptis, V. Dracopoulos, P. Lianos, Renewable energy production by photoelectrochemical oxidation of organic wastes using WO_3 photoanodes, J. Hazard. Mater. 333 (2017) 259–264.

[179] R. Bashiri, N.M. Mohamed, C.F. Kait, S. Sufian, S. Kakooei, M. Khatani, Z. Gholami, Optimization hydrogen production over visible light-driven titania-supported bimetallic photocatalyst from water photosplitting in tandem photoelectrochemical cell, Renew. Energy. 99 (2016) 960–970.

[180] A. Dittmer, J. Menze, B. Mei, J. Strunk, H.S. Luftman, R. Gutkowski, I.E. Wachs, W. Schuhmann, M. Muhler, Surface structure and photocatalytic properties of Bi_2WO_6 nanoplatelets modified by molybdena islands from chemical vapor deposition, J. Phys. Chem. C. 120 (2016) 18191–18200.

[181] K. Wu, M. Cao, Q. Zeng, X. Li, Radical and (photo) Electron Transfer Induced Mechanisms for Lignin Photo-and Electro-catalytic Depolymerization, Green Energy & Environ. (2022).

[182] F. Wang, J.D. Harindintwali, Z. Yuan, M. Wang, F. Wang, S. Li, Z. Yin, L. Huang, Y. Fu, L. Li, others, Technologies and perspectives for achieving carbon neutrality, Innov. 2 (2021) 100180.

[183] J. Zhao, X. Wang, Z. Xu, J.S.C. Loo, Hybrid catalysts for photoelectrochemical reduction of carbon dioxide: a prospective review on semiconductor/metal complex co-catalyst systems, J. Mater. Chem. A. 2 (2014) 15228–15233.

[184] Y. Li, Z. Liu, Z. Li, Q. Wang, Renewable biomass-derived carbon-supported g-C_3N_4 doped with Ag for enhanced photocatalytic reduction of CO_2, J. Colloid Interface Sci. 606 (2022) 1311–1321.

[185] Q. Shen, Z. Chen, X. Huang, M. Liu, G. Zhao, High-yield and selective

photoelectrocatalytic reduction of CO_2 to formate by metallic copper decorated Co_3O_4 nanotube arrays, Environ. Sci. & Technol. 49 (2015) 5828–5835.

[186] K.M.R. Karim, H.R. Ong, H. Abdullah, A. Yousuf, C.K. Cheng, M.M.R. Khan, Photoelectrochemical reduction of carbon dioxide to methanol on p-type $CuFe_2O_4$ under visible light irradiation, Int. J. Hydrogen Energy. 43 (2018) 18185–18193.

[187] G. Soloveichik, Electrochemical synthesis of ammonia as a potential alternative to the Haber--Bosch process, Nat. Catal. 2 (2019) 377–380.

[188] D.L.T. Nguyen, M.A. Tekalgne, T.H.C. Nguyen, M.T.N. Dinh, S.S. Sana, A.N. Grace, M. Shokouhimehr, D.-V.N. Vo, C.K. Cheng, C.C. Nguyen, others, Recent development of high-performance photocatalysts for N2 fixation: A review, J. Environ. Chem. Eng. 9 (2021) 104997.

[189] Y. Bo, H. Wang, Y. Lin, T. Yang, R. Ye, Y. Li, C. Hu, P. Du, Y. Hu, Z. Liu, others, Altering hydrogenation pathways in photocatalytic nitrogen fixation by tuning local electronic structure of oxygen vacancy with dopant, Angew. Chemie Int. Ed. 60 (2021) 16085–16092.

[190] Y. Huang, C. Wang, Y. Yu, Y. Yu, W. Wang, B. Zhang, Atomically Dispersed Ru-Decorated TiO_2 Nanosheets for Thermally Assisted Solar-Driven Nitrogen Oxidation into Nitric Oxide, CCS Chem. (2021) 1468–1476.

[191] D. V Chachkov, O. V Mikhailov, Novel modifications of elemental nitrogen and their molecular structures--a quantum-chemical calculation, Eur. Chem. Bull. 9 (2020) 78–81.

[192] L. Shi, Y. Yin, S. Wang, H. Sun, Rational catalyst design for N_2 reduction under ambient conditions: strategies toward enhanced conversion efficiency, ACS Catal. 10 (2020) 6870–6899.

[193] Y. Bai, J. Lu, H. Bai, Z. Fang, F. Wang, Y. Liu, D. Sun, B. Luo, W. Fan, W. Shi, Understanding the key role of vanadium in p-type $BiVO_4$ for photoelectrochemical N2 fixation, Chem. Eng. J. 414 (2021) 128773.

[194] Y. Shiraishi, S. Shiota, Y. Kofuji, M. Hashimoto, K. Chishiro, H. Hirakawa, S. Tanaka, S. Ichikawa, T. Hirai, Nitrogen fixation with water on carbon-nitride-based metal-free photocatalysts with 0.1% solar-to-ammonia energy conversion efficiency, ACS Appl. Energy Mater. 1 (2018) 4169–4177.

[195] Y. Miao, M. Shao, Photoelectrocatalysis for high-value-added chemicals production, Chinese J. Catal. 43 (2022) 595–610.

[196] M.-I. Jamesh, M. Harb, Tuning the electronic structure of the earth-abundant

electrocatalysts for oxygen evolution reaction (OER) to achieve efficient alkaline water splitting--A review, J. Energy Chem. 56 (2021) 299–342.

[197] N. Danilovic, R. Subbaraman, D. Strmcnik, V. Stamenkovic, N. Markovic, Electrocatalysis of the HER in acid and alkaline media, J. Serbian Chem. Soc. 78 (2013).

[198] S. Jin, X. Ma, J. Pan, C. Zhu, S.E. Saji, J. Hu, X. Xu, L. Sun, Z. Yin, Oxygen vacancies activating surface reactivity to favor charge separation and transfer in nanoporous $BiVO_4$ photoanodes, Appl. Catal. B Environ. 281 (2021) 119477.

[199] Y. Zhao, S. Balasubramanyam, R. Sinha, R. Lavrijsen, M.A. Verheijen, A.A. Bol, A. Bieberle-Hu tter, Physical and chemical defects in WO_3 thin films and their impact on photoelectrochemical water splitting, ACS Appl. Energy Mater. 1 (2018) 5887–5895.

[200] Y. Yang, D. Xu, Q. Wu, P. Diao, Cu_2O/CuO bilayered composite as a high-efficiency photocathode for photoelectrochemical hydrogen evolution reaction, Sci. Rep. 6 (2016) 1–13.

[201] O. Monfort, S. Sfaelou, L. Satrapinskyy, T. Plecenik, T. Roch, G. Plesch, P. Lianos, Comparative study between pristine and Nb-modified $BiVO_4$ films employed for photoelectrocatalytic production of H_2 by water splitting and for photocatalytic degradation of organic pollutants under simulated solar light, Catal. Today. 280 (2017) 51–57.

[202] N.C.D. Nath, S.Y. Choi, H.W. Jeong, J.-J. Lee, H. Park, Stand-alone photoconversion of carbon dioxide on copper oxide wire arrays powered by tungsten trioxide/dye-sensitized solar cell dual absorbers, Nano Energy. 25 (2016) 51–59.

[203] G. Bharath, K. Rambabu, A. Hai, N. Ponpandian, J.E. Schmidt, D. D. Dionysiou, M.A. Haija, F. Banat, Dual-functional paired photoelectrocatalytic system for the photocathodic reduction of CO_2 to fuels and the anodic oxidation of furfural to value-added chemicals, Appl. Catal. B Environ. 298 (2021) 120520.

[204] Z. Zheng, J. He, C. Dong, I.M.C. Lo, Photoelectrochemical sewage treatment by sulfite activation over an optimized $BiVO_4$ photoanode to simultaneously promote PPCPs degradation, H2 evolution and E. coli disinfection, Chem. Eng. J. 419 (2021) 129418.

[205] M.S. Koo, X. Chen, K. Cho, T. An, W. Choi, In situ photoelectrochemical chloride activation using a WO_3 electrode for oxidative treatment with simultaneous H2 evolution under visible light, Environ. Sci. & Technol. 53 (2019) 9926–9936.

[206] H. Rajput, E.E. Kwon, S.A. Younis, S. Weon, T.H. Jeon, W. Choi, K.-H. Kim, Photoelectrocatalysis as a high-efficiency platform for pulping wastewater treatment and energy production, Chem. Eng. J. 412 (2021) 128612.

[207] J. Kim, W. Choi, Hydrogen producing water treatment through solar photocatalysis, Energy & Environ. Sci. 3 (2010) 1042–1045.

[208] J. Kim, D. Monllor-Satoca, W. Choi, Simultaneous production of hydrogen with the degradation of organic pollutants using TiO_2 photocatalyst modified with dual surface components, Energy & Environ. Sci. 5 (2012) 7647–7656.

[209] S. Kim, G. Piao, D.S. Han, H.K. Shon, H. Park, Solar desalination coupled with water remediation and molecular hydrogen production: a novel solar water-energy nexus, Energy & Environ. Sci. 11 (2018) 344–353.

[210] L. Luo, W. Chen, S.-M. Xu, J. Yang, M. Li, H. Zhou, M. Xu, M. Shao, X. Kong, Z. Li, others, Selective Photoelectrocatalytic Glycerol Oxidation to Dihydroxyacetone via Enhanced Middle Hydroxyl Adsorption over a Bi_2O_3-Incorporated Catalyst, J. Am. Chem. Soc. (2022).

[211] C. Lv, L. Zhong, H. Liu, Z. Fang, C. Yan, M. Chen, Y. Kong, C. Lee, D. Liu, S. Li, others, Selective electrocatalytic synthesis of urea with nitrate and carbon dioxide, Nat. Sustain. 4 (2021) 868–876.

Objectives and Strategies

According to the above literature review, we clearly found that photoelectrocatalytic (PEC) technology is an efficient, green and environmentally friendly technology with great prospects. Anodic CO_2-free valorization of biomass via PEC is potentially one of the best routes to convert biomass-based molecules as glycerol into valuable products due to the effective promotion of the separation of photogenerated electrons and holes via the combination of an externally applied electric bias. Meanwhile, cathodic hydrogen evolution reaction (HER) allows for obtaining potential energy carrier H_2 with high energy capacity and environmental friendliness in a clean and rapid way. Due to the fact that most current studies where photocatalyst materials are limited to mineralization with low selectivity towards high value-added products, leading to CO_2 emission, it is attractive and feasible to establish dual-compartment PEC setups to achieve valuable chemicals formation with limited or without CO_2 yielding in one anodic compartment coupling with spatially separate pure gaseous H_2 production in the other cathodic compartment. Thus the ideal bifunctional PEC technology potentially mitigates the current energy crisis and decreases environmental pollution. In order to further promote the development of PEC technology for solar-to-chemical energy conversion, we developed the research target of this thesis: Photocatalytic and photoelectrocatalytic glycerol valorization with simultaneous hydrogen generation.

The objectives of this research are as follows:

I) To explore the relationship between the PC or PEC activity for the glycerol valorization towards value-added products, and the physicochemical properties of single-component TiO_2-based catalysts, WO_3-based catalysts as well as their binary co-catalyst DTW5 (5% WO_3 on TiO_2). Kinetics and selectivity/yield to high-value products will be the main evaluation indicators of glycerol PC or PEC oxidation.

II) To compare the performances, and to establish the global reaction mechanism of PC and PEC technology for the selective oxidation of glycerol towards 3C products (glyceraldehyde and dihydroxyacetone).

III) To develop and construct an advanced bifunctional PEM PEC reaction system with separated dual-compartments (Conf. 1). It will allow to explore the influence of key parameters of PEC operation such as temperature and external voltage on the two half-reactions aiming for the final goal of PEC glycerol valorization with simultaneous hydrogen generation.

According to the above objectives, the research strategy of this thesis is as follows:

In the first part of the work, we selected a series of single-component TiO_2-based catalysts (Anatase, Rutile and P25) and a WO_3-based catalyst (Homemade monoclinic WO_3) for comparison. The optimal catalyst was determined based on the selectivity towards 3C products and the reaction kinetics of PC biomass conversion. Besides, a commercial binary cocatalyst DTW5 (5% WO_3 on Anatase) was also studied in order to understand the merits of binary cocatalyst compared to single-component catalysts. The specific surface area, crystal phase composition and other structural characteristics of the materials were analyzed by various characterization methods such as X-ray diffraction (XRD), scanning electron microscopy (SEM), high-resolution transmission electron microscopy (HRTEM), Brunauer-Emmett-Teller (BET), and Raman spectroscopy; the photophysical properties of the materials are characterized by UV-vis diffuse reflectance spectroscopy (UV-vis DRS) measurements; the acidity of catalysts was characterized via Diffuse reflectance infrared Fourier transform spectroscopy (DRIFTS) and their basic electrochemical properties were studied by photocurrent experiments in a commercial single-compartment photoelectrochemical cell (supplied by redox.me ®). A Shimadzu SPD-M20A prominence ultrafast high-performance liquid chromatography (HPLC) is applied for the detection of oxidation products. Through analyzing the physicochemical properties of materials, together with the detection and selectivity of glycerol oxidation products, the PC glycerol valorization mechanisms of different types of catalysts was properly understood, which laid the foundation for the study of the PEC process.

In the second part of the work, we further modified and improved the homemade single-component photocatalyst WO_3 by defect engineering and compared it with the commercial binary cocatalyst DTW5. We attempted the PEC conversion of glycerol in a conventional 3-electrode PEC cell, where the above-mentioned photocatalysts were coated on an indium-tin-oxide (ITO) glass, acting therefore as the photoanode (with Pt and Ag/AgCl serving as the cathode and reference electrode, respectively). By applying different external voltages (0.3, 0.6, 0.9, 1.2 and 1.5 V), the activities of PEC glycerol valorization were explored. During the reaction, the Faradaic efficiency of the product was used to understand the electron transport process. Furthermore, the role of oxygen vacancies introduced by defect engineering, the effect of external voltage on photogenerated charge separation, and the mechanism of PEC reaction combined with possible OER formation was also investigated.

In the third part of the work, a truly bifunctional PEM PEC system is constructed, where the proton exchange membrane (PEM) acts as a solid electrolyte for proton transport and

simultaneously separation for the two half-reactions (i.e., selective glycerol oxidation at the anode, and hydrogen production at the cathode). The best performing catalyst from the previous two parts was assembled and used as a photoanode in this system to convert glycerol, and a Pt/C catalyst was used as the cathode to generate hydrogen. Notably, temperature, an important reaction parameter, is explored together with the external voltage. The energy production efficiency and the reaction mechanism were evaluated by electrochemical methods such as linear sweep voltammetry (LSV), cyclic voltammetry (CV) and photocurrent. Thus, photoelectrocatalytic glycerol valorization with simultaneous hydrogen generation was achieved under mild conditions.

This study systematically explores the selective conversion and mechanism of PC and PEC glycerol valorization from i) the selection, modification and thorough characterization of different catalysts, ii) the optimization of operational parameters, and iii) towards the development of a state-of-the-art bifunctional PEC system for the simultaneous production and separation of high-value chemicals and hydrogen. This study provides a very meaningful reference for the practical application of PEC technology.

Chapter 2

Glyceraldehyde production by photocatalytic oxidation of glycerol on WO_3-based materials

Jie Yu,[a] Frederic.Dappozze,[a] Juan Martín-Gomez,[b] Jesús Hidalgo-Carrillo,[b] Alberto Marinas,[b] Philippe Vernoux,[a] Angel Caravaca,[a]* Chantal Guillard [a]*

[a] Univ Lyon, Université Claude Bernard Lyon 1, CNRS, IRCELYON, F-69626, Villeurbanne, France

[b] Departamento de Química Orgánica. Instituto Universitario de Investigación en Nanoquímica (IUNAN). Universidad de Córdoba. Edf. Marie Curie (Annex). Campus de Rabanales, E-14071 Córdoba. España
E-mail: angel.caravaca@ircelyon.univ-lyon1.fr, chantal.guillard@ircelyon.univ-lyon1.fr

Abstract

Valorization of glycerol into high added-value products by photocatalysis can not only create good economic benefits, but also cater to the global low-carbon and energy-saving environmental protection needs. In this study we proposed, for the very first time, to perform the photo-oxidation of glycerol towards added-value products with WO_3-based materials (homemade WO_3 and commercial WO_3/TiO_2 (DTW5)). Their performance was compared with that of state-of-the-art TiO_2-based photocatalysts (Anatase, Rutile, and P25). We found that, while TiO_2 favours the total oxidation of glycerol, WO_3-based materials exhibit an outstanding selectivity towards one of the most valuable oxidation products: glyceraldehyde. It was attributed to their enhanced acidity, which selectively activates C-O bonds in glycerol and facilitates the further desorption of glyceraldehyde to the liquid phase. This study establishes therefore a new starting point towards the development of advanced materials for an efficient valorization of glycerol.

Keywords: photocatalysis, valorization, glycerol, glyceraldehyde, WO_3

1. Introduction

The current development of the economy has nowadays a significant ecological impact. Therefore, the generation of clean energy, together with the production of high-value chemicals to replace the utilization of petroleum-derivate products via efficient/non-expensive technologies, has become a major challenge for human beings. In particular, the current energy sector in this world mainly depends on limited sources of fossil fuels, which limits the long-term development of the economy. Thus, the production of biodiesel fuel derived from a renewable biomass source has become one of the main strategic alternatives to overcome these issues. As a matter of fact, according to the report provided by the Food and Agriculture Organization of the United Nations (OECD/FAO), the production of biodiesel is increasing year by year and it is forecasted to remain at a high level. [1,2] However, the production of biodiesel is accompanied by a significant co-production of glycerol. Around 100 kg of glycerol (～110 kg of crude glycerol) is generated from 1 ton of biodiesel production, [3] leading to a significant devaluation of this product on the market. As a consequence, an important amount of glycerol is finally incinerated for heat energy production. Nevertheless, considering that biomass is the only alternative to fossil fuels for the production of chemicals, it would be more interesting to convert glycerol into value-added products. Therefore, a better valorization of glycerol will have great economical and environmental benefits.

Glycerol, with three hydroxyl groups, can be transformed into a wide variety of value-added products, including dihydroxyacetone, glyceraldehyde, glyceric acid, tartronic acid, glycolic acid, formic acid and oxalic acid. [4,5] All these products, except for oxalic acid and formic acid, with high production volumes, are economically more interesting than glycerol. For example, glyceraldehyde could be applied in the domains of cosmetic and pharmaceutical industries as well as organic chemistry. [6] Dihydroxyacetone could be used in cosmetics as an ingredient in tanning lotions. [7] Glyceric acid has found applications in the field of medicine to cure skin disorders. [8] Glycolic acid could be utilized in daily necessities such as degreasing agents, tanning agents, and skincare products. [9] Tartronic acid and oxalic acid are used as an agent of chelating in fine chemistry. [10] Nevertheless, among them, glyceraldehyde is one of the most value-added products. [11,12] Thus, selective catalytic oxidation of glycerol to glyceraldehyde possesses great commercial value.

To achieve the production of high value chemicals, different technologies have been applied in glycerol oxidation, such as thermo-, [13–15] photo-, [16–18] electro-, [19–21] and photoelectrocatalytic technologies. [22] Among them, photocatalysis is considered a green and

energy-saving technology that attracts scientists' attention all over the world, since it utilizes light (potentially sunlight) to generate charge carriers (holes and electrons) and active species, which can activate the target molecules. [23–25] In this sense, most photo-oxidation reactions usually take place at room temperature and atmospheric pressure, by using a semiconductor with the proper band gap to ensure a good potential application prospect. [26] Since V. Maurino et al. [27] firstly reported the photocatalytic oxidation of glycerol as a possible route to produced added-value chemicals in 2008, many studies have been carried out to investigate this reaction over different catalytic materials. Most of them were performed on the most popular photocatalytic material, i.e., TiO_2. As an example, some of those works focused on the performance of glycerol oxidation over TiO_2 or TiO_2-doped with noble metals such as Au or Pt. [28,29] V. Augugliaro and co-workers [30] used commercial and home-made TiO_2 samples in the anatase, rutile or anatase-rutile phases to investigate the glycerol oxidation products in an aqueous solution and showed that1,3-dihydroxyacetone (DHA), glyceraldehyde, formic acid and carbon dioxide are the main products. In their study, the highest selectivity of the value-added glyceraldehyde was 13% and that of DHA was 8% at a 35% glycerol conversion. C. Minero et al. [31] used two different commercial TiO_2 powders (Degussa P25 and anatase Merck TiO_2) to investigate the photocatalytic oxidation mechanism of glycerol and found that various TiO_2 specimens could lead to different selectivities of products.

WO_3 is an excellent metal oxide semiconductor photocatalyst, [32,33] with better visible light response than TiO_2. [34] However, to the best of the authors´ knowledge, although it has been widely used in many fields such as H_2 evolution by glycerol electro-reforming, [35,36] the degradation of pollutants, [37,38] gas sensor [39] and electrochemical energy storage, [40] the photocatalytic oxidation of glycerol towards high-value chemicals has never been investigated on WO_3. Therefore, this work aims to study and thoroughly characterize a series of WO_3-based materials for the photocatalytic oxidation of glycerol towards added-value chemicals. An outstanding performance was found towards the production of glyceraldehyde, one of the most valuable derivatives of glycerol. The activity and selectivity provided by such materials were compared with those of commercial TiO_2-based photocatalysts.

2. Experimental

2.1 Photocatalytic materials and photocatalytic activity measurements

Several WO_3- and TiO_2-based materials were used in this study. First of all, a pure WO_3 photocatalyst was prepared by a simple hydrothermal method. Firstly, 0.6 g of WCl_6 was dissolved in 120 mL of Ethanol solution under constant stirring at room temperature for 10 min. Then, the obtained solution was transferred to a Teflon-lined stainless-steel autoclave (200 mL)

and kept in an oven for 12 h (180 ºC). Finally, after cooling down to room temperature, WO_3 powder was withdrawn, washed with Ethanol (3 × 90 mL) and deionized water (3 × 90 mL), and dried at 80 ºC in air overnight. This material was tested as prepared. For comparison purposes, the as-prepared WO_3 catalyst was also calcined at 450 ºC.

In addition, a series of TiO_2-based materials were acquired commercially, including Anatase (HPX-200), Rutile (HPX-400C) and DTW5 (5 wt% WO_3/TiO_2), all of them provided by Tronox®, while P25 (a very well-known heterojunction of anatase/rutile) was supplied by Evonik®.

A typical photocatalytic experiment was carried out according to the following protocol: 7.5 mg of the catalyst were introduced in a quartz reactor containing 30 mL of glycerol (in aqueous solution concentration of 1.10 mmol L^{-1}). The photocatalytic reactions were conducted under ultraviolet light with a UV lamp (UV-A PL-L, 18 W) which delivers an irradiation intensity of 5.60 mW cm^{-2}. The reactor is open to the air without bubbling. Prior to the photocatalytic reaction, the suspension was stirred for 30 min in the dark to achieve the adsorption-desorption equilibrium of glycerol on the surface of catalysts. Every 30 min, a sample (0.5 mL) was taken from the mixture solution and immediately filtered by a Millipore 0.45 μm (hydrophilic PVDF) membrane using a plastic syringe. In the case of WO_3, the sampling interval is 2 h and its photooxidation performance is tested by two parallel experiments owing to its low kinetic. The concentrations of glycerol and derivate products were analysed by a Shimadzu SPD-M20A prominence ultrafast high-performance liquid chromatography (HPLC) assembled with a Transgenomic ICSep ICE-COREGEL-87H3 organic acid column. The mobile phase is 5 mmol/L of H_2SO_4 and its flow rate is 0.7 mL/min. The temperature of the oven is 30 ºC. The products of glycerol oxidation could be determined by the ultraviolet detector at the wavelength of 210 nm except from glyceric acid which is identified at 240 nm. Glycerol could be analyzed by the refractive index detector (RID).

The Glycerol conversion (in %) was calculated according to equation (1):

$$\text{Glycerol conversion (\%)} = \left(\frac{C_{0\ \text{glycerol}} - C_{t\ \text{glycerol}}}{C_{0\ \text{glycerol}}}\right) \times 100 \quad (1)$$

where $C_{0\ glycerol}$ and $C_{t\ glycerol}$ stand for the initial and real-time concentrations of glycerol, respectively.

The Yield (in %) of every product was calculated according to equation (2):

$$\text{Yield (\%)} = \left(\frac{C_{t\ \text{product}}}{C_{0\ \text{glycerol}}}\right) \times 100 \times n \quad (2)$$

where $C_{t\ product}$ stands for the real-time concentration of the product and n is the ratio of the carbon number present in the product divided by the number of carbon present in the glycerol. The Selectivity (in %) of every product was calculated according to equation (3):

$$\text{Selectivity}\ (\%) = \left(\frac{C_{t\ \text{product}}}{C_{0\ \text{glycerol}} - C_{t\ \text{glycerol}}}\right) \times 100 \times n \qquad (3)$$

where all the parameters were already defined in equations (1) and (2).

2.2 Characterization

X-ray diffraction (XRD) was conducted with a Bruker D8 diffractometer using Cu Kα (λ= 0.15406 nm) radiation equipped with a 1-D fast multistrip detector (LynxEye, 192 channels on 2.95°) and a Ni filter. Other test conditions included a current of 100 mA, an operating voltage of 40 kV, a scanning range between 2θ = 4-80°and a scan rate of 0.02°/ s. Phase, crystallinity and average crystallite size identification were carried out using the Diffrac.Eva software (Bruker) and the ICDD-PDF4+ database.

Scanning electron microscopy (SEM) was conducted by FEI-XL30. Each sample was sprinkled on a conductive tape and sprayed with gold under a 15 kV work voltage. The high-resolution transmission electron microscopy (HRTEM) was performed on a JEOL-2010 microscope equipped with an EDX detector.

The Brunauer−Emmett−Teller (BET) surface area of the catalysts was measured via nitrogen adsorption at −196 °C (Micromeritics ASAP 2020). The catalysts were degassed at 160 °C for 3 h under vacuum. The porous volume and the pore size distribution were calculated via the Barrett-Joyner-Halenda (BJH) method.

UV-vis diffuse reflectance spectroscopy (UV-vis DRS) measurements were conducted using an AvaSpec-2048 Fiber Optic Spectrometer. Spectra were recorded from 200 to 600 nm using a 2048 pixel CCD detector array. Barium sulfate ($BaSO_4$) was used as a blank reference.

The electrochemical photocurrent experiments were carried out in a photoelectrochemical cell (supplied by redox.me ®) with a standard three-electrode system consisting of a Pt wire as the counter electrode, a saturated Ag/AgCl as the reference electrode and a working electrode prepared by the following process: 5 mg of the catalyst (as-prepared WO_3 or commercial samples) were dispersed in 0.5 mL ethanol. Then, 20 μL of that dispersion were impregnated over an indium-tin oxide (ITO) substrate, with an active area of ca. 1 cm^2, and dried at room temperature. Different electrical potentials were applied with a potentiostat-galvanostat (VoltaLab PGZ402).

The concentrations of total organic carbon (TOC) of the solutions before and after the photocatalytic tests on different materials were measured using a Shimadzu TOC-VCPN analyzer equipped with an auto-sampler.

Acid properties of the different samples were determined by using pyridine as a probe molecule. Pyridine adsorption was followed by Diffuse reflectance infrared Fourier transform spectroscopy (DRIFTS), which were carried out on a Fourier-transform infrared spectroscopy (FTIR) instrument (Perkin Elmer Frontier) equipped with an environmental chamber (Harrick HVC-DRM). A resolution of 4 cm^{-1} was used with 125 scans averaged to obtain a spectrum from 4000 to 400 cm^{-1}. Prior to each experiment, pyridine adsorption was carried out at 100 °C for 45 min allowing the saturation of the catalyst surface. The physically adsorbed pyridine was then removed from the surface with an air flow (50 $mL \cdot min^{-1}$). Finally, the IR spectra were recorded at 100 °C. Bands at 1448 and 1537 cm^{-1} (corresponding to Lewis and Brönsted acid sites, respectively) were integrated and acidity was determined using the corresponding molar extinction coefficients.

3. Results and discussion

3.1 Catalysts characterization

First of all, the physicochemical properties of the materials proposed in this study were characterized by XRD and microscopy techniques (SEM and HRTEM). Fig. 2. 1a shows the XRD patterns for Anatase, Rutile and P25, while Fig. 2. 1b shows the patterns for the as-prepared WO_3 catalyst, together with the commercial DTW5 (5 % WO_3 on TiO_2). As expected, pure Anatase and Rutile samples only exhibit corresponding pure crystalline phases (PDF #89-4921 and #77-0440, respectively). In addition, P25, well known as a very efficient heterojunction of anatase and rutile for a wide variety of photocatalytic processes, exhibits diffraction peaks corresponding to both crystalline phases.

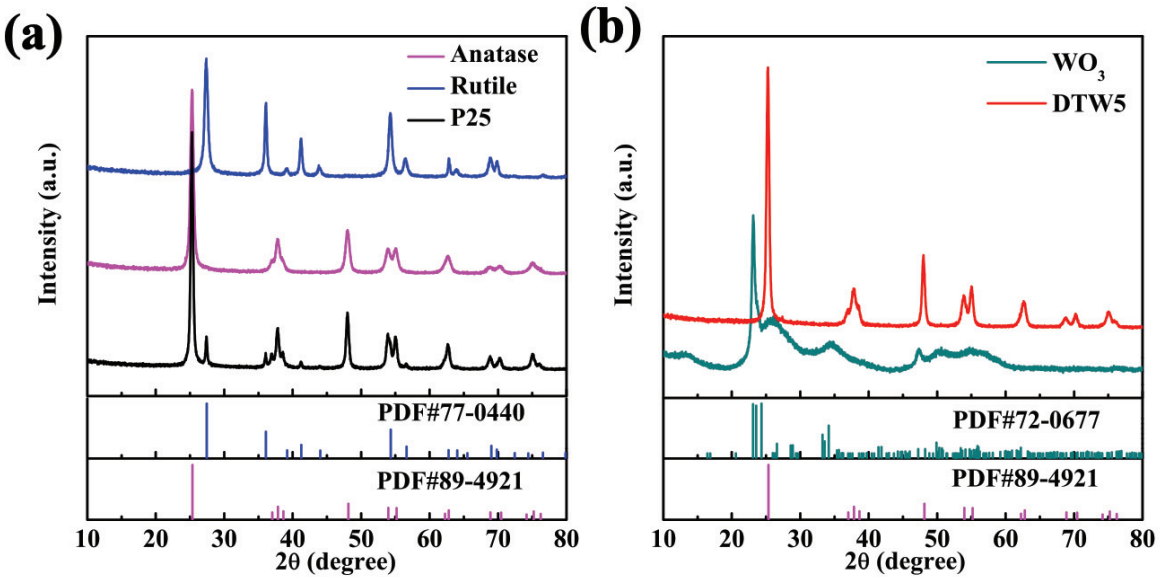

Fig. 2. 1. X-ray diffraction (XRD) patterns of commercial catalysts (Anatase, Rutile, P25 and DTW5) and as-prepared WO_3.

Fig. 2. 1 b indicates that the as-prepared WO_3 catalyst exhibits a rather amorphous behavior, although a well-defined peak at $2\theta = 23.1^{o}$ could be identified, which belongs to the (001) phase of a monoclinic structure of WO_3 (PDF #72-0677). [41] Its low crystallinity (48.6 %, Table 2. 1) compared to the commercial catalytic materials (80 – 85 %, Table 2. 1) could be attributed to the hydrothermal synthesis method, which was performed at low temperature (180 ^{o}C) without any additional calcination step. For comparison purposes, a similar WO_3 material was calcined at 450 ^{o}C in air (1 h, 5 ^{o}C min^{-1} heating rate), and the XRD patterns are shown in Fig. S2. 1. After the calcination step, the material evolved to a highly crystalline monoclinic catalyst. Finally, regarding the DTW5 sample, the titanium oxide phase belongs to anatase, and no peaks related to any WO_3 crystalline phase could be identified by XRD. In principle, this could be attributed to a very high dispersion of small WO_3 nanoparticles on the TiO_2 (anatase) support, and/or to a very low crystallinity of WO_3 compared to TiO_2. All materials and phases present similar crystallite sizes in the range of 16-33 nm (Table 2. 1).

Table 2. 1. BET specific surface area, pore volume, pore size, crystallinity and average crystallite size of the photocatalysts

Sample	S_{BET} ($m^2\ g^{-1}$)	Porous volume ($cm^3\ g^{-1}$)	Mean Pore Size (nm)	Crystallinity[a] (%)	Crystal size[a] (nm)
Anatase	92	0.43	15.2	82.0	17
Rutile	85	0.39	16.9	80.8	16
P25	63	0.17	10.5	81.6	23 (Anatase) 33 (Rutile)
DTW5	78	0.31	13.8	84.9	20 (Anatase)
WO_3	33	0.07	13.3	48.6	17

[a]Calculated from XRD spectra

To get more insights into the structural parameters of these catalysts, they were further characterized by HRTEM. Fig. 2. 2 reveals sharp and clear lattice fringes for all the materials, regardless of the crystallinity level. The lattice spacing of Anatase and Rutile is 0.367 nm and 0.249 nm, respectively, in good agreement with theoretical values of (101) plane of the anatase phase [42] and (101) plane of the rutile phase. [43] It is worth noting that for the commercial DTW5 sample, although there are no significant peaks of WO_3 in the XRD pattern, the lattice spacing of 0.388 nm was found, corresponding to the (001) plane of WO_3. [44] This clearly revealed the existence of well-dispersed WO_3 with the size of ~14 nm on the TiO_2 (anatase) matrix. Finally, the as-prepared WO_3 synthesized using WCl_6 as the precursor possesses a similar lattice spacing of 0.381 nm, which matches well with the (001) plane of the monoclinic WO_3 previously reported with a similar precursor. [44] In addition, the overall morphology of the catalyst grains was observed by SEM. As shown in Fig. S2. 2, it was found that anatase, P25, DTW5 and WO_3 presented spherical shapes while rutile shows rods-like shape agglomerates.

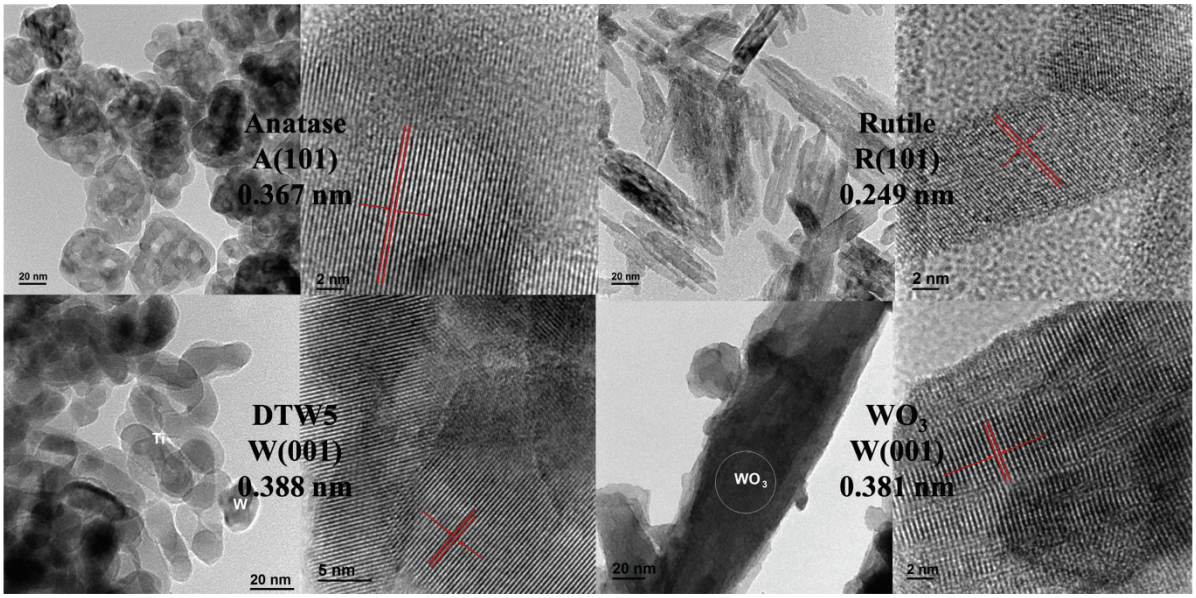

Fig. 2. 2. High-resolution transmission electron microscopy (HRTEM) images of Anatase, Rutile, DTW5 and as-prepared WO_3 catalysts.

N_2 adsorption-desorption was carried out to determine the specific surface area (S_{BET}, Table 2. 1) together with the pore size and the porous volume of each material. These parameters could eventually affect their performance for glycerol conversion, owing to the fact that the catalyst active sites along with the adsorption of glycerol as well as its oxidation products usually positively relate to the specific surface area. As shown in Fig. S2. 3, type IV isotherms were obtained with a small hysteresis loop at a relative pressure of 0.7–1.00. Therefore, all materials exhibit, as expected, a mesoporous structure with pore sizes between 10-15 nm (Table 2. 1). In addition, while Anatase, Rutile and DTW5 showed the highest S_{BET} (78 – 92 m^2 g^{-1}), this value was slightly lower for P25 (63 m^2 g^{-1}) and drastically decreased for the as-prepared WO_3 (33 m^2 g^{-1}).

All in all, it seems that in general, the commercial materials exhibit a more crystallized structure with higher specific surface areas compared to the as-prepared WO_3 catalyst. Therefore, in principle, a lower overall catalytic performance could be expected for the latter to a certain extent. Nevertheless, other important features, such as their electronic properties (band gap, charges separation), and concentration of acid sites are known to play a key role in the performance of such photocatalytic materials.

The electronic properties of these materials were first investigated by diffuse reflectance spectroscopy (DRS) in the UV-Vis range. The obtained spectra of samples are shown in Fig.

2. 3a. Comparing Anatase and Rutile samples, a slightly higher adsorption towards the visible range could be observed for the latter, as previously reported. [45] In addition, as expected, it was found that all the samples could absorb UV light while the as-prepared WO_3 could respond to not only UV light but also partially to visible light.

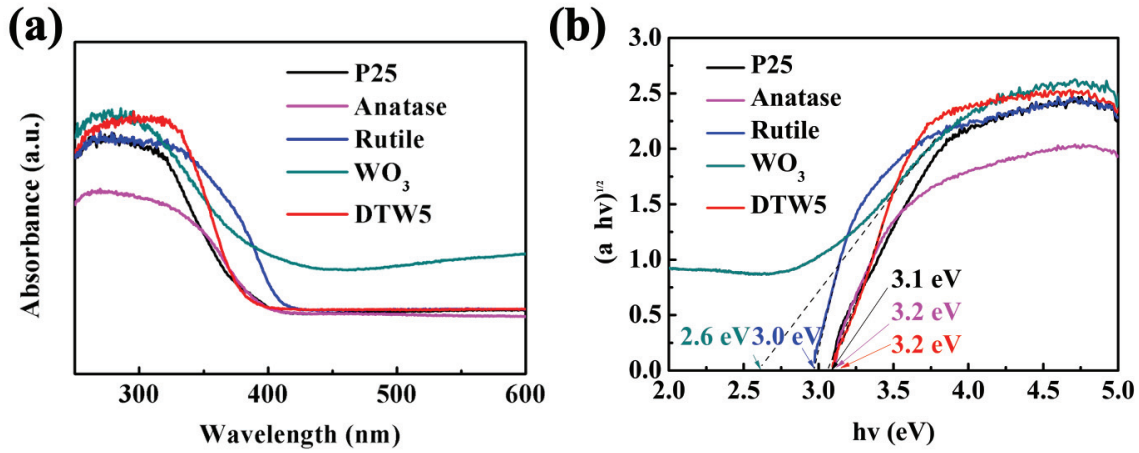

Fig. 2. 3. (a) UV-Vis diffuse reflectance spectroscopy (DRS) spectra and (b) Tauc plot for band gap determination for commercial catalysts (Anatase, Rutile, P25 and DTW5) and as-prepared WO_3.

Fig. 2. 3b shows the Tauc plots for band gap calculations using the Kubelka–Munk equation. Briefly, an extrapolation of the linear part of the curve $(\alpha \cdot hv)^{1/2}$ (where α is the absorption coefficient) as a function of *hv* defines the band gap energy of the samples considered as indirect band gap semiconductors. [46] As previously mentioned, all the commercial TiO_2-based materials exhibit a band gap compatible with the use of UVA light (> 3.0 eV). Anatase and DTW5 showed an almost identical band gap value, which seems to indicate that the addition of 5 % WO_3 on TiO_2 (anatase) does not significantly affect its electronic properties. In addition, P25, with an anatase/rutile heterojunction, exhibited a slightly smaller band gap, closer to that of rutile. Finally, for the as-prepared WO_3 catalyst, its band gap was 2.61 eV, in good agreement with previous studies, which indicates that its response range to photoirradiation could be expanded to visible light. [22] According to these results, we chose UV light to compare the performance of glycerol photocatalytic oxidation as all catalysts respond to UV light.

In a new effort to characterize the electronic properties of the materials, photocurrent experiments were performed. These tests were carried out in the photoelectrochemical cell described in the experimental section, in neutral media (0.5 M Na_2SO_4 liquid electrolyte, in order to avoid any potential degradation of the materials in acid or alkaline media), upon the

application of a constant potential of 0.9 V vs Ag/AgCl reference electrode. All materials were subjected to UV irradiation in step changes of 30 seconds. The higher the photocurrent intensity usually indicates the better separation situation of photo-generated electrons and holes, which generally contributes to the progress of photocatalytic oxidation. [47,48] As shown in Fig. 2. 4, the photocurrent intensity obtained upon irradiation follows this rank: P25 > Anatase≈Rutile≈DTW5 > WO_3. These results indicate that a better separation rate of photo-generated charges (electrons and holes) upon irradiation could be expected on TiO_2-based materials.

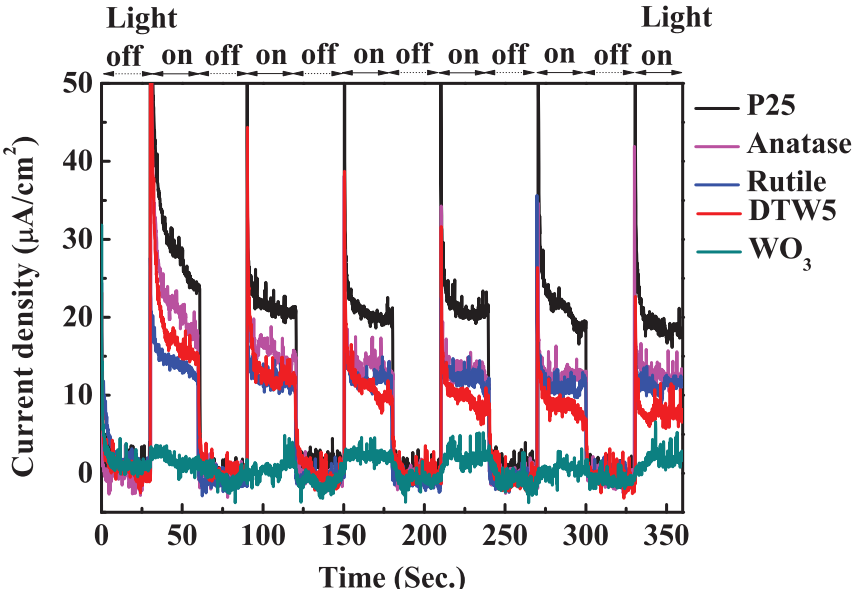

Fig. 2. 4. Transient photocurrent response for commercial catalysts (Anatase, Rutile, P25 and DTW5) and as-prepared WO_3. Conditions: neutral reaction media (0.5 M Na_2SO_4), applied potential: 0.9 V vs Ag/AgCl. The experiments were performed in a photoelectrochemical cell, where the catalyst was supported on an ITO glass (working electrode), and a Pt counter electrode was used for polarization purposes.

Therefore, the addition of WO_3 seemed to have a detrimental effect on such a phenomenon. If the separation of these photo-generated charges is related to the overall activity of oxidation on these materials, we could expect a higher glycerol photo-oxidation rate on TiO_2 than on WO_3-based catalysts.

Finally, the nature and relative amount of acid sites of P25, DTW5 and WO_3 were characterized by adsorption of pyridine followed by diffuse reflection infrared spectroscopy (DRIFT).

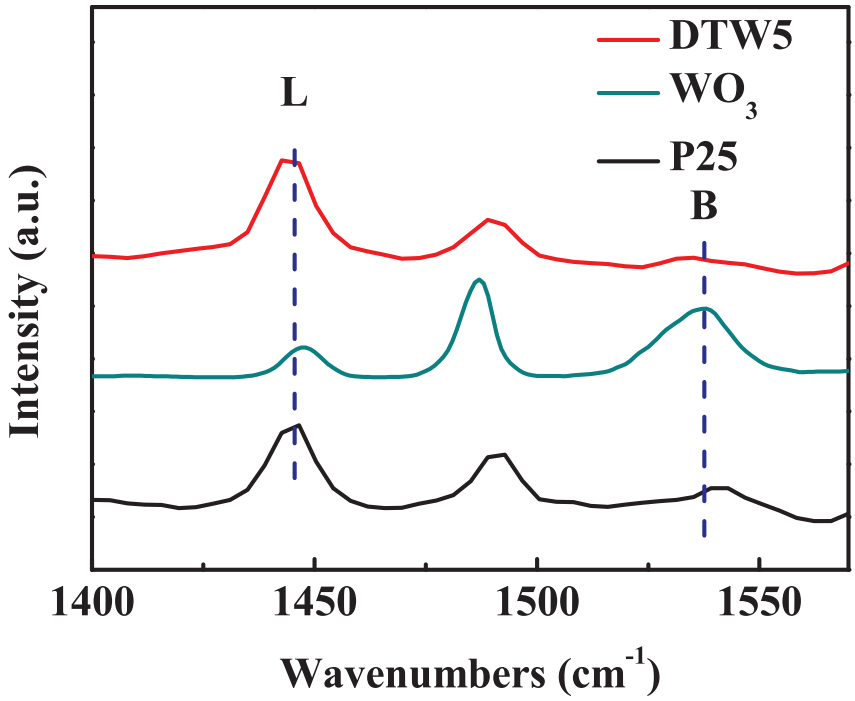

Fig. 2. 5. Pyridine-DRIFTS spectra of P25, DTW5 and WO_3. B and L denote Brönsted and Lewis acid sites, respectively.

Fig. 2. 5 depicts the spectra of pyridine chemisorbed at 100 ºC. The bands obtained at 1448 and 1542 cm^{-1} could be attributed to Lewis acid sites and to protonated pyridine molecules bound to surface Brönsted acid sites, respectively. [49,50] In addition, Table 2. 2 presents the calculated quantitative values of both acid sites, the overall amount and the ratio between them. If we compare the results for P25 (TiO_2) and WO_3, it can be clearly observed that WO_3 possesses the highest percentage of Brönsted and total acid sites. This is expected considering that tungsten-based catalysts are well-known for their acidic properties. For instance, Ganji et al. [51] reported an overall higher acidity of WO_3 and WO_3/TiO_2 materials compared to TiO_2, obtained by both pyridine-FTIR and NH_3-TPD (temperature programmed desorption). That could explain that the DTW5, compared with P25, also exhibited a higher amount of Brönsted and total acid sites. These acidic properties are expected to play a very important role in the photocatalytic activity of these materials towards glycerol activation. For instance, $Pt/WO_3/Al_2O_3$ catalysts have been reported as one of the most successful catalytic systems for the effective conversion of glycerol to 1,3-propanediol by thermal-hydrogenolysis, [52] where Brønsted acid sites are considered to play a key role in the adsorption/activation of the secondary C-O bond in glycerol. [53] Also, in a previous study by Checa et al. dealing with

the same reaction, [44] it was found that the addition of tungsten to a Pt/ZrO_2 catalyst enhanced its selective performance of the target product 1,3-propanediol, most likely due to the creation of a higher concentration of Brönsted acid sites.

Table 2. 2. Comparison of Lewis, Brönsted and total acid sites of P25, DTW5 and WO_3, obtained by pyridine-DRIFTS

	µmol Py · g^{-1} · m^{-2} Cat.			
Catalyst	**Lewis**	**Brönsted**	**Total**	**L/B**
P25	0.87	0.21	1.08	4.2
DTW5	0.95	0.50	1.45	1.9
WO_3	0.64	3.33	3.97	0.2

To summarize this section, the characterization results exhibit overall enhanced physicochemical properties of TiO_2-based materials compared to WO_3 catalysts in terms of specific surface area, crystallinity, and photo-generated charge separation. However, the WO_3-based materials are much more acidic, containing a higher amount of Brönsted acid sites.

3. 2 Photocatalytic activity

All the catalysts previously characterized were tested for photocatalytic oxidation of glycerol. Fig. 2. 6 shows the evolution of the glycerol conversion with time upon irradiation. Regarding all the TiO_2-based materials, significant oxidation of glycerol was achieved after 5 hours (Fig. 2. 6a). However, for the as-prepared WO_3 catalyst, the glycerol consumption rate is lower, and therefore the reaction time was extended up to 22 h (Fig. 2. 6b). In order to prove that the activity was due to photocatalysis, blank experiments over P25, DTW5 and WO_3 (in the dark, Fig. S2. 4a-c) and direct photolysis of glycerol (without any catalyst in the light, Fig. S2. 4d) were performed, where the glycerol conversion was negligible.

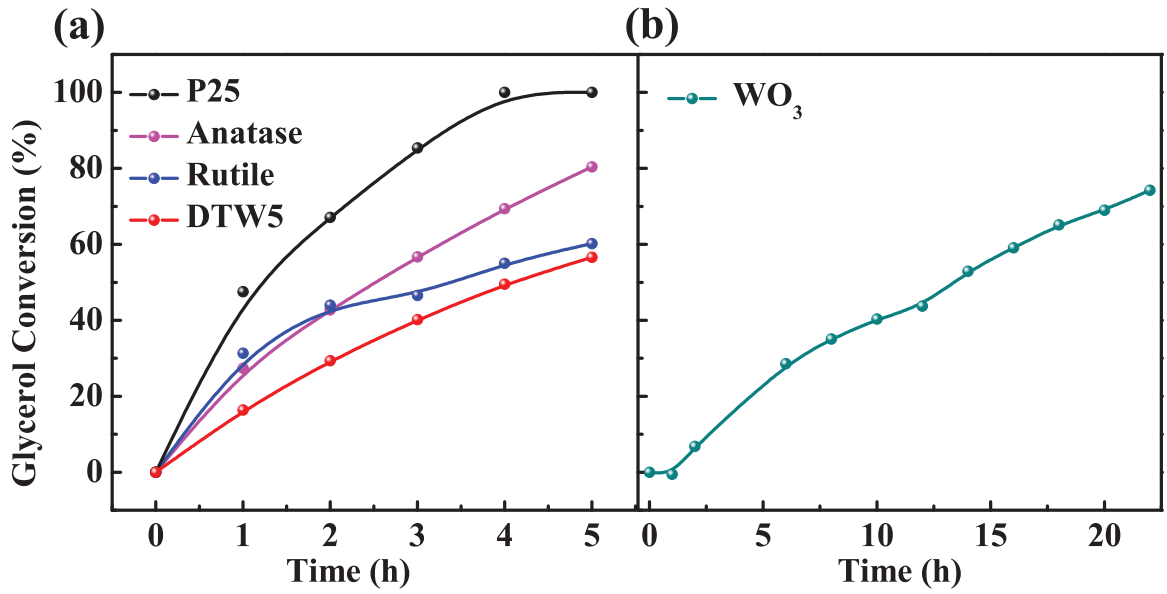

Fig. 2. 6. Glycerol conversion over commercial catalysts (Anatase, Rutile, P25 and DTW5) and as-prepared WO_3. Reaction conditions: Room temperature, Glycerol initial concentration: 1.10 mmol L^{-1}, Volume of glycerol solution: 30 mL, UV irradiation intensity of 5.60 mW cm^2.

As observed in Fig. 2. 6a, P25 seemed to be the most active material, achieving a complete glycerol conversion after 4 h. Therefore, the photocatalytic activity obtained upon irradiation for glycerol oxidation obeys the order P25＞Anatase＞Rutile>DTW5＞WO_3. With regards to P25, its outstanding activity has been already proven for a wide variety of photocatalytic processes, including glycerol photooxidation. [24,27,28] P25 consists of a mixed phase of anatase and rutile in a ratio of about 4:1. In the so-called anatase/rutile heterojunctions, upon UV irradiation, the photogenerated electrons from the anatase phase are transferred to the rutile phase on account of its lower conduction band energy. [54] This results in more efficient separation of the photogenerated charge carriers, as observed in the photocurrent experiments (Fig. 2. 4). Another evidence of the creation of this heterojunction was observed in the DRS experiments, where the band gap for P25 was in-between that of anatase and rutile (Fig. 2. 3b). One may expect a similar behavior for the DTW5 material. As a matter of fact, WO_3/TiO_2 composites have been previously developed and reported to enhance the separation of photogenerated charge carriers on the heterojunctions between both phases together with a modification of the band gap of TiO_2 towards a more visible-light range. [55] However, in this case, we could not observe a significant heterojunction, since the band gap for DTW5 was found to be almost identical to that of anatase (Fig. 2. 3b). Furthermore, the photocurrent

obtained for DTW5 was even slightly lower than that for Anatase (Fig. 2. 4). Therefore, we conclude that the low loading of WO_3 (5 %) on anatase can neither enhance the separation of charge carriers nor the conversion of glycerol. It is worth noting therefore that the photocurrent activity observed in Fig. 2. 4 obeys the same order as the overall glycerol conversion activity after 5 h of irradiation observed in Fig. 2. 6. This suggests that the photocatalytic degradation of glycerol is strongly related to the separation of the electrons and holes produced upon irradiation.

This study aims to enhance the production of added-value products by photocatalytic oxidation of glycerol. Fig. 2. 7 shows the distribution of products with time for all the materials. The main oxidation products observed were glyceraldehyde, DHA, glycolic acid, tartronic acid, oxalic acid, formic acid and acetic acid. Nevertheless, the amount and distribution of each of these products are highly influenced by the nature of the photocatalytic material. Starting with the most active material, P25, we can clearly observe that some of the main oxidation products, including glyceraldehyde, DHA and formic acid are produced during a short period of around 1 h. A similar effect was observed in the Anatase catalyst, although the products distribution and amount were different, as expected in view of the observed lower overall conversion (Fig. 2. 6). On the other hand, the Rutile catalyst seemed to produce a significant amount of formic acid.

Our results for both, P25 and Anatase photocatalysts are in good agreement with the model proposed by Jedsukontorn et al. [51,52] for glycerol conversion on TiO_2 (anatase). According to those studies, upon UV irradiation, glycerol acts as a hole scavenger of the photogenerated holes, [56] or reacts with the reactive oxidizing species, [57] oxidizing it to both glyceraldehyde and DHA. Minero et al. [31] also proposed that the formation of these species could be mediated by $^{\bullet}OH$ radicals. Glyceraldehyde is produced when the primary –OH group is adsorbed and oxidized, while DHA is produced upon the oxidation of the secondary –OH group of glycerol. The glyceraldehyde could be then oxidized to produce glyceric acid, while the DHA could be rearranged into glyceraldehyde. [56] It could be expected afterward that the products keep evolving into smaller organic molecules, such as tartronic acid, oxalic acid, and as observed in this study, formic acid. These reaction routes are in good agreement with the results obtained for Anatase and P25, since the observed reaction products evolved with time and then disappeared.

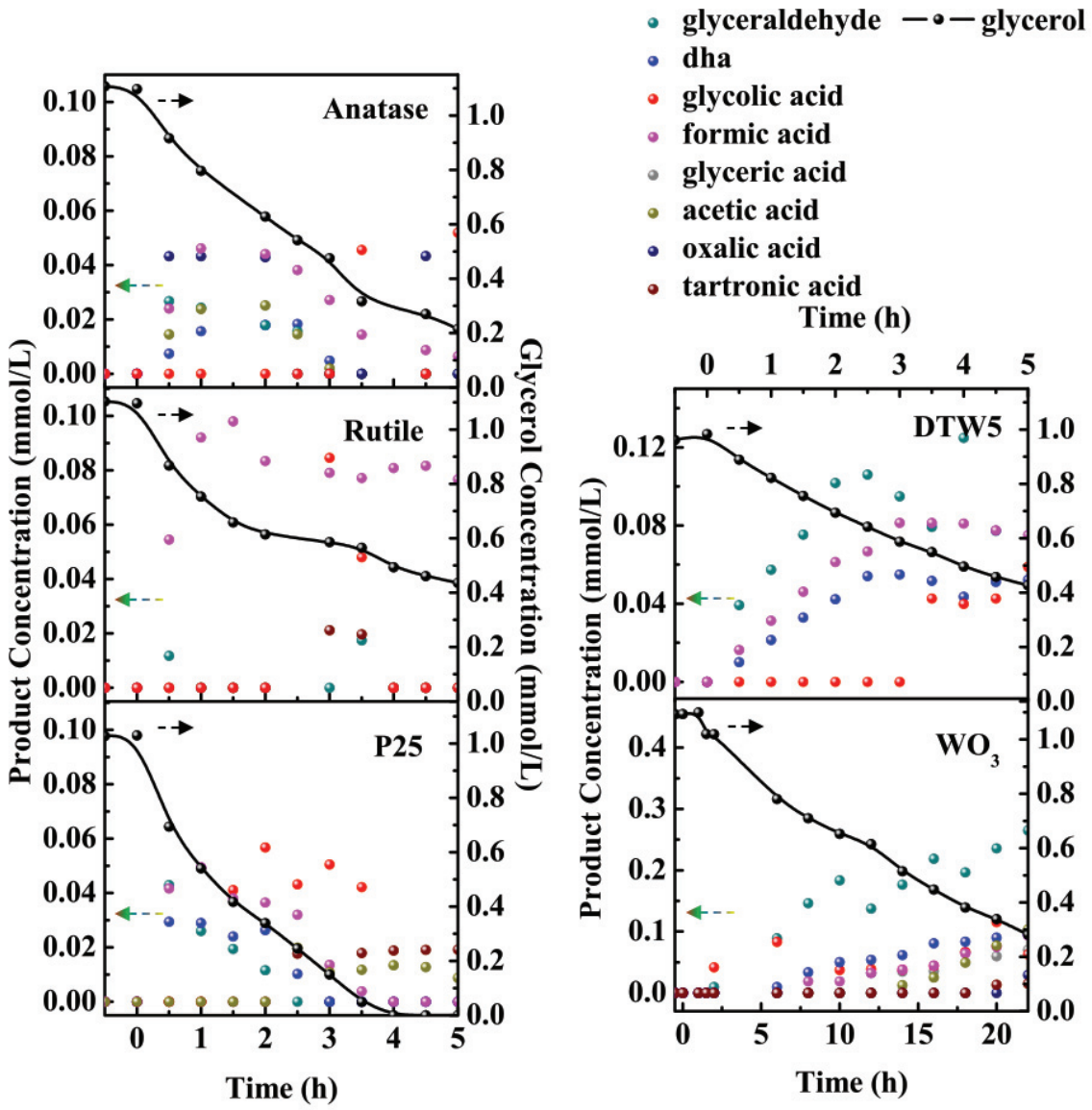

Fig. 2. 7. Evolution of products with time over commercial catalysts (Anatase, Rutile, P25 and DTW5) and as-prepared WO_3. Reaction conditions: Room temperature, Glycerol initial concentration: 1.10 mmol L^{-1}, Volume of glycerol solution: 30 mL, UV irradiation intensity of 5.60 mW cm^{-2}.

However, for Rutile, the main product seemed to be formic acid, and we could not observe a similar evolution for the other TiO_2 catalysts. In this sense, Augugliaro et al. [30] proposed a mechanism where all the species are produced in parallel on P25, anatase and rutile catalysts, including glyceraldehyde, DHA, formic acid and CO_2. Minero et al. [31] also suggested a model where C2 + C1 products could also be produced in parallel by direct electron transfer (in this case over P25). We believe that these mechanisms are in good agreement with the

results obtained for Rutile, where the formation of formic acid seemed to be the product of a parallel process.

The most interesting results were obtained with the WO_3-based materials. Starting with the as-prepared WO_3, a completely different behavior was observed. In this case, as opposed to Anatase and P25, the concentration of reaction products gradually increased with time. The main product was glyceraldehyde, followed by DHA and then by smaller quantities of further oxidized products. These results suggest a similar first oxidation step as previously explained for TiO_2, where glycerol undergoes the first oxidation towards glyceraldehyde and DHA. Considering that the former is the result of the oxidation of primary (terminal) –OH groups of glycerol and that we have two primary -OH groups its likelihood to be produced is much higher compared to that for the production of DHA, which is the result of the oxidation of the secondary -OH group in glycerol. Moreover, on the one hand, in presence of WO_3, the ratio glyceraldehyde/DHA is higher than 2. It suggests that in the presence of WO_3, a fraction of the DHA formed is probably converted into glyceraldehyde and on the other hand, these high added-value products seemed to desorb in the liquid phase, rather than to undergo further oxidation towards smaller molecules. These photocatalytic properties are of paramount importance for the development of novel catalysts with high selectivity towards glyceraldehyde. However, as discussed in Fig. 2. 6, the photocatalytic reaction on this material is rather slow compared to that of Anatase, Rutile and P25, and longer reaction times were required with this system for practical purposes.

Before discussing the photocatalytic behavior of the DTW5 material, two parameters will be introduced to compare the performance of pure TiO_2-based materials (Anatase, Rutile and P25) and the as-prepared WO_3. Fig. 2. 8 shows the variation of the selectivity of products while Fig. 2. 9 shows the variation of the yield of products, both of them as a function of the glycerol conversion.

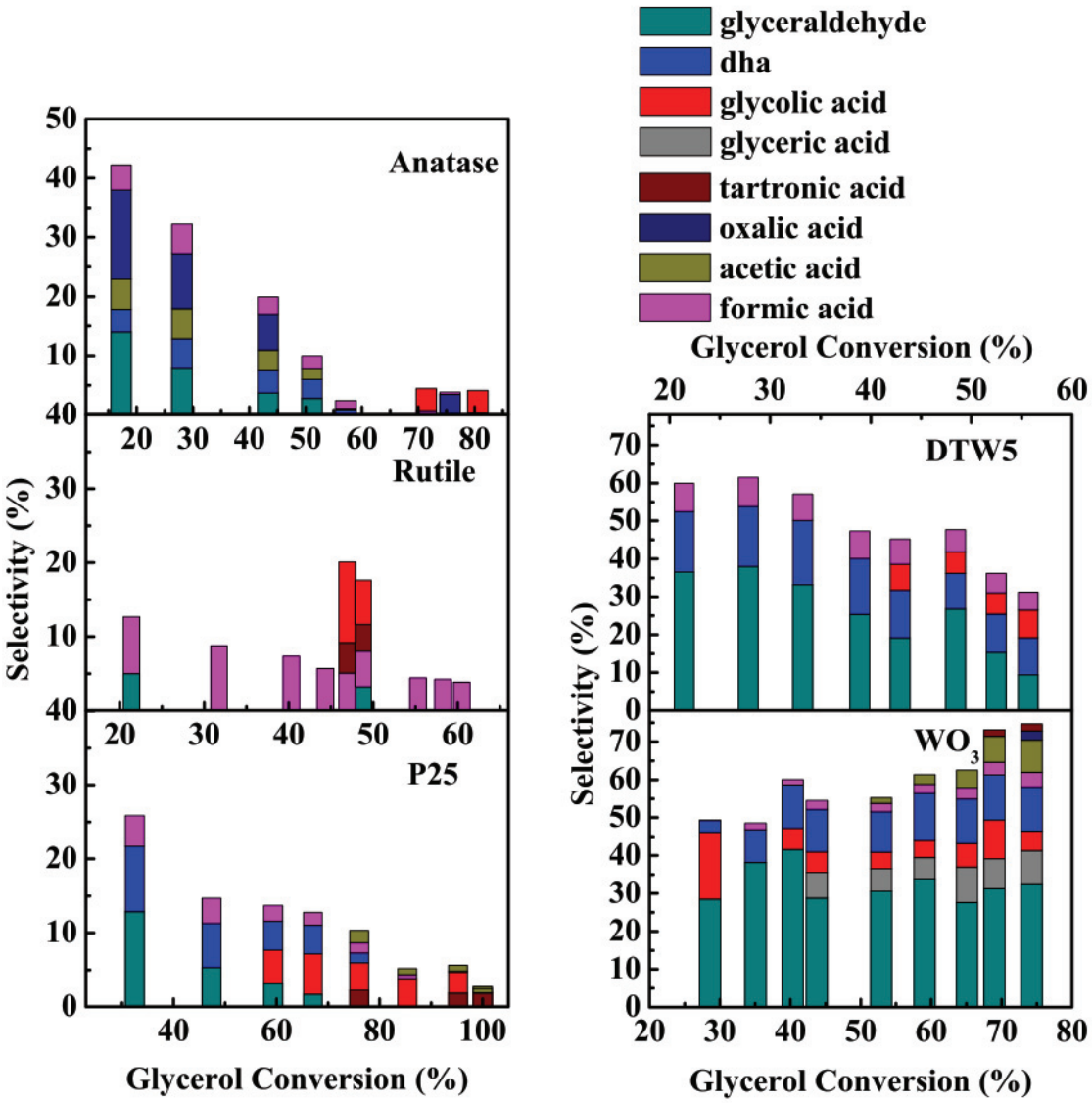

Fig. 2. 8. Variation of the selectivity of products with respect to the glycerol conversion over commercial catalysts (Anatase, Rutile, P25 and DTW5) and as-prepared WO_3. Reaction conditions: Room temperature, Glycerol initial concentration: 1.10 mmol L^{-1}, Volume of glycerol solution: 30 mL, UV irradiation intensity of 5.60 mW cm^{-2}.

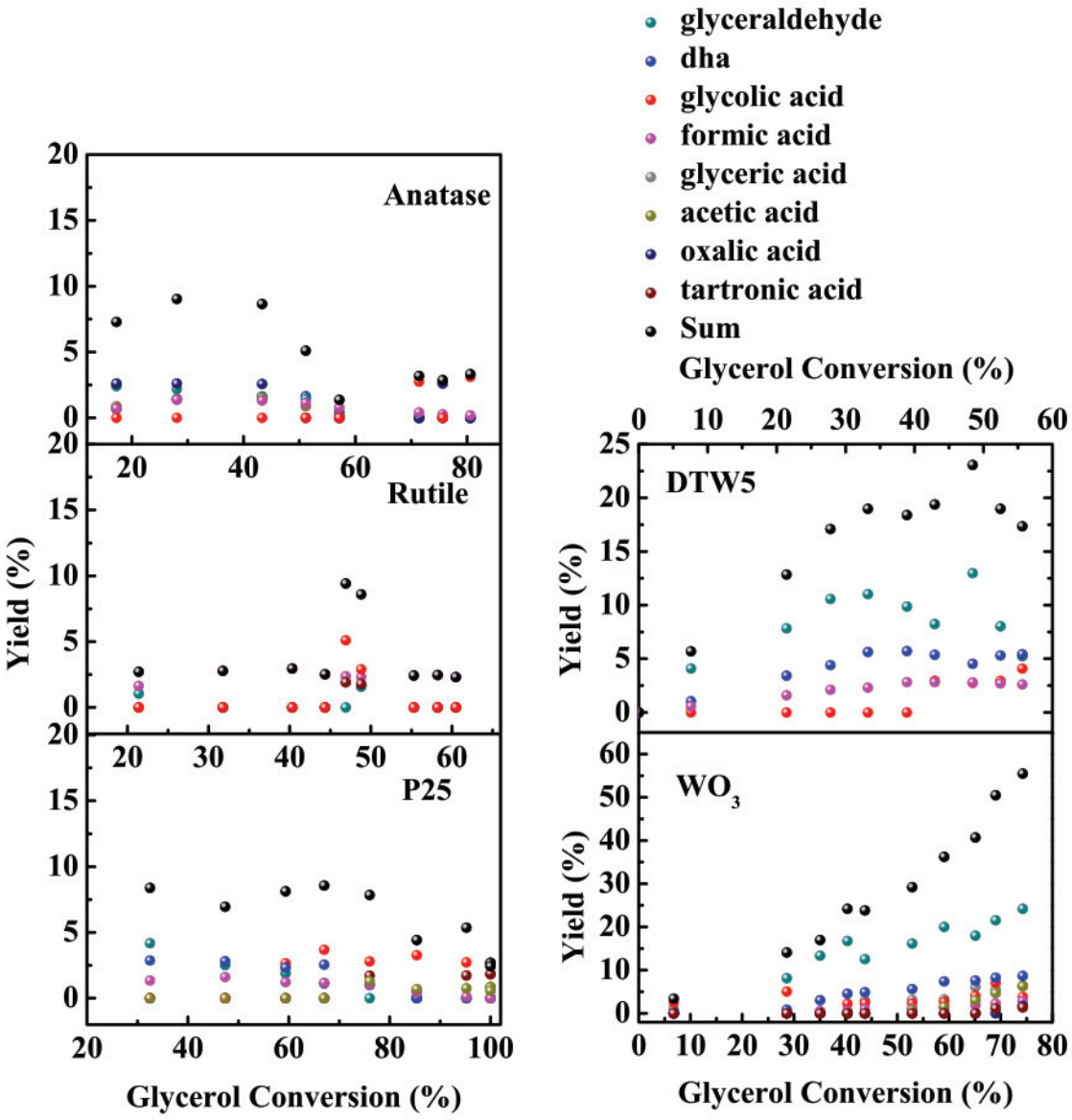

Fig. 2. 9. Variation of the yield of products with respect to the glycerol conversion over commercial catalysts (Anatase, Rutile, P25 and DTW5) and as-prepared WO_3. Reaction conditions: Room temperature, Glycerol initial concentration: 1.10 mmol L^{-1}, Volume of glycerol solution: 30 mL, UV irradiation intensity of 5.60 mW cm^{-2}.

These figures allow us to compare the production of the added-value products of interest (in this case glyceraldehyde) at glycerol isoconversion conditions. As expected for P25 and Anatase according to the results discussed in Fig. 2. 7, high selectivities and yields to oxidation products are only achieved at low conversion levels. Unfortunately, there was only one products analysis below 40% of conversion due to the fast kinetics on P25. As the system

evolved in time, the conversion increased but the production of valuable products decreased. In addition, since the sum of all the liquid products selectivity is far from 100 % at all the conversion levels, it could be assumed that CO_2 could be also produced. This hypothesis is confirmed considering the TOC measured after about 45% of conversion (Fig. 2. 10).

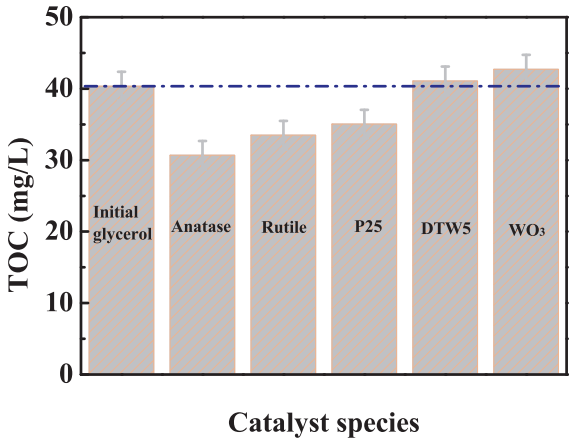

Fig. 2. 10. Total organic carbon (TOC) measurement of the liquid solutions for commercial catalysts (Anatase, Rutile, P25 and DTW5) and as-prepared WO_3, after the achieved glycerol conversion was ~45 %. Reaction conditions: Room temperature, Glycerol initial concentration: 1.10 mmol L^{-1} (TOC: 40.4 ± 2 mg/L), Volume of glycerol solution: 30 mL, UV irradiation intensity of 5.60 mW cm^{-2}.

This was also the case for the Rutile catalyst which predominantly produces formic acid. Therefore, none of the pure TiO_2-based catalysts exhibited a significant performance towards the production of glyceraldehyde.

Nevertheless, in these figures, we could clearly observe that the as-prepared WO_3 catalyst exhibited an outstanding activity towards the production of the desired product, glyceraldehyde, even under high conversion levels. As a matter of fact, with a relatively constant selectivity towards this product, its yield gradually increased with the overall glycerol conversion. In addition, the overall selectivity of liquid organic products over this catalyst is much higher than that of the TiO_2 materials, which indicates that the total glycerol oxidation towards CO_2 is much more unlikely as confirmed by TOC analysis (Fig. 2. 10). Besides, WO_3 post-treated via calcination at 450 ^oC exhibited a slightly superior glycerol conversion owing to its higher crystallinity (Fig. S2. 1), with similar values of glyceraldehyde selectivity and yield (Fig. S2. 5). Therefore, TiO_2-based materials (mainly Anatase and P25) exhibited, as expected, a great

overall catalytic performance for the oxidation of glycerol, but a rather poor selectivity to glyceraldehyde, while the as-prepared (and calcined) WO_3 catalysts exhibited an interesting selectivity/yield towards this product, even under high conversion levels. The main issue of this material is related to the rather slow kinetics, which could lower the added value of this material for practical purposes.

To overcome this issue, the DTW5 catalyst was tested for the photocatalytic oxidation of glycerol. In Figs. 7-9 we can clearly observe that the presence of a small amount of WO_3 (5 %) in the anatase support led to completely different behavior in the desired direction. Hence, as opposed to the Anatase photocatalyst, the reaction products formed on DTW5 did not seem to disappear with time, but rather to increase in a similar way to that obtained with the as-prepared WO_3 material. In addition, the selectivity/yield towards glyceraldehyde was much higher for DTW5 compared to the TiO_2 catalysts. Table 2. 3 shows the values for glyceraldehyde selectivity and yield at similar glycerol conversion values (43-47 %) over all the photocatalysts. While both parameters are rather low for TiO_2 materials in our study (< 5 %) and for other noble metal-free TiO_2-based photocatalysts in publications, [30,31,58,59] glyceraldehyde yields/selectivities of 13 %/29 % and 8 %/19 % were obtained for the as-prepared WO_3 and for DTW5, respectively.

Table 2. 3. Comparison of glyceraldehyde Yield and Selectivity for all the photocatalysts at similar levels of glycerol conversion

Sample	**Glycerol conversion (%)**	**Yield of glyceraldehyde (%)**	**Selectivity of glyceraldehyde (%)**
Anatase	43	2	4
Rutile	44	/	/
P25	47	3	5
DTW5	43	8	19
WO_3	44	13	29
Homogeneous TiO_2 [27]	35	5	13

Sample	Glycerol conversion (%)	Yield of glyceraldehyde (%)	Selectivity of glyceraldehyde (%)
P25 [28]	36	5	13
Lab-made TiO_2 [53]	97	5	5
Black TiO_2 [54]	92	3	3

In addition, total organic carbon analysis (TOC) of the liquid solutions was performed for the different photocatalytic systems when the glycerol conversion achieved a value ~ 45 %. The obtained values were compared with the initial concentration of glycerol (Fig. 2. 10). The results obtained allowed us to confirm the level of mineralization of glycerol over the different catalysts upon irradiation. In addition, as we discussed in the previous figures, the modification of anatase with WO_3 (DTW5) allowed avoiding the mineralization compared to the Anatase catalyst, in good agreement with the higher selectivity exhibited by this material towards liquid added-value products, mainly glyceraldehyde.

Therefore, the photocatalytic activity results obtained in this study clearly demonstrated, for the first time in literature, an outstanding performance of WO_3-based materials for the selective photocatalytic oxidation of glycerol to glyceraldehyde. In particular, the commercial 5 % WO_3/TiO_2 (anatase) catalyst allows combining the main features of anatase (fast kinetics for glycerol conversion) and WO_3 (high selectivity towards glyceraldehyde). These results are in good agreement with the characterization study described in section 3.1. The textural parameters (crystallinity, crystal size and specific surface area, Table 2. 1) for Anatase, Rutile, P25 and DTW5 were relatively similar and cannot explain the differences observed in photocatalytic properties. Nevertheless, the overall activity for glycerol conversion was strongly correlated with the electronic properties of these materials, namely the separation of photogenerated charge carriers (as observed by the photocurrent characterization tests, Fig. 2. 4). This phenomenon was previously observed in many photocatalytic processes, since an enhanced separation of e^- and holes is indeed one of the most common strategies to improve the overall performance of the photocatalytic system. This is usually managed either by doping the semiconductor catalyst with a metal (e^- trap), or by the formation of heterojunctions between different materials or different phases of the same material. [54]

However, the enhanced glyceraldehyde selectivity observed for DTW5 catalyst compared to Anatase (or any other TiO_2-based catalyst) could not be explained by its electronic properties. Considering that both materials exhibit an almost identical band gap (Fig. 2. 3b), and the fact that DTW5 shows lower photocurrent activity (i.e., worse separation of photogenerated carriers, Fig. 2. 4), the formation of a successful heterojunction between TiO_2 and WO_3 could be disregarded. We believe therefore that the outstanding performance of DTW5 towards glyceraldehyde production could be attributed to its enhanced surface acidity.

In this sense, previous studies dealing with the thermal catalytic hydrogenolysis of glycerol already proved that WO_3 plays a role of paramount importance due to the presence of Bronsted sites, which allow for the selective activation of C-O bonds in glycerol. [52] Furthermore, the obtained results could be correlated with a previous study by Lopez-Tenllado et al. [60] dealing with the selective photooxidation of organic molecules (crotyl alcohol to crotonaldehyde). This reaction was performed on titania, ceria and bismuth tungstate catalysts, where the latter was the most selective. This phenomenon was attributed to the lowest adsorption of the aldehyde reaction product on the tungsten-based catalyst. In other words, this material seemed to favor the desorption of the desired product, avoiding its further photooxidation. Therefore, according to the obtained results and the above-mentioned studies, we suggest that the higher selectivity/yield achieved by the WO_3-based catalysts can be attributed to the incorporation of additional acid sites to the anatase semiconductor. These new sites would allow enhancing the selective activation of primary C-O bonds in glycerol towards the production of glyceraldehyde and, on the other hand, to quickly desorb aldehyde products in the liquid phase. A possible path of reactions over TiO_2-based and WO_3-based materials has been put forward according to the above discussion (Scheme 2. 1).

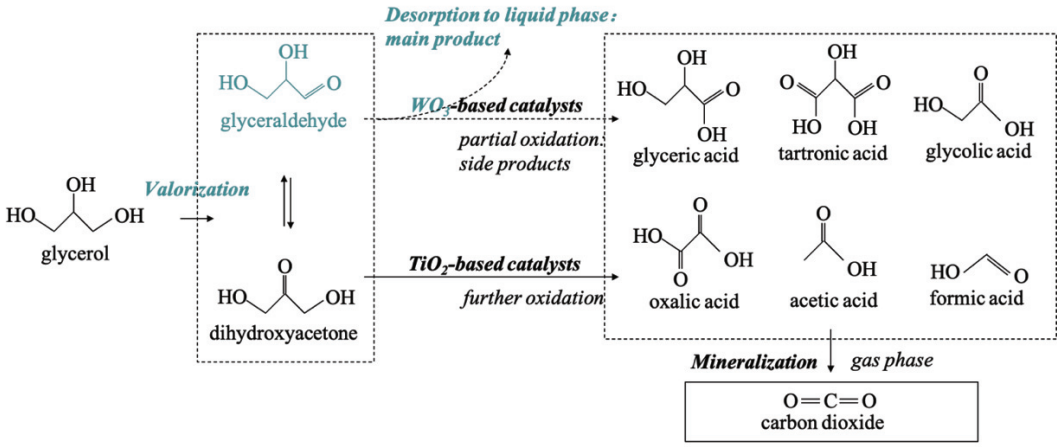

Scheme 2. 1. A possible path for photocatalytic glycerol oxidation

All in all, this study demonstrates that WO_3-based materials are active for the valorization of glycerol towards a high added-value product: glyceraldehyde. All these materials exhibit outstanding advantages. On the one hand, the as-prepared WO_3 catalyst leads to a high yield of glyceraldehyde even at very high conversion levels. However, its applicability could be compromised by its slow overall kinetics. In this sense, the calcined WO_3 catalyst, with improved crystallinity, seemed to enhance the kinetics without compromising the glyceraldehyde yield, although the calcination step could eventually increase the overall production cost of this material. Finally, commercial DTW5 led to lower glyceraldehyde yields than pure WO_3 catalysts (but still much higher than those for pure TiO_2-based materials), and overall faster kinetics. Therefore, further studies could optimize the composition and synthesis procedure of the photocatalyst for practical purposes.

4. Conclusions

In this study, we demonstrated, for the first time in literature, the high performance of WO_3-based catalysts for the selective photooxidation of glycerol towards glyceraldehyde. By comparing the activity of pure TiO_2 (Anatase, Rutile and $P25_{anatase/rutile}$) and pure WO_3 (prepared by a simple hydrothermal method), we can conclude that: i) TiO_2 catalysts allowed for a higher overall conversion of glycerol, where the selectivity to glyceraldehyde was hindered by its further photooxidation, and ii) WO_3 catalysts exhibit slower kinetics for glycerol oxidation, but show an outstanding selectivity and yield of glyceraldehyde. While the activity of TiO_2 was attributed to electronic effects (better separation of photogenerated charge carriers), the high glyceraldehyde selectivity of WO_3 was linked to its enhanced acidity, which selectively activates C-O bonds in glycerol, and facilitates the desorption of glyceraldehyde (avoiding its further photooxidation). Hence, a commercial WO_3/TiO_2 material (DTW5) was proven to combine the best features of both semiconductors, with high levels of glycerol conversion and selectivity to glyceraldehyde. This study opens therefore a new field dealing with the development of advanced photocatalytic materials for an advanced valorization of glycerol into high added-value products.

Acknowledgment

The authors would like to thank the CSC (CHINA SCHOLARSHIP COUNCIL) for the Jie Yu Ph.D. grant (CSC No. 201906740016). The authors also thank L. Burel (HRTEM) Y. Aizac (PXRD) and P. Mascunan (BET measurements) of IRCELYON.

References

[1] OECD/FAO, OECD-FAO Agricultural Outlook 2016-2025. OECD Publishing, Paris,

(2016).

[2] O.P. Paris/FAO, OECD-FAO Agricultural Outlook 2020-2029, 2020.

[3] C. Santibáñez, M.T. Varnero, M. Bustamante, Residual glycerol from biodiesel manufacturing, waste or potential source of bioenergy: a review, Chil. J. Agric. Res. 71 (2011) 469–475.

[4] M. Pagliaro, R. Ciriminna, H. Kimura, M. Rossi, C. Della Pina, From glycerol to value-added products, Angew. Chemie - Int. Ed. 46 (2007) 4434–4440.

[5] Y. Kwon, M.T.M. Koper, Combining voltammetry with HPLC: Application to electro-oxidation of glycerol, Anal. Chem. 82 (2010) 5420–5424.

[6] E. Diguilio, E.D. Galarza, M.E. Domine, L.B. Pierella, M.S. Renzini, Tuning product selectivity in the catalytic oxidation of glycerol by employing metal-ZSM-11 materials, New J. Chem. 44 (2020) 4363–4375.

[7] P.M. Walgode, R.P. V Faria, A.E. Rodrigues, A review of aerobic glycerol oxidation processes using heterogeneous catalysts: a sustainable pathway for the production of dihydroxyacetone, Catal. Rev. (2020) 1–90.

[8] C. Detoni, A.R.P. da Silva, M.M.V.M. Souza, Effect of Pt/HZSM-5 dealumination by high temperature reduction on glycerol oxidation, J. Porous Mater. (2020) 1–11.

[9] D.E. Castillo, J.E. Keri, Chemical peels in the treatment of acne: patient selection and perspectives, Clin. Cosmet. Investig. Dermatol. 11 (2018) 365.

[10] L.C.D. Coelho, M.L. Nelson Filho, R.P. V Faria, A.F.P. Ferreira, A.M. Ribeiro, A.E. Rodrigues, Separation of tartronic and glyceric acids by simulated moving bed chromatography, J. Chromatogr. A. 1563 (2018) 62–70.

[11] A. Mendoza, R. Romero, G.P. Gutiérrez-Cedillo, G. López-Tellez, O. Lorenzo-González, R.M. Gómez-Espinosa, R. Natividad, Selective production of dihydroxyacetone and glyceraldehyde by photo-assisted oxidation of glycerol, Catal. Today. 358 (2020) 149–154.

[12] A. Behr, J. Eilting, K. Irawadi, J. Leschinski, F. Lindner, Improved utilisation of renewable resources: New important derivatives of glycerol, Green Chem. 10 (2008) 13–30.

[13] D. Liang, J. Gao, H. Sun, P. Chen, Z. Hou, X. Zheng, Selective oxidation of glycerol with oxygen in a base-free aqueous solution over MWNTs supported Pt catalysts, Appl. Catal. B Environ. 106 (2011) 423–432.

[14] H. Kimura, K. Tsuto, T. Wakisaka, Y. Kazumi, Y. Inaya, Selective oxidation of glycerol on a platinum-bismuth catalyst, Appl. Catal. A, Gen. 96 (1993) 217–228.

[15] H. Tan, C. Yao, T. Zhan, W. Li, J. Zhu, G. Wang, W. Liu, M. Sun, S. Wang, Selective oxidation of glycerol to dihydroxyacetone over N-doped porous carbon stabilized Cu_xO supported Au catalysts, Mol. Catal. 498 (2020) 111243.

[16] A. Mendoza, R. Romero, G.P. Gutiérrez-Cedillo, G. López-Tellez, O. Lorenzo-González, R.M. Gómez-Espinosa, R. Natividad, Selective production of dihydroxyacetone and glyceraldehyde by photo-assisted oxidation of glycerol, Catal. Today. (2020) 0–1.

[17] J. Payormhorm, R. Idem, Synthesis of C-doped TiO_2 by sol-microwave method for photocatalytic conversion of glycerol to value-added chemicals under visible light, Appl. Catal. A Gen. 590 (2020) 117362.

[18] A.L. Imbault, R. Farnood, Selective oxidation of crude glycerol to dihydroxyacetone in a biphasic photoreactor, Catalysts. 10 (2020).

[19] Z. Zhang, L. Xin, W. Li, Electrocatalytic oxidation of glycerol on Pt/C in anion-exchange membrane fuel cell: Cogeneration of electricity and valuable chemicals, Appl. Catal. B Environ. 119–120 (2012) 40–48.

[20] C. Liu, M. Hirohara, T. Maekawa, R. Chang, T. Hayashi, C.Y. Chiang, Selective electro-oxidation of glycerol to dihydroxyacetone by a non-precious electrocatalyst-CuO, Appl. Catal. B Environ. 265 (2020) 118543.

[21] D. Lee, Y. Kim, H. Han, W.B. Kim, H. Chang, T.M. Chung, J.H. Han, H.W. Kim, H.J. Kim, Atomic-layer-deposited SnO_2 on Pt/C prevents sintering of Pt nanoparticles and affects the reaction chemistry for the electrocatalytic glycerol oxidation reaction, J. Mater. Chem. A. 8 (2020) 15992–16005.

[22] D. Raptis, V. Dracopoulos, P. Lianos, Renewable energy production by photoelectrochemical oxidation of organic wastes using WO_3 photoanodes, J. Hazard. Mater. 333 (2017) 259–264.

[23] L. Zhou, L. Wang, J. Zhang, J. Lei, Y. Liu, The preparation, and applications of g-C_3N_4/TiO_2 heterojunction catalysts-a review, Res. Chem. Intermed. 43 (2017) 2081–2101.

[24] B. Qiu, M. Xing, J. Zhang, Recent advances in three-dimensional graphene based materials for catalysis applications, Chem. Soc. Rev. 47 (2018) 2165–2216.

[25] H. Photocatalysis, From Fundamentals to Green Applications, (2016).

[26] J.C. Colmenares, Nanophotocatalysis in selective transformations of lignocellulose-derived molecules: a green approach for the synthesis of fuels, fine chemicals, and pharmaceuticals, in: Green Photo-Active Nanomater., 2015: pp. 168–201.

[27] V. Maurino, A. Bedini, M. Minella, F. Rubertelli, E. Pelizzetti, C. Minero, Glycerol transformation through photocatalysis: A possible route to value added chemicals, J. Adv. Oxid. Technol. 11 (2008) 184–192.

[28] P. Panagiotopoulou, E.E. Karamerou, D.I. Kondarides, Kinetics and mechanism of glycerol photo-oxidation and photo-reforming reactions in aqueous TiO_2 and Pt/TiO_2 suspensions, Catal. Today. 209 (2013) 91–98.

[29] M. de Oliveira Melo, L.A. Silva, Visible light-induced hydrogen production from glycerol aqueous solution on hybrid Pt--CdS--TiO_2 photocatalysts, J. Photochem. Photobiol. A Chem. 226 (2011) 36–41.

[30] V. Augugliaro, H.A.H. El Nazer, V. Loddo, A. Mele, G. Palmisano, L. Palmisano, S. Yurdakal, Partial photocatalytic oxidation of glycerol in TiO_2 water suspensions, Catal. Today. 151 (2010) 21–28.

[31] C. Minero, A. Bedini, V. Maurino, Glycerol as a probe molecule to uncover oxidation mechanism in photocatalysis, Appl. Catal. B Environ. 128 (2012) 135–143.

[32] I.M. Szilágyi, E. Santala, M. Heikkilä, V. Pore, M. Kemell, T. Nikitin, G. Teucher, T. Firkala, L. Khriachtchev, M. Räsänen, M. Ritala, M. Leskelä, Photocatalytic properties of WO_3/TiO_2 core/shell nanofibers prepared by electrospinning and atomic layer deposition, Chem. Vap. Depos. 19 (2013) 149–155.

[33] I.M. Szilágyi, B. Fórizs, O. Rosseler, Á. Szegedi, P. Németh, P. Király, G. Tárkányi, B. Vajna, K. Varga-Josepovits, K. László, A.L. Tóth, P. Baranyai, M. Leskelä, WO_3 photocatalysts: Influence of structure and composition, J. Catal. 294 (2012) 119–127.

[34] Y. Lin, Y. Zhu, A. Li, T. Wu, Y. Song, Preparation and photocatalytic properties of biomorphic hierarchical WO_3 based on bionic rice hull, Res. Chem. Intermed. 46 (2020) 1405–1424.

[35] M. Tahir, M. Siraj, B. Tahir, M. Umer, H. Alias, N. Othman, Au-NPs embedded Z--scheme WO_3/TiO_2 nanocomposite for plasmon-assisted photocatalytic glycerol-water reforming towards enhanced H_2 evolution, Appl. Surf. Sci. 503 (2020) 144344.

[36] M. Stelmachowski, M. Marchwicka, E. Grabowska, M. Diak, The photocatalytic conversion of (biodiesel derived) glycerol to hydrogen-A short review and preliminary experimental results part 1: A review, J. Adv. Oxid. Technol. 17 (2014) 167–178.

[37] X. Liu, H. Zhai, P. Wang, Q. Zhang, Z. Wang, Y. Liu, Y. Dai, B. Huang, X. Qin, X. Zhang, Synthesis of a WO_3 photocatalyst with high photocatalytic activity and stability using synergetic internal Fe^{3+} doping and superficial Pt loading for ethylene degradation under visible-light irradiation, Catal. Sci. Technol. 9 (2019) 652–658.

[38] J.-Y. Wu, Y.-W. Chen, Preparation of WO_3-modified TiO_2 thin film by peroxo sol--gel method and its photocatalytic activity in degradation of methylene blue, Res. Chem. Intermed. 46 (2020) 4627–4643.

[39] C.M. Hung, N. Van Duy, V. Van Quang, N. Van Toan, N. Van Hieu, N.D. Hoa, others, Facile synthesis of ultrafine rGO/WO_3 nanowire nanocomposites for highly sensitive toxic NH_3 gas sensors, Mater. Res. Bull. 125 (2020) 110810.

[40] Z. Chen, Y. Peng, F. Liu, Z. Le, J. Zhu, G. Shen, D. Zhang, M. Wen, S. Xiao, C.-P. Liu, others, Hierarchical nanostructured WO_3 with biomimetic proton channels and mixed ionic-electronic conductivity for electrochemical energy storage, Nano Lett. 15 (2015) 6802–6808.

[41] M.S. Koo, X. Chen, K. Cho, T. An, W. Choi, In Situ Photoelectrochemical Chloride Activation Using a WO_3 Electrode for Oxidative Treatment with Simultaneous H_2 Evolution under Visible Light, Environ. Sci. Technol. 53 (2019) 9926–9936.

[42] Y. Ren, L.J. Hardwick, P.G. Bruce, Lithium Intercalation into Mesoporous Anatase with an Ordered 3D Pore Structure, Angew. Chemie. 122 (2010) 2624–2628.

[43] L. Miao, P. Jin, K. Kaneko, A. Terai, N. Nabatova-Gabain, S. Tanemura, Preparation and characterization of polycrystalline anatase and rutile TiO_2 thin films by rf magnetron sputtering, Appl. Surf. Sci. 212–213 (2003) 255–263.

[44] S. Pokhrel, J. Birkenstock, M. Schowalter, A. Rosenauer, L. Mädler, Growth of ultrafine single crystalline WO_3 nanoparticles using flame spray pyrolysis, Cryst. Growth Des. 10 (2010) 632–639.

[45] L. Elsellami, F. Dappozze, N. Fessi, A. Houas, C. Guillard, Highly photocatalytic activity of nanocrystalline TiO_2 (anatase, rutile) powders prepared from $TiCl_4$ by sol–gel method in aqueous solutions., Process Saf. Environ. Prot. 113 (2018) 109–121.

[46] N. Fessi, M.F. Nsib, L. Cardenas, C. Guillard, F. Dappozze, A. Houas, F. Parrino, L. Palmisano, G. Ledoux, D. Amans, Y. Chevalier, Surface and Electronic Features of Fluorinated TiO_2 and Their Influence on the Photocatalytic Degradation of 1-Methylnaphthalene, J. Phys. Chem. C. 124 (2020) 11456–11468.

[47] S. Wu, X. Tan, J. Lei, H. Chen, L. Wang, J. Zhang, Ga-Doped and Pt-Loaded Porous TiO_2-SiO_2 for Photocatalytic Nonoxidative Coupling of Methane, J. Am. Chem. Soc. 141 (2019) 6592–6600.

[48] J. Hu, L. Wang, P. Zhang, C. Liang, G. Shao, Construction of solid-state Z-scheme carbon-modified TiO_2/WO_3 nanofibers with enhanced photocatalytic hydrogen production, J. Power Sources. 328 (2016) 28–36.

[49] M. Checa, V. Montes, J. Hidalgo-Carrillo, A. Marinas, F.J. Urbano, Influence of Boron, Tungsten and Molybdenum Modifiers on Zirconia Based Pt Catalyst for Glycerol Valorization, Nanomaterials. 9 (2019).

[50] J. Gonzalez, J.A. Wang, L.F. Chen, M.E. Manriquez, J.M. Dominguez, Structural defects, Lewis acidity, and catalysis properties of mesostructured WO_3/SBA-15 nanocatalysts, J. Phys. Chem. C. 121 (2017) 23988–23999.

[51] P. Ganji, S. Roy, Trade-off between acidic sites and crystallinity of the WO_3-TiO_2 catalyst toward dehydration of glucose to 5-hydroxymethylfurfural, Energy and Fuels. 33 (2019) 5293–5303.

[52] T. Kurosaka, H. Maruyama, I. Naribayashi, Y. Sasaki, Production of 1,3-propanediol by hydrogenolysis of glycerol catalyzed by Pt/WO_3/ZrO_2, Catal. Commun. 9 (2008) 1360–1363.

[53] T. Aihara, H. Miura, T. Shishido, Investigation of the mechanism of the selective hydrogenolysis of CO bonds over a Pt/WO_3/Al_2O_3 catalyst, Catal. Today. 352 (2020) 73–79.

[54] N. Subramanian, A. Caravaca, F.R. García-García, M. Bowker, Sustainable hydrogen and/or syngas production: New approaches to reforming, 2017.

[55] S. Palmas, P.A. Castresana, L. Mais, A. Vacca, M. Mascia, P.C. Ricci, TiO_2–WO_3 nanostructured systems for photoelectrochemical applications, RSC Adv. 6 (2016) 101671–101682.

[56] T. Jedsukontorn, V. Meeyoo, N. Saito, M. Hunsom, Route of glycerol conversion and product generation via TiO_2-induced photocatalytic oxidation in the presence of H_2O_2, Chem. Eng. J. 281 (2015) 252–264.

[57] T. Jedsukontorn, T. Ueno, N. Saito, M. Hunsom, Mechanistic aspect based on the role of reactive oxidizing species (ROS) in macroscopic level on the glycerol photooxidation over defected and defected-free TiO_2, J. Photochem. Photobiol. A Chem. 367 (2018) 270–281.

[58] A.L. Imbault, J. Gong, R. Farnood, Photocatalytic production of dihydroxyacetone from glycerol on TiO_2 in acetonitrile, RSC Adv. 10 (2020) 4956–4968.

[59] T. Jedsukontorn, T. Ueno, N. Saito, M. Hunsom, Narrowing band gap energy of defective black TiO_2 fabricated by solution plasma process and its photocatalytic activity on glycerol transformation, J. Alloys Compd. 757 (2018) 188–199.

[60] F.J. López-Tenllado, S. Murcia-López, D.M. Gómez, A. Marinas, J.M. Marinas, F.J. Urbano, J.A. Nav\'\io, M.C. Hidalgo, J.M. Gatica, A comparative study of Bi_2WO_6,

CeO_2, and TiO_2 as catalysts for selective photo-oxidation of alcohols to carbonyl compounds, Appl. Catal. A Gen. 505 (2015) 375–381.

Chapter 2

Electronic Supplementary Information

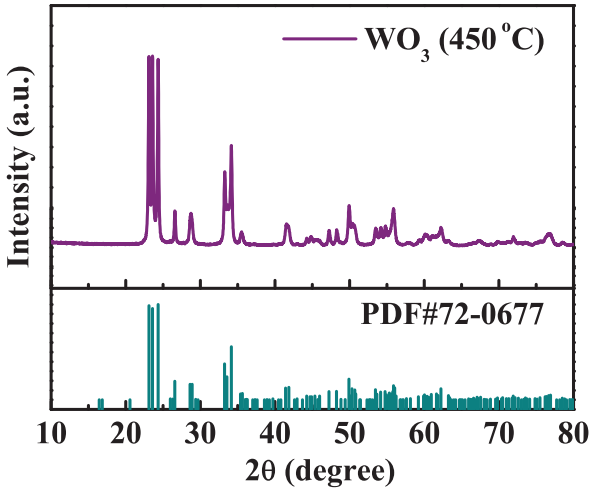

Fig. S2. 1. X-ray diffraction (XRD) patterns of WO_3 obtained after calcination at 450 °C.

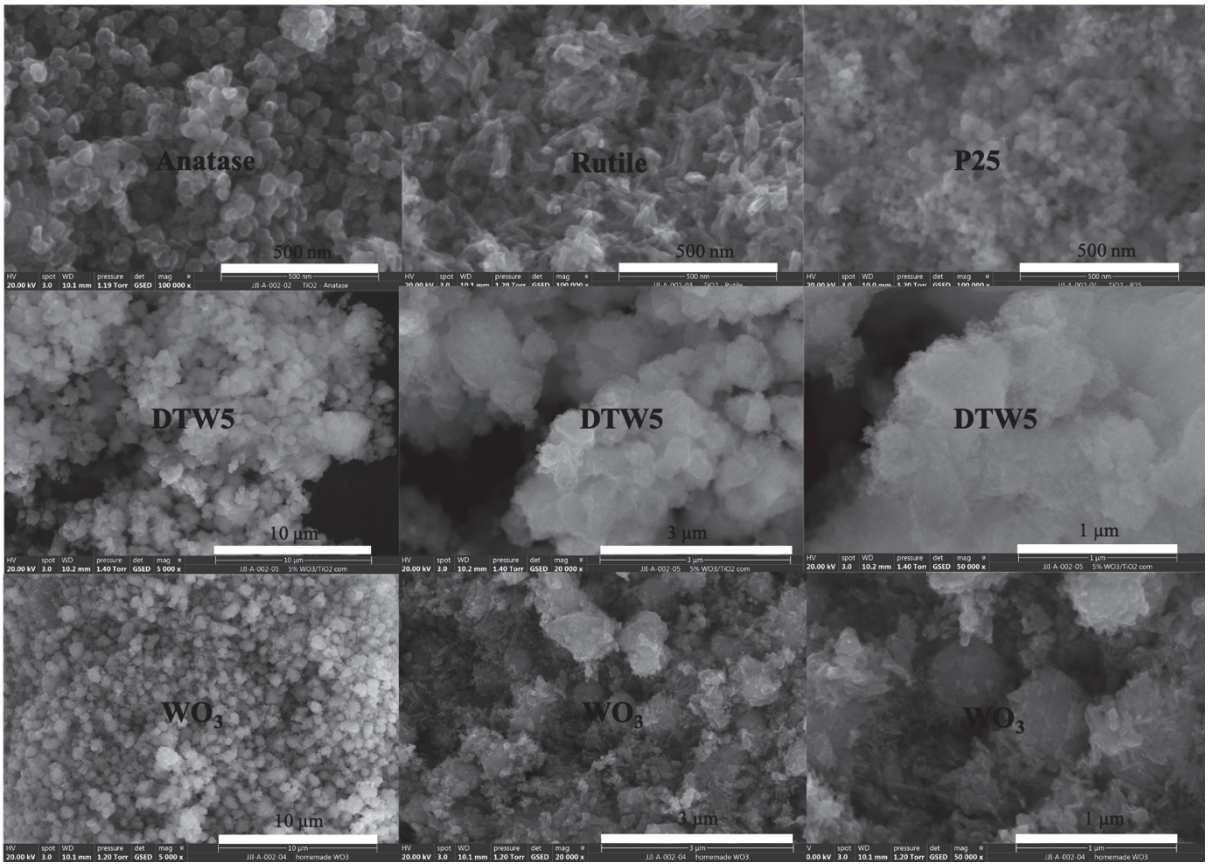

Fig. S2. 2. Scanning electron microscopy (SEM) images of commercial (Anatase, Rutile, P25 and DTW5) and as-prepared WO_3 catalyst.

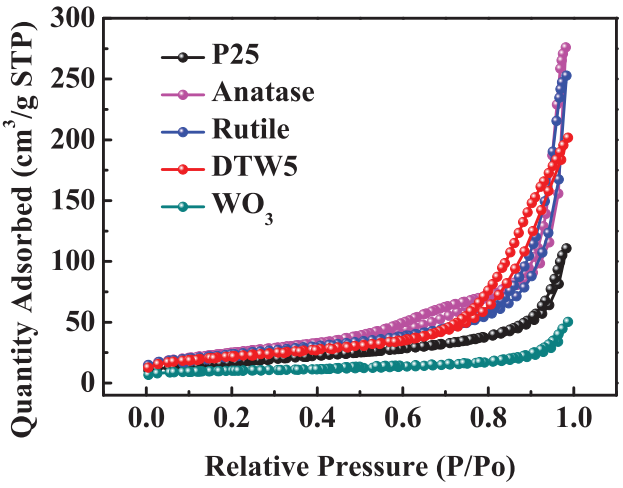

Fig. S2. 3. BET N_2 adsorption-desorption isotherms of commercial (Anatase, Rutile, P25 and DTW5) and as-prepared WO_3 catalyst.

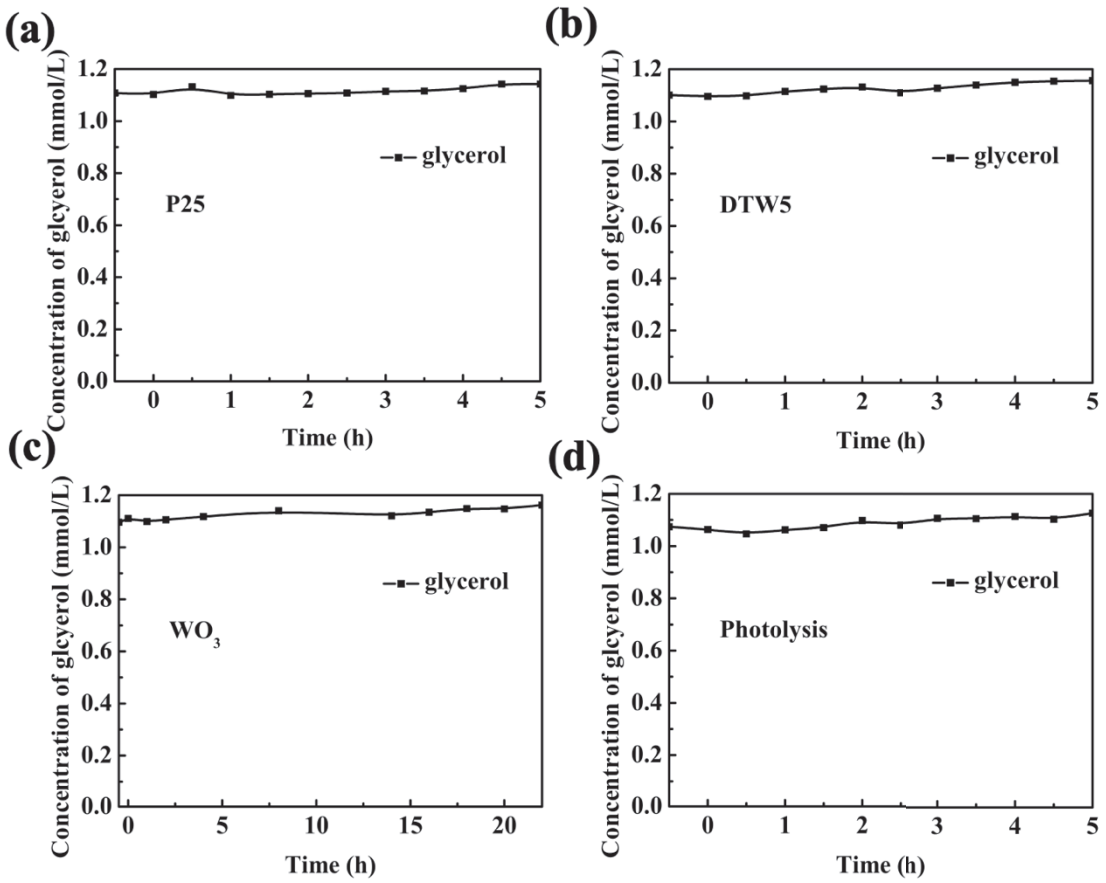

Fig. S2. 4. Blank experiments for (a) P25, (b) DTW5 and (c)WO_3. Reaction conditions: Room temperature, Glycerol initial concentration: 1.10 mmol L^{-1}, Volume of glycerol solution: 30 mL, no UV irradiation.

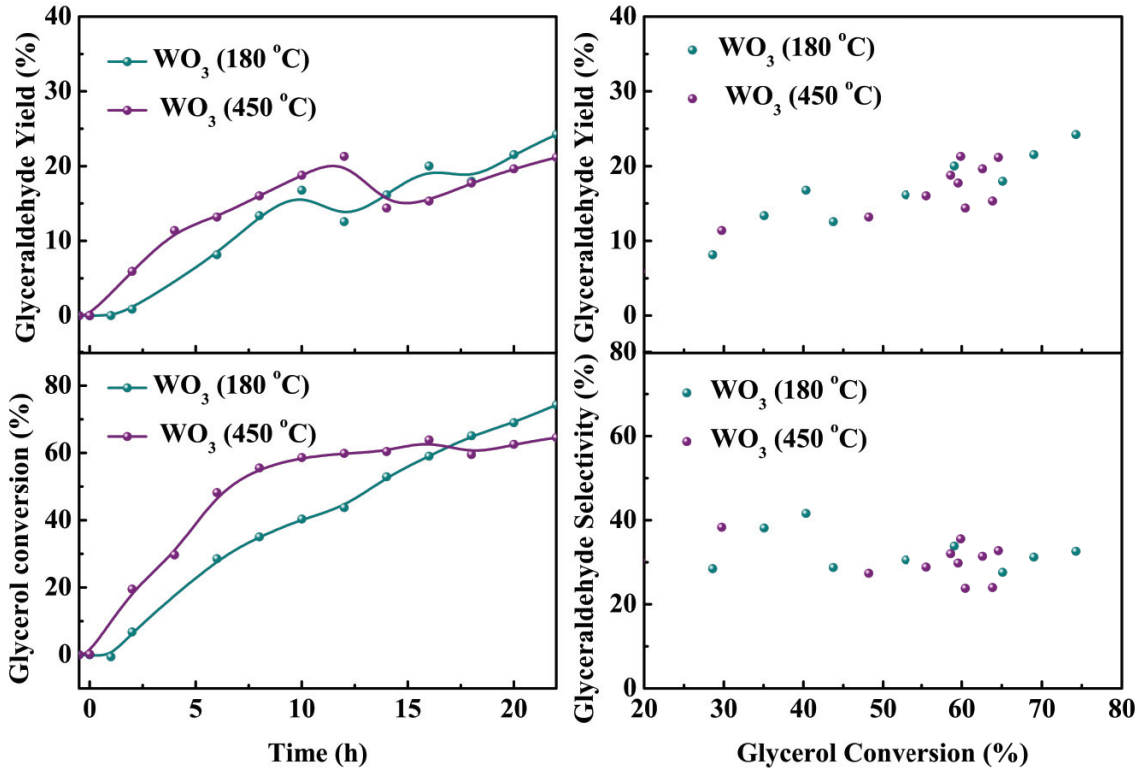

Fig. S2. 5. Glyceraldehyde yield and glycerol conversion with time as well as glyceraldehyde yield and selectivity with glycerol conversion over WO_3 obtained via a simple hydrothermal method at 180 ºC and WO_3 post-treated at 450 ºC. Reaction conditions: Room temperature, Glycerol initial concentration: 1.10 mmol L^{-1}, Volume of glycerol solution: 30 mL, UV irradiation intensity of 5.60 mW cm^{-2}.

Chapter 3

WO_3-based materials for photoelectrocatalytic glycerol upgrading into glyceraldehyde: Unravelling the synergistic photo- and electro-catalytic effects

Jie Yu,[a] Jesús González-Cobos,[a] Frederic Dappozze,[a] Francisco J. López-Tenllado,[b] Jesús Hidalgo-Carrillo,[b] Alberto Marinas,[b] Philippe Vernoux,[a] Angel Caravaca,[a]* Chantal Guillard[a]*

[a] Univ Lyon, Université Claude Bernard Lyon 1, CNRS, IRCELYON, F-69626, Villeurbanne, France

[b] Departamento de Química Orgánica. Instituto Universitario de Investigación en Nanoquímica (IUNAN). Universidad de Córdoba. Edf. Marie Curie (Annex). Campus de Rabanales, E-14071 Córdoba. España

E-mail: angel.caravaca@ircelyon.univ-lyon1.fr, chantal.guillard@ircelyon.univ-lyon1.fr

Abstract

The application of photoelectrocatalysis (PEC) to glycerol oxidation has emerged as a promising technology for the simultaneous valorization of this biomass waste and hydrogen production. However, very few PEC studies have accomplished the selective production of value-added oxidation products such as glyceraldehyde or dihydroxyacetone (DHA), especially under near-neutral conditions. Herein, we report the outstanding photocatalytic (PC) activity and stability of a monoclinic WO_3 catalyst synthesized by a simple hydrothermal method for the selective generation of these C_3 chemicals. The joint selectivity of glyceraldehyde and DHA, among all liquid products, remained above 87% in a wide potential range (0.5-2.0 V vs. RHE). Besides, for the first time, the effect of the electric polarization on the PC glycerol valorization has been investigated. Glyceraldehyde and DHA production was enhanced up to 4.5 and 11.5 times, respectively, by means of the external bias, with a stable faradaic efficiency above 50% of the additional holes hypothetically generated, in the whole studied potential range. Through different characterization techniques and the comparative analysis of the results obtained with a commercial WO_3/TiO_2 catalyst, the influence of the

applied potential and the catalyst activity for water oxidation in the glycerol reaction mechanism are discussed, as well as the key role of the sub-stoichiometric tungsten oxide content and the corresponding catalyst oxygen vacancies along with suitable acid sites, which confer very advantageous properties to WO_3-based materials for the selective PEC valorization of glycerol.
Keywords: photoelectrocatalysis, valorization, glycerol, glyceraldehyde, WO_3

1. Introduction

Photoelectrocatalytic (PEC) technology, as an electrochemically assisted photocatalytic (PC) system, has been widely identified as a superior alternative to conventional PC technology. This is due to the effective promotion of the separation of photogenerated electrons and holes via the application of an externally applied electric bias [1,2] However, up to now, most PEC research has been limited to water splitting [3], H_2 evolution [4] and organic pollutant degradation [5]. Furthermore, the necessary semiconductor material is commonly doped with high-cost precious metals such as platinum [6–8], gold [9–11] and palladium [12–14] to achieve excellent PEC performances. Therefore, the application of PEC technology to highly cost-effective selective reactions, such as the chemical valorization of organic renewable wastes under mild conditions, has attracted increasing interest.

According to a recent report in Nature, by 2050, around 90% of coal, 60% of oil and fossil methane gas, must be kept unextracted to limit global warming [15]. Thus, the restructuring of the energy framework via the replacement of fossil fuels by renewable sources is vital to achieving the targets of carbon neutrality that have already been put forward by more than 120 countries around the world [16,17]. In this sense, biofuels such as biodiesel are a potential alternative to fossil fuels [18]. However, every ton of biodiesel derived from biomass generates 100 kg of glycerol as a by-product, which is usually used to generate energy through processes such as combustion or pyrolysis. Nevertheless, there are some associated problems like the low/moderate heating value of glycerol or the potential release of toxic products such as acrolein into the atmosphere [19]. Glycerol is also a side waste of soap manufacturers and its annual production exceeds the demand of around 1 million tons per year [20]. Thus, the CO_2-free valorization of this oversupplied glycerol to produce high-value renewable chemicals such as glyceraldehyde and dihydroxyacetone (DHA) is of great economic and environmental significance [21,22]. Currently, the most widely studied catalysts for glycerol selective oxidation are still noble metals and their metal alloys, which have been applied in

photocatalysis, thermal catalysis and electrocatalysis [23–25]. The application of PEC to glycerol oxidation has also emerged as a promising technology for the selective synthesis of value-added chemicals and, besides, the simultaneous generation of pure hydrogen [26]. Few PEC studies can be found in literature, where Pt- [27] or Au-based catalysts [28,29] were utilized in strongly alkaline electrolytic solutions using KOH or NaOH, which are prone to safety risks during storage and transportation. In recent years, some research groups have also studied the PEC oxidation of glycerol by using non-noble metal materials such as $BiVO_4$ [30,31], W-$BiVO_4$ [32], $NiO_x(OH)_y$/W-$BiVO_4$ [32], WO_3 [33], WO_3/TiO_2 [34], $TiO_2/CsPbBr_3$ [35], Co-ZnO [36] or α-Fe_2O_3 [37], although only a few of them were carried out in neutral or near-neutral electrolytic operation conditions [30,32,33,35]. For example, Dong Liu et al. [30] found that the $BiVO_4$ semiconductor was highly selective towards DHA at low pH, due to the acid environment preventing the further oxidation of this product, while, at neutral conditions, $BiVO_4$-based photoanodes preferentially oxidized glycerol to formic acid [30,32]. The group of Qu [34] has prepared WO_3/TiO_2 heterostructures and found that the microfluidic platform results in higher glyceraldehyde selectivity than the conventional planar configuration. However, the role of the acidic properties of WO_3 in the PEC activity is still not clear. Another study has explored the PEC glycerol oxidation on WO_3 but was mainly focused on the hydrogen evolution reaction at the cathode without quantifying the glycerol conversion at the anode [33].

In our previous work, TiO_2- and WO_3-based materials were investigated for the selective PC oxidation of glycerol [38]. It was found that homemade pseudo-amorphous WO_3 with high acidity synthesized by a simple hydrothermal method shows an outstanding selectivity to glyceraldehyde but the kinetics were not high enough for practical application. This limitation was attributed to the low crystallinity of the oxide and to a high recombination rate of photo-generated carriers. Therefore, in this work, a commercial WO_3/TiO_2 (DTW5) and a pure monoclinic WO_3 with upgraded physicochemical properties were investigated for the PEC valorization of glycerol in a neutral electrolytic solution. Our results demonstrate that the coupling of the green PEC technology (to accelerate the separation of photo-generated charge carriers) with the merits of crystallized tungsten trioxide materials can lead to outstanding selectivity towards glyceraldehyde and DHA production. In addition, several different characterization techniques were used to unravel the mechanism of PEC glycerol oxidation over WO_3-based materials.

2. Experimental

2.1 Preparation of monoclinic WO_3

Firstly, 0.6 g of WCl_6 as precursor was dissolved in 120 mL of Ethanol solution, transferred to a Teflon-lined stainless-steel autoclave (200 mL) and kept in an oven for 12 h at 180 ^oC. Then, low-crystalline WO_3 powder was withdrawn, washed with Ethanol (3 × 90 mL) and deionized water (3 × 90 mL), and dried at 80 ^oC in air overnight. Finally, the calcination of the well-grinded pseudo-amorphous WO_3 at 450 ^oC in air (1 h, 5 ^oC min^{-1} heating rate) allowed obtaining a pure monoclinic WO_3 (hereafter referred to as WO_3 or calcined WO_3). Commercial DTW5 (5 wt.% WO_3/TiO_2) material was provided by Tronox®.

2.2 Characterization

X-ray diffraction (XRD) was conducted with a Bruker D8 diffractometer using Cu Kα (λ= 0.15406 nm) radiation equipped with a 1-D fast multistrip detector (LynxEye, 192 channels on 2.95°) and a Ni filter. Other test conditions included a current of 100 mA, an operating voltage of 40 kV, a scanning range of 2θ = 4-80° and a scan rate of 0.02° s^{-1}. Phase, crystallinity and average crystallite size identification were carried out using the Diffrac. Eva software (Bruker) and the ICDD-PDF4+ database. X-ray photoelectron spectra (XPS) were conducted via a Thermo Scientific ESCALAB 250 spectrometer equipped with a monochromatic Al Kα radiation source. C 1s peak at 284.6 eV was used as a reference to correct the binding energy. High-resolution transmission electron microscopy (HRTEM) was performed on a JEOL-2010 microscope equipped with an EDX detector. The Brunauer−Emmett−Teller (BET) surface area of the catalysts was measured via nitrogen adsorption at −196 °C (Micromeritics ASAP 2020). Prior to these measurements, the catalysts were degassed at 160 °C for 3 h under vacuum. The porous volume and the pore size distribution were calculated via the Barrett-Joyner-Halenda (BJH) method. UV-vis diffuse reflectance spectroscopy (UV-vis DRS) measurements were conducted via an AvaSpec-2048 Fiber Optic Spectrometer. A 2048 pixel CCD detector array was used to record the spectra from 200 to 600 nm and Barium sulfate ($BaSO_4$) served as a blank reference.

The acidity of the catalysts was determined by using pyridine as a probe molecule. Pyridine adsorption was recorded by Diffuse Reflectance Infrared Fourier Transform Spectroscopy (DRIFTS) by using a Fourier-transform infrared spectroscopy (FTIR) instrument (Perkin Elmer Frontier) equipped with an environmental chamber (Harrick HVC-DRM). A resolution of 4 cm^{-1} was used with 125 scans averaged to obtain a spectrum from 4000 to 400 cm^{-1}. Before each test, pyridine adsorption was conducted at 100 °C for 45 min to achieve the saturation of

the catalyst surface. The physically adsorbed pyridine was then removed from the surface with an air flow (50 mL min^{-1}). Finally, the infrared radiation (IR) spectra were recorded at 100 °C. Bands at 1448 and 1537 cm^{-1} (corresponding to Lewis and Brönsted acid sites, respectively) were integrated and acidity was determined using the corresponding molar extinction coefficients. The Electron Paramagnetic Resonance (EPR) spectra of solids were recorded on a Bruker EMX micro instrument operating at a frequency of 9.75 GHz. The acquisition parameters were as follows: the center field: 3480 G, the sweep time: 60 s, the number of points: 4200, the modulation amplitude: 4 G, the power: 0.6 mW and the field frequency modulation: 100 kHz. All the measurements were carried out at -173.25 ºC to avoid the fast recombination of electron-hole pairs. Spectra were recorded without illumination and upon illumination with a solar simulated light radiation. The Raman spectra were recorded on a Jasco NRS-5500 with an excitation wavelength of 514 nm. The scanned wavenumber range was from 1000 to 100 cm-1 and gathered 25 scans. In the case of DTW5, an additional Raman spectrum focusing on the 750-850 cm^{-1} region was performed.

The electrochemical (EC) and photoelectrocatalytic (PEC) properties of the catalysts were investigated with an Origalys OGBO5A electrochemical station (OrigaLys ElectroChem SAS), via cyclic voltammetry (CV) and transient photocurrent tests at room temperature. A photoelectrochemical cell (supplied by redox.me®) with a standard three-electrode system, which consists of a DTW5 or WO_3 working electrode (deposited on a Indium Tin Oxide (ITO) support), with a geometric area of ca. 1 cm^{-2} and a catalyst loading of ca. 1 mg cm^{-2}, a Pt wire as the counter electrode and a KCl-saturated Ag/AgCl acting as the reference electrode, was filled with 15 mL of either 0.5 M Na_2SO_4 solution or the mixed solution of 0.1 M glycerol and 0.5 M Na_2SO_4 (pH 5.5). CV was recorded from 0 to 1.5 V vs. Ag/AgCl at a scan rate of 20 mV s^{-1} in dark conditions (EC) or with the light irradiation (PEC) from a LED UV lamp (350 mW cm^{-2}). Photocurrent tests of the catalysts were also carried out at different applied potentials from 0.3 V to 1.5 V vs. Ag/AgCl with 15 seconds of irradiation interval. Unless otherwise stated, all potential values reported in this work are referred to KCl-saturated Ag/AgCl reference electrode and the current density values are normalized per electrode geometric area.

2.3 Photocatalytic and photoelectrocatalytic performances

PEC experiments of glycerol valorization were carried out at room temperature using the same setup employed for the photoelectrochemical measurements above described. Firstly, 30 min of dark reaction was required to achieve a steady-state. Then, different external potentials (0.3, 0.6, 0.9, 1.2, and 1.5 V vs. Ag/AgCl) were successively applied for 5 h each. During this process,

0.6 mL of solution was sampled from the glycerol/Na_2SO_4 solution in dark conditions (at a time denoted as -30 min) and every 1 h during the PEC experiments, and immediately filtered via a Millipore 0.45 μm (hydrophilic PVDF) membrane in a plastic syringe. The concentrations of oxidized products were analyzed through an ultrafast high-performance liquid chromatography (HPLC) (Shimadzu SPD-M20A) assembled with a Transgenomic ICSep ICE-COREGEL-87H3 organic acid column. 5 mM H_2SO_4 served as the mobile phase at a flow rate of 0.7 mL min^{-1} and the temperature of the oven was 30 ºC. The nature and concentration of the products of glycerol oxidation were determined using the UV detector at the wavelength of 210 nm. For the evaluation of EC and PC performances, analogous measurements were carried out without any light irradiation (i.e., only driven by external polarization) and without any applied potential (i.e., only driven by illumination), respectively.

From the quantified amounts of liquid products obtained by PC/PEC, the yield and the selectivity of each of them have been calculated, as well as the corresponding faradaic efficiency (FE) values. Furthermore, to better discriminate the contribution of pure PC from the overall PEC performance, the faradaic efficiencies have also been calculated after subtracting to the quantified chemicals production from the PEC tests, that from the corresponding purely PC measurement. In this way, the modified parameters, FE*, will stand for the chemicals production hypothetically only derived from the additional effect of the external polarization. A detailed description of all parameter's calculations can be found in Electronic Supplementary Information (ESI, Section S1).

3. Results and discussion

3.1 Structural characterization

N_2 adsorption-desorption was performed on the commercial DTW5 (5 wt.% WO_3 on TiO_2) and homemade WO_3 catalysts to survey the specific surface area (SBET) along with the porous volume and the pore size distribution of the catalysts, which usually play important roles in glycerol conversion for the adsorption and reaction of chemicals. Type IV isotherm can be observed in both cases in Fig. S1 (ESI), and DTW5 shows higher SBET (78 m^2 g^{-1}) and pore volume (0.31 m^3 g^{-1}) than WO_3 (20 m^2 g^{-1} and 0.07 m^3 g^{-1}, respectively). However, WO_3 surface area and pore volume were not significantly affected by the high-temperature calcination (i.e., 450 °C), with respect to the pseudo-amorphous WO_3 catalyst previously reported [38], which was not calcined (see Table 3. 1). The main impact of the calcination was the growth of the crystallites. From HRTEM images presented in Fig. 3. 1, it can be observed that DTW5 and WO_3 catalysts consist of globular particles with average sizes of 25 nm and 59 nm, respectively.

The lattice spacings of 0.3752 and 0.3564 nm found in DTW5 represent WO_3 (020) and TiO_2 (101), respectively [39,40]. Besides WO_3 (020), WO_3 (002) with a lattice spacing of 0.3840 nm is also observed in WO_3 catalyst, similarly to the previously reported pseudo-amorphous WO_3, which retain the same [001] facet [38,41,42].

Table 3. 1. BET specific surface area, pore volume, mean pore size, crystallinity and average crystallite size of catalysts.

Sample	**S_{BET} ($m^2\ g^{-1}$)**	**Pore volume ($cm^3\ g^{-1}$)**	**Mean Pore Size (nm)**	**Crystallinity[a] (%)**	**Crystal size[a] (nm)**	**Ref.**
DTW5	78	0.31	13.8	84.9	20 (Anatase)	This work
WO_3	20	0.07	13.0	82.6	49	This work
Uncalcined WO_3	33	0.07	13.3	48.6	17	[38]

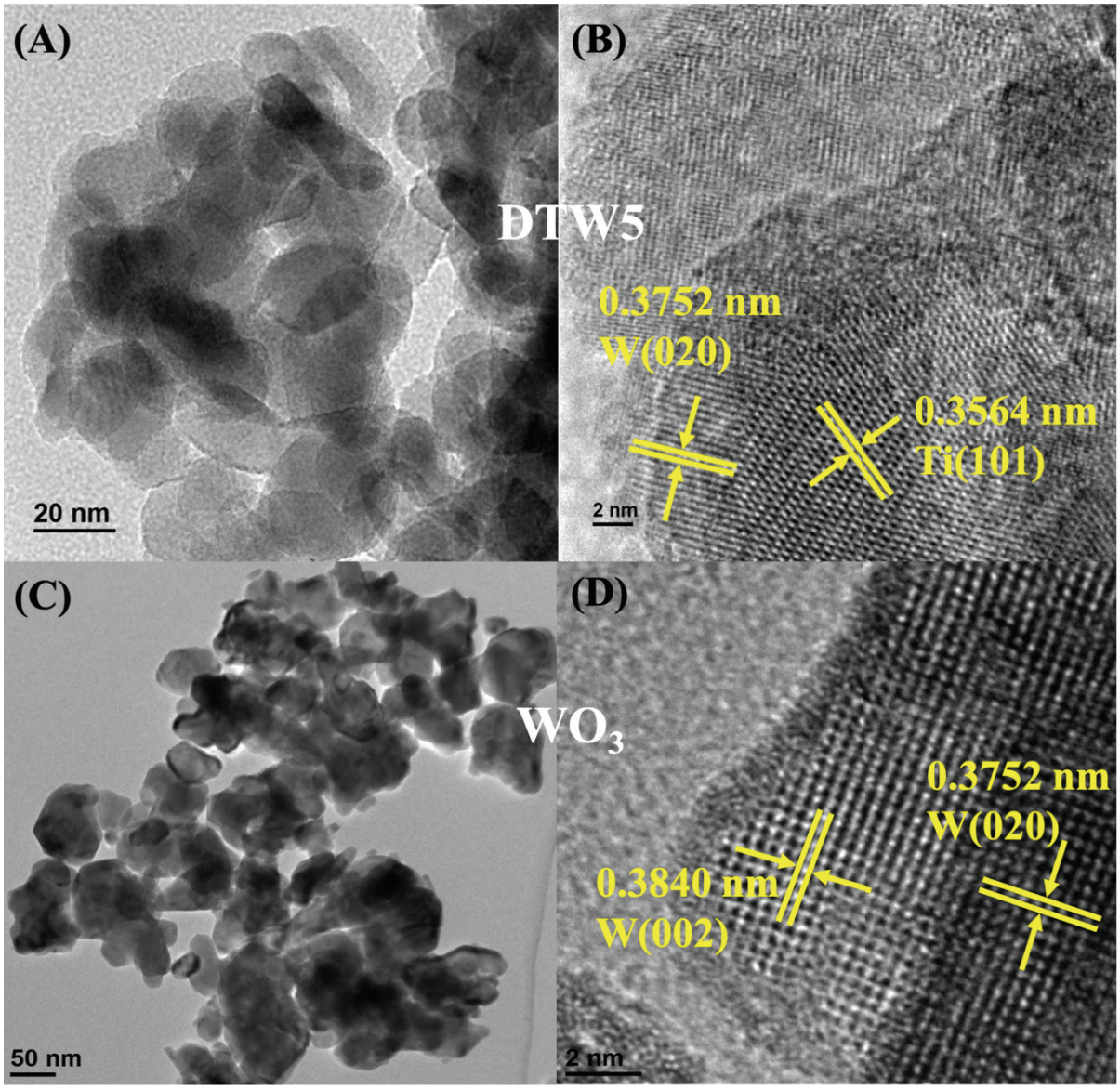

Fig. 3. 1. High-resolution transmission electron microscopy (HRTEM) images of (a, b) DTW5 and (c, d) WO_3 catalysts.

The XRD patterns for DTW5 and WO_3 are shown in Fig. 3. 2a. The commercial WO_3/TiO_2 catalyst possesses a good crystallinity up to 84.9% and its diffractogram matches PDF #89-4921 of anatase. WO_3 catalyst exhibits pure monoclinic crystalline phases (PDF #72-0677) with a similar crystallinity of 82.6% (Table 3. 1). The average crystallite size of this catalyst (49 nm) is much higher than that observed on the commercial DTW5 (20 nm) as well as on our previously reported uncalcined WO_3 catalyst (17 nm) [38]. However, a superior crystallinity is obtained in the present work, which is in agreement with the reported beneficial effect of calcination at temperatures above 400 °C on the crystallinity of WO_3 materials [43,44].

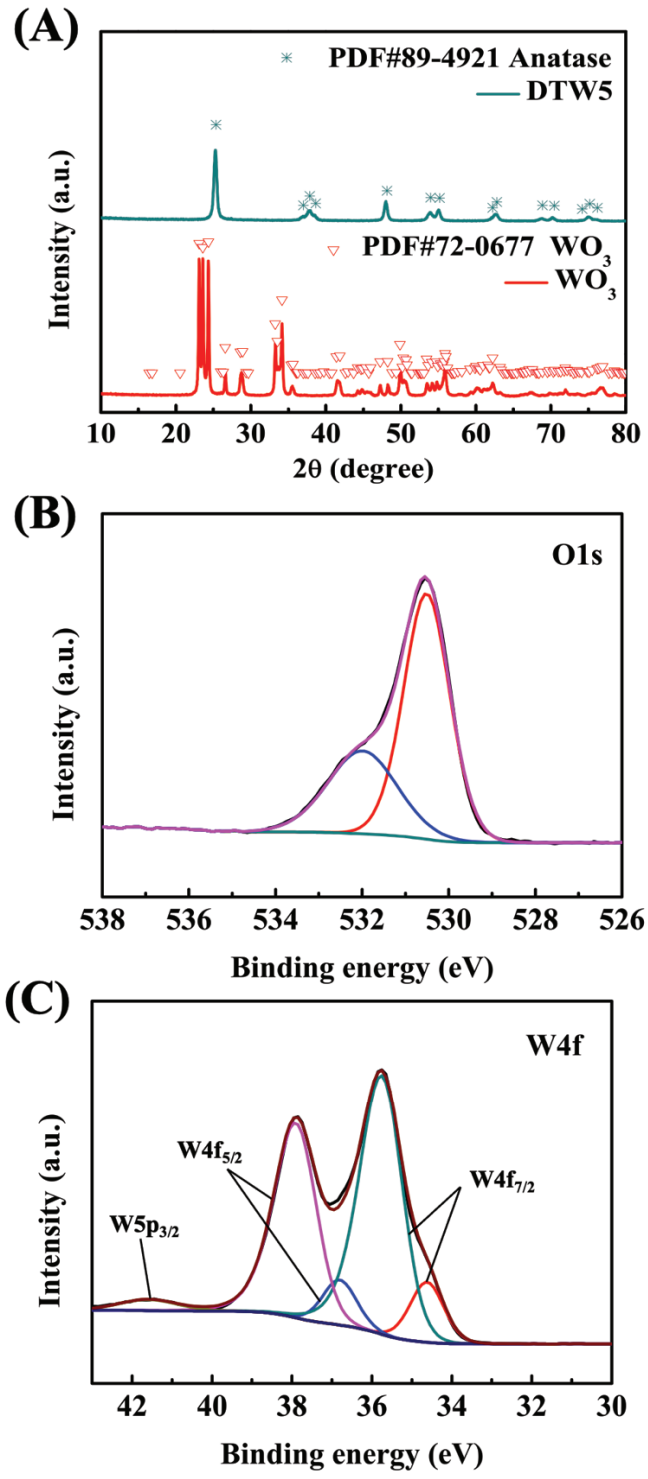

Fig. 3. 2. (a) X-ray diffraction (XRD) patterns of commercial catalyst DTW5 and as-prepared WO_3. (b) O1s, (c) W4f and W5p regions in X-ray photoelectron spectroscopy (XPS) spectra of WO_3.

The surface chemical states of both catalysts were estimated using XPS analysis. O1s spectra (Fig. 3. 2b) present a peak at 530.5 eV characteristic of the lattice oxygen in stoichiometric WO_3. The band at 532.0 eV could be attributed either to adsorbed OH groups [45,46] or to

oxygen atoms in sub-stoichiometric WO_{3-x} structures [47–49]. Fig. 3. 2c shows the W4f spectra, where the peaks at 37.9 eV and 35.8 eV belong to $W4f_{5/2}$ and $W4f_{7/2}$, respectively, of W^{6+} oxidation state, and two characteristic orbital spins of W^{5+}, centred at 36.8 eV and 34.6 eV, can be also observed [47,50]. These O1s and W4f spectra demonstrate the presence of W^{5+} and, thus, of oxygen defects on the surface of the WO_3 catalyst, with a ratio of W^{5+}/W^{6+} of 0.18, calculated from the area of the respective peaks. Among the different nonstoichiometric tungsten oxide phases, also known as Magneli phases, the obtained surface composition corresponds to monoclinic $W_{25}O_{73}$ (or $WO_{2.92}$) [51]. On the other hand, Fig. S3. 2 (ESI) shows the XPS spectra obtained for the commercial DTW5 catalyst. In this case, one can observe the characteristic $Ti2p_{3/2}$, $Ti2p_{1/2}$ and O1s bands of TiO_2 [52,53] as well as also those attributed to W^{6+} and W^{5+}, with a similar W^{5+}/W^{6+} ratio as in the previous case (i.e., 0.16). However, it must be noted the much lower surface tungsten concentration in this sample, 0.9 at.% W, with respect to that in pure WO_3, 22.1 at.% W. Besides, the similar or even higher actual content of W on the surface of DTW5 with respect to its nominal value (c.a. 0.4 at.%) agrees with the assumption of the likely arrangement of WO_3 as particles dispersed on the surface of anatase, as opposed to pure WO_3 catalyst, where the determined surface content of W is consistent with its nominal bulk concentration (i.e., 25.0 at.%). The presence of sub-stoichiometric WO_{3-x} on the surface will likely play a key role in the PEC performance of these materials for the selective glycerol photo(electro)oxidation. In addition, the surface oxygen defects are supposed to benefit the reaction kinetics thanks to the enhancement of the adsorption capability of reactant molecules onto the surface of catalysts [54].

The structure of WO_3 and DTW5 catalysts has also been investigated by Raman spectroscopy (Fig. S3. 3, (ESI)). In the first catalyst, one can observe the main peak at c.a. 800 cm^{-1}, attributed to the ν (W–O–W) stretching of the monoclinic phase, along with all other characteristic peaks of WO_3 [55]. Instead, the WO_3/TiO_2 catalyst shows the four bands attributed to anatase (146, 395, 516 and 639 cm^{-1}) [56], whereas a very weak band of WO_3 can be also observed at 797 cm^{-1} (see the inset in Fig. S3. 3 (ESI)). Thus, the amount of oxygen vacancies linked to the WO_3 phase is expected to be much more significant in the pure monoclinic WO_3 catalyst than in commercial DTW5. Besides, given the broadening and left-shifting of the peaks observed in the uncalcined pseudo-amorphous WO_3 catalyst, one could hypothesize that the amount of oxygen vacancies is even higher in this latter case [57]. A similar trend in terms of oxygen defects can be deduced by Electron Paramagnetic Resonance (EPR) (Fig. S3. 4 (ESI)). Given that the signal at g-factor of 2.002-2.005, which is typically attributed to the presence of electrons trapped in oxygen vacancies [34,58], is present in all

samples, it can be attributed to WO_3 rather than to TiO_2. Besides, despite the likely higher amount of oxygen vacancies and W^{5+} (signal at g = 1.82) on the uncalcined WO_3 in dark conditions, its signals are unaltered upon irradiation, while those of DTW5 and calcined monoclinic WO_3 evidenced the photogeneration of electrons or holes in these catalysts. These results suggest the likely detrimental effect of an excessive amount of oxygen vacancies and explains low photocurrents reported in our previous work with pseudo-amorphous WO_3 [38]. Diffuse reflectance spectroscopy (DRS) of samples was performed in the UV-Vis range, as shown in Fig. 3. 3a. Both DTW5 and WO_3 catalysts could absorb UV light, while the latter could expand its response range to photoirradiation with visible light at a wavelength close to 500 nm. Tauc plots for bandgap calculations using the Kubelka–Munk equation are shown in Fig. 3. 3b, where the extrapolation of the linear part of the curve $(\alpha \cdot h\nu)^{1/2}$ (α: absorption coefficient) as a function of $h\nu$ determines the optical bandgap energy of these semiconductor catalysts [59]. The measured bandgap of DTW5 of 3.28 eV can be explained according to its main component, i.e. anatase, which generally shows an indirect bandgap of 3.2 eV [60]. However, for monoclinic WO_3, the obtained bandgap is 2.66 eV, which is much narrower than in the case of DTW5 and among the lowest values found in WO_3-based photoelectrocatalysts (2.6-3.0 eV) [34,38,44]. The low bandgap and thus the wide light harvesting of the WO_3 catalyst is likely linked to the important presence of oxygen vacancies in this material, in agreement with some previous studies on WO_3 semiconductors [44,61]. Given that both DTW5 and WO_3 catalysts are sensitive to UV light, a LED UV lamp was used in all PC and PEC measurements.

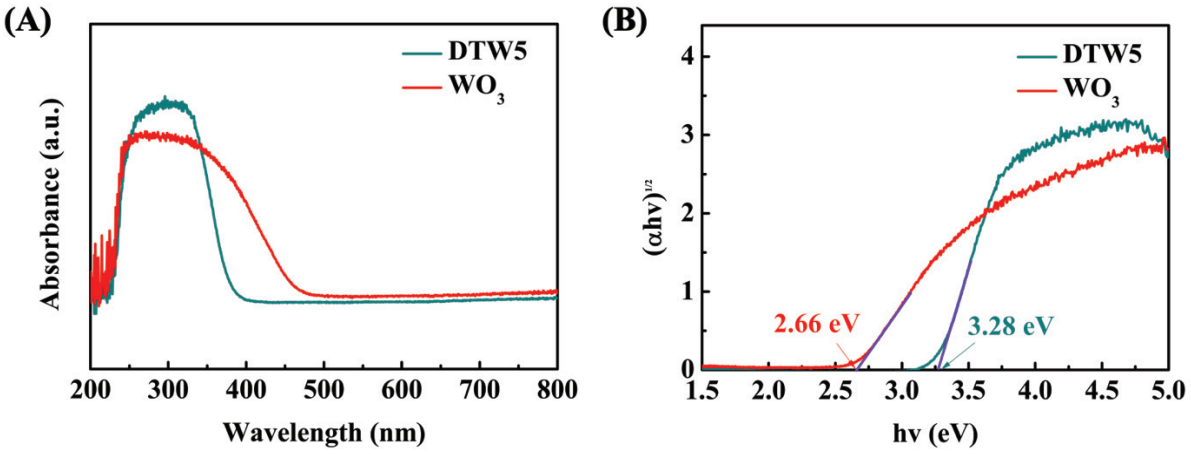

Fig. 3. 3. (a) UV-Vis diffuse reflectance spectroscopy (DRS) spectra and (b) Tauc plot for band gap determination for commercial DTW5 and as-prepared WO_3.

Catalyst acidity was proven to play a key role in the increase in selectivity of C_3 products from glycerol oxidation [38], due to the activation of the C-O bond and enhanced desorption of the target chemical [62,63]. Acidity measurements have also been carried out in this work by pyridine chemisorption. Fig. S3. 5 (ESI) depicts the DRIFT spectra obtained for DTW5 and WO_3 catalysts and Table S3. 1 (ESI) shows the acid sites quantification. Although the calcination of the WO_3 catalyst removed part of the adsorbed OH groups and caused a decrease in the acidity, the resultant Brönsted and total acidity of homemade WO_3 remains similar to that of DTW5 and much higher than that of other TiO_2-based catalysts [38], where Lewis and Brönsted acid sites can be generically ascribed to the surface Ti^{4+} species and to the WO_3 clusters, respectively [64].

To summarize this section, calcined WO_3 exhibits a monoclinic phase while the commercial DTW5 catalyst shows a structure close to anatase in the bulk (by XRD, Raman spectroscopy and EPR) and the presence of low amounts of WO_3 just on the surface (by XPS and pyridine-DRIFT). Accordingly, with respect to DTW5, the WO_3 catalyst shows a similar acidity whereas it seems to present a wider light response and a likely higher overall amount of sub-stoichiometric WO_{3-x} (i.e., of oxygen vacancies).

3.2 Electrochemical characterization

Upon light irradiation (*hν*) on a semiconductor like WO_3 or DTW5, electrons are excited to the conduction band (CB), leaving an equal number of holes (h^+) in the valence band (VB) (reaction (1)). Then, a part of these holes diffuses to the WO_3 or WO_3/TiO_2 surface and participate in the PC oxidation of glycerol/water, and another part is lost by fast recombination with the electrons.

$$\text{Catalyst} + h\nu \rightarrow \text{Catalyst}(e^-_{CB}) + \text{Catalyst}(h^+_{VB}) \quad (1)$$

In order to evaluate the separation efficiency of photo-generated carriers in DTW5 and WO_3 catalysts, transient photocurrent response and cyclic voltammetry measurements were performed. Generally, the higher the current intensity obtained upon illumination, the better the separation rate of carriers, i.e., electrons and holes, thus the lower their recombination rate and the more efficient the PC/PEC oxidation performance. Transient photocurrent response tests were conducted with both catalysts in nearly neutral media (0.5 M Na_2SO_4, pH 5.5), in the presence (Fig. 3. 4a and b) and in the absence (Fig. S3. 6a and b (ESI)) of 0.1 M glycerol. In all cases, one can observe that the obtained current density is weak in every interval under dark conditions, which anticipates that the purely electrocatalytic activity of both catalysts is almost negligible. However, every time that the light is switched on, photocurrent is sharply

generated with values up to 150-800 μA cm^{-2}, depending on the catalyst and on the applied potential, and it is stable for several cycles. The overall photocurrent intensity obtained in the mixed solution (0.5 M Na_2SO_4 and 0.1 M glycerol) on both DTW5 (Fig. 3. 4a) and WO_3 (Fig. 3. 4b) is higher than that obtained in the absence of glycerol (Fig. S3. 6a and b (ESI)). In this latter case, the obtained current density is attributed to the PEC water oxidation while, in the former case, it is also due to the PEC oxidation of glycerol, which acts as highly efficient hole scavenger to prevent the recombination of electron-hole pairs [65,66]. For instance, Huang et al. found a remarkable cathodic shift of the onset potential for oxygen evolution reaction (OER) on $BiVO_4$, after glycerol was introduced into the PEC system [67].

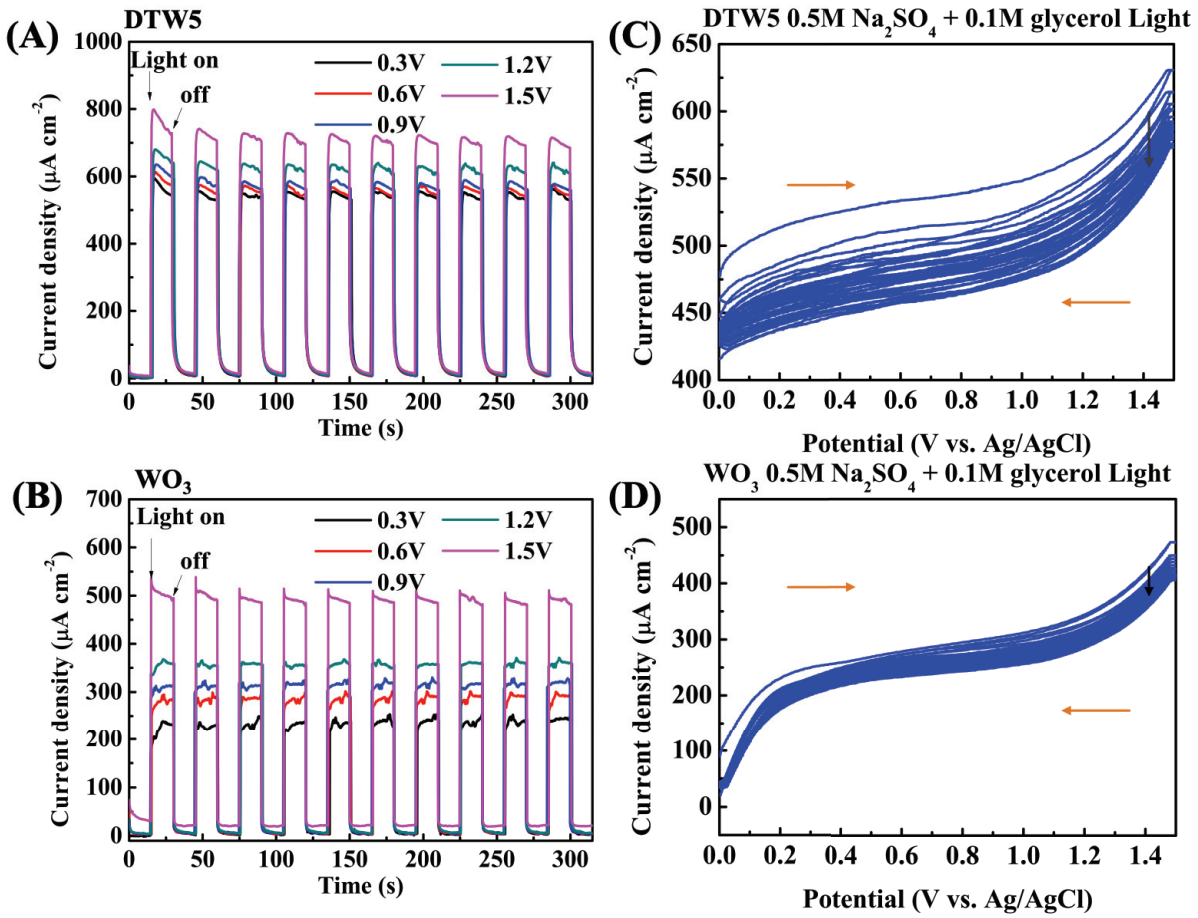

Fig. 3. 4. (a, b) Transient photocurrent response at different applied cell voltages (i.e., 0.3, 0.6, 0.9, 1.2, 1.5 V vs. Ag/AgCl) and (c, d) cyclic voltammetry under light irradiation (20 mV s^{-1}, 10 cycles) on commercial DTW5 and as-prepared WO_3 catalysts supported on ITO glass (working electrode). Pt wire was used as counter electrode. Conditions: neutral reaction media (0.5 M Na_2SO_4 and 0.1 M glycerol).

DTW5 performs with relatively higher photocurrent intensity than WO_3, especially at low applied potentials in the presence of glycerol (Fig. 3. 4a and b), which denotes that the carriers

generated in DTW5 are more difficult to be recombined than in pure WO_3. Composition differences aside, the obtained photocurrents likely depend on the morphological and textural properties of the catalysts [55,68,69] which are certainly different in DTW5 and WO_3, as previously discussed (i.e., lower particle size and higher surface area for DTW5). However, whilst the photocurrent density obtained in a previous study with pseudo-amorphous WO_3 in 0.5 M Na_2SO_4 was negligible with respect to that of DTW5 [38], those obtained herein with monoclinic WO_3 and DTW5 catalysts are comparable, or even superior for WO_3 upon 1.5 V (Fig. S3. 6 (ESI)). Some studies have directly correlated the different photocurrents on WO_3 catalysts with their crystallinity [43] and their amount of oxygen vacancies [44,70]. For example, Wei et al. showed that WO_3 with defects in its structure could generate more electron trapping states during the PC process, which greatly inhibited the direct recombination of photogenerated carriers resulting in the enhancement of PC oxygen evolution performance [71]. However, the role of oxygen vacancies is still under debate because some authors warn that these defects may also deteriorate the carrier mobility and act as recombination sites for e^- and h^+, thus decreasing the PEC performance of the semiconductors [61,72,73]. In other study using WO_3 photoanodes, Corby et al. [74] showed that oxygen vacancies can actually help to form trap sites and to promote the separation of photogenerated electrons and holes, but the proper amount of oxygen defects seems to be the key point. A moderate oxygen vacancy concentration related to a W^{5+}/W^{6+} ratio between 0.1 and 0.2 exhibited the best performance for PEC water oxidation [74]. Thus, it is reasonable that the calcined WO_3, with good crystallinity and oxygen vacancies concentration in this range (i.e., W^{5+}/W^{6+} ratio of 0.18) possesses enhanced photocurrent performance compared to the pseudo-amorphous WO_3. Regarding the influence of the applied potential in the generated photocurrent, the increase from 0.3 to 1.5 V vs. Ag/AgCl in Fig. 3. 4a, b and Fig. S3. 6 (ESI) leads to higher photocurrents with both DTW5 and WO_3 catalysts, which can be attributed to an accelerated charge transfer and, thus, an enhanced separation of electrons and holes [1,2]. Besides, it can be noticed a stronger influence of the applied potential on WO_3 and a particularly strong enhancement of photocurrent density at a potential above 1.2 V vs. Ag/AgCl, which can be well explained on the basis the cyclic voltammetry (CV) results.

All CVs performed without any illumination show negligible activities of both catalysts in either glycerol (Fig. S3. 7a and b) or water (Fig. S3. 7c and d) electrooxidation, i.e., by purely electrocatalytic (EC) route, at least, in the studied potential range of 0-1.5 V vs. Ag/AgCl. Indeed, the onset oxidation potential found in all these cases is as high as 1.3-1.4 vs. Ag/AgCl, which corresponds to 1.8-1.9 V vs. reversible hydrogen electrode (RHE). The main features

that can be observed on WO_3 in dark conditions are a cathodic and an anodic peak at potentials below 0.3 V vs. Ag/AgCl, which are derived from the reduction/oxidation of the redox couple W^{5+}/W^{6+} detected by XPS and, most likely, from the intercalation/de-intercalation of cations in the WO_3 network (i.e., H^+ or Na^+ from the electrolyte) [51,75,76]. On the contrary, upon UV irradiation, both materials are active for the PEC oxidation of glycerol (Fig. 3. 4c and d) and water (Fig. S3. 8a and b). In agreement with the above discussion, the generated photocurrents increase with the potential and are far above those obtained under purely EC conditions, in the whole studied potential range. The glycerol oxidation onset potential seems to be below 0 V vs. Ag/AgCl (i.e., below 0.5 V vs. RHE) with both DTW5 and WO_3 catalysts and the obtained currents are slightly higher in the former case, as expected from the previous transient photocurrent tests. However, WO_3 is more active than DTW5 for PEC water oxidation (Fig. S3. 8 (ESI)). The higher amount of oxygen vacancies in the former would favor the dissociation of H_2O molecule and the overall performance of the PEC OER process, which is typically divided into reactions (2-4) [77–79].

$$H_2O + h^+_{VB} \rightarrow H^+ + OH^* \quad (2)$$

$$OH^* + h^+_{VB} \rightarrow H^+ + O^* \quad (3)$$

$$O^* + H_2O + 2h^+_{VB} \rightarrow 2H^+ + O_2 \quad (4)$$

The influence of water oxidation reaction in the overall PEC glycerol oxidation process is especially evident at high applied potentials. A turning point takes place at 1.0-1.2 V vs. Ag/AgCl in the voltammograms from Fig. 3. 4c and d, which is attributed to the competition between PEC reactions, glycerol oxidation and OER. Thus, the electrochemical results prove that the triggering factor for the PEC glycerol oxidation is the light irradiation. The application of external bias helps separate the photogenerated carriers leading to higher photocurrents and, with respect to the commercial WO_3/TiO_2 catalyst, the homemade WO_3 generates slightly lower currents in the PEC glycerol oxidation, but higher ones in the PEC water oxidation.

3.3 PC/PEC valorization of glycerol

The same photoelectrochemical cell was used for carrying out experiments of photocatalytic (PC)/photoelectrocatalytic (PEC) glycerol oxidation with both catalysts. We focused on the liquid products and, especially, on glyceraldehyde and dihydroxyacetone (DHA) due to their higher industrial interest. Fig. 3. 5 shows the evolution of the concentration of the products detected in the electrolyte solution during these tests with the homemade WO_3 catalyst, while Fig. S9 (ESI) shows the results obtained with the commercial WO_3/TiO_2 catalyst. One can observe that the light irradiation without any applied potential (Fig. 3. 5a and S3. 9a (ESI))

immediately drives the glycerol oxidation on both catalysts, proving their PC activities, as expected in view of our previous work [38]. Under these PC conditions, glycerol is selectively oxidized to glyceraldehyde on both catalysts, along with lower amounts of dihydroxyacetone (DHA), formic acid, oxalic acid and tartronic acid (Reactions (5-8)).

$$C_3H_8O_3 + 2h^+_{VB} \rightarrow 2H^+ + C_3H_6O_3 \text{ (glyceraldehyde/DHA)} \quad (5)$$

$$C_3H_8O_3 + 2H_2O + 8h^+_{VB} \rightarrow 8H^+ + C_3H_4O_5 \text{ (tartronic acid)} \quad (6)$$

$$2C_3H_8O_3 + 6H_2O + 22h^+_{VB} \rightarrow 22H^+ + 3C_2H_2O_4 \text{ (oxalic acid)} \quad (7)$$

$$C_3H_8O_3 + 3H_2O + 8h^+_{VB} \rightarrow 8H^+ + 3CH_2O_2 \text{ (formic acid)} \quad (8)$$

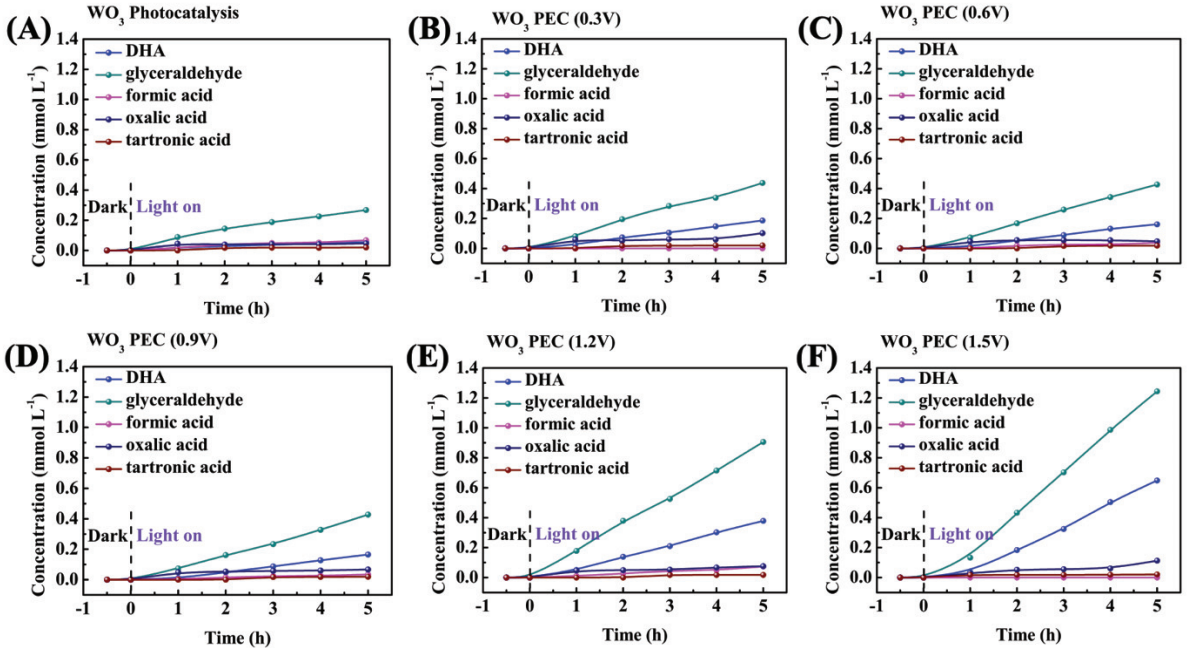

Fig. 3. 5. Evolution of liquid products concentration in the cell with time during (a) photocatalytic and (b-f) photoelectrocatalytic oxidation of glycerol on WO_3 catalyst. Reaction conditions: Room temperature; glycerol initial concentration: 0.1 M; Na_2SO_4 concentration: 0.5 M; UV irradiation intensity: 350 mW cm^{-2}.

The main difference, in terms of product distribution, is found under PEC conditions (Fig. 3. 5b-f, and S9b-f (ESI)). On DTW5, formic acid becomes the main obtained product in the potential range of 0.3-1.2 V vs. Ag/AgCl, likely owing to the presence of TiO_2 as the main component of the catalyst, which previously showed to further oxidize initial C_3 products to C_1 products, such as formic acid and CO_2 [38]. However, WO_3 can selectively produce glyceraldehyde and DHA under all explored PEC conditions, with the preferential oxidation of the primary alcohol group. In these figures, it is generally observed that the concentration of the target C_3 products (i.e., glyceraldehyde and DHA) reaches much higher values during PEC

glycerol oxidation than during the first PC process, which could be attributed to the enhanced separation rate of photogenerated carriers by the external voltages. The higher the applied potential, the slower the e^-/h^+ recombination rate and the more the holes available for glycerol oxidation. Thus, despite the poor activity shown by these anodes under purely electrocatalytic (EC) conditions (see, for instance, the negligible production of glyceraldehyde by EC at 1.2 V vs. Ag/AgCl in Fig. S3. 10 (ESI)), these results illustrate the essential role of the external applied potential in the overall PEC process to overcome the PC glycerol valorization. Interestingly, the linear increase in C_3 products concentration in the cell with time denotes fairly constant production rates of these chemicals, even at higher potentials, i.e., 1.2 and 1.5 V vs. Ag/AgCl, where the PEC OER is also expected to take place. Furthermore, the enhancement of target C_3 molecules production by PEC, with respect to PC, is more pronounced on the homemade WO_3 catalyst than on DTW5.

To understand the different product distributions obtained with the two catalysts, it must be noted that glycerol photoelectrooxidation may take place through two main routes [80,81]: i) the direct reaction by photogenerated holes (reactions (5-8)), and ii) an indirect pathway, where glycerol or its derived molecules react with some oxidant species, for instance, adsorbed hydroxyl radicals generated from the PEC water oxidation process (reaction (2)), thus leading to the generic oxidation reaction (9).

$$OH^* + \text{Organic} \rightarrow \text{Oxidized product} \quad (9)$$

Among the two pathways, the indirect one is expected to lead to more oxidized reaction products, e.g., formic acid or CO_2, given the strong oxidizing character of the OH radicals. This is the reason why these species are typically used, for example, in electro- and photoelectrocatalytic processes for the removal (full oxidation) of organic pollutants [81,82], for which an OER onset potential as high as possible is preferable. In our case, it seems that the relatively higher PEC activity shown by WO_3 for water oxidation, compared to DTW5 (Fig. S3. 6 and S3. 8 (ESI)), likely favors the consumption of the adsorbed hydroxyl groups for the oxygen evolution, thus decreasing their availability for glycerol-derived molecules oxidation and then increasing the selectivity to C_3 products (Fig. 3. 5). On the opposite, the lower OER activity of the commercial WO_3/TiO_2 catalyst could promote the hydroxyl-mediated glycerol oxidation, explaining its high production rate of formic acid (Fig. S3. 9 (ESI)) at low cell voltages. As expected, the application of a high enough potential (e.g., 1.5 V vs. Ag/AgCl) slows down the production of C_2 and C_1 chemicals and boosts the production of C_3 together with the very likely formation of CO_2, as OH radicals are consumed by OER upon those polarizations.

In order to deeper evaluate the potential of these catalysts for the selective glycerol valorization to glyceraldehyde and dihydroxyacetone, the influence of the operation conditions on the yield and liquid selectivity values, after 5 hours test, has been investigated (Fig. 3. 6). The corresponding values obtained for the other liquid products can be observed in Fig. S3. 11 (ESI). It must be noted that, for both catalysts, a glycerol conversion below 2% was roughly estimated. In spite of the low % yield values reached in Fig.3. 6a and b, i.e., lower than 1% of glyceraldehyde, one can clearly observe that the PEC glycerol oxidation outperforms the purely PC process. For instance, in the potential range of 0.3 to 0.9 V vs. Ag/AgCl, the glyceraldehyde yield is enhanced by c.a. 1.6 times, with respect to PC conditions, on both DTW5 and WO_3, while the DHA yields increase by 1.1-2.4 and 2.9-3.3 times, respectively. Then, upon applying higher potentials, the production of both target compounds on WO_3 experiences a further improvement, with glyceraldehyde and DHA yield enhancements of 4.5 and 11.5 times, respectively, by PEC at 1.5 V vs. Ag/AgCl. Under the same conditions, these yields are increased by 4.2 and 6.7 times, respectively, on the commercial DTW5 catalyst. Thus, the obtained results confirm the higher improvement of the PEC performance on the homemade WO_3 with respect to DWT5 for the production of both target chemicals. This is particularly the case for DHA, given its sluggish PC production rate.

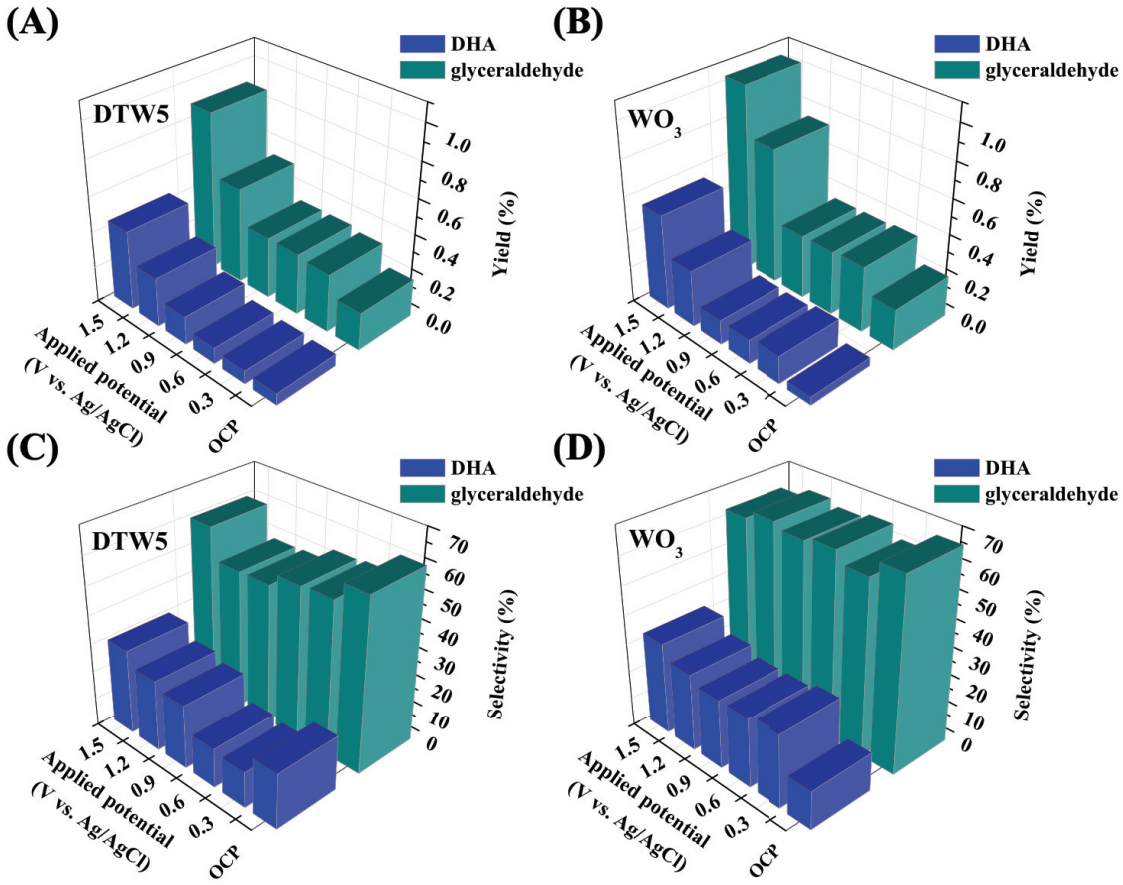

Fig. 3. 6. Variation of (a-b) the yield and (c-d) the liquid product selectivity of glyceraldehyde and DHA on DTW5 and WO_3 catalysts as a function of the applied potential during photoelectrocatalytic experiments after 5 h of operation in all cases. For comparison, the photocatalytic properties at open circuit potential (OCP) are also reported. Same reaction conditions as in Fig. 3. 5 and S3. 9.

The better PEC performance of WO_3 is also proven in terms of catalyst selectivity towards glyceraldehyde and DHA production, among all liquid products (Fig. 3. 6c and d). The commercial WO_3/TiO_2 catalyst shows a slight decrease of both product selectivities by PEC at low potentials, with respect to PC conditions, with minimum glyceraldehyde and DHA selectivity values of 49% (at 0.9 V vs. Ag/AgCl) and 12% (at 0.3 V vs. Ag/AgCl), respectively, and maximum values of 60% and 30% at 1.5 V vs. Ag/AgCl. However, in the case of homemade WO_3, the glyceraldehyde selectivity remains between 62 and 67%, regardless of the operation conditions, and DHA selectivity is more than twice as high, from 14% (PC conditions) to 32% (PEC at 1.5 v vs. Ag/AgCl). On the other hand, regarding formic acid selectivity, both catalysts show a very similar selectivity of c.a. 6% under purely PC conditions but, interestingly, under PEC conditions, DTW5 experiences an increase of this value up to a maximum of 23%, at 0.6 V vs. Ag/AgCl, while in the case of WO_3, formic acid selectivity decreases below 2% (Fig. S3. 11 (ESI)). The high selectivity of these catalysts for C_3 compounds and, specifically, for glyceraldehyde, is likely influenced by their strong acidity, which can enhance the desorption of these products from the catalyst surface, as previously reported on glycerol oxidation and dehydrogenation reactions [83,84]. Indeed, different TiO_2-based photocatalysts with lower acidity than these WO_3 and DTW5 catalysts obtained a lower glyceraldehyde selectivity in previous work [38]. Besides, the high selectivity towards primary C_3 products of WO_3 is also linked to its high activity for the PEC oxygen evolution, which could promote the direct glycerol oxidation mechanism, as previously discussed. The high selectivity towards glyceraldehyde and DHA production reached on the WO_3 catalyst also contrasts with the few published works on PEC glycerol oxidation under neutral or near-neutral operation conditions, where catalysts based on $BiVO_4$ [30,32] were rather selective to formic acid, with estimated glycerol conversion values ranging from 1% to 20%. In the case of DHA, one can find few cases where a higher selectivity (i.e., above 50%) was reached [30,31,35], but they were performed under strongly acidic conditions (i.e., pH 2), which are expected to suppress DHA over-oxidation. Regarding glyceraldehyde selectivity, the only study with comparable results is the one from Gu et al. [34], where an absolute selectivity for

glyceraldehyde+DHA of 88% was reached on WO_3/TiO_2, for a similar glycerol conversion of c.a. 2%, by using a microfluidic photoelectrochemical architecture with 3-D microchannels. In the present work, a joint selectivity for glyceraldehyde and DHA between 87% and 95% is obtained in the studied applied potential range although we did not consider the plausible gaseous side products like CO_2.

3.4 Evaluation of electron transfer efficiency

The electrochemical measurements provide another perspective to explain the activities of the PEC glycerol oxidation. Fig. 3. 7a and b show the current evolution with time in the chronoamperometry (CA) measurements performed during the PEC glycerol oxidation tests. It can be observed that the measured current density values are especially enhanced at potentials above 0.9 V vs. Ag/AgCl, which is in agreement with the transient photocurrent response (Fig. 3. 4a and b) and cyclic voltammetry (Fig. 3. 4c and d) measurements. This is due to the contribution of the photoelectrochemical oxidation of water at higher potentials. In general, both DTW5 and WO_3 catalysts show a sharp decrease of the current for the first seconds of each CA, due to the fast decay of capacitive current, followed by a progressive loss of current. PEC measurements did not significantly affect the structure and the crystallite size of the catalysts, as shown by XRD (Table S3. 2 (ESI)). Therefore, the current decrease can be ascribed to the glycerol consumption and/or to the catalyst deactivation, mostly by the accumulation of adsorbed reaction intermediates on the surface active sites. However, the most striking difference between the two electrodes is that even though DTW5 shows higher initial current densities than WO_3 in all cases, as it was also observed during the short transitions of Fig. 4a and b, interestingly, the latter catalyst shows a better stability that allows keeping higher current densities after 5 hours at 1.2 and 1.5 V vs. Ag/AgCl. This improved photostability could be attributed to the formation of sub-stoichiometric WO_{3-x}, since it is expected to be highly resistive to photocorrosion induced by peroxo-species generated during water oxidation, as previously reported [85]. Moreover, the hydroxyl and oxygen species generated during the photoelectrochemical water oxidation (reactions (2-3)) likely helped remove adsorbed intermediates and prevent the deactivation of both catalysts at increasing potentials, which is expected to affect WO_3 more, given its higher activity for OER (Fig. S3. 6 and S3. 8 (ESI)). For example, for the last 3 hours operating at 1.2 and 1.5 V vs. Ag/AgCl, the current obtained with DTW5 decreases in 27 and 30%, respectively, while the WO_3 catalyst losses only 10% of current in the former case and, at the highest potential, it even gains a 10% of activity.

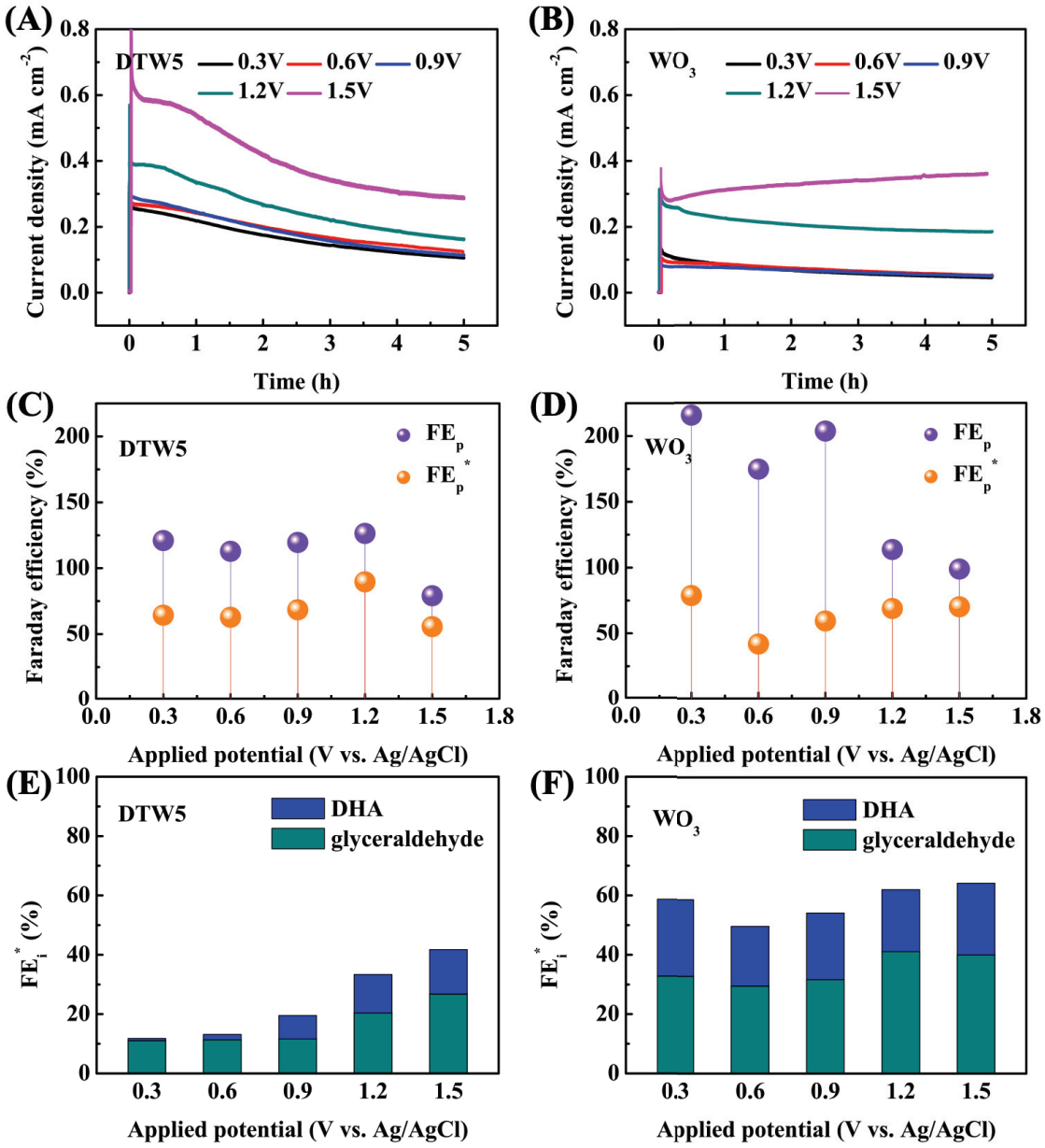

Fig. 3. 7. (a, b) Current density evolution with time during photoelectrocatalytic measurements performed at different applied potentials on DTW5 and WO_3 catalysts. (c, d) Faradaic efficiency (FE_p) and modified Faradaic efficiency (FE_p^*) of all liquid products and (e,f) FE_i^* values for the two main target products, after 5 h, on both catalysts. Same reaction conditions as in Fig. 3. 5 and S3. 9.

To better understand the mechanism of PEC glycerol valorization, Faradaic efficiency values have been calculated for each liquid product (FE_i) as well as for the sum of all of them (FE_p). These parameters allow correlating the overall amounts of obtained products during the PEC tests (Fig. 3. 5b-f and S3. 9b-f (ESI)) with the transferred electric charges obtained from the corresponding current vs. time curves (Fig. 3. 7a and b). Besides, modified Faradaic

efficiencies have also been calculated (FE_i^* and FE_p^*), after subtracting to the overall quantified PEC products the contribution from those quantities obtained by pure PC under analogous conditions. Fig. 3. 7c and d show both the overall PEC faradaic efficiency (FE_p) and the modified faradaic efficiency (FE_p^*) for the sum of liquid oxidation products, after 5 hours, on DTW5 and WO_3 catalysts, respectively. It can be observed that, under most operation conditions, the overall PEC faradaic efficiency values (FE_p) are well in excess of 100%, especially in the case of WO_3 catalyst, which is a sign of the important contribution of the purely PC reactions to the formation of liquid oxidation products from glycerol in these PEC processes. In the lower potential regime (i.e., 0.3-0.9 V vs. Ag/AgCl), the liquid products faradaic efficiency even reaches 200% on this catalyst, with a value between 113% and 124% for glyceraldehyde+DHA. This means a great yield-to-charge efficiency, even if the glycerol valorization, in absolute terms, is very low under these conditions, as it was observed in Fig. 3. 6b.

Then, by considering the modified faradaic efficiencies for liquid products (FE_p^*), i.e., after subtracting, in each case, the product quantities hypothetically obtained via pure PC, we can gain insight into the PEC performance improvement attributed to the charge transfer under external bias. This analytical approach is totally innovative since the PEC studies on glycerol oxidation cited in the introduction did not even perform purely PC (blank) measurements to know the performance obtained by those materials in the absence of external bias. The FE_p^* parameter obtained for DTW5 catalyst is stable at 63-70% in the potential range from 0.3 to 0.9 V vs. Ag/AgCl, and increases up to 90 % at an optimum potential of 1.2 V, to finally decrease to 56% upon further increasing the potential to 1.5 V vs. Ag/AgCl. On the other hand, in the case of homemade WO_3 catalyst, the modified faradaic efficiency for liquid products reaches a maximum value of 78% at the lowest applied potential, i.e., 0.3 V vs. Ag/AgCl, then it decreases to 41% at 0.6 V and it finally stabilizes at 69-70% at 1.2-1.5 V vs. Ag/AgCl. After jointly analyzing the two types of faradaic efficiency parameters shown in Fig. 3. 7d for WO_3, one can suggest that, upon increasing the applied potential, the overall faradaic efficiency of the PEC glycerol valorization and the specific contribution from the purely PC process, are strongly altered by competing side reactions like the over-oxidation of glycerol-derived chemicals to molecules not considered herein (e.g., CO_2) and, most likely, the oxygen evolution from water. However, the fact of obtaining fairly stable values of the modified faradaic efficiency indicates that, under PEC conditions, additional available holes can be efficiently valorized for the formation of liquid products from glycerol oxidation, even at the highest applied potentials.

Fig. 3. 7e and f show the individual modified faradaic efficiency values (FE_i^*) obtained with both catalysts for the main glycerol valorization products, i.e., glyceraldehyde and dihydroxyacetone. The corresponding FE_i^* values estimated for the other detected liquid products are also shown in Fig. S3. 12a and b (ESI). It can be clearly observed that, in the overall studied potential range, WO_3 presents significantly higher and less potential-dependent FE^* values for glyceraldehyde (30-41%) and DHA (20-26%) than DTW5 (11%-27% for glyceraldehyde and 1-15% for DHA). This can be explained, at least in part, on the basis of its higher activity towards OER, which hinders the OH-mediated glycerol oxidation pathway, thus avoiding further oxidation reactions to C_2 or C_1 compounds. Indeed, in the case of WO_3, the joint FE^* values for glyceraldehyde+DHA are much closer to those estimated for the overall liquid products (FE_p^*) than in the case of DTW5, where formic acid is also produced in a high extent. Beyond this, by analyzing the influence of the applied potential on all the individual PC-subtracted faradaic efficiency (FE^*) values (Fig. 3. 7e, f and S12 (ESI)), one can observe that: i) the faradaic efficiency of the additional holes, generated under PEC conditions, for glyceraldehyde and DHA generally increases on both catalysts with the applied potential (Fig. 3. 7e and f), proving that the strongest improvement of the performance for PEC glycerol valorization, per unit of charge transferred, is achieved under OER conditions; and ii) the corresponding FE^* values for formic acid do not increase but decrease with the external polarization, i.e., from 44% to 11% at 0.3 and 1.5 V vs. Ag/AgCl, respectively, on WO_3/TiO_2, and formic acid production was even lower under PEC conditions (vs. PC) in the case of WO_3 catalyst (Fig. S3. 12 (ESI)). All these insights demonstrate the promoting effect of water oxidation reaction at increasing potentials on the glycerol oxidation mechanism and, thus, on the product selectivity. Finally, it is also interesting to analyze the time evolution of the different faradaic efficiency parameters during PEC glycerol oxidation (Fig. S3. 13 (ESI)). The overall PEC faradaic efficiencies, FE_p, as well as the individual glyceraldehyde and DHA FE values are rather stable during the 5-hour tests performed on both catalysts. However, the modified FE^* values (i.e., PC-subtracted) generally increase with time, which is especially pronounced in the case of WO_3 catalyst. This indicates that the impact of PC processes diminishes with time.

3.5 Mechanism for photoelectrocatalytic glycerol valorization

According to the above analysis, we propose a reaction mechanism (Scheme 3. 1) for the selective PEC oxidation of glycerol on WO_3 catalyst, mainly focusing in four key points: i) the light irradiation as initiator; ii) the effect of the external electrical polarization; iii) the role of

surface oxygen vacancies; and iv) the influence of the catalyst activity for water electrooxidation.

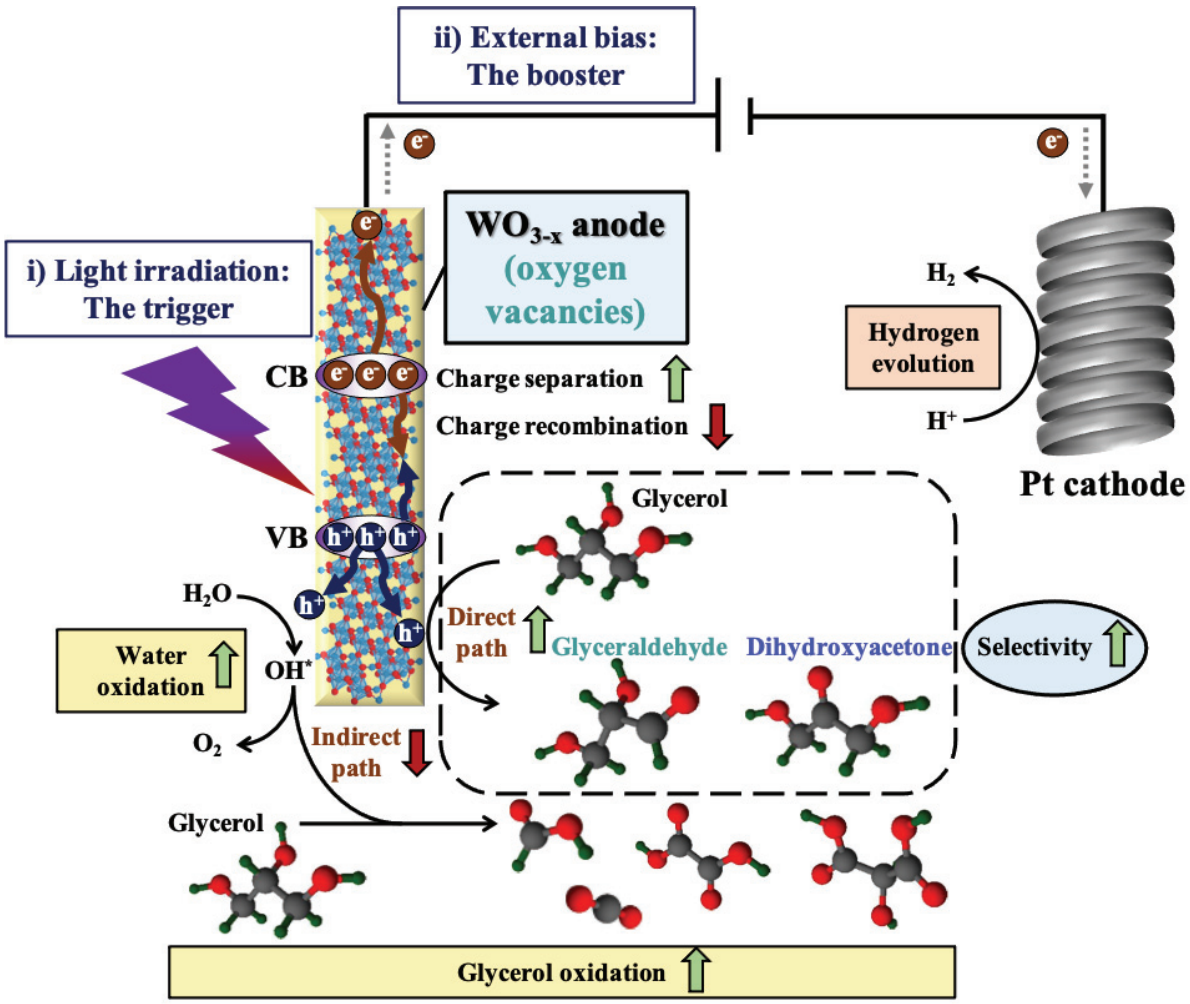

Scheme 3. 1. Mechanism of photoelectrocatalytic glycerol valorization to high value-added chemicals and simultaneous hydrogen production using WO_3 catalyst under mild conditions.

In first place, the results obtained from chronoamperometry (CA) and cyclic voltammetry (CV) measurements undoubtedly prove that, in the studied potential range (potential < 1.5 V vs. Ag/AgCl), WO_3 is inactive for glycerol oxidation by purely electrocatalytic (EC) means, and photocatalysis (PC) is the basis of the reaction, since illumination is an indispensable trigger. Indeed, WO_3 is a promising photocatalyst for selective glycerol oxidation to glyceraldehyde, even in the absence of any electric polarization. When light is irradiated with a photonic energy at least as high as the band gap of the catalyst, electron (e^-)/hole (h^+) pairs are generated in the bulk and the formers are excited from the valence band (VB) to the conduction band (CB), leaving an equal number of holes (reaction (1)). In this regard, one of the strengths of this catalyst is its low band gap, of only 2.66 eV, which provides a wide light gathering, allowing

to operate with UV light (from 3 to over 100 eV), like in this work, but also with part of visible light (2-2.75 eV). Instead, with the other catalyst tested in this work, i.e., WO_3(5 wt.%)/TiO_2, with a band gap of 3.28 eV, the latter option would not be possible. Then, under conventional PC conditions (with light irradiation as the only driving force), e^- and h^+ migrate to the catalyst surface and the former participate in the hydrogen evolution reaction (HER, reaction (10)) while the latter are involved either in glycerol oxidation (e.g., reactions (5-8)) or in water dissociation to form hydroxyl radicals (reaction (2)) which, in turn, may either lead to oxygen evolution (reactions (3-4)) or participate in the oxidation of glycerol or derived organic molecules (reaction (9)). Unfortunately, a part of the photogenerated holes and electrons are often rapidly lost by their recombination, generating either heat or photoluminescence. Then, in the PEC configuration, i.e., by introducing an external bias, the performance of both WO_3 and DTW5 catalysts is enhanced, because the transfer of electrons to the Pt cathode (where HER takes place) helps the charge carriers separation at the anode, decreasing their recombination rate. In other words, by PEC, additional holes become available for oxidation reactions. Then, the higher the applied potential, the more accelerated the charge transfer and the higher the generated photocurrent density.

$$2H^+ + 2e^-_{CB} \rightarrow H_2 \quad (10)$$

The glycerol oxidation photocurrents obtained with WO_3 are slightly lower than those obtained with the commercial DTW5, at least for short operation times. This is likely influenced by some convenient morphological properties, like a smaller average grain size (25 nm vs. 59 nm on WO_3) and a higher BET surface area (78 $m^2\ g^{-1}$ vs. 20 $m^2\ g^{-1}$ on WO_3). However, for longer operation times, the homemade WO_3 catalyst displays higher and more stable photocurrents. In this sense, the presence of sub-stoichiometric WO_{3-x} and of certain amount of oxygen defects on the catalyst surface, in greater quantity than DTW5, seems to play a key role. These oxygen vacancies could act as electron trapping sites, thus improving the charge carriers separation, the light response, as previously mentioned, and the electrical conductivity of the catalyst. The promising photocurrent densities obtained in this work contrast with those previously reported with a pseudo-amorphous WO_3 catalyst synthesized without any calcination step, even if the latter presented much higher amount of oxygen vacancies. The particular behavior of the WO_3 catalyst proposed herein likely arises from the superior crystallinity achieved and the presence of a moderate amount of oxygen defects, related to a W^{5+}/W^{6+} ratio of 0.18 while, in the case of the pseudo-amorphous WO_3 catalyst, the oxygen vacancies in excess could even behave as recombination centers and hinder the carriers mobility. Thus, although the beneficial properties of the homemade WO_3 affects its PC performance, they acquire a further relevance

upon the application of an external potential (i.e., in a PEC configuration). Finally, the outstanding selectivity of the WO_3 towards glyceraldehyde and dihydroxyacetone can be linked with its acidic properties and good activities for water PEC oxidation. Indeed, water dissociation and oxygen evolution reaction are known to be favored by the presence of oxygen vacancies, as confirmed by PEC tests performed in the absence of glycerol. Thus, beyond improving the overall PEC performance and stability of the catalyst, this feature is also likely responsible for the particularly high glyceraldehyde and DHA selectivities and the great usage of the additional holes generated by PEC in this work. This would also explain the big differences found between the proposed WO_3 catalyst and the commercial WO_3/TiO_2, in terms of selectivity. Among the two mechanisms for glycerol photoelectrooxidation mentioned above, the additional high activity of this WO_3 catalyst towards oxygen evolution reaction could hinder the availability of surface hydroxyl radicals for the indirect glycerol oxidation mechanism, and thus the production of C_2 and C_1 chemicals. In this way, the more selective, direct oxidation pathway to primary C_3 chemicals is favored on the WO_3 catalyst and is enhanced by increasing the applied potential.

4. Conclusions

We have investigated the photoelectrocatalytic (PEC) performance of a monoclinic WO_3 catalyst for glycerol valorization to high value-added chemicals achieving very promising results in terms of dihydroxyacetone (DHA) and, especially, glyceraldehyde selectivity under ambient conditions and near-neutral pH. With respect to a previously tested uncalcined WO_3 catalyst, the one synthesized herein by a simple hydrothermal method and calcined in air at 450 ^oC shows a much higher crystallinity and much better photogenerated current densities upon light irradiation. This catalyst also shows a wider light harvesting and a higher and more stable PEC activity for glycerol oxidation, in terms of generated current density and C_3 chemicals production, than a commercial DTW5 catalyst (WO_3(5 wt.%)/TiO_2) at potentials above 0.9 V vs. Ag/AgCl. On both materials, the PEC oxidation of glycerol shows to be triggered by the light irradiation and boosted by the application of an external bias, due to a more efficient charge carriers (h^+/e^-) separation, thus hindering their recombination and providing more holes available for glycerol (and water) oxidation. However, the presence of sub-stoichiometric WO_{3-x}, which in the case of DTW5 catalyst is likely limited to the outermost surface, and the corresponding amount of oxygen vacancies seem to be the key feature of the pure tungsten oxide catalyst. The presence of proper oxygen defects may explain the better light response, charge carrier separation and electrical conductivity. These characteristics are

likely responsible for the better WO_3 PEC activity for glycerol oxidation and also for the water oxidation reaction. Therefore, the selectivity towards C_3 products, already favored by the strong acidity of this catalyst, is further upgraded under PEC operation conditions by the OER influence. This can be explained by the lower availability of strongly oxidant OH species for the over-oxidation of glycerol or its derived products unlike, for instance, the commercial WO_3/TiO_2 catalyst, which shows a lower oxygen evolution activity and much higher formic acid selectivity. Besides, the proposed monoclinic WO_3 catalyst (actually $WO_{2.92}$) shows a joint selectivity for glyceraldehyde/DHA of 87-95%, among liquid products, that is nearly-stable (potential-independent) in the studied potential window of 0-1.5 V vs. Ag/AgCl (pH 5.5). Indeed, after carefully disclosing the quantitative liquid products obtained under purely PC conditions and those hypothetically derived from the assistance of the external polarization, we found that the additional active holes are employed for the C_3 selective production with an efficiency (50-64%) that is stable or even slightly increases with the applied potential. Thus, the obtained results show the great potential of this kind of WO_3 catalyst for the PEC valorization of glycerol, especially taking into account its wide margin of improvement in terms of overall performance. For example, by enhancing its morphological and textural characteristics (such as particle size, surface area, film thickness) or by using dopants that further improved the band edge positions, higher photocurrents and product yields could be expected, while maintaining such a high C_3 selectivity.

Acknowledgment

This work was financially supported by the China Scholarship Council (Grant No. 201906740016). The authors would like to thank L. Burel (HRTEM) P. Bargiela (XPS) and Y. Aizac (XRD) of IRCELYON. UCO researchers are thankful to MICINN, Spain, Grant Nr PID-2019-104953RB-100.

References

[1] R. Li, C. Li, Photocatalytic Water Splitting on Semiconductor-Based Photocatalysts, Adv. Catal. 60 (2017) 1–57.

[2] F. X. Xiao, J. Miao, H.B. Tao, S. F. Hung, H. Y. Wang, H. Bin Yang, J. Chen, R. Chen, B. Liu, One-dimensional hybrid nanostructures for heterogeneous photocatalysis and photoelectrocatalysis, Small. 11 (2015) 2115–2131.

[3] T. Yao, X. An, H. Han, J.Q. Chen, C. Li, Photoelectrocatalytic materials for solar water splitting, Adv. Energy Mater. 8 (2018) 1800210.

[4] M.S. Koo, X. Chen, K. Cho, T. An, W. Choi, In situ photoelectrochemical chloride

activation using a WO_3 electrode for oxidative treatment with simultaneous H_2 evolution under visible light, Environ. Sci. & Technol. 53 (2019) 9926–9936.

[5] H. Wang, Y. Liang, L. Liu, J. Hu, P. Wu, W. Cui, Enriched photoelectrocatalytic degradation and photoelectric performance of BiOI photoelectrode by coupling rGO, Appl. Catal. B Environ. 208 (2017) 22–34.

[6] L. Wang, N.T. Nguyen, X. Huang, P. Schmuki, Y. Bi, Hematite photoanodes: synergetic enhancement of light harvesting and charge management by sandwiched with Fe_2TiO_5/Fe_2O_3/Pt structures, Adv. Funct. Mater. 27 (2017) 1703527.

[7] Y. Zuo, Y. Liu, J. Li, R. Du, X. Yu, C. Xing, T. Zhang, L. Yao, J. Arbiol, J. Llorca, others, Solution-processed ultrathin SnS_2--Pt nanoplates for photoelectrochemical water oxidation, ACS Appl. Mater. & Interfaces. 11 (2019) 6918–6926. https://doi.org/10.1021/acsami.8b17622

[8] R.-T. Gao, S. Liu, X. Guo, R. Zhang, J. He, X. Liu, T. Nakajima, X. Zhang, L. Wang, Pt-Induced Defects Curing on $BiVO_4$ Photoanodes for Near-Threshold Charge Separation, Adv. Energy Mater. (2021) 2102384.

[9] Z. Yin, B. Chen, M. Bosman, X. Cao, J. Chen, B. Zheng, H. Zhang, Au nanoparticle-modified MoS_2 nanosheet-based photoelectrochemical cells for water splitting, Small. 10 (2014) 3537–3543.

[10] L. Wu, F. Li, Y. Xu, J.W. Zhang, D. Zhang, G. Li, H. Li, Plasmon-induced photoelectrocatalytic activity of Au nanoparticles enhanced TiO_2 nanotube arrays electrodes for environmental remediation, Appl. Catal. B Environ. 164 (2015) 217–224.

[11] C. Li, T. Wang, B. Liu, M. Chen, A. Li, G. Zhang, M. Du, H. Wang, S.F. Liu, J. Gong, Photoelectrochemical CO_2 reduction to adjustable syngas on grain-boundary-mediated a-Si/TiO_2/Au photocathodes with low onset potentials, Energy & Environ. Sci. 12 (2019) 923–928.

[12] T. Sharifi, T. Mohammadi, M.M. Momeni, H. Kusic, M.K. Rokovic, A.L. Bozic, Y. Ghayeb, Influence of photo-deposited Pt and Pd onto chromium doped TiO_2 nanotubes in photo-electrochemical water splitting for hydrogen generation, Catalysts. 11 (2021) 212.

[13] W. Liu, Q. Tian, J. Yang, Y. Zhou, H. Chang, W. Cui, Q. Xu, A Two-dimensional Amorphous Plasmonic Heterostructure of Pd/MoO_{3-x} for Enhanced Photoelectrochemical Water Splitting Performance, Chem. Asian J. 16 (2021) 1253–1257.

[14] J. He, M. Wang, X. Wu, Y. Sun, K. Huang, H. Chen, L. Gao, S. Feng, Influence of

controlled Pd nanoparticles decorated TiO_2 nanowire arrays for efficient photoelectrochemical water splitting, J. Alloys Compd. 785 (2019) 391–397.

[15] D. Welsby, J. Price, S. Pye, P. Ekins, Unextractable fossil fuels in a 1.5 C world, Nature. 597 (2021) 230–234.

[16] K. Fang, C. Li, Y. Tang, J. He, J. Song, China's pathways to peak carbon emissions: New insights from various industrial sectors, Appl. Energy. 306 (2022) 118039.

[17] J. Rogelj, D. Huppmann, V. Krey, K. Riahi, L. Clarke, M. Gidden, Z. Nicholls, M. Meinshausen, A new scenario logic for the Paris Agreement long-term temperature goal, Nature. 573 (2019) 357–363.

[18] A. Demirbas, Importance of biodiesel as transportation fuel, Energy Policy. 35 (2007)

[19] M. Checa, S. Nogales-Delgado, V. Montes, J.M. Encinar, Recent advances in glycerol catalytic valorization: A review, Catalysts. 10 (2020) 1279.

[20] R. Ciriminna, C. Della Pina, M. Rossi, M. Pagliaro, Understanding the glycerol market, Eur. J. Lipid Sci. Technol. 116 (2014) 1432–1439.

[21] G.M. Lari, C. Mondelli, S. Papadokonstantakis, M. Morales, K. Hungerbühler, J. Pérez-Ramírez, Environmental and economic assessment of glycerol oxidation to dihydroxyacetone over technical iron zeolite catalysts, React. Chem. & Eng. 1 (2016) 106–118.

[22] C. Liu, M. Hirohara, T. Maekawa, R. Chang, T. Hayashi, C.Y. Chiang, Selective electro-oxidation of glycerol to dihydroxyacetone by a non-precious electrocatalyst -CuO, Appl. Catal. B Environ. 265 (2020) 118543.

[23] G. Dodekatos, S. Schünemann, H. Tüysüz, Recent Advances in Thermo-, Photo-, and Electrocatalytic Glycerol Oxidation, ACS Catal. 8 (2018) 6301–6333.

[24] J. Liu, C. Fan, X. Xie, L. Jiang, Recent Progress on Photo-Promoted Alcohol Electrooxidation for Fuel Cells, Energy Technol. 9 (2021) 2000842.

[25] P.M. Walgode, R.P. V Faria, A.E. Rodrigues, A review of aerobic glycerol oxidation processes using heterogeneous catalysts: a sustainable pathway for the production of dihydroxyacetone, Catal. Rev. 63 (2021) 422–511.

[26] R. Beranek, Selectivity of Chemical Conversions: Do Light-Driven Photoelectrocatalytic Processes Hold Special Promise? Angew. Chemie. 131 (2019) 16878–16883.

[27] P. Song, H. Xu, J. Wang, Y. Zhang, F. Gao, F. Ren, Y. Shiraishi, C. Wang, Y. Du, Visible-light-driven trimetallic Pt-Ag-Ni alloy nanoparticles for efficient nanoelectrocatalytic oxidation of alcohols, J. Taiwan Inst. Chem. Eng. 93 (2018) 616–

624.

[28] Y. Sun, G. Han, L. Du, C. Du, X. Zhou, Q. Sun, Y. Gao, G. Yin, Y. Li, Y. Wang, Photoelectrochemistry-driven selective hydroxyl oxidation of polyols: Synergy between Au nanoparticles and C_3N_4 nanosheets, Chem Catal. (2021).

[29] M. Rasmussen, A. Serov, K. Artyushkova, D. Chen, T.C. Rose, P. Atanassov, J.M. Harris, S.D. Minteer, Enhancement of electrocatalytic oxidation of glycerol by plasmonics, ChemElectroChem. 6 (2019) 241–245.

[30] D. Liu, J.-C. Liu, W. Cai, J. Ma, H. Bin Yang, H. Xiao, J. Li, Y. Xiong, Y. Huang, B. Liu, Selective photoelectrochemical oxidation of glycerol to high value-added dihydroxyacetone, Nat. Commun. 10 (2019) 1–8.

[31] T.-G. Vo, C.-C. Kao, J.-L. Kuo, C. Chiu, C.-Y. Chiang, Unveiling the crystallographic facet dependence of the photoelectrochemical glycerol oxidation on bismuth vanadate, Appl. Catal. B Environ. 278 (2020) 119303.

[32] Y.-H. Wu, D.A. Kuznetsov, N.C. Pflug, A. Fedorov, C.R. Müller, Solar-driven valorisation of glycerol on $BiVO_4$ photoanodes: effect of co-catalyst and reaction media on reaction selectivity, J. Mater. Chem. A. 9 (2021) 6252–6260.

[33] D. Raptis, V. Dracopoulos, P. Lianos, Renewable energy production by photoelectrochemical oxidation of organic wastes using WO_3 photoanodes, J. Hazard. Mater. 333 (2017) 259–264.

[34] Z. Gu, X. An, R. Liu, L. Xiong, J. Tang, C. Hu, H. Liu, J. Qu, Interface-modulated nanojunction and microfluidic platform for photoelectrocatalytic chemicals upgrading, Appl. Catal. B Environ. 282 (2021) 119541.

[35] R. Tang, L. Wang, Z. Zhang, W. Yang, H. Xu, A. Kheradmand, Y. Jiang, R. Zheng, J. Huang, Fabrication of MOFs' derivatives assisted perovskite nanocrystal on TiO_2 photoanode for photoelectrochemical glycerol oxidation with simultaneous hydrogen production, Appl. Catal. B Environ. 296 (2021) 120382.

[36] Y. Lee, S. Kim, S.Y. Jeong, S. Seo, C. Kim, H. Yoon, H.W. Jang, S. Lee, Surface-modified Co-doped ZnO photoanode for photoelectrochemical oxidation of glycerol, Catal. Today. 359 (2021) 43–49.

[37] N. Perini, C. Hessel, J.L. Bott-Neto, C.T. Pires, P.S. Fernandez, E. Sitta, Photoelectrochemical oxidation of glycerol on hematite: thermal effects, in situ FTIR and long-term HPLC product analysis, J. Solid State Electrochem. 25 (2021) 1101–1110.

[38] J. Yu, F. Dappozze, J. Martín-Gomez, J. Hidalgo-Carrillo, A. Marinas, P. Vernoux, A. Caravaca, C. Guillard, Glyceraldehyde production by photocatalytic oxidation of

glycerol on WO_3-based materials, Appl. Catal. B Environ. 299 (2021) 120616.

[39] H. Gong, R. Ma, F. Mao, K. Liu, H. Cao, H. Yan, Light-induced spatial separation of charges toward different crystal facets of square-like WO_3, Chem. Commun. 52 (2016) 11979–11982.

[40] X. Yu, X. Fan, L. An, G. Liu, Z. Li, J. Liu, P. Hu, Mesocrystalline Ti^{3+} TiO_2 hybridized g-C_3N_4 for efficient visible-light photocatalysis, Carbon N. Y. 128 (2018) 21–30.

[41] J. Zhang, P. Zhang, T. Wang, J. Gong, Monoclinic WO_3 nanomultilayers with preferentially exposed (002) facets for photoelectrochemical water splitting, Nano Energy. 11 (2015) 189–195.

[42] W. Shi, X. Guo, C. Cui, K. Jiang, Z. Li, L. Qu, J.-C. Wang, Controllable synthesis of Cu_2O decorated WO_3 nanosheets with dominant (0 0 1) facets for photocatalytic CO_2 reduction under visible-light irradiation, Appl. Catal. B Environ. 243 (2019) 236–242.

[43] C. Ng, Y.H. Ng, A. Iwase, R. Amal, Influence of annealing temperature of WO_3 in photoelectrochemical conversion and energy storage for water splitting, ACS Appl. Mater. & Interfaces. 5 (2013) 5269–5275.

[44] A.K. Mohamedkhair, Q.A. Drmosh, M. Qamar, Z.H. Yamani, Tuning structural properties of WO_3 thin films for photoelectrocatalytic water oxidation, Catalysts. 11 (2021) 381.

[45] E. McCafferty, J.P. Wightman, Determination of the concentration of surface hydroxyl groups on metal oxide films by a quantitative XPS method, Surf. Interface Anal. An Int. J. Devoted to Dev. Appl. Tech. Anal. Surfaces, Interfaces Thin Film. 26 (1998) 549–564.

[46] J. Pouilleau, D. Devilliers, H. Groult, P. Marcus, Surface study of a titanium-based ceramic electrode material by X-ray photoelectron spectroscopy, J. Mater. Sci. 32 (1997) 5645–5651.

[47] K. Senthil, K. Yong, Growth and characterization of stoichiometric tungsten oxide nanorods by thermal evaporation and subsequent annealing, Nanotechnology. 18 (2007) 395604.

[48] F. Yang, F. Wang, Z. Guo, Characteristics of binary WO_3@CuO and ternary WO_3@PDA@CuO based on impressive sensing acetone odor, J. Colloid Interface Sci. 524 (2018) 32–41.

[49] G. Leftheriotis, S. Papaefthimiou, P. Yianoulis, A. Siokou, D. Kefalas, Structural and electrochemical properties of opaque sol--gel deposited WO_3 layers, Appl. Surf. Sci. 218 (2003) 276–281.

[50] M. Tong, J. Yang, Q. Jin, X. Zhang, J. Gao, G. Li, Facile preparation of amorphous carbon-coated tungsten trioxide containing oxygen vacancies as photocatalysts for dye degradation, J. Mater. Sci. 54 (2019) 10656–10669.

[51] P.A. Shinde, S.C. Jun, Review on recent progress in the development of tungsten oxide based electrodes for electrochemical energy storage, ChemSusChem. 13 (2020) 11–38.

[52] P. Stefanov, M. Shipochka, P. Stefchev, Z. Raicheva, V. Lazarova, L. Spassov, XPS characterization of TiO_2 layers deposited on quartz plates, in: J. Phys. Conf. Ser., 2008: p. 12039.

[53] R. Ji, D. Zheng, C. Zhou, J. Cheng, J. Yu, L. Li, Low-temperature preparation of tungsten oxide anode buffer layer via ultrasonic spray pyrolysis method for large-area organic solar cells, Materials (Basel). 10 (2017) 820.

[54] Q. Liu, F. Wang, H. Lin, Y. Xie, N. Tong, J. Lin, X. Zhang, Z. Zhang, X. Wang, Surface oxygen vacancy and defect engineering of WO_3 for improved visible light photocatalytic performance, Catal. Sci. & Technol. 8 (2018) 4399–4406.

[55] N. Wang, D. Wang, M. Li, J. Shi, C. Li, Photoelectrochemical water oxidation on photoanodes fabricated with hexagonal nanoflower and nanoblock WO_3, Nanoscale. 6 (2014) 2061–2066.

[56] W.F. Zhang, Y.L. He, M.S. Zhang, Z. Yin, Q. Chen, Raman scattering study on anatase TiO_2 nanocrystals, J. Phys. D. Appl. Phys. 33 (2000) 912–916.

[57] S. Chen, Y. Xiao, W. Xie, Y. Wang, Z. Hu, W. Zhang, H. Zhao, Facile strategy for synthesizing non-stoichiometric monoclinic structured tungsten trioxide (WO_{3-x}) with plasma resonance absorption and enhanced photocatalytic activity, Nanomater. . 8 (2018).

[58] Z. Shen, Z. Zhao, J. Wen, J. Qian, Z. Peng, X. Fu, Role of oxygen vacancies in the electrical properties of WO_{3-x} nano/microrods with identical morphology, J. Nanomater. 2018 (2018).

[59] N. Fessi, M.F. Nsib, L. Cardenas, C. Guillard, F. Dappozze, A. Houas, F. Parrino, L. Palmisano, G. Ledoux, D. Amans, Y. Chevalier, Surface and electronic features of fluorinated TiO_2 and their influence on the photocatalytic degradation of 1-methylnaphthalene, J. Phys. Chem. C. 124 (2020) 11456–11468.

[60] S. Mansingh, K.K. Das, A. Behera, S. Subudhi, S. Sultana, K. Parida, Bandgap engineering via boron and sulphur doped carbon modified anatase TiO_2: a visible light stimulated photocatalyst for photo-fixation of N_2 and TCH degradation, Nanoscale Adv. 2 (2020) 2004–2017.

[61] S.S. Kalanur, I.-H. Yoo, I.-S. Cho, H. Seo, Effect of oxygen vacancies on the band edge properties of WO_3 producing enhanced photocurrents, Electrochim. Acta. 296 (2019) 517–527.

[62] A.T. Marshall, R.G. Haverkamp, Production of hydrogen by the electrochemical reforming of glycerol--water solutions in a PEM electrolysis cell, Int. J. Hydrogen Energy. 33 (2008) 4649–4654.

[63] T. Aihara, H. Miura, T. Shishido, Investigation of the mechanism of the selective hydrogenolysis of CO bonds over a $Pt/WO_3/Al_2O_3$ catalyst, Catal. Today. 352 (2020) 73–79.

[64] F. Can, X. Courtois, D. Duprez, Tungsten-based catalysts for environmental applications, Catalysts. 11 (2021) 703.

[65] N. Fajrina, M. Tahir, A critical review in strategies to improve photocatalytic water splitting towards hydrogen production, Int. J. Hydrogen Energy. 44 (2019) 540–577.

[66] M. Ibadurrohman, K. Hellgardt, Photoelectrochemical performance of graphene-modified TiO_2 photoanodes in the presence of glycerol as a hole scavenger, Int. J. Hydrogen Energy. 39 (2014) 18204–18215.

[67] L.-W. Huang, T.-G. Vo, C.-Y. Chiang, Converting glycerol aqueous solution to hydrogen energy and dihydroxyacetone by the $BiVO_4$ photoelectrochemical cell, Electrochim. Acta. 322 (2019) 134725.

[68] Y. Zhao, S. Balasubramanyam, R. Sinha, R. Lavrijsen, M.A. Verheijen, A.A. Bol, A. Bieberle-Hu tter, Physical and chemical defects in WO_3 thin films and their impact on photoelectrochemical water splitting, ACS Appl. Energy Mater. 1 (2018) 5887–5895.

[69] R. Boddula, A.M. Asiri, others, Methods for electrocatalysis: Advanced materials and allied applications, Springer, 2020.

[70] Y. Liu, Y. Yang, Q. Liu, H. He, W. Liu, D. Meng, Y. Li, W. Li, J. Li, Films of WO_3 plate-like arrays with oxygen vacancies proportionally controlled via rapid chemical reduction, Int. J. Hydrogen Energy. 43 (2018) 208–218.

[71] Z. Wei, W. Wang, W. Li, X. Bai, J. Zhao, E.C.M. Tse, D.L. Phillips, Y. Zhu, Steering electron--hole migration pathways using oxygen vacancies in tungsten oxides to enhance their photocatalytic oxygen evolution performance, Angew. Chemie Int. Ed. 60 (2021) 8236–8242.

[72] L. Hao, H. Huang, Y. Zhang, T. Ma, Oxygen vacant semiconductor photocatalysts, Adv. Funct. Mater. 31 (2021) 2100919.

[73] F.M. Pesci, G. Wang, D.R. Klug, Y. Li, A.J. Cowan, Efficient suppression of electron-

-hole recombination in oxygen-deficient hydrogen-treated TiO_2 nanowires for photoelectrochemical water splitting, J. Phys. Chem. C. 117 (2013) 25837–25844.

[74] S. Corby, L. Francàs, A. Kafizas, J.R. Durrant, Determining the role of oxygen vacancies in the photoelectrocatalytic performance of WO_3 for water oxidation, Chem. Sci. 11 (2020) 2907–2914.

[75] S. Darmawi, S. Burkhardt, T. Leichtweiss, D.A. Weber, S. Wenzel, J. Janek, M.T. Elm, P.J. Klar, Correlation of electrochromic properties and oxidation states in nanocrystalline tungsten trioxide, Phys. Chem. Chem. Phys. 17 (2015) 15903–15911.

[76] S. Sfaelou, L.-C. Pop, O. Monfort, V. Dracopoulos, P. Lianos, Mesoporous WO_3 photoanodes for hydrogen production by water splitting and PhotoFuelCell operation, Int. J. Hydrogen Energy. 41 (2016) 5902–5907.

[77] M. Sun, C. Yuan, R.-T. Gao, R. Zhang, X. Liu, T. Nakajima, X. Zhang, Y. Su, L. Wang, A bridging coordination of urea tailoring metal hydroxides oxygen evolution catalysts promotes stable solar water splitting, Chem. Eng. J. 426 (2021) 131062.

[78] X. Pan, M. Q. Yang, X. Fu, N. Zhang, Y. J. Xu, Defective TiO_2 with oxygen vacancies: synthesis, properties and photocatalytic applications, Nanoscale. 5 (2013) 3601–3614.

[79] Y. Zhang, Z. Xu, G. Li, X. Huang, W. Hao, Y. Bi, Direct observation of oxygen vacancy self-healing on TiO_2 photocatalysts for solar water splitting, Angew. Chemie Int. Ed. 58 (2019) 14229–14233.

[80] H. Luo, J. Barrio, N. Sunny, A. Li, L. Steier, N. Shah, I.E.L. Stephens, M. M. Titirici, Progress and perspectives in photo-and electrochemical-oxidation of biomass for sustainable chemicals and hydrogen production, Adv. Energy Mater. 11 (2021) 2101180.

[81] E. Kusmierek, Semiconductor electrode materials applied in photoelectrocatalytic wastewater treatment-an overview, Catalysts. 10 (2020) 439.

[82] C. Bustillo-Lecompte, Advanced oxidation processes: applications, trends, and prospects, 2020.

[83] A. Villa, S. Campisi, K.M.H. Mohammed, N. Dimitratos, F. Vindigni, M. Manzoli, W. Jones, M. Bowker, G.J. Hutchings, L. Prati, Tailoring the selectivity of glycerol oxidation by tuning the acid-base properties of Au catalysts, Catal. Sci. & Technol. 5 (2015) 1126–1132.

[84] M. Velásquez, C. Batiot-Dupeyrat, J.F. Espinal, A. Sánchez, A. Santamar\'\ia, Mechanism of glycerol dehydration and dehydrogenation: an experimental and computational correlation, Dyna. 86 (2019) 126–135.

[85] G. Wang, Y. Ling, H. Wang, X. Yang, C. Wang, J.Z. Zhang, Y. Li, Hydrogen-treated

WO_3 nanoflakes show enhanced photostability, Energy & Environ. Sci. 5 (2012) 6180–6187.

Chapter 3

Electronic Supplementary Information

Section S1. Calculation of glycerol photoelectrocatalytic oxidation parameters.

Glycerol oxidation has been studied on WO_3-based catalysts through electrocatalytic (EC), photocatalytic (PC) and photoelectrocatalytic (PEC) processes, i.e., driven by electric bias, light irradiation of both, respectively. In the first case (EC), according to the liquid products experimentally detected, the following electrocatalytic reactions should be considered:

$C_3H_8O_3 \rightarrow 2H^+ + 2e^- + C_3H_6O_3$ (glyceraldehyde/DHA) (S1)

$C_3H_8O_3 + 2H_2O \rightarrow 8H^+ + 8e^- + C_3H_4O_5$ (tartronic acid) (S2)

$2C_3H_8O_3 + 6H_2O \rightarrow 22H^+ + 22e^- + 3C_2H_2O_4$ (oxalic acid) (S3)

$C_3H_8O_3 + 3H_2O \rightarrow 8H^+ + 8e^- + 3CH_2O_2$ (formic acid) (S4)

In the case of PC and PEC glycerol oxidation processes, analogous reactions to (1-4) can be considered, but driven by the excitation of electrons to the conduction band (CB) of the catalyst upon illumination (hv), thus leaving empty holes (h^+) in its valence band (VB) (reaction (S5)), which could be available for interacting with the glycerol molecules (reactions (S6-S9)).

$\text{Catalyst} + h\nu \rightarrow \text{Catalyst}(e^-_{CB}) + \text{Catalyst}(h^+_{VB})$ (S5)

$C_3H_8O_3 + 2h^+_{VB} \rightarrow 2H^+ + C_3H_6O_3$ (glyceraldehyde/DHA) (S6)

$C_3H_8O_3 + 2H_2O + 8h^+_{VB} \rightarrow 8H^+ + C_3H_4O_5$ (tartronic acid) (S7)

$2C_3H_8O_3 + 6H_2O + 22h^+_{VB} \rightarrow 22H^+ + 3C_2H_2O_4$ (oxalic acid) (S8)

$C_3H_8O_3 + 3H_2O + 8h^+_{VB} \rightarrow 8H^+ + 3CH_2O_2$ (formic acid) (S9)

The produced amount ($N_{t,i}$, in mmol) of each liquid product, i, at a given time, t, which is defined as an integer number of hours, was calculated from the concentration values quantified by HPLC, according to equation (S10):

$$N_{t,i} = V_t \times (C_{t,i} - C_{0,i}) + V_s \times \sum_{t=0}^{t-1}(C_{t,i} - C_{0,i}) \quad \text{(S10)}$$

where $C_{t,i}$ and $C_{0,i}$ (in mM) stand, respectively, for the concentration of the target product, i, in the cell at a given time and before the test starts (in principle, $C_{0,i} = 0$), V_t (in L) is the solution volume in the cell at sampling time, V_s is the sample volume (i.e., 6 x 10^{-4} L) and, thus, the

term $[V_s \times \sum_{t=0}^{t-1}(C_{t,i}\text{-}C_{0,i})]$ stands for the accumulated amount of product collected in previous samplings.

Then, the yield (in %) of each target product, *i*, was calculated at a given time, *t*, according to equation (S11):

$$\text{Yield}_i = \frac{N_{t,i}}{f_i \times V_0 \times C_0} \times 100 \quad \text{(S11)}$$

where V_0 (in L) and C_0 (in mM) stand for the initial electrolytic solution volume and the glycerol concentration in the cell, respectively, and f_i stands for the stoichiometric factor of the product *i* with respect to glycerol in the corresponding reaction among reactions (S1-S4) or (S6-S9).

The liquid product selectivity (in %) of each target chemical was calculated with respect to the overall production of the *n* liquid organic compounds detected by HPLC, according to equation (S12):

$$\text{Selectivity}_i = \frac{N_{t,i}}{f_i \times \sum_{i=1}^{n} \frac{N_{t,i}}{f_i}} \times 100 = \frac{\text{Yield}_i}{\sum_{i=1}^{n} \text{Yield}_i} \times 100 \quad \text{(S12)}$$

On the other hand, the number of electrons electrochemically transferred during the EC/PEC measurements, N_e (in mmol), can be calculated according to Faraday's law, from the electric charge, Q (in C), transferred at a given time, i.e., from the integration of the current (I, in mA) vs. time (t, in h) curve, via equation (S13).

$$N_e = \frac{Q}{F} \times 1000 = \frac{\int_0^t I\, dt}{F} \times 3600 \quad \text{(S13)}$$

Where F is the Faraday constant (96485 C $mol_{e^-}^{-1}$). Then, the faradaic efficiency of each target product, FE_i (in %) and the overall faradaic efficiency of the liquid products, FE_p (in %), can be calculated through equations (S14) and (S15), respectively:

$$FE_i = \frac{Np,i}{N_e} \times 100 \quad \text{(S14)}$$

$$FE_p = \frac{Np}{N_e} \times 100 = \sum_{i=1}^{n} FE_i \quad \text{(S15)}$$

Where $N_{p,i}$ and N_p (in mmol) stand for the number of electrons/holes that would be transferred for the electrocatalytic/photoelectrocatalytic production of the quantified amounts of product *i* and all liquid products, respectively, and they can be calculated, at a given time, through equations (S16) and (S17):

$$N_{p,i} = n_{e,i} \times N_{t,i} \quad \text{(S16)}$$

$$N_p = \sum_{i=1}^{n} N_{p,i} \quad \text{(S17)}$$

Where $n_{e,i}$ (in mol_{e^-} mol_i^{-1}) is the number of moles of electrons/holes theoretically transferred for the production of each mol of target product, *i* (i.e., according to reactions (S1-S4) or (S6-S9)).

To better discriminate the contribution of pure PC from the ultimate PEC performance, the faradaic efficiencies have also been calculated by using modified values of accumulated amounts of products, $N_{t,i}^*$ (in mmol), obtained after subtracting to the quantified production from the PEC test, $N_{t,i(PEC)}$, that from the corresponding purely PC measurements, i.e., without any external potential, $N_{t,i(PC)}$ (equation (S18)). Thus, analogously to equations (S14-S17), the modified parameters FE_i^*, FE_p^*, $N_{p,i}^*$ and N_p^* are defined, respectively, by means of equations (S19-S22), which refer to the chemicals production hypothetically derived only from the additional effect of the external polarization.

$$N_{t,i}^* = N_{t,i(PEC)} - N_{t,i(PC)} \quad \text{(S18)}$$

$$FE_i^* = \frac{N_{p,i}^*}{N_e} \times 100 \quad \text{(S19)}$$

$$FE_p^* = \frac{N_p^*}{N_e} \times 100 = \sum_{i=1}^{n} FE_i^* \quad \text{(S20)}$$

$$N_{p,i}^* = n_{e,i} \times N_{t,i}^* \quad \text{(S21)}$$

$$N_p^* = \sum_{i=1}^{n} N_{p,i}^* \quad \text{(S22)}$$

Section S2. Characterization of the catalysts.

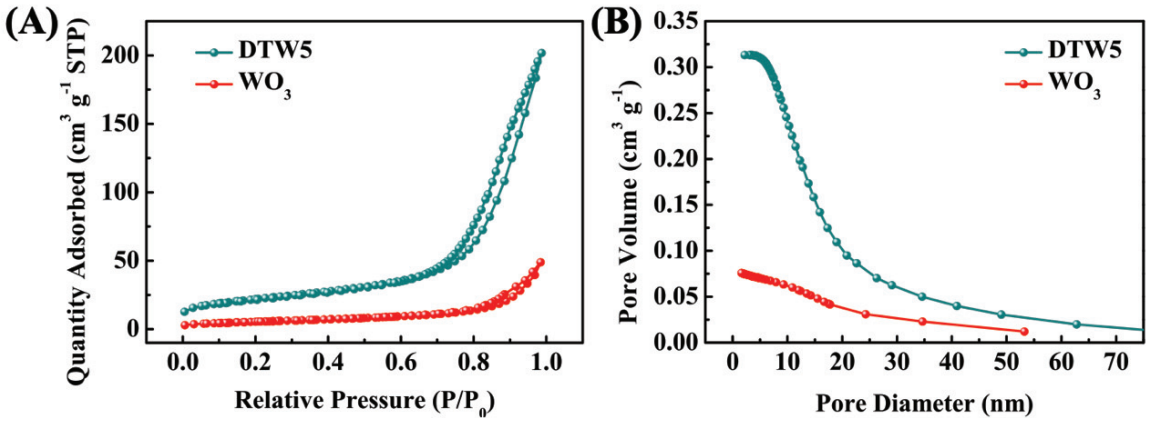

Fig. S3. 1. (a) N_2 adsorption/desorption isotherms and (b) the pore diameter distribution for DTW5 and WO_3 catalysts.

Classical type IV isotherms with a small hysteresis loop in the range of 0.7-1.00 of relative pressure can be observed, which denote that both WO_3 and DTW5 catalysts possess a mesoporous structure. BET surface areas, pore volumes and mean pore sizes are shown in Table 3. 1 in main text.

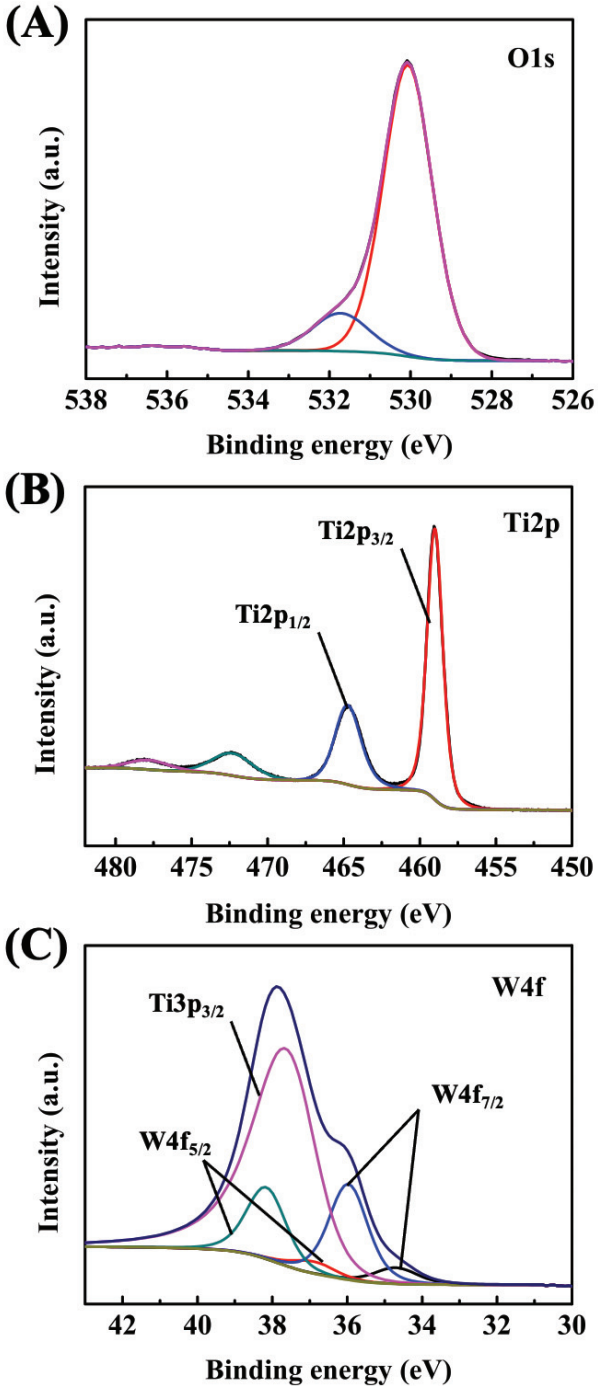

Fig. S3. 2. XPS spectra of DTW5 (a) O1s, (b) Ti2p and (d) W4f regions spectra of DTW5.

The $Ti2p_{3/2}$ and $Ti2p_{1/2}$ peaks found on DTW5 at 459.1 eV and 464.7 eV, respectively, along with the satellite separated from the former one in c.a. 14 eV and the O1s band at 530.0 eV, are a fingerprint of TiO_2 [1,2]. One can also observe the $W4f_{5/2}$ and $W4f_{7/2}$ peaks attributed to W^{6+} (38.2 eV and 36.0 eV, respectively) and to W^{5+} (36.8 eV and 34.7 eV) [3,4].

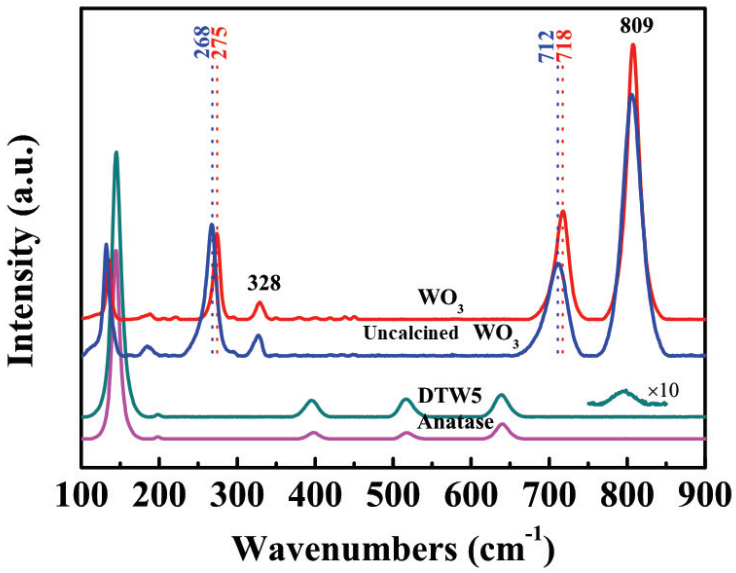

Fig. S3. 3. Raman spectra of DTW5, as-prepared WO_3 along with that of uncalcined WO_3 and Anatase for comparison.

The spectrum of the WO_3 catalyst proposed herein exhibits some characteristic peaks at 275, 328, 718, and 809 cm^{-1}. The first two signals are assigned in the literature to the δ (O–W–O) bending mode whereas the two latter are attributed to the ν (W–O–W) stretching of the monoclinic phase [5]. Raman peaks of an uncalcined pseudo-amorphous WO_3 catalyst like that used in a previous study [6], are comparatively broader and shifted to lower wavenumbers, which suggests a higher amount of defects in the structure of this catalyst, in the form of WO_{3-x}, and thus the presence of more oxygen vacancies with respect to the monoclinic WO_3. On the other hand, the Raman spectrum of DTW5 exhibits four bands at 146, 395, 516 and 639 cm^{-1} attributed to the active modes of anatase with the symmetries Eg, B1g, A1g and Eg, respectively [7]. The presence of WO_3 is also confirmed in this sample with a very weak band at ca. 797 cm^{-1}.

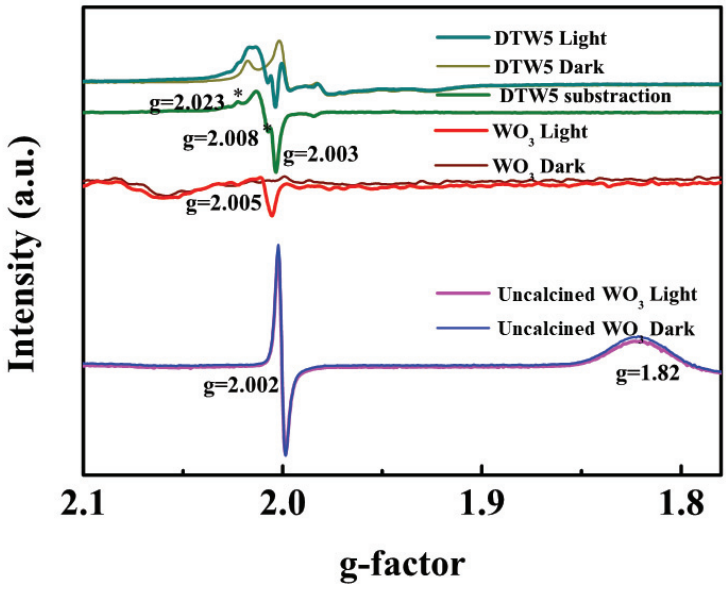

Fig. S3. 4. Electron paramagnetic resonance (EPR) spectra of DTW5, WO_3, and uncalcined WO_3 in dark conditions and with light illumination. In the case of DTW5, the spectrum obtained by subtracting data (light-dark) has also been included to show new bands appearing upon illumination.

Electron paramagnetic resonance (EPR), also known as electron spin resonance (ESR), is generally utilized to detect the unpaired electrons in semiconductor materials [8]. In the case of DTW5, the spectrum obtained in dark conditions was similar to that of the pure anatase [9] with no evidence of W^{5+}, unlike XPS spectra, which are limited to the outermost surface. After light irradiation, some new EPR signals appeared at g = 2.023, g = 2.008 and g = 2.003, which are typical of O^{2-} generated upon illumination [10]. Considering the dark spectra of WO_3 solids, uncalcined pseudo-amorphous WO_3 exhibited a symmetrical EPR signal at g = 2.002, assigned to electrons trapped in oxygen vacancies [11,12], and a broader EPR signal at g = 1.82, ascribed to W^{5+} [10]. After the calcination at 450 °C, both EPR signals in the WO_3 sample disappeared, which can be attributed to the higher crystallinity of the calcined WO_3 structure, with fewer existing oxygen defects, and to the presence of W^{5+} below the detection limit of this technique. Upon irradiation, the EPR spectrum of uncalcined WO_3 was barely affected, thus evidencing the low amount of generated electrons or holes and explaining therefore the low photocurrent reported elsewhere with this material [6]. On the contrary, illumination of the calcined WO_3 sample resulted in the appearance of a new EPR signal at g = 2.005 due to unpaired electrons captured by oxygen defects of W-O, which suggests a higher stability of the photogenerated electron-hole pair on the calcined WO_3 as compared to the uncalcined one.

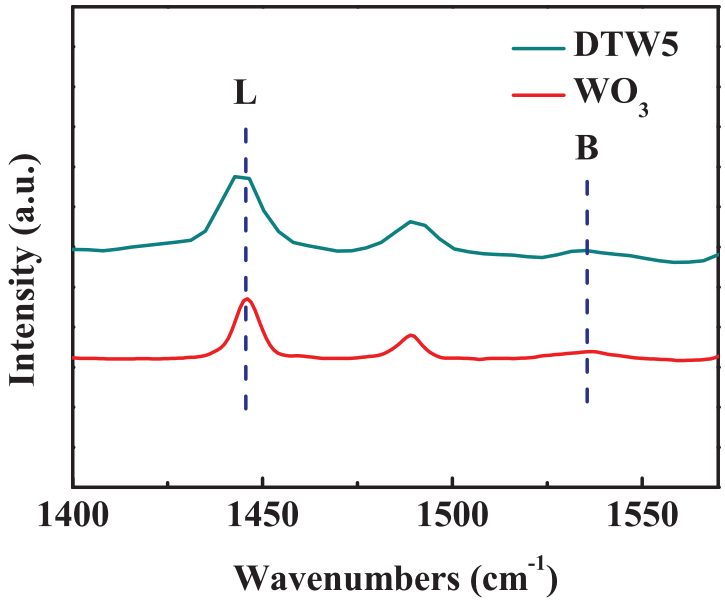

Fig. S3. 5. Pyridine-DRIFTS spectra of DTW5 and WO_3. B and L denote Brönsted and Lewis acid sites, respectively.

In the Diffuse reflectance infrared Fourier transform (DRIFT) spectra obtained on DTW5 and WO_3 catalysts, bands centered at 1448 and 1542 cm^{-1} are attributed to Lewis and Brönsted acid sites, respectively [13,14]. Data summarized in Table S3. 1 evidence that calcination of WO_3 resulted in a decrease in total acidity, mainly at the expense of Brönsted acids which were partially transformed into Lewis ones. Nevertheless, the density of both acid types remains in the same order (in the case of Lewis even higher) than in DTW5 catalyst.

Table S3. 1. Comparison of Lewis (L), Brönsted (B) and total acid sites of DTW5, WO_3 and uncalcined WO_3 obtained by pyridine (Py)-DRIFTS.

Catalyst	µmol Py · g^{-1} · m^{-2} Cat.			L/B	Ref.
	Lewis	Brönsted	Total		
DTW5	0.95	0.50	1.45	1.9	This work
WO_3	1.13	0.46	1.59	2.5	This work
Uncalcined WO_3	0.64	3.33	3.97	0.2	[6]

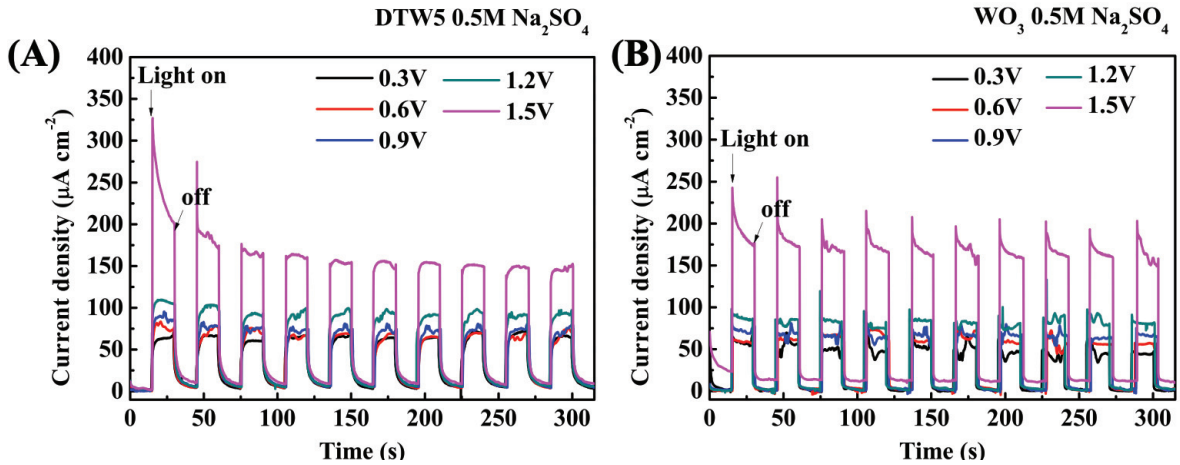

Fig. S3. 6. Transient photocurrent response at different applied potentials (i.e. 0.3, 0.6, 0.9, 1.2, 1.5 V vs. Ag/AgCl) on (a) commercial DTW5 and (b) as-prepared WO_3 catalysts supported on ITO glass (working electrode). Pt wire was used as counter electrode. Conditions: neutral reaction media (0.5 M Na_2SO_4).

In the absence of glycerol, these measurements show the transient photocurrent response for water oxidation on both catalysts. In the potential range of 0.3-1.2 V vs. Ag/AgCl, the obtained photocurrent densities are slightly higher on commercial WO_3/TiO_2 catalyst than on homemade WO_3. However, the influence of the applied potential is stronger in the latter case, reaching even higher photocurrents than DTW5 at 1.5 V vs. Ag/AgCl.

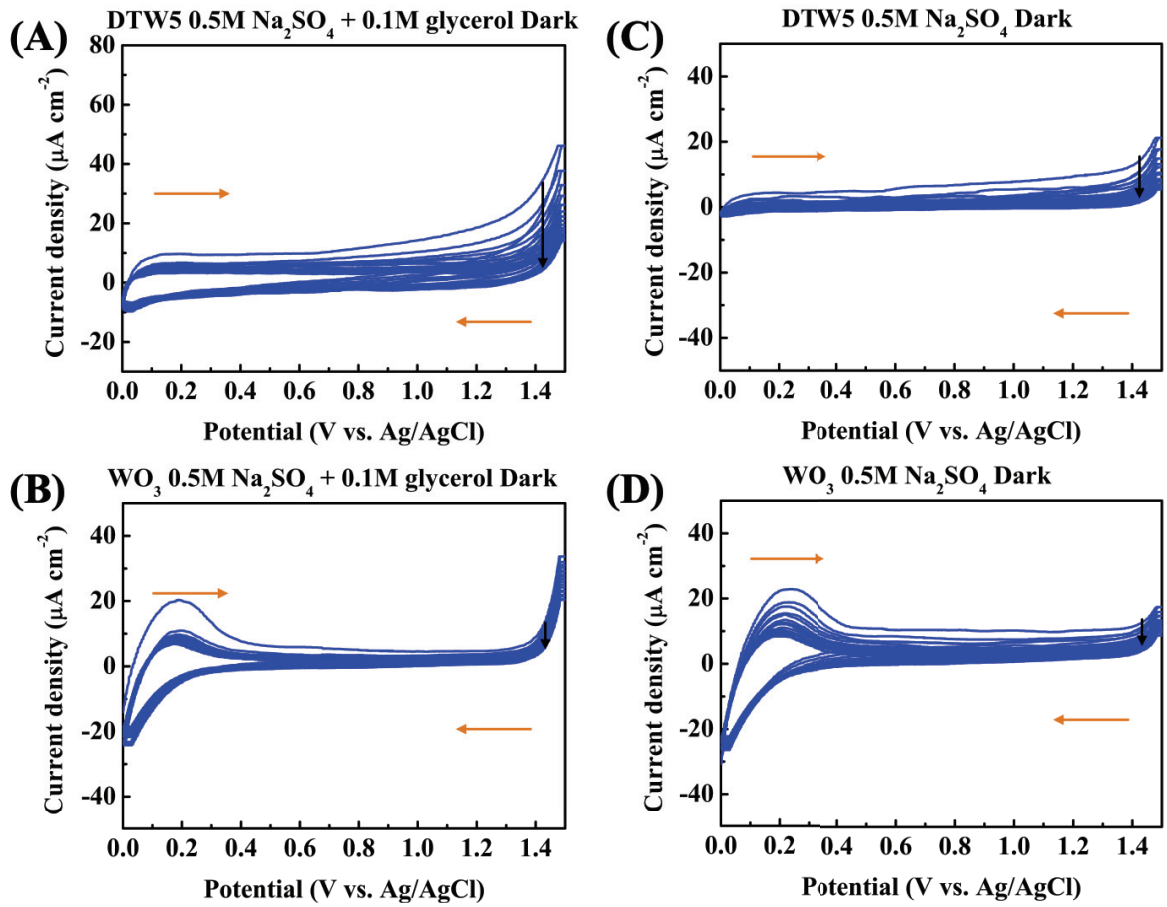

Fig. S3. 7. Cyclic voltammetry on DTW5 and WO_3 catalysts without light irradiation. Conditions: (a,b) 0.5 M Na_2SO_4 and 0.1 M glycerol; (c,d) 0.5 M Na_2SO_4. Scan rate: 20 mV s^{-1}; number of cycles: 10.

The CVs recorded under dark conditions show a negligible electrocatalytic (EC) activity of both WO_3 and DTW5 catalysts below 1.5 V vs. Ag/AgCl, both in the presence and in the absence of glycerol. The cathodic and anodic peaks observed at potentials below 0.3 V vs. Ag/AgCl, especially on the homemade WO_3 catalyst, are attributed to the reduction/oxidation of the redox couple W^{5+}/W^{6+} and/or the intercalation/de-intercalation of cations in the WO_3 [15–19], through reaction (S23).

$$WO_3 + xM^+ + xe^- \leftrightarrow M_xWO_3\ (0 \leq x \leq 1) \qquad \text{(S23)}$$

Where M^+ can be H^+ or Na^+ from the electrolyte.

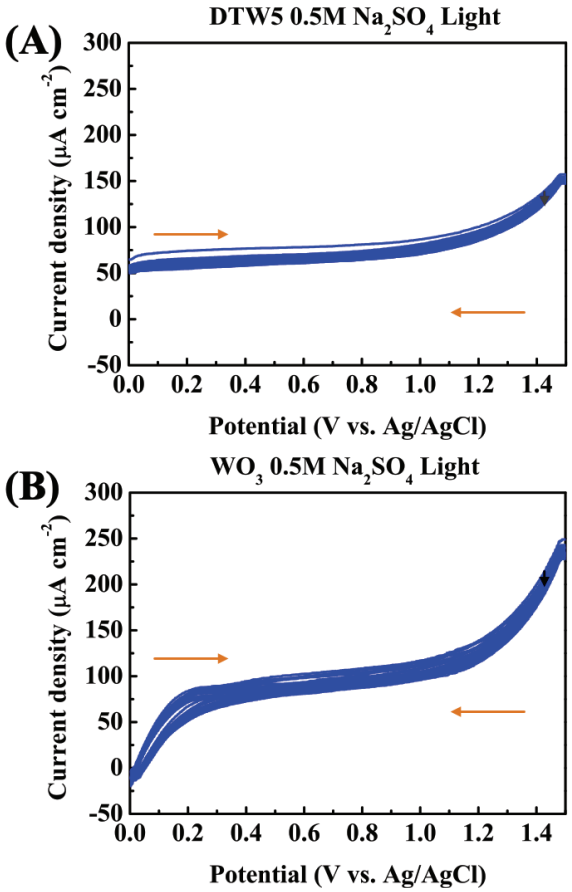

Fig. S3. 8. Cyclic voltammetry on (a) DTW5 and (b) WO_3 catalysts in the absence of glycerol (electrolyte of 0.5 M Na_2SO_4) under light irradiation. Scan rate: 20 mV s^{-1}; number of cycles: 10.

The CVs performed in the absence of glycerol show the photoelectrocatalytic activity of each catalyst for water oxidation, which shows to be higher in the case of homemade WO_3, unlike in the presence of glycerol, where the highest photocurrents are obtained on DTW5 (Fig. 3. 4c, d from main text).

Section S3. Evaluation of the photocatalytic and photoelectrocatalytic performances

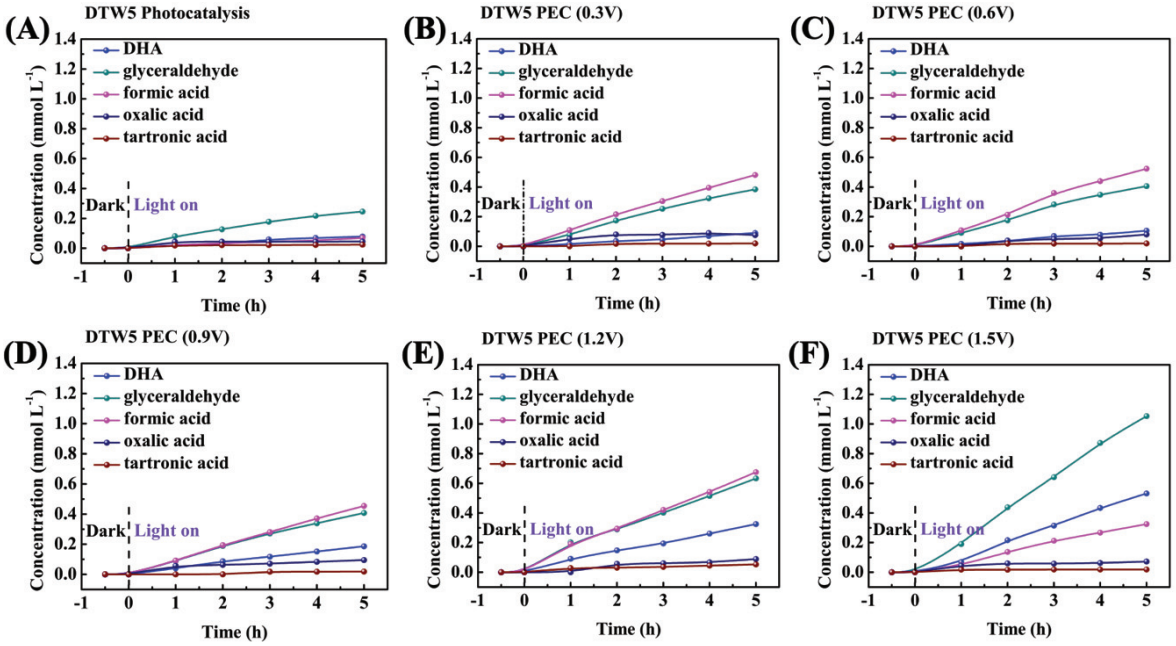

Fig. S3. 9. Evolution of dihydroxyacetone (DHA), glyceraldehyde, formic acid, oxalic acid and tartronic acid concentration in the cell with time during (a) photocatalytic and (b-f) photoelectrocatalytic oxidation of glycerol on DTW5 catalyst. Reaction conditions: Room temperature; glycerol initial concentration: 0.1 M; Na_2SO_4 concentration: 0.5 M; UV irradiation intensity: 350 mW cm^{-2}.

The concentration evolution observed during the different PC/PEC tests performed with the commercial DTW5 show lower glyceraldehyde and DHA production rates and higher formic acid production rate than in the case of the WO_3 catalyst (Fig. 3. 5 from the main text). Besides, on DTW5, one can also observe that the use of PEC conditions and the increase in the applied potential favours the glycerol oxidation to C_3 products and, at high enough potential (i.e., 1.5 V vs. Ag/AgCl), the formic acid production rate decreases (see the main text for the discussion).

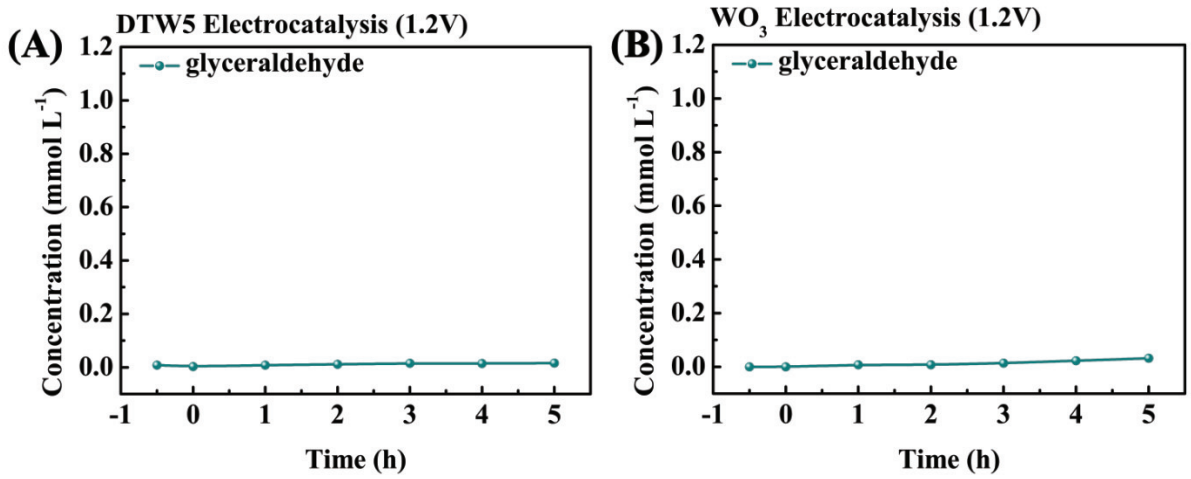

Fig. S3. 10. Evolution of glyceraldehyde concentration with time on (a) DTW5 and (b) WO_3 catalysts during the electrocatalytic test (without light irradiation) at 1.2 V vs. Ag/AgCl. Reaction conditions: Room temperature; glycerol initial concentration: 0.1 M. Na_2SO_4 concentration: 0.5 M.

This figure shows a clear example of the negligible activity of both DTW_5 and WO_3 catalysts with the sole driving force of electric bias at potentials as high as 1.2 V vs. Ag/AgCl.

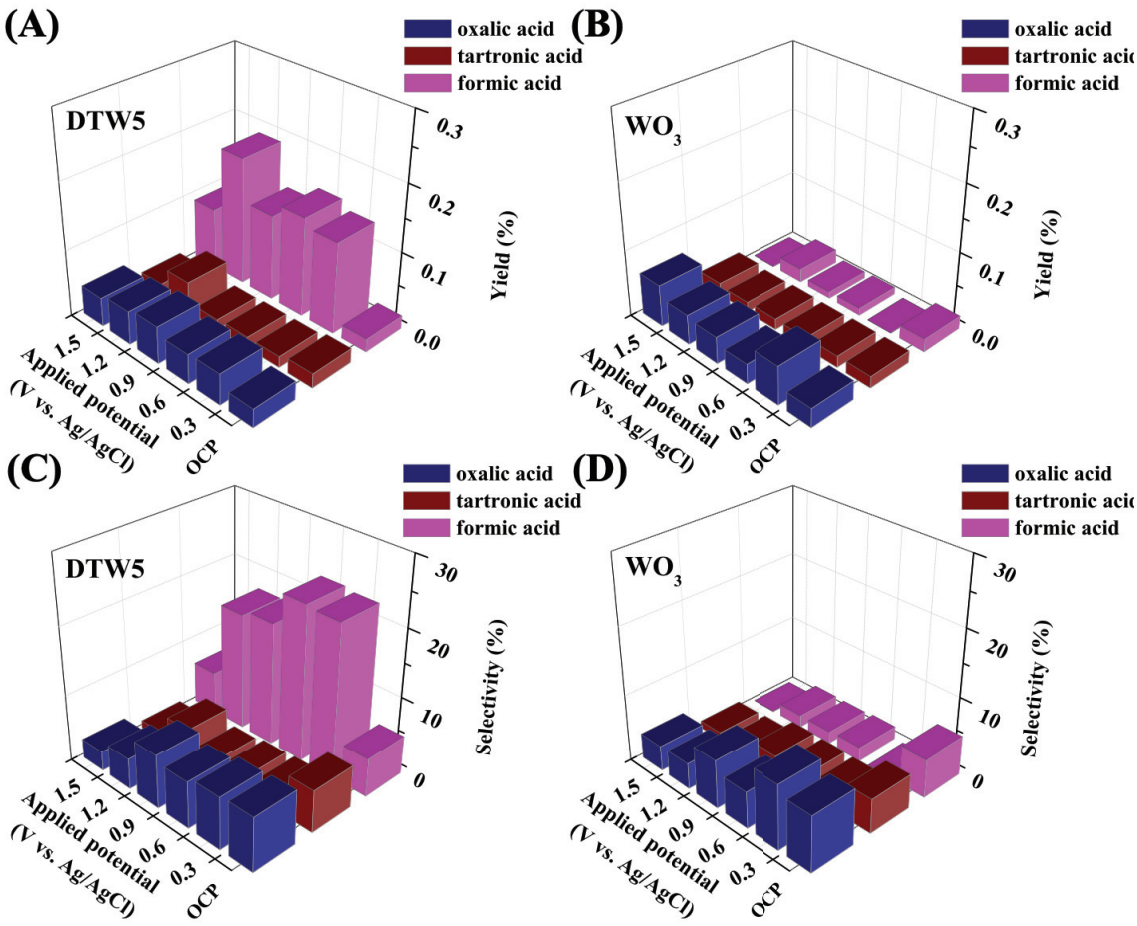

Fig. S3. 11. Variation of (a-b) the yield and (c-d) the liquid product selectivity of oxalic acid, tartronic acid and formic acid on DTW5 and WO_3 catalysts as a function of the applied potential in the photoelectrocatalytic tests as well as in the photocatalytic test (denoted as open circuit potential, OCP), after 5 h in all cases. Same reaction conditions as in Fig. 3. 5 and Fig. S3. 9.

The much higher yield and liquid selectivity values obtained for formic acid with the commercial DTW5 catalyst with respect to the homemade WO_3 contrast with the results shown in Fig. 3. 6 from the main text, regarding glyceraldehyde and DHA yield and selectivity, which are higher for WO_3. It is also interesting to note the significant decrease of the C_1 and C_2 selectivity observed upon increasing the applied potential (see the main text for the discussion).

Table S3. 2. Average crystallite size of catalysts before and after photoelectrocatalytic tests obtained from XRD spectra.

Sample	Crystal size (nm)	Sample	Crystal size (nm)
DTW5 (fresh)	20	WO_3 (fresh)	49
DTW5 (0.3V)	20	WO_3 (0.3V)	48
DTW5 (0.6V)	21	WO_3 (0.6V)	52
DTW5 (0.9V)	19	WO_3 (0.9V)	52
DTW5 (1.2V)	21	WO_3 (1.2V)	53
DTW5 (1.5V)	19	WO_3 (1.5V)	53

The XRD analysis on DTW5 and WO_3 catalysts after the PEC tests performed under different applied potentials show a stable crystallite size in both cases.

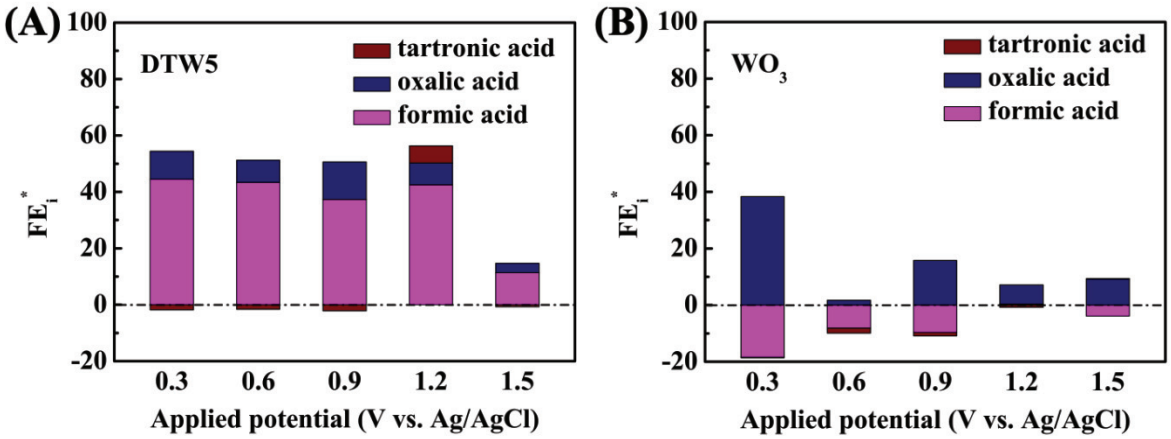

Fig. S3. 12. (a-b) Modified Faradaic efficiency (FE_i^*) of liquid products other than glyceraldehyde and DHA, on (a) DTW5 and (b) WO_3 catalysts at different applied potentials after 5 h. Same reaction conditions as in Fig. 3. 5 and Fig. S3. 9.

This figure shows the modified faradaic efficiency (FE^*) values, i.e., after subtraction of the PC contribution, calculated for all liquid products except glyceraldehyde and DHA (shown in Fig. 3. 7e, f from main text). The negative values are due to the production of higher quantities of certain products under PC conditions than under PEC conditions. The high FE^* values for formic acid reached with DTW5 catalyst contrast with the results obtained for the preferred C_3 compounds, whose FE^* values are higher in the case of WO_3 catalyst. It is also very interesting to note the great decrease of the formic acid and oxalic faradaic efficiencies at 1.5 V vs. Ag/AgCl (see the main text for the discussion).

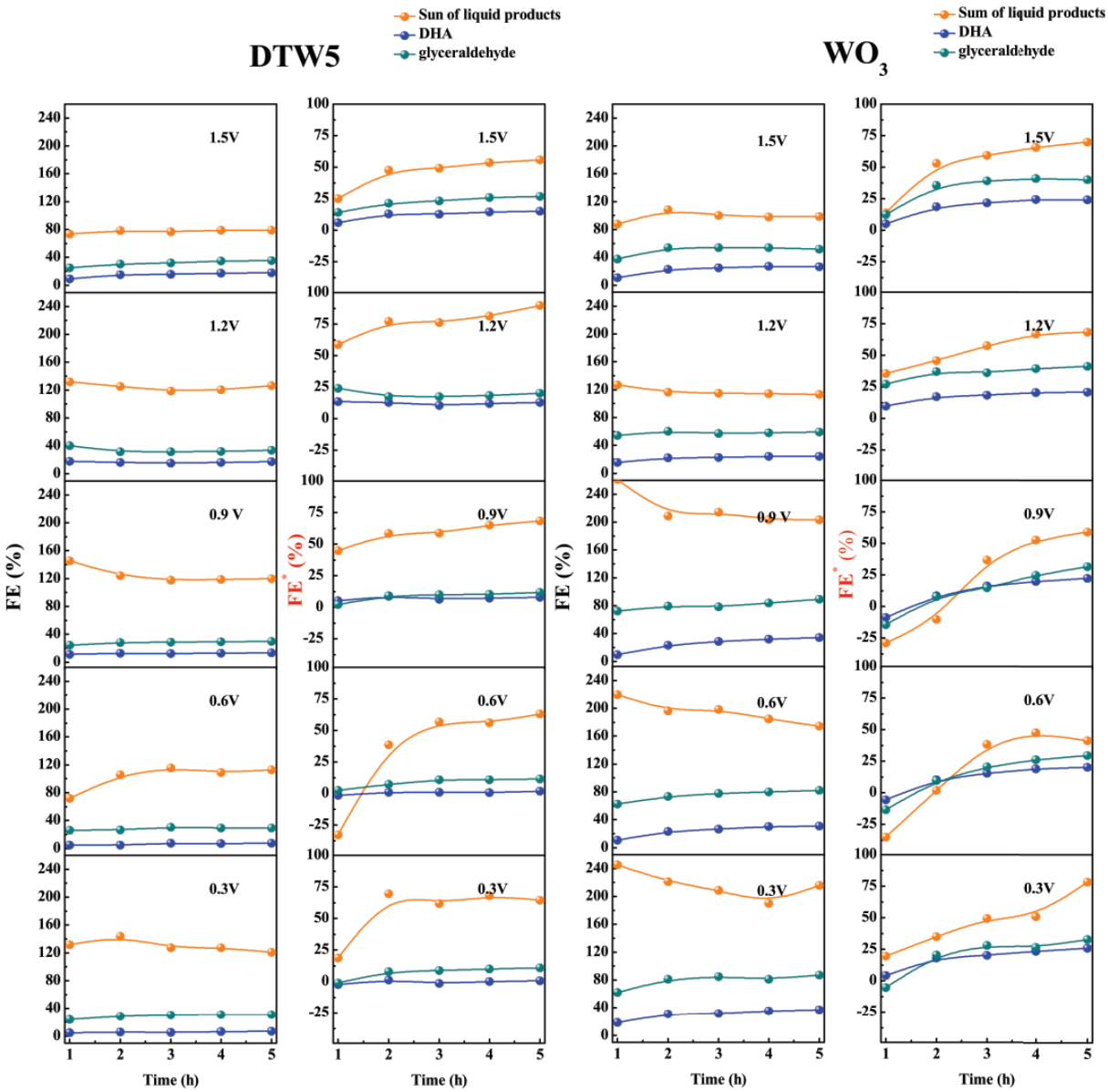

Fig. S3. 13. Evolution of Faraday efficiency (FE, columns 1 and 3) and modified Faraday efficiency (FE^*, columns 2 and 4) for DHA, glyceraldehyde and the sum of all liquid products with time at different applied potentials on DTW5 and WO_3 catalysts.

The time evolution of the FE and FE^* values shows that the former values are rather constant during the tests while the latter ones have an increasing trend, which denotes the increasing influence of the electric bias with time and the initiator character of the light irradiation in the PEC glycerol valorization.

References

[1] P. Stefanov, M. Shipochka, P. Stefchev, Z. Raicheva, V. Lazarova, L. Spassov, XPS characterization of TiO_2 layers deposited on quartz plates, in: J. Phys. Conf. Ser., 2008: p. 12039.

[2] R. Ji, D. Zheng, C. Zhou, J. Cheng, J. Yu, L. Li, Low-temperature preparation of tungsten oxide anode buffer layer via ultrasonic spray pyrolysis method for large-area organic solar cells, Materials (Basel). 10 (2017) 820.

[3] K. Senthil, K. Yong, Growth and characterization of stoichiometric tungsten oxide nanorods by thermal evaporation and subsequent annealing, Nanotechnology. 18 (2007) 395604.

[4] M. Tong, J. Yang, Q. Jin, X. Zhang, J. Gao, G. Li, Facile preparation of amorphous carbon-coated tungsten trioxide containing oxygen vacancies as photocatalysts for dye degradation, J. Mater. Sci. 54 (2019) 10656–10669.

[5] N. Wang, D. Wang, M. Li, J. Shi, C. Li, Photoelectrochemical water oxidation on photoanodes fabricated with hexagonal nanoflower and nanoblock WO_3, Nanoscale. 6 (2014) 2061–2066.

[6] J. Yu, F. Dappozze, J. Martín-Gomez, J. Hidalgo-Carrillo, A. Marinas, P. Vernoux, A. Caravaca, C. Guillard, Glyceraldehyde production by photocatalytic oxidation of glycerol on WO_3-based materials, Appl. Catal. B Environ. 299 (2021) 120616.

[7] W. F. Zhang, Y.L. He, M. S. Zhang, Z. Yin, Q. Chen, Raman scattering study on anatase TiO_2 nanocrystals, J. Phys. D. Appl. Phys. 33 (2000) 912–916.

[8] F. Zhan, Y. Liu, K. Wang, Y. Liu, X. Yang, Y. Yang, X. Qiu, W. Li, J. Li, In situ formation of WO_3-based heterojunction photoanodes with abundant oxygen vacancies via a novel microbattery method, ACS Appl. Mater. & Interfaces. 11 (2019) 15467–15477.

[9] J. Hidalgo-Carrillo, J. Martín-Gómez, M.C. Herrera-Beurnio, R.C. Estévez, F.J. Urbano, A. Marinas, Olive leaves as biotemplates for enhanced solar-light harvesting by a titania-based solid, Nanomaterials. 10 (2020) 1057.

[10] M. Occhiuzzi, D. Cordischi, D. Gazzoli, M. Valigi, P.C. Heydorn, WO_x/ZrO_2 catalysts: Part 4. Redox properties as investigated by redox cycles, XPS and EPR, Appl. Catal. A Gen. 269 (2004) 169–177.

[11] Z. Shen, Z. Zhao, J. Wen, J. Qian, Z. Peng, X. Fu, Role of oxygen vacancies in the electrical properties of WO_{3-x} nano/microrods with identical morphology, J. Nanomater. 2018 (2018).

[12] Z. Gu, X. An, R. Liu, L. Xiong, J. Tang, C. Hu, H. Liu, J. Qu, Interface-modulated nanojunction and microfluidic platform for photoelectrocatalytic chemicals upgrading, Appl. Catal. B Environ. 282 (2021) 119541.

[13] J. González, J.A. Wang, L.F. Chen, M.E. Manríquez, J.M. Dominguez, Structural Defects, Lewis Acidity, and Catalysis Properties of Mesostructured WO_3/SBA-15 Nanocatalysts, J. Phys. Chem. C. 121 (2017) 23988–23999.

[14] M. Checa, V. Montes, J. Hidalgo-Carrillo, A. Marinas, F.J. Urbano, Influence of Boron, Tungsten and Molybdenum Modifiers on Zirconia Based Pt Catalyst for Glycerol Valorization, Nanomaterials. 9 (2019).

[15] S. Darmawi, S. Burkhardt, T. Leichtweiss, D.A. Weber, S. Wenzel, J. Janek, M.T. Elm, P.J. Klar, Correlation of electrochromic properties and oxidation states in nanocrystalline tungsten trioxide, Phys. Chem. Chem. Phys. 17 (2015) 15903–15911.

[16] P.A. Shinde, S.C. Jun, Review on recent progress in the development of tungsten oxide based electrodes for electrochemical energy storage, ChemSusChem. 13 (2020) 11–38.

[17] K. K. Upadhyay, M. Altomare, S. Eugénio, P. Schmuki, T. M. Silva, M. F. Montemor, On the supercapacitive behaviour of anodic porous WO_3-based negative electrodes, Electrochim. Acta. 232 (2017) 192–201.

[18] S.P. Gupta, H.H. Nishad, S.D. Chakane, S.W. Gosavi, D.J. Late, P.S. Walke, Phase transformation in tungsten oxide nanoplates as a function of post-annealing temperature and its electrochemical influence on energy storage, Nanoscale Adv. 2 (2020) 4689–4701.

[19] S. Sfaelou, L. C. Pop, O. Monfort, V. Dracopoulos, P. Lianos, Mesoporous WO_3 photoanodes for hydrogen production by water splitting and PhotoFuelCell operation, Int. J. Hydrogen Energy. 41 (2016) 5902–5907.

Chapter 4

Optimization of a bifunctional PEM photoelectrocatalytic system for the simultaneous selective glycerol valorization and hydrogen generation

Jie Yu,[a] Jesús González-Cobos,[a] Frederic Dappozze,[a] Nicolas Grimaldos-Osorio,[a] Philippe Vernoux,[a] Angel Caravaca,[a]* Chantal Guillard [a]*

[a] Univ Lyon, Université Claude Bernard Lyon 1, CNRS, IRCELYON, F-69626, Villeurbanne, France

E-mail: angel.caravaca@ircelyon.univ-lyon1.fr, chantal.guillard@ircelyon.univ-lyon1.fr

Abstract

The photoelectrocatalytic (PEC) valorization of glycerol is emerging in the last decades as a way to generate hydrogen and value-added organics like glyceraldehyde or dihydroxyacetone (DHA). However, most of the studies reported in literature are only focused on one of the half-reactions, use anodes containing noble metals, or strongly acidic or basic media. Besides, all fundamental studies performed in 3-electrode cells entail a lack of overall efficiency and product separation. In this work, we have addressed all mentioned bottlenecks at once, by designing and optimizing a pioneering PEC cell with a proton-exchange membrane (PEM) and a WO_3 photoanode under near-neutral conditions. The influence of light irradiation, external bias and cell temperature has been studied, leading to maximum glyceraldehyde and DHA production rates of 11.1 and 5.2 mmol m^{-2} h^{-1} at 60 ºC and 1.2 V, along with the production of 44.0 mmol H_2 m^{-2} h^{-1}. The long-term stability of the PEC cell has been evaluated and the results have been discussed by disclosing the photocatalytic (PC), electrocatalytic (EC) and thermocatalytic (TC) effects on the overall performance. PEC has proved to be the most promising among the explored technologies, opening important prospective for developing simultaneous H_2 generation and biomass valorization processes.

Keywords: photoelectrocatalysis, PEM, valorization, glycerol, glyceraldehyde, WO_3

1. Introduction

Glycerol is an important by-product of the production of biodiesel as an alternative to fossil fuels, and its valorization is not only encouraged for the global consensus on carbon neutralization, but also highly economically profitable. This is especially relevant when dealing with the selective production of its primary 3C oxidation products, glyceraldehyde and dihydroxyacetone (DHA), which are key precursors in the synthesis of cosmetics, polymers and biodegradable emulsifiers. [1–5] Besides, green hydrogen is regarded as one of the most important energy carriers for global energy transformation and development, given its high gravimetric energy density and environmental friendliness. [6,7] In this sense, a promising pathway for simultaneous glycerol valorization into value-added chemicals and hydrogen is the photoelectrocatalysis (PEC). This technology possesses better performance than photocatalysis (PC), by promoting the separation of photogenerated electrons and holes through external voltage, and has gradually attracted the attention of academia and industry in recent years. [8–10]

Glycerol-upgrading by PEC generally possesses two half-reactions: glycerol oxidation/oxygen evolution reaction (OER) on the anodic side, and hydrogen evolution reaction (HER) on the cathodic side. Despite several achievements in glycerol oxidation or reforming, the current research on PC and PEC glycerol oxidation has four main bottlenecks:

i) In the case of PEC, there is insufficient attention on both half-reactions simultaneously, i.e., glycerol oxidation and hydrogen evolution. The chemical generation in the anode is commonly neglected [11–16] and, when studied, this reaction has not always resulted in the production of the desired primary products. For example, in some cases, the selectively obtained product is glyceric acid [17,18] or formic acid/formate. [19–22]

ii) The utilization of precious metals like Pt, [23–26] Au, [27–29] and Pd, [30–32] either as main active phase or as co-catalyst, decreases the PC and PEC economic competitiveness.

iii) Most of the studies are carried out under non-mild reaction conditions, i.e., using acid (e.g., H_2SO_4) [22,33,34] or alkaline solutions (e.g., KOH, NaOH) [17–19] as electrolytes, which leads to safety risks of storage and transportation and environmental hazards in large-scale production. For instance, Wang et al. proposed a CoNiFe-LDHs-decorated Ta_3N_5 nanotube array for the simultaneous generation of anodic formate and cathodic hydrogen in a 1.0 M NaOH electrolyte, [19] while the highest DHA selectivities (above 50%) have been reached by using solutions with pH

= 2. [22,33,34] There are only two PEC studies under neutral or near-neutral conditions, performed by Gu et al. [35] and by this group. [Chapter 3] In both cases, WO_3-based anodes showed to be excellent materials for the selective glycerol oxidation, with selectivities up to c.a. 90% for glyceraldehyde+DHA.

iv) The separation of glycerol oxidation products from the liquid electrolyte, as well as from gaseous hydrogen, is complicated in the traditional 3-electrode PEC cells. [36,37] This is the case of the above-mentioned works, where both anodic and cathodic half-reactions took place in the same gas/liquid space. In view of its practical application, this configuration would increase the process complexity and economical cost due to the need for products post-purification operations.

Proton exchange membrane (PEM) cells using a thin solid electrolyte membrane to separate anode and cathode electrodes show several advantages with respect to liquid electrolyte cells, such as the separation of the oxidation products from the hydrogen effluent, their lower ohmic resistance, and their compactness and typically superior fluid dynamics, which lead to improved durability and efficiency. [38,39] PEM cells have been widely used in the field of electrocatalytic hydrogen generation from alcohols. [40–45] In particular, glycerol electrolysis was studied in PEM configuration with a Nafion membrane by Marshall and Haverkamp [46] and Kim et al. [47] There are also two works using an anion-exchange membrane, by Bambagioni et al. [48] and de Paula et al. [49] However, in all these cases, platinum-group metal (PGM) catalysts were employed in the anode and either glycerate [47,48] or tartronate [48,49] were the products selectively generated from the anodic reaction. Thus, to the best of our knowledge, this is the first work using a PEM cell configuration for the simultaneous hydrogen production and selective glycerol valorization to glyceraldehyde or dihydroxyacetone, and also the first attempt to carry out these processes in a PEM cell via the photoelectrocatalytic route.

In this work, a PEM PEC cell was designed to perform the separated glycerol oxidation to high value-added products in the anode compartment, together with the simultaneous green H_2 generation in the cathodic compartment. Monoclinic WO_3 synthesized by a simple hydrothermal method with proper crystallinity, acidity and a certain amount of oxygen vacancies (a ratio of W^{5+}/W^{6+} of ~18%) was selected as the photoanode electrode due to its precedent high selectivity observed towards glyceraldehyde under near-neutral pH conditions in our previous work. [Chapter 3] The operation parameters of this cell have been optimized, focusing not only on the applied potential but also on the cell temperature. The latter is a key parameter that could significantly affect the reaction kinetics, mass transfer and photo- or

electro-induced charge separation rate, but it has not been deeply studied in a three-electrode cell configuration. Besides, the operation parameters have been optimized to enhance both, the selective glycerol valorization and hydrogen production. For this purpose, the bifunctional PEM system has also been studied under (thermo)catalytic (TC), photocatalytic (PC), electrocatalytic (EC) and combined PEC conditions. A highly selective generation of C_3 primary products and considerable photocurrents were achieved, along with long-term stable faradaic efficiencies, without employing any noble metals at the anode. The superiority of PEC over other technologies (TC/PC/EC) for the simultaneous production of H_2 and targeted C_{3s} chemicals is proved, and the synergy between photo- and electro-induced mechanisms is discussed. Thus, we believe that this study provides a meaningful reference for PEC technology in the solar-to-chemical energy conversion in academic research and industrial application.

2. Experimental section

2.1 Preparation of WO_3 photoanode

The synthesis procedure of monoclinic WO_3 was based on that reported in a previous study. [50] Typically, 0.6 g of WCl_6 (Sigma-Aldrich) was firstly dissolved in Ethanol (99.8% purity, Sigma-Aldrich) solution (120 mL) and transferred to a 200 mL of Teflon-lined stainless-steel autoclave for hydrothermal treatment at 180 ºC for 12 h. Then, the light-blue WO_3 was carefully withdrawn and washed using Ethanol and deionized water 3 times. The collected powder was dried at 80 ºC overnight. Finally, the bright yellow monoclinic WO_3 with high crystallinity (82.6%) and suitable oxygen defects (with a ratio of W^{5+}/W^{6+} of ~0.18) was obtained by post-calcination treatment at 450 ºC for 1 h (5 ºC min^{-1} of heating rate) in air. Samples were well-grinded before use. A catalyst ink was prepared by mixing the obtained WO_3 catalyst powder with a 5 wt.% Nafion (Sigma-Aldrich) perfluorinated resin solution in aliphatic alcohols and water (to reach a WO_3:Nafion wt. ratio of 1:1) and 5 mL isopropanol (HPLC-isocratic grade, Carlo Erba Reagents). Then the ink was sprayed with an aerograph on a Carbon Cloth (W1S1011, FuelCellStore) electrode-support with a thickness of 410 μm and an area of 5.3 cm^2. The alcohol/water solvent was evaporated at 80 ºC, and the catalyst loading on the Carbon Cloth was controlled by weight measurement, reaching a value of 3.5 mg cm^{-2}. A detailed physicochemical characterization of this WO_3 material can be found in previous work from this group. [Chapter 3]

2.2 Membrane Electrode Assembly (MEA) and PEM cell setup

The synthesized carbon cloth-supported WO_3 was used as the photoanode, and a commercial carbon cloth-supported Pt (20% wt.)/C (Fuel Cell Store) with a loading of 0.2 mg·cm^{-2} was used as cathode. In the latter case, the carbon cloth behaves as gas diffusion layer (GDL) with

microporous layer (MPL) and a thickness of 365 µm. A NafionTM 117 membrane was used as the proton-exchange membrane (PEM) with a thickness of 183 µm, which does not only serve as the solid electrolyte, but also as the separator for the obtained redox products. Prior to assembly, the membrane was pretreated by successive immersions in 3 different 150 mL-solutions, 3% wt. H_2O_2, 0.5 M H_2SO_4 and deionized water, in that order. The membrane electrode assembly (anodic photoelectrode/PEM/cathodic electrode) was prepared by hot-pressing under 1 metric ton at 120 ºC for 3 min.

The employed (photo)electrochemical cell was adapted from a 5 cm^2-commercial electrochemical cell (Dioxide Materials), by designing and constructing one of the two bipolar plates, i.e., the anode side, to house a suitable quartz window for the PEC measurements. The PEC was also modified to introduce heating resistance rods (see Fig. S4. 1 in Electronic Supplementary Information). The MEA was held between two Teflon gaskets to ensure the correct sealing of the PEC cell, and it was placed so that the catalyst on the photoanode faces the cell window (3.8 cm^2), while the catalyst on the cathode faces the membrane. As depicted in Fig. 4. 1, a temperature control system was used, and 30 mL-solutions of 0.1 M glycerol and pure water (pH 5.5 both) were continuously fed (recycled) by means of a peristaltic pump (ISMATEC SA, Switzerland) through the anode and cathode sides of the cell from the respective reservoirs at a flow rate of approximately 3 mL min^{-1} each.

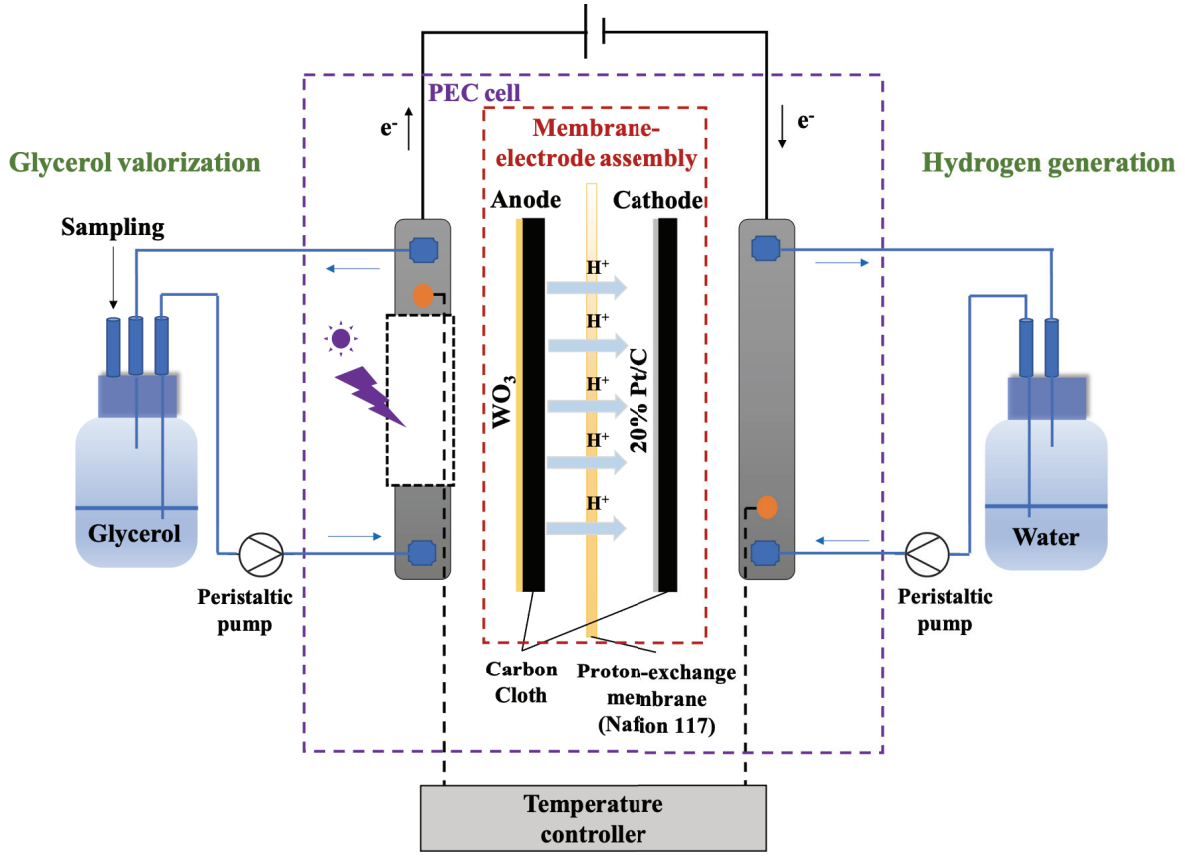

Fig. 4. 1. Scheme of the Proton-exchange membrane (PEM) photoelectrocatalytic (PEC) cell set-up employed in this study.

2.3 Electrochemical characterization

An Origalys OGBO5A electrochemical station (OrigaLys ElectroChem SAS, Rillieux-la-Pape, France) was used to measure the photoelectrochemical properties of the PEC PEM system, by feeding either 0.1 M glycerol (or pure water) to the anodic side of the cell, while feeding pure water to the cathodic side. Photocurrent, linear sweep voltammetry (LSV), cyclic voltammetry (CV), and open circuit potential (OCP) measurements were performed. The transient photocurrent tests were carried out at different applied cell voltages from 0.3 V to 1.5 V with 15 seconds of irradiation interval, using a LED UV lamp as the light source (41 mW cm^{-2}), with an incidence area of 1 cm^2. Prior to these measurements, the system was kept in dark conditions for 2 min to stabilize the current derived from the external bias. CV was recorded between 0 and 1.5 V (cell voltages) at a scan rate of 10 mV s^{-1} for 10 cycles under light irradiation. All the tests presented in this study were carried out in the same system, without changing the electrodes nor the membrane.

2.4 TC/PC/EC/PEC glycerol oxidation

PEC experiments were carried out under ultraviolet light using the same setup and LED UV lamp above mentioned. The PEC was measured under different applied cell voltages, between 0.3 and 1.2 V, and at different temperatures between 25 and 80 ºC. Purely PC, EC and TC experiments were also carried out at different cell temperatures in the absence of either external bias, light irradiation or both, respectively. Prior to all measurements, the anolyte and catholyte solutions were flowing through the cell for 30 min under dark and open-circuit conditions, at room temperature to achieve the adsorption-desorption equilibrium of glycerol on the surface of the catalyst. Then, the PEC/PC/EC/TC measurements were initiated and, every hour, a sample (0.6 mL) was collected from the anode solution and immediately filtered by a Millipore 0.45 μm (hydrophilic PVDF) membrane using a plastic syringe. The reaction time was generally 6 h, except for the long-term experiment (27 h). The concentrations of glycerol and derived products were analyzed by a Shimadzu SPD-M20A ultrafast high-performance liquid chromatography (HPLC) equipped with a Transgenomic ICSep ICE-COREGEL-87H3 organic acid column. 5 mmol L^{-1} of H_2SO_4 with a flow rate of 0.7 mL min^{-1} served as the mobile phase and the column temperature was 30 ºC. The products of glycerol oxidation were determined by the ultraviolet detector at the wavelength of 210 nm. Glycerol was analyzed by the refractive index detector (RID). The concentration of total organic carbon (TOC) of the solutions before

and after the PEC tests were measured using a Shimadzu TOC-VCPN analyzer equipped with an auto-sampler.

According to the liquid products detected, the photo- (or electro-)catalytic reactions (1-5) were assumed to take place on the WO_3 catalyst surface, by considering the transfer of either holes left in the valence band (h^+_{VB}) upon illumination (under PEC or PC operation conditions) or electrons (e^-, under EC conditions).

$$C_3H_8O_3 + 2h^+_{VB}(-2e^-) \rightarrow 2H^+ + C_3H_6O_3 \text{ (glyceraldehyde/DHA)} \quad (1)$$

$$C_3H_8O_3 + 2H_2O + 8h^+_{VB}(-8e^-) \rightarrow 8H^+ + C_3H_4O_5 \text{ (tartronic acid)} \quad (2)$$

$$2C_3H_8O_3 + 3H_2O + 10h^+_{VB}(-10e^-) \rightarrow 10H^+ + 3C_2H_4O_3 \text{ (glycolic acid)} \quad (3)$$

$$2C_3H_8O_3 + 6H_2O + 22h^+_{VB}(-22e^-) \rightarrow 22H^+ + 3C_2H_2O_4 \text{ (oxalic acid)} \quad (4)$$

$$C_3H_8O_3 + 3H_2O + 8h^+_{VB}(-8e^-) \rightarrow 8H^+ + 3CH_2O_2 \text{ (formic acid)} \quad (5)$$

The total amount ($N_{t,i}$, in mmol) of unreacted glycerol and each produced chemical, *i*, at a given time (i.e., sampling time), *t*, was calculated from the concentration values quantified by HPLC, according to equation (6):

$$N_{t,i} = V_t \times C_{t,i} + V_s \times \sum_{t=0}^{t-1} C_{t,i} \quad (6)$$

where V_t (in L) and $C_{t,i}$ (in mM) are the solution volume and the concentration of the chemical *i* in the cell, respectively, at the time *t*, V_s is the sample volume (i.e., 6 x 10^{-4} L) and, thus, the term $[V_s \times \sum_{t=0}^{t-1} C_{t,i}]$ stands for the accumulated amount of product or unreacted glycerol collected in previous samplings.

The Glycerol conversion (in %) at a given time was calculated according to equation (7):

$$\text{Glycerol conversion (\%)} = \frac{V_0 x C_{0\ \text{glycerol}} - N_{t\ \text{glycerol}}}{V_0 x C_{0\ \text{glycerol}}} \times 100 \quad (7)$$

Where V_0 (in L) and $C_{0,glycerol}$ (in mM) stand for the initial electrolytic solution volume and glycerol concentration, respectively, and $N_{t,glycerol}$ is the unreacted amount of glycerol at a given time, t.

The Yield (in %) and the Selectivity (in %) of every product were calculated at a given time, t, according to equations (8) and (9), respectively:

$$\text{Yield (\%)} = \frac{N_{t,i}}{V_0 x C_{0\ \text{glycerol}} x f_i} \times 100 \quad (8)$$

$$\text{Selectivity (\%)} = \frac{N_{t,i}}{(V_0 x C_{0\ \text{glycerol}} - N_{t\ \text{glycerol}}) x f_i} \times 100 \quad (9)$$

where f_i is the stoichiometric factor of the product i with respect to glycerol (i.e., according to reactions (1-5)).

Then, the faradaic efficiency of each target product, *FE* (in %) was calculated through equation (10).

$$FE = \frac{Ni}{N_e} \times 100 \quad (10)$$

Where N_i and N_e (in mmol) stand, respectively, for the number of electrons/holes that would be transferred for the EC/PEC production of the quantified amounts of product *i*, and those electrochemically transferred according to the measured electric charge, Q (in C), which can be calculated, at a given time, through equations (11) and (12):

$$N_i = n_{e,i} \times N_{t,i} \quad (11)$$

$$N_e = \frac{Q}{F} \times 1000 = \frac{\int_0^t I\,dt}{F} \times 3600 \quad (12)$$

Where $n_{e,i}$ is the number of mol of electrons/holes theoretically transferred for the production of each mol of target product i (i.e., according to reactions (1-5)), F is the Faraday constant (96485 C $mol_{e^-}^{-1}$) and I (in mA) is the current obtained at a given time, t (in h).

3. Results and discussion

3.1 Photoelectrochemical characterization

The homemade WO_3 photoanode was coated on a commercial carbon cloth and tested in the PEC proton-exchange membrane (PEM) cell shown in Fig. 4. 1 and Fig. S4. 1, where a commercial Pt/C electrode behaved as the cathode. Through the quartz window, the UV light with a radiation density of 41 mW cm^{-2} activates the photocatalyst to excite electrons to the conduction band (e^-_{CB}), leaving the same number of holes in the valence band (h^+_{VB}), which may participate in the glycerol valorization (reactions (1-5)) and/or water oxidation (reactions (13-14)). Meanwhile, the resultant protons and electrons are transferred to the cathode through the proton-exchange membrane and the external circuit, respectively, leading to the hydrogen evolution reaction (HER, reaction (15)). Hence, the external bias contributes to separating the photo-generated electrons from the holes, thus avoiding their recombination and increasing the holes availability for oxidation reactions, while the PEM configuration is expected to improve the EC performance and to allow the elution of a purified H_2 cathodic stream from the cell.

$$H_2O + 2h^+_{VB} \rightarrow 2H^+ + 1/2O_2 \quad (13)$$

$$2H_2O + 2h^+_{VB} \rightarrow 2H^+ + H_2O_2 \quad (14)$$

$$2H^+ + 2e^-_{CB} \rightarrow H_2 \quad (15)$$

Transient photocurrent response tests were performed at different applied cell voltages (0.3, 0.6, 0.9, 1.2 and 1.5 V) and temperatures (25, 40, 60 and 80 ºC) to investigate the photoelectrochemical performance of the synthesized photoanode in 0.1 M glycerol (Fig. 4. 2). Both the resultant currents and photocurrents showed to be enhanced by increasing the cell voltage at any reaction temperature. One can observe that this PEM PEC system is

electrocatalytically active in a potential range in which the previously published works on WO_3-based photoanodes, [16,35,50][Chapter 3] tested in 3-electrodes cell configuration, showed a negligible activity under dark conditions. It suggests that, in terms of overall activity, the PEM configuration implies an especially important upgrading from the electrocatalytic (rather than photocatalytic) point of view. It could be attributed to the compactness of the MEA configuration, which leads to presumably much lower ohmic losses between anode and cathode. Also, the use of carbon cloth as catalyst support and gas diffusion electrode herein increases the electrode roughness and enhances the diffusion of reactants and products, thus favouring their access to the catalyst active sites. For instance, at 60 ºC the obtained current (in the dark) was enhanced from 0.4 to 3.1 mA at cell voltages from 0.3 to 1.5 V, with photo-induced current increments from 0.1 to 0.5 mA, respectively, upon illumination.

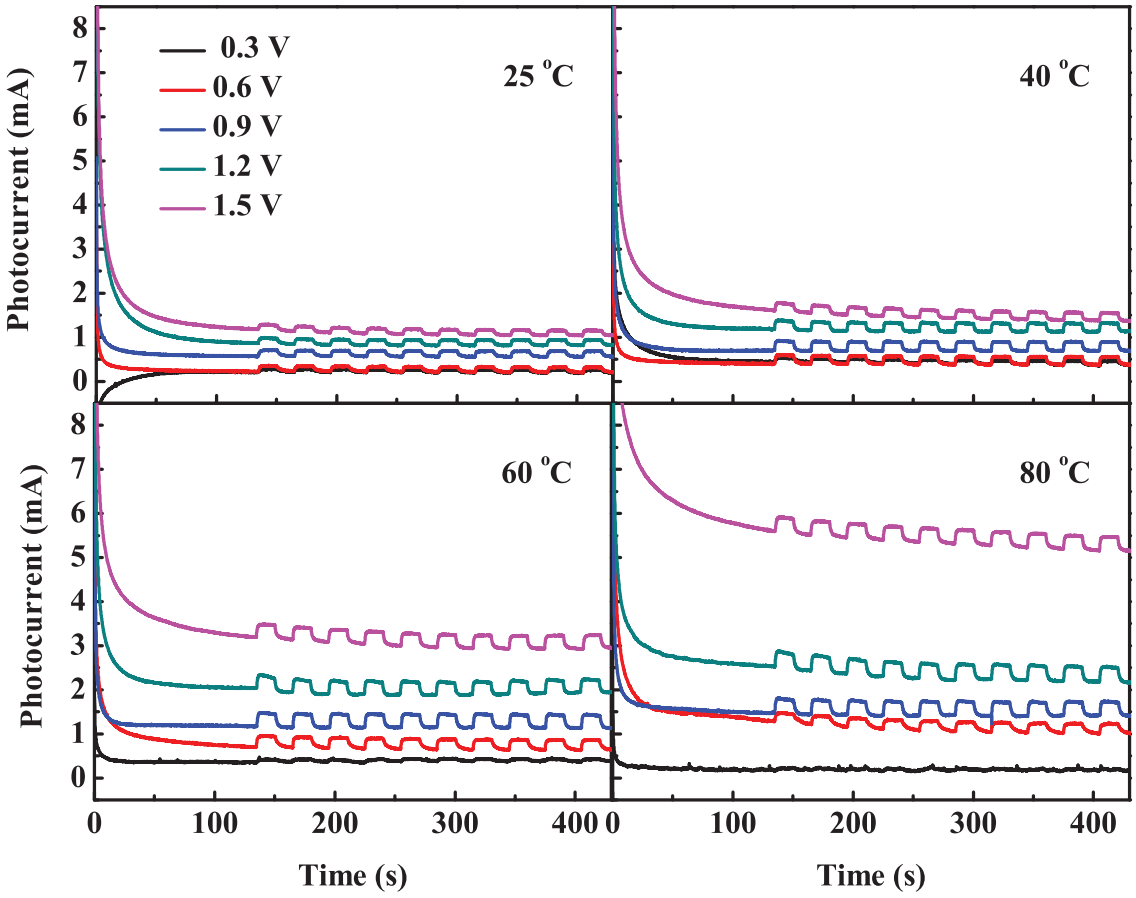

Fig. 4. 2. Transient photocurrent response at different cell voltages (0.3-1.5 V) and temperatures (25-80 ºC). Anode: WO_3/carbon cloth; cathode: Pt (20 wt.%)/C/carbon cloth; Membrane: Nafion 117; anodic solution: 0.1 M glycerol (30 mL); cathodic solution: water (30 mL). UV light irradiation pulses: 41 mW cm^{-2}.

The rise of the temperature also favored the obtained currents, reaching a value at 1.5 V that was four times higher at 80 ºC than that at 25 ºC. However, this influence was much less pronounced on the photo-generated currents, with similar current increases upon illumination above 40 ºC, which can be attributed to a likely detrimental temperature effect on the charge carriers' separation. [51,52] On the other hand, if we compare these transient photocurrent tests in the presence of glycerol (Fig. 4. 2) with those performed in pure water at the same temperatures and applied potentials (Fig. S4. 2), we can observe that the obtained current intensities are very similar in both cases, which denotes that the high baseline current obtained in this system under dark conditions is strongly related to a large capacitive current of the photoanode, as typically found on carbon-supported photoanodes, [53] and maybe also to its EC activity for water electrooxidation in the experiments performed at 1.5 V. However, very interestingly, there is a significant increase in the photo-generated current upon irradiation in the presence of glycerol, which acts as a hole-scavenger and benefits the separation of photo-induced charges. [54,55]

Cyclic voltammetry (CV) tests have also been performed upon UV irradiation, and the 10^{th} cycle obtained at each temperature is shown in Fig. 4. 3, both in the presence and in the absence of glycerol. At low cell voltage (0-0.3 V), apart from some cathodic hydrogen on the WO_3 electrode, cathodic and anodic peaks were expected due to the reduction/oxidation of the redox couple W^{5+}/W^{6+} [56] and, mostly, the intercalation/de-intercalation of H^+ in the WO_3. [57–59] Then, during the forward scan in pure water (Fig. 4. 3a), an increase in the anodic current can be observed at 0.5-0.6 V, likely due to the intercalation of oxygen into the vacancies of the photoanode oxide network, [60,61] followed by the oxygen evolution curve at higher potentials. On the other hand, in the presence of glycerol (Fig. 4. 3b), the anodic peaks obtained at low potentials were likely overlapped with the current increase derived from glycerol oxidation. Indeed, under cell voltages below c.a. 0.7 V, the obtained currents are higher in glycerol solution than in pure water, which can be attributed to the much lower onset oxidation potential in the former case. Then, there is an intermediate potential range where the currents obtained in the presence of glycerol are lower likely due to the partial poisoning of the catalyst surface by adsorbed reaction intermediates. However, as the potential is further increased and these surface species are desorbed/oxidized, the currents obtained in glycerol solution reach again similar or even higher values than those obtained in pure water, likely due to the contribution from oxygen evolution reaction and the oxidation of fresh glycerol and its derived molecules.

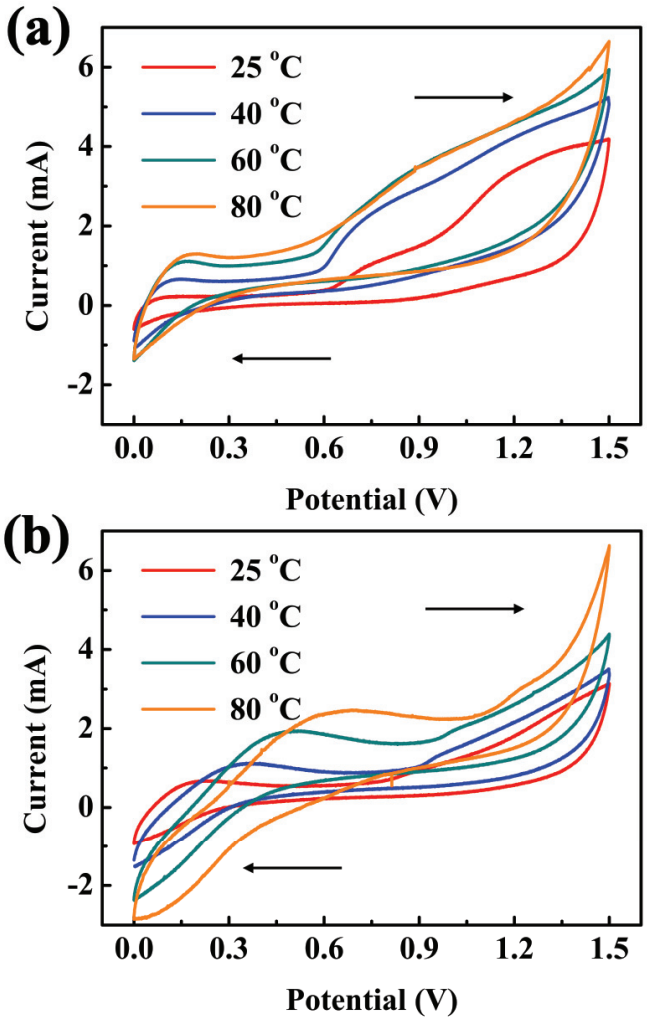

Fig. 4. 3. Cyclic voltammetry (CV) performed in the PEC cell at different temperatures (25-80 ºC) under UV light irradiation (41 mW cm^{-2}) using (a) water or (b) 0.1 M glycerol as anodic solution, and water as cathodic solution. Scan rate: 10 mV s^{-1}. The 10^{th} cycle is shown in each case. Anode: WO_3/carbon cloth; cathode: Pt (20 wt.%)/C/carbon cloth; Membrane: Nafion 117.

Thus, from the transient photocurrent and CV measurements, it is clear the beneficial influence of both the cell voltage and temperature in the overall photo-electro-catalytic activity of the proposed PEM PEC cell. It is worth noting that, under given PEC operation conditions, the expected hydrogen production rate in this PEM cell is directly related to the obtained current intensity, since both glycerol oxidation and water oxidation reactions at the anode imply the reduction of protons at the cathode. Thus, regardless of the products obtained in the anodic side of the cell, an increase in both parameters, i.e., potential and temperature, was found to be beneficial when dealing with the maximization of the obtained current intensity and, therefore, of the hydrogen production on the cathode side (reaction (15)). However, for the optimization

of the bifunctional PEC cell, the anodic performance for biomass valorization (in terms of products selectivity) must be also evaluated.

3.2 Glycerol valorization by PEC

The operation conditions of the PEM PEC system have also been optimized for the selective glycerol valorization to produce high-value-added products, by focusing on the obtained liquid products, and with special interest in glyceraldehyde and dihydroxyacetone (DHA), which are the most valuable ones.

3. 2. 1 Effect of cell temperature

Fig. 4. 4 shows the effect of cell temperature on the PEC performance, in the range from 25 to 80 ºC, at a fixed applied cell voltage of 1.2 V. In all the tests, under light irradiation on the WO_3 photoanode, glyceraldehyde and DHA were obtained as the main products, along with some formic acid and trace amounts of glycolic, tartronic, and oxalic acids. Besides these, other unknown product was detected by HPLC in some cases and, given that the overall liquid products selectivity remained below 100% in all cases, significant amounts of CO_2 were also expected to be evolved, derived from glycerol mineralization, according to the carbon mass balance. In Fig. 4. 4a-d, one can observe that the concentration of the main products in the cell linearly increased with time in all cases. However, their production was only slightly enhanced by heating, and it even decreased at 80 ºC. Although there are very few publications about the effects of reaction temperature on PC and PEC performances, in general terms, the temperature increase is expected to enhance the reaction kinetics, as reported for water splitting [62,63] and organic matter degradation. [64,65] For instance, Velazquez et al. [63] found a positive effect of the cell temperature in the PC production of H_2 from water and water/methanol solutions. However, the rise of the temperature may also disfavor the charge carriers' separation, as recently reported, for instance, by Chen et al. [51]. These authors observed that the PC activity of TiO_2-based materials for the degradation of methylene blue decreased at temperatures higher than 70 ºC. Moreover, the temperature may also strongly influence the products' desorption and reactants' adsorption, which are typically considered the rate-limiting steps in PC systems at temperatures below 20 ºC and above 80 ºC, respectively. [52,66] For these reasons, the temperature range of 20-80 ºC seems to be optimum for the PEC oxidation of organic matter. In the present work, the glycerol conversion values reached after 6 hours-test slightly increased from 3 to 5% in the studied temperature range, 25-80 ºC, with moderate glyceraldehyde and DHA yields of 1.0-1.3% and 0.4-0.6%, respectively (Fig. 4. 4e-h).

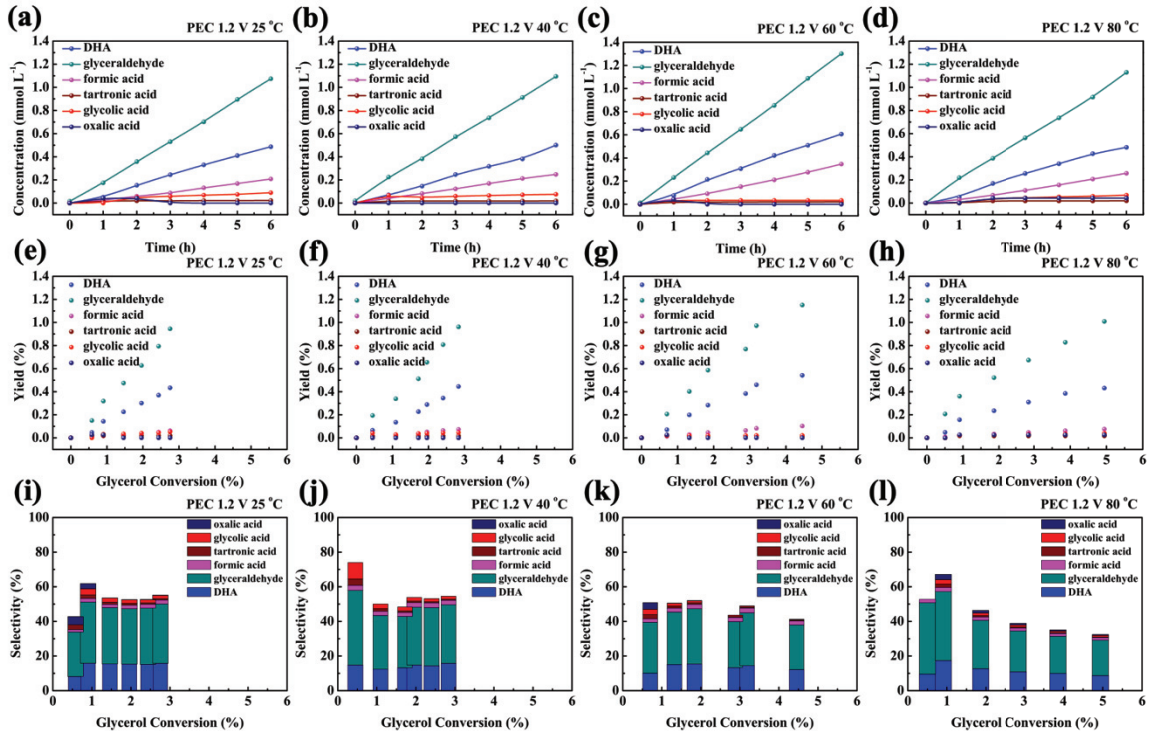

Fig. 4. 4. Influence of the PEC cell temperature. (a-d) Evolution of liquid products concentration in the anodic solution with time; evolution of (e-h) yield and (i-l) selectivity of liquid products with glycerol conversion. Anode: WO_3/carbon cloth; cathode: Pt (20 wt.%)/C/carbon cloth; Membrane: Nafion 117. Cell temperature: 25, 40, 60 and 80 ºC. Cell voltage: 1.2 V. Initial glycerol concentration in anodic solution: 0.1 M. Initial volume of anodic solution: 30 mL. UV irradiation intensity: 41 mW cm^{-2}.

Regarding the selectivity obtained for the identified liquid products (Fig. 4. 4i-l), very stable overall values of 50-60% were obtained in the 6-hours test performed between 25 and 60 ºC. In particular, stable selectivity values of 25-35% and 10-15% were obtained for glyceraldehyde and DHA, respectively. The obtained liquid product selectivity values also denote a significant overoxidation of glycerol and its derived products to CO_2 or other organic compounds, especially at 80 ºC. In this latter case, the C_3 product selectivity clearly shows a decreasing trend with time. Indeed, the amount of the aforementioned *unknown* liquid product detected by HPLC increased with the temperature (see Fig. S4. 3). Likewise, the obtained current after 6 hours seemed to find an optimum at 60 ºC (Fig. S4. 4a). As previously mentioned, this current can be directly related to the production of hydrogen at the cathode, and therefore one can expect an enhanced production of this valuable product at this temperature. Thus, in view of these experiments, we can conclude that the maximum operating temperature to enhance both,

the hydrogen generation (at the cathode) and the selective glycerol valorization (at the anode) by PEC should be 60 ºC.

3. 2. 2 Effect of cell voltage

In our previous study using a similar WO_3 photoelectrode for the selective glycerol oxidation in a conventional PEC reactor, the light showed to be the trigger of the reaction, and the external voltage seemed to promote the separation of photogenerated electrons and holes in the photocatalyst, thus raising the PEC activity and the glyceraldehyde and DHA yields, in particular. [Chapter 3] The WO_3 catalyst has also shown the enhancing effect upon the external bias in this PEM PEC cell, as can be observed, for instance, at 60 ºC in Fig. 4. 4c and Fig. 4. 5b-d. Under purely PC conditions, i.e., without any electric polarization (Fig. 4. 5a), glyceraldehyde and dihydroxyacetone were already selectively generated. Their production was very similar under PEC conditions at 0.3 V (Fig. 4. 5b), but it increased upon the application of higher cell voltages, i.e., 0.6-1.2 V (Fig. 4. 5c-d and Fig. 4. 4c). Indeed, as opposed to the cell temperature, the applied potential had a significant promoting effect on the PEC glycerol valorization. Although similar glycerol conversions were reached under all applied potentials after 6 hours-test, i.e., 4.5-5.0%, glyceraldehyde and DHA yields were increased by up to more than 2 and 3 times, respectively, from 0.3 V to 1.2 V (Fig. 4. 5e-h and Fig. 4. 4g). Consequently, the glyceraldehyde+DHA selectivity gradually increased with the applied potential from c.a. 15% (0.3 V) to 40% (1.2 V) (Fig. 4. 5j-l and Fig. 4. 4k). With respect to purely PC conditions, the glyceraldehyde and DHA selectivity slightly increased, but the corresponding glycerol conversion more than doubled by PEC at 1.2 V. This explains the enhanced yield of the desired products at 1.2 V compared with the purely PC conditions.

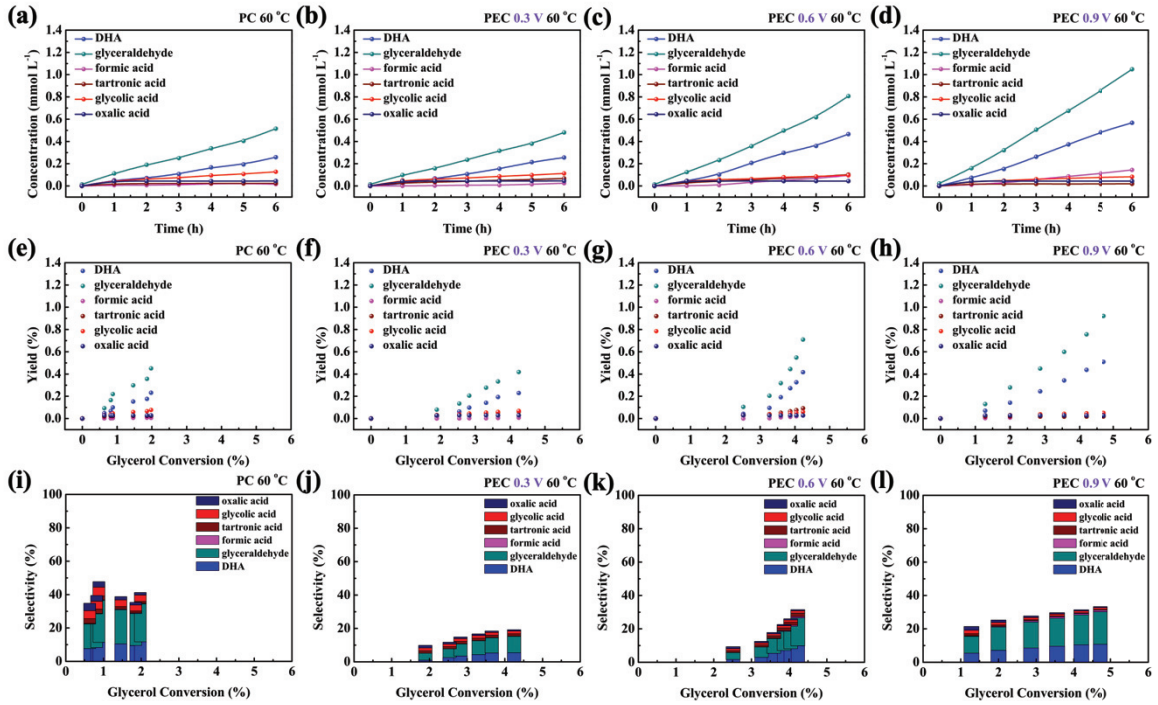

Fig. 4. 5. Influence of the PEC cell voltage. (a-d) Evolution of liquid products concentration in the anodic solution with time during PC and PEC experiments; evolution of (e-h) yield and (i-l) selectivity of liquid products with glycerol conversion. Anode: WO_3/carbon cloth; cathode: Pt (20 wt.%)/C/carbon cloth; Membrane: Nafion 117. Cell temperature: 60 ºC. Cell voltage: open circuit potential (PC) and 0.3-1.2 V (PEC). Initial glycerol concentration in anodic solution: 0.1 M. Initial volume of anodic solution: 30 mL. UV irradiation intensity: 41 mW cm^{-2}.

Given the important competition of glycerol overoxidation reactions expected in the studied potential range, the enhanced C_{3s} selectivity by PEC upon increasing potentials is of especial relevance. Besides, the influence of the potential was even greater on the obtained current intensities, and therefore on the hydrogen production at the cathode (Fig. S4. 4b). Thus, among all the studied PEC operation conditions, the best PEM cell performance, from both glycerol valorization and H_2 generation points of view, has been obtained at 1.2 V and 60 ºC, with stable glyceraldehyde and DHA production rates at the anode side of 11.1 and 5.2 mmol m^{-2} h^{-1}, respectively, and a simultaneous H_2 production rate at the cathode side of 44.0 mmol m^{-2} h^{-1}, as estimated from a steady-state current intensity of c.a. 1.25 mA (Fig. S4. 4b).

3.2.3 Stability evaluation

In order to evaluate the stability of the system, another PEC measurement was performed under relatively harsh conditions (1.2 V, 80 ºC) for three successive days, with operation periods of

9 hours (27 h in total) (Fig. S4. 5). Reproducible results were obtained after 6 hours (as compared to Fig. 4. 4d) and, interestingly, the targeted value-added products, glyceraldehyde and DHA, were still the main obtained products for 27 h, reaching yields of c.a. 4% and 1.5%, respectively, with an increase in the glycerol conversion to ~45%, i.e., around 8 times higher than that reached in the short-term experiment (6 h). According to the continuous increase in glycerol conversion and the stable current intensity (with a decrease of c.a. 0.1 mA in the last 24 hours) observed during this test (Fig. S4. 5), the proposed PEM PEC cell using a WO_3 photoanode showed not only the capability for simultaneous hydrogen generation and glycerol valorization, but also an outstanding stability in long-term operation. However, it should be noted that, under the studied operation conditions, the glyceraldehyde and DHA production rates slowed down for the last operation hours while that of formic acid gradually increased, reaching a yield of c.a. 1% after 27 hours, as well as also likely that of CO_2. Consequently, the joint selectivity of the targeted C_3 compounds continuously decreased for the 27 hours-test, down to c.a. 13%. In view to the practical application of the PEC PEM cell for the selective glycerol valorization, higher solution volumes should be treated, thus operating under low-conversion conditions and, preferably, the targeted products should be continuously separated from the anode effluent and collected, in order to avoid their recycling and overoxidation.

3. 3 Technology comparison with EC, TC and PC

The PEC performance of the PEM cell for glycerol valorization has also been evaluated in a broader context by comparing the above-discussed results with those obtained at different temperatures under purely electrocatalytic (EC), photocatalytic (PC) and thermocatalytic (TC) conditions, i.e., by removing the light irradiation, the external bias, and both effects, respectively. An overview of the results obtained with the different technologies can be found in Fig. S4. 6. Among them, the only technology capable to produce value-added organics and pure hydrogen gas separately, apart from PEC, is the electrocatalysis. In this way, glycerol oxidation (reactions (1-5)) takes place on the WO_3 catalyst surface releasing protons and electrons that are transferred through the proton-exchange membrane and the external circuit, respectively, to the Pt cathode, where H_2 evolves. Fig. 4. 6a-d show the liquid products distribution obtained by EC glycerol oxidation at different temperatures between 25 and 80 ºC under an applied cell voltage of 1.2 V. The temperature increase is expected to enhance the reaction kinetics, the mass transport and the membrane electrical conductivity. Indeed, the PEM cell configuration has been widely employed for hydrogen production from alcohols electro-reforming at temperatures closed to 80 ºC. [43–46,49] However, in the present case,

although a significant EC activity for glyceraldehyde production was observed at room temperature, the heating showed a clear detrimental effect on the selective glycerol valorization, which became negligible at 80 ºC. Instead, the obtained currents increased with the temperature (Fig. 4. 6e-h), as expected from the previous results on transient photocurrent measurements in dark conditions (Fig. 4. 2). This enhanced EC activity can be mainly attributed to glycerol overoxidation reactions to gaseous CO_2 or other compounds which, in turn, are expected to be favored by hydroxyl or oxygen radicals generated from water. [67,68]

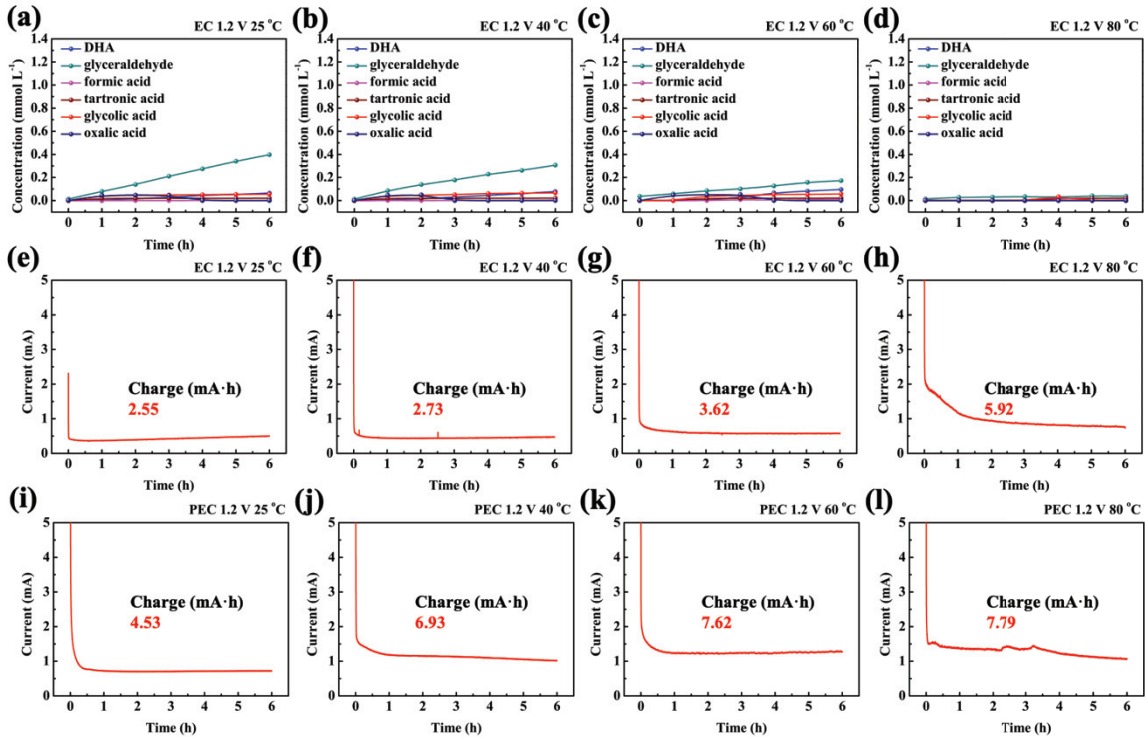

Fig. 4. 6. Evolution of (a-d) liquid products concentration in the anodic solution and (e-h) current intensity with time during EC experiments (in the absence of light irradiation). (i-l) Evolution of current intensity with time during PEC experiments (UV irradiation intensity: 41 mW cm^{-2}). Anode: WO_3/carbon cloth; cathode: Pt (20 wt.%)/C/carbon cloth; Membrane: Nafion 117. Cell temperature: 25-80 ºC. Cell voltage: 1.2 V. Initial glycerol concentration in anodic solution: 0.1 M. Initial volume of anodic solution: 30 mL.

The EC behavior is therefore different from that observed in PEC measurements, in which both the glyceraldehyde/DHA production rates (Fig. 4. 4) and the obtained currents (Fig. 4. 6i-l) were slightly enhanced with temperature up to 60 ºC. Hence, if this dual compartment cell were to be used for pure EC reactions, a high temperature is favorable for hydrogen production, while a low temperature is beneficial for selective glycerol valorization. Besides, a suitable external voltage is also necessary for the hydrogen generation by EC. For instance, at a low

cell voltage of 0.3 V, the obtained current was negligible, even at 60 ºC (Fig. S4. 7), and the observed glycerol oxidation products were likely derived from a purely thermocatalytic (TC) process, as can be observed in Fig. S4. 6. Glycerol can be fully converted into DHA, glyceric acid or other organic compounds by TC at temperatures between 25 and 160 ºC by using 1-10 bar oxygen, as reviewed by Dodekatos et al. [69] In this work, the measurements carried out in the absence of any light irradiation or external bias showed a negligible TC activity of the WO_3 catalyst at room temperature, but significant glyceraldehyde production rates were observed upon increasing the temperature, likely involving dissolved oxygen in the glycerol solution (Fig. S4. 6a-d).

Regarding pure PC reactions (Fig. S4. 6e-h), the WO_3 photoanode showed an important production of glyceraldehyde, with an optimum temperature of 40 ºC, in this case. As discussed in section 3.2.1, the sensitivity to temperature in the range of 25-80 ºC mostly stems from the influence on the recombination efficiency of photogenerated electrons and holes in WO_3. [51,52] This was also evidenced in the PEC measurements performed at different temperatures (Fig. 4. 4) although, in this operation mode, the optimum value was 60 ºC. Another sign of the temperature effect on the PC activity was noticed by analyzing the time response of the open circuit potential (OCP) upon illumination (Fig. S4. 8). At 25 ºC, the decay in the OCP for the first seconds under light irradiation was higher than that observed at 80 ºC, which could be linked to a higher photoactivity in the former case due to a higher accumulation of photogenerated electrons. [53,70] More interestingly, after this pioneering analysis of the glycerol oxidation results obtained in all operation modes, i.e., PEC, PC and EC, one can state that the PEC performance for glycerol valorization is not only better than that obtained by pure PC, due to the promotional effect of the external bias on the charge carriers separation, but also better than the sum of the individual yields obtained by PC and EC, at a given cell temperature. The superior PEC performance was especially evident at high temperatures. In fact, at 80 ºC, the production rates of glyceraldehyde, DHA and all other identified liquid products were negligible in all configurations except in PEC.

The synergistic effect between photo- and electro-catalysis was also found in terms of obtained current intensity, and thus hydrogen generation. For instance, in Fig. 4. 6 one can observe that the steady-state current intensities obtained by PEC at 1.2 V at different temperatures were higher than those obtained by EC in all cases. From this, one can deduce that not only the application of an external potential facilitates the separation of the charge carriers and thus increases the availability of the photogenerated holes for the glycerol oxidation reactions, but also the light irradiation and the consequent generation of those charge carriers results in an

increase in the overall number of electrons transferred between the photoanode and the cathode, for their consumption in HER. In other words, PEC technology proves to be the most promising among the explored technologies for the synthesis of both hydrogen and value-added C_3 compounds.

3.3.1 Electron transfer efficiency assessment

In order to get more insights into the reactions preferably taking place on the WO_3 photoanode, the faradaic efficiency (FE) obtained under the different PEC and EC operation conditions has also been evaluated, along with the total organic carbon (TOC) measurements. Fig. 4. 7a shows the electric charges transferred in the EC and PEC measurements performed for 6 h-each at different temperatures, as calculated from the intensity vs. time curves shown in Fig. 4. 6. The accumulated charges transferred in the PEC reactions were 4.53, 6.93, 7.62 and 7.79 mA·h at 25, 40, 60 and 80 ^{o}C, respectively, which are 1.77, 2.54, 2.10 and 1.32 times higher than those obtained in pure EC processes. The charge enhancement observed by increasing the temperature, and also by operating in the PEC cell configuration with respect to EC, can be linked to an increase in the consequent hydrogen production as above discussed. The improvements in the production rates of glyceraldehyde and DHA by PEC vs. EC observed in the previous section were even greater than the respective increases in the transferred charges, which denotes that the faradaic efficiency values of the selective glycerol valorization reactions were higher by PEC than by EC, as can be observed in Fig. 4. 7b, c.

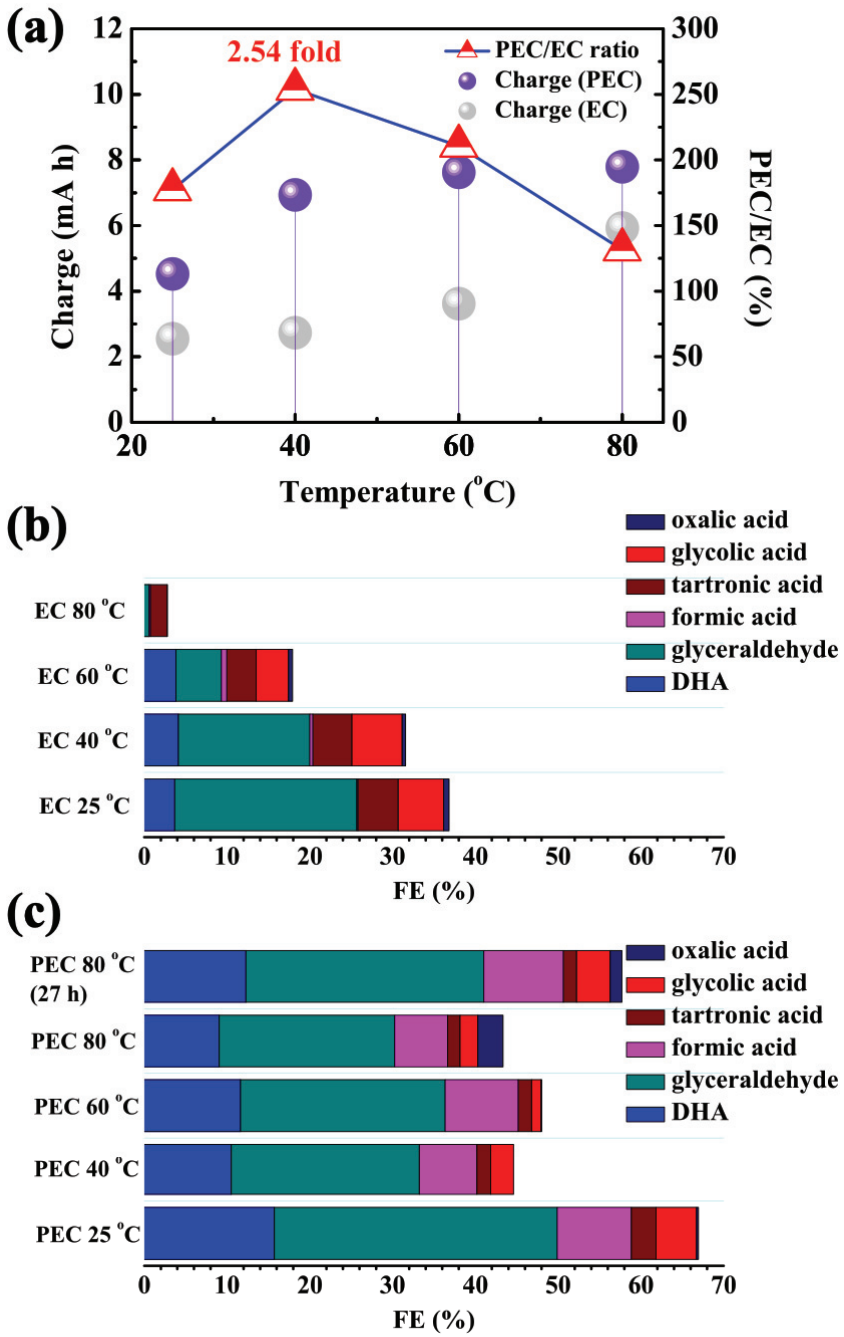

Fig. 4. 7. (a) Comparison of the charge transferred during electrocatalytic (EC) and photoelectrocatalytic (PEC) processes at 1.2 V and different temperatures (25-80 ºC) as well as the enhancement ratio by PEC; Faraday efficiencies (FE) of liquid products in EC (b) and PEC (c) experiments. These data are associated with those shown in Fig. 4 and 6.

The influence of the temperature on faradaic efficiency was different depending on the operation mode, i.e., EC or PEC. The FE values obtained for the targeted C_3 products by pure electrocatalysis strongly decreased with the temperature, from 25% at room temperature, to

only 1%, at 80 ºC (Fig. 4. 7b). On the other hand, the total organic carbon content found in the anodic solution after each EC test showed a decreasing trend with the temperature (Fig. S4. 9a). This denotes that, in dark conditions, the increase in the electric charge transferred from the WO_3 catalyst upon increasing the temperature (Fig. 4. 7a) is mostly attributed to the enhancement of glycerol overoxidation reactions and that CO_2 is the main obtained product, especially at high temperature. However, in the tests performed under both light irradiation and external bias (Fig. 4. 7c), the FE values obtained for glyceraldehyde+DHE were higher and much more stable with the temperature, decreasing from 50% (25ºC), to 30% (80 ºC). At this high temperature, the C_3 FE even increased to 4% when the measurement was extended from 6 to 27 hours. On the other hand, unlike in the case of EC configuration, the TOC values obtained under PEC conditions were generally much more stable, and only in the measurements performed at 80 ºC the TOC showed a clear decrease, likely due to CO_2 evolution at this high temperature (Fig. S4. 9b). Thus, the results obtained in this operation mode seem to indicate that the increased number of electrons transferred under PEC conditions by increasing the temperature from 25 to 60 ºC is derived from both selective glycerol oxidation and water oxidation reactions. One can conclude that, from the energy efficiency point of view, the PEC cell is also more favorable for the simultaneous hydrogen generation and glycerol valorization than the conventional EC configuration.

4. Conclusions

A photoelectrocatalytic (PEC) cell with a proton-exchange membrane (PEM) configuration has been applied, for the first time, to the simultaneous glycerol valorization and pure green hydrogen generation under near-neutral conditions. For this purpose, a WO_3 catalyst (supported on a carbon substrate) with suitable properties for the selective glycerol oxidation to value-added products such as glyceraldehyde and dihydroxyacetone (DHA) has been employed as photoanode. The PEC performance of the system has been evaluated under different temperatures and cell voltages, and it has been compared with that obtained under electrocatalytic (EC), photocatalytic (PC) and thermocatalytic (TC) conditions. The following main conclusions can be drawn from this study:

- An increase in either the cell voltage or the temperature leads to an enhancement of the obtained current in the PEC cell, and thus of the hydrogen production rate at the cathode although, in the case of temperature, its promotional effect is limited by the concurrent acceleration of the charge recombination. The cell voltage has also a positive effect on the selective glycerol oxidation to C_3 compounds at the anode, due to the enhanced photogenerated

charge carriers' separation, but in the case of the temperature, its increase also favours the overoxidation of glycerol and derived molecules.

- Under optimum PEC operation conditions, 60 ºC and 1.2 V, stable glyceraldehyde and DHA production rates of 11.1 and 5.2 mmol m^{-2} h^{-1} are obtained, respectively, along with the simultaneous production of 44.0 mmol H_2 m^{-2} h^{-1}. Under such conditions, the selectivity of glyceraldehyde+DHA reaches 40% after 6 hours operation, corresponding with 4.5% glycerol conversion. The system also proved a remarkable stability even at 80 ºC for 27 hours. However, for its practical application at a larger scale, the targeted C_3 products should be online collected from the anode effluent to avoid their recycling and overoxidation.

- In this PEM configuration, the WO_3 photoanode shows a much higher EC activity in dark conditions than other conventional PEC systems reported in literature, but it is mainly attributed to glycerol mineralization. In this case, the increase of either the temperature (up to 80ºC) or the cell voltage (up to 1.2 V) specifically favours the EC hydrogen production at the cathode but hinders the selective glycerol valorization at the anode. However, at low applied potentials, the EC glycerol oxidation is significant and can be attributed to the purely TC reactions.

- Under purely PC conditions, the catalyst performs a high selectivity for glyceraldehyde production with an optimum operation temperature of 40 ºC. Thus, in the studied temperature and cell voltage ranges, while the direct electron transfer from the anode under EC conditions favours the deep oxidation of glycerol and its derived molecules, likely to CO_2, the holes photogenerated by PC seem to be rather involved in the selective glycerol oxidation reactions to produce the targeted C_{3s}.

- The PEC performance shows to be better than the sum of the individual PC and EC performances, which is likely attributed to a strong synergistic effect found between both electro- and photo-catalytic effects. Thus, PEC proves to be the most promising among the explored technologies studied for the synthesis of both hydrogen and glyceraldehyde/DHA in a PEM cell, as well as from the energy efficiency point of view, given the higher faradaic efficiency values obtained by PEC.

Author Contributions

Jie Yu: Investigation, Conceptualization, Writing - Original Draft, Writing - Review & Editing, Visualization. Jesús González-Cobos: Formal analysis, Review & Editing, Visualization. Frederic Dappozze: Resources, Formal analysis. Philippe Vernoux: Visualization, Formal analysis, Review & Editing. Angel Caravaca: Visualization, Project administration,

Supervision, Review & Editing. Chantal Guillard: Funding acquisition, Project administration, Supervision, Review & Editing.

Declaration of Competing Interest

The authors reported no declarations of interest.

Acknowledgments

This work was financially supported by the China Scholarship Council (Grant No. 201906740016). The authors would like to thank Frederic Bourgain (fabrication of PEC cell) of IRCELYON.

References

[1] M.R. Karimi Estahbanati, M. Feilizadeh, F. Attar, M.C. Iliuta, Current developments and future trends in photocatalytic glycerol valorization: photocatalyst development, Ind. & Eng. Chem. Res. 59 (2020) 22330–22352.

[2] A. Mendoza, R. Romero, G.P. Gutiérrez-Cedillo, G. López-Tellez, O. Lorenzo-González, R.M. Gómez-Espinosa, R. Natividad, Selective production of dihydroxyacetone and glyceraldehyde by photo-assisted oxidation of glycerol, Catal. Today. 358 (2020) 149–154.

[3] M.S.E. Houache, K. Hughes, E.A. Baranova, Study on catalyst selection for electrochemical valorization of glycerol, Sustain. Energy & Fuels. 3 (2019) 1892–1915.

[4] M.R.A. Arcanjo, I.J. da Silva Jr, C.L. Cavalcante Jr, J. Iglesias, G. Morales, M. Paniagua, J.A. Melero, R.S. Vieira, Glycerol valorization: Conversion to lactic acid by heterogeneous catalysis and separation by ion exchange chromatography, Biofuels, Bioprod. Biorefining. 14 (2020) 357–370.

[5] M. Simões, S. Baranton, C. Coutanceau, Electrochemical valorisation of glycerol, ChemSusChem. 5 (2012) 2106–2124.

[6] T. Montini, V. Gombac, L. Sordelli, J.J. Delgado, X. Chen, G. Adami, P. Fornasiero, Nanostructured Cu/TiO_2 photocatalysts for H_2 production from ethanol and glycerol aqueous solutions, ChemCatChem. 3 (2011) 574–577.

[7] Z.G. Schichtl, S.K. Conlin, H. Mehrabi, A.C. Nielander, R.H. Coridan, Characterizing Sustained Solar-to-Hydrogen Electrocatalysis at Low Cell Potentials Enabled by Crude Glycerol Oxidation, ACS Appl. Energy Mater. (2022).

[8] J. Gong, C. Li, M.R. Wasielewski, Advances in solar energy conversion, Chem. Soc. Rev. 48 (2019) 1862–1864.

[9] Y. Li, J. Li, W. Yang, X. Wang, Implementation of ferroelectric materials in photocatalytic and photoelectrochemical water splitting, Nanoscale Horizons. 5 (2020)

1174–1187.

[10] X. Lu, S. Xie, H. Yang, Y. Tong, H. Ji, Photoelectrochemical hydrogen production from biomass derivatives and water, Chem. Soc. Rev. 43 (2014) 7581–7593.

[11] A. Caravaca, W. Jones, C. Hardacre, M. Bowker, H2 production by the photocatalytic reforming of cellulose and raw biomass using Ni, Pd, Pt and Au on titania, Proc. R. Soc. A Math. Phys. Eng. Sci. 472 (2016) 20160054.

[12] A.K. Seferlis, S.G. Neophytides, Photoelectrocatalytic electricity and/or H2 production from alcohols: the effect of TiO_2 film Thickness, J. Electrochem. Soc. 158 (2010) H183.

[13] W. Sheng, Y. Song, M. Dou, J. Ji, F. Wang, Constructing 1D hierarchical heterostructures of MoS_2/In_2S_3 nanosheets on CdS nanorod arrays for enhanced photoelectrocatalytic H_2 evolution, Appl. Surf. Sci. 436 (2018) 613–623.

[14] N. Lakshmana Reddy, K.K. Cheralathan, V. Durga Kumari, B. Neppolian, S. Muthukonda Venkatakrishnan, Photocatalytic reforming of biomass derived crude glycerol in water: a sustainable approach for improved hydrogen generation using Ni $(OH)_2$ decorated TiO_2 nanotubes under solar light irradiation, ACS Sustain. Chem. & Eng. 6 (2018) 3754–3764.

[15] G. Iervolino, I. Tantis, L. Sygellou, V. Vaiano, D. Sannino, P. Lianos, Photocurrent increase by metal modification of Fe_2O_3 photoanodes and its effect on photoelectrocatalytic hydrogen production by degradation of organic substances, Appl. Surf. Sci. 400 (2017) 176–183.

[16] D. Raptis, V. Dracopoulos, P. Lianos, Renewable energy production by photoelectrochemical oxidation of organic wastes using WO_3 photoanodes, J. Hazard. Mater. 333 (2017) 259–264.

[17] S. Bhattacharjee, V. Andrei, C. Pornrungroj, M. Rahaman, C.M. Pichler, E. Reisner, Reforming of Soluble Biomass and Plastic Derived Waste Using a Bias-Free $Cu_{30}Pd_{70}$|Perovskite|Pt Photoelectrochemical Device, Adv. Funct. Mater. 32 (2022) 2109313.

[18] R. Bashiri, N.M. Mohamed, C.F. Kait, S. Sufian, M. Khatani, Enhanced hydrogen production over incorporated Cu and Ni into titania photocatalyst in glycerol-based photoelectrochemical cell: Effect of total metal loading and calcination temperature, Int. J. Hydrogen Energy. 42 (2017) 9553–9566.

[19] Q. Wang, X. Ma, P. Wu, B. Li, L. Zhang, J. Shi, CoNiFe-LDHs decorated Ta_3N_5 nanotube array photoanode for remarkably enhanced photoelectrochemical glycerol conversion coupled with hydrogen generation, Nano Energy. 89 (2021) 106326.

[20] Y.-H. Wu, D.A. Kuznetsov, N.C. Pflug, A. Fedorov, C.R. Müller, Solar-driven

valorisation of glycerol on $BiVO_4$ photoanodes: effect of co-catalyst and reaction media on reaction selectivity, J. Mater. Chem. A. 9 (2021) 6252–6260.

[21] L. W. Huang, T. G. Vo, C. Y. Chiang, Converting glycerol aqueous solution to hydrogen energy and dihydroxyacetone by the $BiVO_4$ photoelectrochemical cell, Electrochim. Acta. 322 (2019) 134725.

[22] D. Liu, J.-C. Liu, W. Cai, J. Ma, H. Bin Yang, H. Xiao, J. Li, Y. Xiong, Y. Huang, B. Liu, Selective photoelectrochemical oxidation of glycerol to high value-added dihydroxyacetone, Nat. Commun. 10 (2019) 1–8.

[23] V. Maslova, A. Fasolini, M. Offidani, S. Albonetti, F. Basile, Solar-driven valorization of glycerol towards production of chemicals and hydrogen, Catal. Today. 380 (2021) 147–155.

[24] M. Li, Y. Li, S. Peng, G. Lu, S. Li, Photocatalytic hydrogen generation using glycerol wastewater over Pt/TiO_2, Front. Chem. China. 4 (2009) 32–38.

[25] P. Ribao, M.A. Esteves, V.R. Fernandes, M.J. Rivero, C.M. Rangel, I. Ortiz, Challenges arising from the use of TiO_2/rGO/Pt photocatalysts to produce hydrogen from crude glycerol compared to synthetic glycerol, Int. J. Hydrogen Energy. 44 (2019) 28494–28506.

[26] V. Maslova, E.A. Quadrelli, P. Gaval, A. Fasolini, S. Albonetti, F. Basile, Highly-dispersed ultrafine Pt nanoparticles on microemulsion-mediated TiO_2 for production of hydrogen and valuable chemicals via oxidative photo-dehydrogenation of glycerol, J. Environ. Chem. Eng. 9 (2021) 105070.

[27] G. Dodekatos, H. Tüysüz, Plasmonic Au/TiO_2 nanostructures for glycerol oxidation, Catal. Sci. & Technol. 6 (2016) 7307–7315.

[28] L. Guo, Q. Sun, K. Marcus, Y. Hao, J. Deng, K. Bi, Y. Yang, Photocatalytic glycerol oxidation on Au_xCu-CuS@TiO_2 plasmonic heterostructures, J. Mater. Chem. A. 6 (2018) 22005–22012.

[29] Y. Shen, A. Mamakhel, X. Liu, T.W. Hansen, T. Tabanelli, D. Bonincontro, B.B. Iversen, L. Prati, Y. Li, J.W.H. Niemantsverdriet, others, Promotion mechanisms of Au supported on TiO_2 in thermal-and photocatalytic glycerol conversion, J. Phys. Chem. C. 123 (2019) 19734–19741.

[30] T. Jedsukontorn, N. Saito, M. Hunsom, Photoinduced glycerol oxidation over plasmonic AU and AuM (M= Pt, Pd and Bi) nanoparticle-decorated TiO_2 photocatalysts, Nanomaterials. 8 (2018) 269.

[31] L. Abis, N. Dimitritatos, M. Sankar, S.J. Freakley, G.J. Hutchings, Plasmonic oxidation

of glycerol using AuPd/TiO_2 catalysts, Catal. Sci. & Technol. 9 (2019) 5686–5691.

[32] T.P.A. Ruberu, N.C. Nelson, I.I. Slowing, J. Vela, Selective alcohol dehydrogenation and hydrogenolysis with semiconductor-metal photocatalysts: toward solar-to-chemical energy conversion of biomass-relevant substrates, J. Phys. Chem. Lett. 3 (2012) 2798–2802.

[33] R. Tang, L. Wang, Z. Zhang, W. Yang, H. Xu, A. Kheradmand, Y. Jiang, R. Zheng, J. Huang, Fabrication of MOFs' derivatives assisted perovskite nanocrystal on TiO_2 photoanode for photoelectrochemical glycerol oxidation with simultaneous hydrogen production, Appl. Catal. B Environ. 296 (2021) 120382.

[34] T. G. Vo, C. C. Kao, J. L. Kuo, C. Chiu, C.-Y. Chiang, Unveiling the crystallographic facet dependence of the photoelectrochemical glycerol oxidation on bismuth vanadate, Appl. Catal. B Environ. 278 (2020) 119303.

[35] Z. Gu, X. An, R. Liu, L. Xiong, J. Tang, C. Hu, H. Liu, J. Qu, Interface-modulated nanojunction and microfluidic platform for photoelectrocatalytic chemicals upgrading, Appl. Catal. B Environ. 282 (2021) 119541.

[36] C.S. Çetinkaya, G. Khamidov, O.L. Özcan, L. Palmisano, S. Yurdakal, Selective photoelectrocatalytic oxidation of glycerol by nanotube, nanobelt and nanosponge structured TiO_2 on Ti plates, J. Environ. Chem. Eng. (2022) 107210.

[37] V. Augugliaro, G. Camera-Roda, V. Loddo, G. Palmisano, L. Palmisano, J. Soria, S. Yurdakal, Heterogeneous photocatalysis and photoelectrocatalysis: from unselective abatement of noxious species to selective production of high-value chemicals, J. Phys. Chem. Lett. 6 (2015) 1968–1981.

[38] V. Malik, S. Srivastava, M.K. Bhatnagar, M. Vishnoi, Comparative study and analysis between Solid Oxide Fuel Cells (SOFC) and Proton Exchange Membrane (PEM) fuel cell--A review, Mater. Today Proc. (2021).

[39] G. Cognard, G. Ozouf, C. Beauger, G. Berthomé, D. Riassetto, L. Dubau, R. Chattot, M. Chatenet, F. Maillard, Benefits and limitations of Pt nanoparticles supported on highly porous antimony-doped tin dioxide aerogel as alternative cathode material for proton-exchange membrane fuel cells, Appl. Catal. B Environ. 201 (2017) 381–390.

[40] C. Coutanceau, S. Baranton, Electrochemical conversion of alcohols for hydrogen production: a short overview, Wiley Interdiscip. Rev. Energy Environ. 5 (2016) 388–400.

[41] A. Rodriguez-Gómez, F. Dorado, P. Sánchez, A.R. de la Osa, Boosting hydrogen and chemicals production through ethanol electro-reforming on Pt-transition metal anodes,

J. Energy Chem. 70 (2022) 394–406.

[42] A. de Lucas-Consuegra, R. Ana, A.B. Calcerrada, J.J. Linares, D. Horwat, A novel sputtered Pd mesh architecture as an advanced electrocatalyst for highly efficient hydrogen production, J. Power Sources. 321 (2016) 248–256.

[43] C. Lamy, B. Guenot, M. Cretin, G. Pourcelly, Kinetics analysis of the electrocatalytic oxidation of methanol inside a DMFC working as a PEM electrolysis cell (PEMEC) to generate clean hydrogen, Electrochim. Acta. 177 (2015) 352–358.

[44] F.M. Sapountzi, M.N. Tsampas, H.O.A. Fredriksson, J.M. Gracia, J.W. Niemantsverdriet, Hydrogen from electrochemical reforming of C_1-C_3 alcohols using proton conducting membranes, Int. J. Hydrogen Energy. 42 (2017) 10762–10774.

[45] A. Caravaca, F.M. Sapountzi, A. de Lucas-Consuegra, C. Molina-Mora, F. Dorado, J.L. Valverde, Electrochemical reforming of ethanol--water solutions for pure H_2 production in a PEM electrolysis cell, Int. J. Hydrogen Energy. 37 (2012) 9504–9513.

[46] A.T. Marshall, R.G. Haverkamp, Production of hydrogen by the electrochemical reforming of glycerol--water solutions in a PEM electrolysis cell, Int. J. Hydrogen Energy. 33 (2008) 4649–4654.

[47] H.J. Kim, J. Lee, S.K. Green, G.W. Huber, W.B. Kim, Selective glycerol oxidation by electrocatalytic dehydrogenation, ChemSusChem. 7 (2014) 1051–1056.

[48] V. Bambagioni, M. Bevilacqua, C. Bianchini, J. Filippi, A. Lavacchi, A. Marchionni, F. Vizza, P.K. Shen, Self-sustainable production of hydrogen, chemicals, and energy from renewable alcohols by electrocatalysis, ChemSusChem. 3 (2010) 851–855.

[49] J. De Paula, D. Nascimento, J.J.L. Leon, Electrochemical reforming of glycerol in alkaline PBI-based PEM reactor for hydrogen production, Chem. Eng. Trans. 41 (2014) 205–210.

[50] J. Yu, F. Dappozze, J. Martin-Gomez, J. Hidalgo-Carrillo, A. Marinas, P. Vernoux, A. Caravaca, C. Guillard, Glyceraldehyde production by photocatalytic oxidation of glycerol on WO_3-based materials, Appl. Catal. B Environ. 299 (2021) 120616.

[51] Y.-W. Chen, Y.-H. Hsu, Effects of reaction temperature on the photocatalytic activity of TiO_2 with Pd and Cu cocatalysts, Catalysts. 11 (2021) 966.

[52] M. Umar, H.A. Aziz, Photocatalytic degradation of organic pollutants in water, Org. Pollut. Risk Treat. 8 (2013) 196–197.

[53] A. Gomis-Berenguer, J. Iniesta, D.J. Fermin, C.O. Ania, Photoelectrochemical response of WO_3/nanoporous carbon anodes for photocatalytic water oxidation, C. 4 (2018) 45.

[54] M. Ibadurrohman, K. Hellgardt, Photoelectrochemical performance of graphene-

modified TiO_2 photoanodes in the presence of glycerol as a hole scavenger, Int. J. Hydrogen Energy. 39 (2014) 18204–18215.

[55] F.K. Chong, E. Nurlaela, B.K. Dutta, Impact of glycerol as scavenger for solar hydrogen production from water, Int. J. Energy Environ. (2014) 19–26.

[56] S. Darmawi, S. Burkhardt, T. Leichtweiss, D.A. Weber, S. Wenzel, J. Janek, M.T. Elm, P.J. Klar, Correlation of electrochromic properties and oxidation states in nanocrystalline tungsten trioxide, Phys. Chem. Chem. Phys. 17 (2015) 15903–15911.

[57] K.K. Upadhyay, M. Altomare, S. Eugénio, P. Schmuki, T.M. Silva, M.F. Montemor, On the supercapacitive behaviour of anodic porous WO_3-based negative electrodes, Electrochim. Acta. 232 (2017) 192–201.

[58] S.P. Gupta, H.H. Nishad, S.D. Chakane, S.W. Gosavi, D.J. Late, P.S. Walke, Phase transformation in tungsten oxide nanoplates as a function of post-annealing temperature and its electrochemical influence on energy storage, Nanoscale Adv. 2 (2020) 4689–4701.

[59] S. Sfaelou, L.-C. Pop, O. Monfort, V. Dracopoulos, P. Lianos, Mesoporous WO_3 photoanodes for hydrogen production by water splitting and PhotoFuelCell operation, Int. J. Hydrogen Energy. 41 (2016) 5902–5907.

[60] J.C. Grenier, A. Wattiaux, J.P. Doumerc, P. Dordor, L. Fournes, J.P. Chaminade, M. Pouchard, Electrochemical oxygen intercalation into oxide networks, J. Solid State Chem. 96 (1992) 20–30.

[61] H. Liang, Z. Cao, C. Xia, F. Ming, W. Zhang, A. H. Emwas, L. Cavallo, H.N. Alshareef, Tungsten blue oxide as a reusable electrocatalyst for acidic water oxidation by plasma-induced vacancy engineering, CCS Chem. 3 (2021) 1553–1561.

[62] D. Katakis, C. Mitsopoulou, E. Vrachnou, Photocatalytic splitting of water: increase in conversion and energy storage efficiency, J. Photochem. Photobiol. A Chem. 81 (1994) 103–106.

[63] J.J. Velázquez, R. Fernández-González, L. Díaz, E.P. Melián, V.D. Rodriguez, P. Núñez, Effect of reaction temperature and sacrificial agent on the photocatalytic H_2-production of Pt-TiO_2, J. Alloys Compd. 721 (2017) 405–410.

[64] Z. Ghasemi, H. Younesi, A.A. Zinatizadeh, Kinetics and thermodynamics of photocatalytic degradation of organic pollutants in petroleum refinery wastewater over nano-TiO_2 supported on Fe-ZSM-5, J. Taiwan Inst. Chem. Eng. 65 (2016) 357–366.

[65] Q. Hu, B. Liu, M. Song, X. Zhao, others, Temperature effect on the photocatalytic degradation of methyl orange under UV-vis light irradiation, J. Wuhan Univ. Technol.

Sci. Ed. 25 (2010) 210–213.

[66] J.-M. Herrmann, Heterogeneous photocatalysis: fundamentals and applications to the removal of various types of aqueous pollutants, Catal. Today. 53 (1999) 115–129.

[67] Y. Xue, Y. Wang, Z. Pan, K. Sayama, Electrochemical and photoelectrochemical water oxidation for hydrogen peroxide production, Angew. Chemie Int. Ed. 60 (2021) 10469–10480.

[68] K. Zhang, J. Liu, L. Wang, B. Jin, X. Yang, S. Zhang, J.H. Park, Near-complete suppression of oxygen evolution for photoelectrochemical H_2O oxidative H_2O_2 synthesis, J. Am. Chem. Soc. 142 (2020) 8641–8648.

[69] G. Dodekatos, S. Schünemann, H. Tüysüz, Recent Advances in Thermo-, Photo-, and Electrocatalytic Glycerol Oxidation, ACS Catal. 8 (2018) 6301–6333.

[70] J.E. Carrera-Crespo, I. Fuentes-Camargo, R.E. Palma-Goyes, U.M. Garcia-Pérez, J. Vazquez-Arenas, I. Chairez, T. Poznyak, Unrevealing the effect of transparent fluorine-doped tin oxide (FTO) substrate and irradiance configuration to unmask the activity of FTO-$BiVO_4$ heterojunction, Mater. Sci. Semicond. Process. 128 (2021) 105717.

Chapter 4

Electronic Supplementary Information

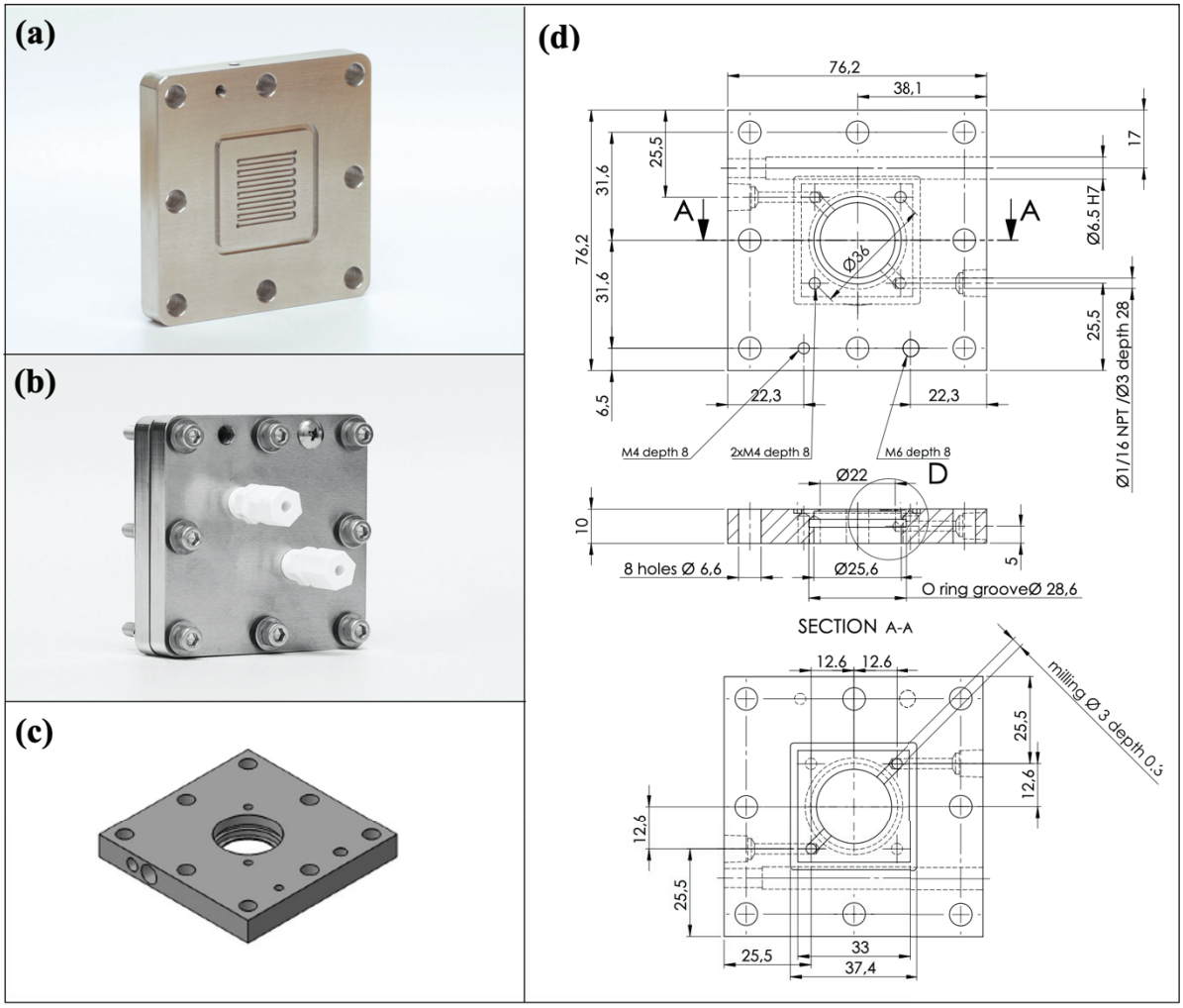

Fig. S4. 1. Pictures of the (a) inner and (b) outer sides of the commercial cathodic bipolar plate (5 cm^2-electrolysis cell from Dioxide Materials) used in the PEM cell; (c) drawing and (d) schematics of the anodic bipolar plate designed and constructed in this work to be adapted to PEC measurements.

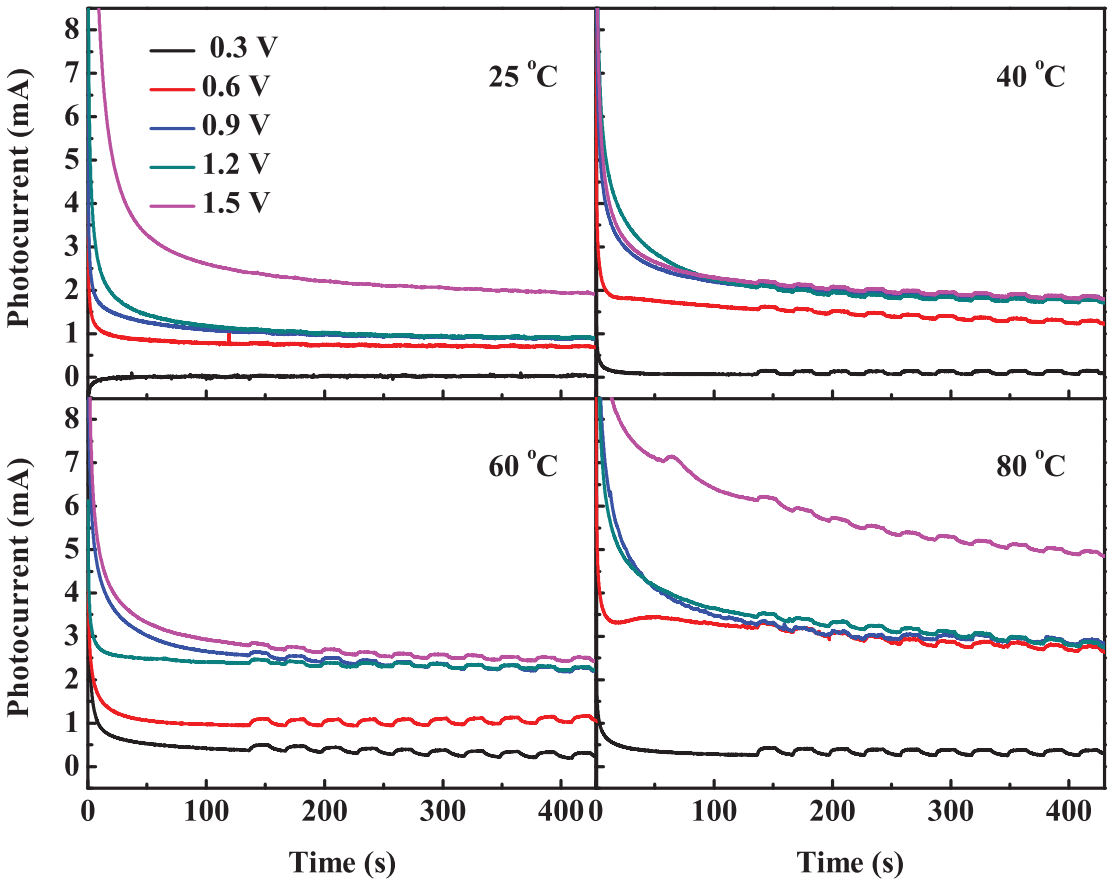

Fig. S4. 2. Transient photocurrent response at different cell voltages (0.3-1.5 V) and temperatures (25-80 ºC). Anode: WO_3/carbon cloth; cathode: Pt (20 wt.%)/C/carbon cloth; Membrane: Nafion 117; Anodic and cathodic solutions: water (30 mL each).

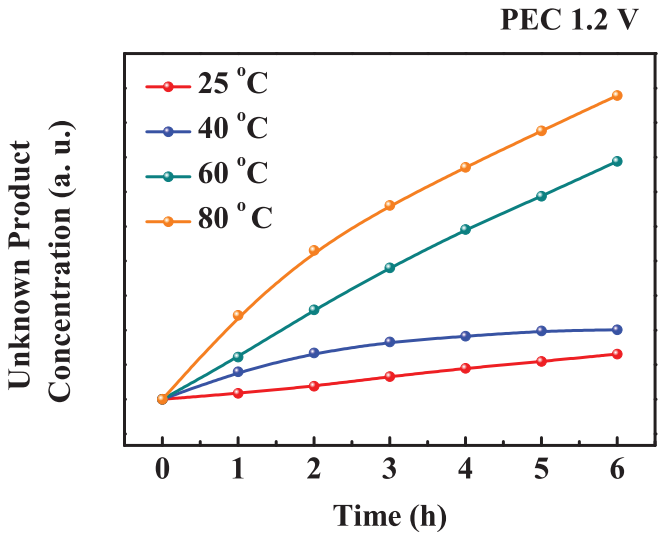

Fig. S4. 3. Evolution of the concentration of the unknown liquid product detected by HPLC in the anodic solution with time in PEC experiments performed at 1.2 V at different temperatures: 25, 40, 60 and 80 ºC. Same reaction conditions as in Fig. 4. 4.

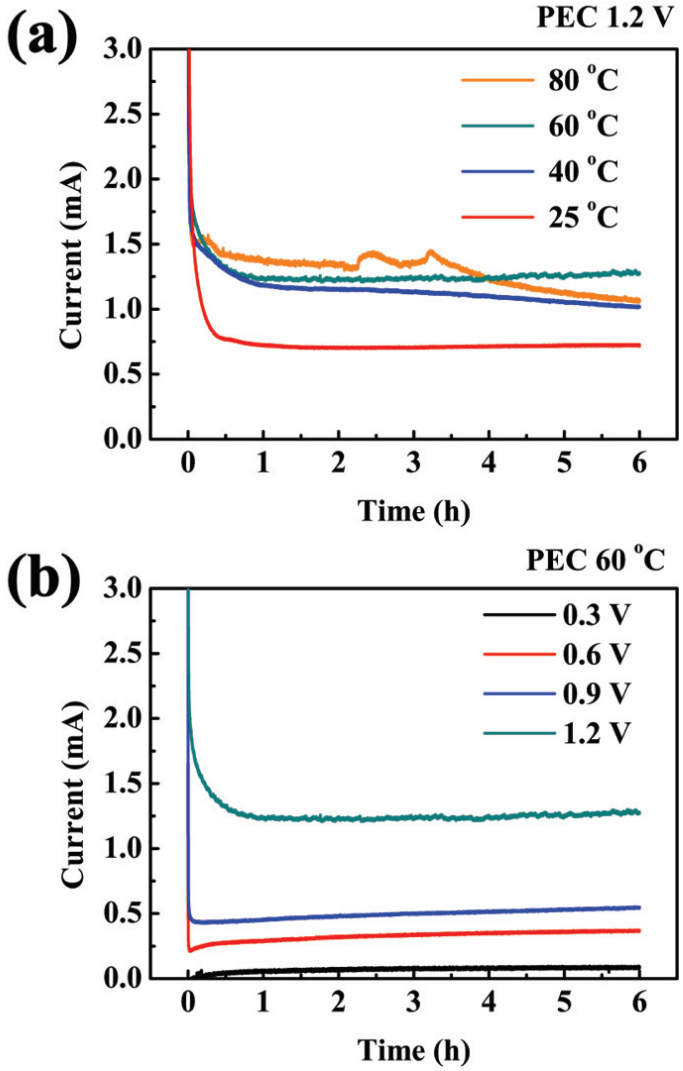

Fig. S4. 4. Evolution of current intensity with time in the PEC experiments performed under UV light irradiation (41 mW cm^{-2}) at (a) different temperatures (25-80 ºC), at 1.2 V, and (b) at 60 ºC, at different cell voltages (0.3-1.2 V). Anode: WO_3/carbon cloth; cathode: Pt (20 wt.%)/C/carbon cloth; Membrane: Nafion 117; anodic solution: 0.1 M glycerol (30 mL); cathodic solution: water (30 mL). These data are associated with those shown in Fig. 4. 4 and 4. 5, respectively.

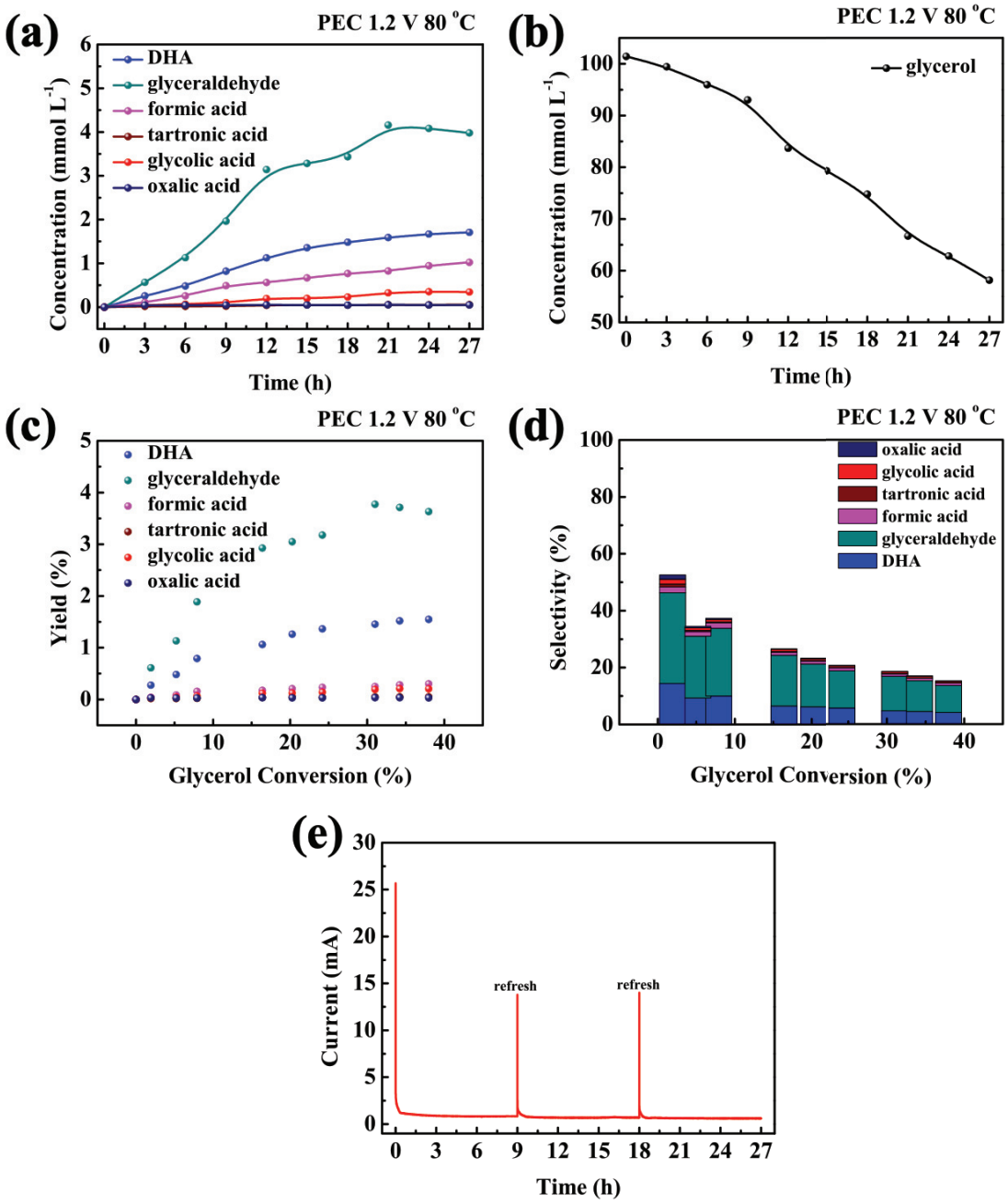

Fig. S4. 5. Long-term stability PEC test for 3 successive periods of 9 hours-each (27 h operation in total). Evolution of (a) liquid products concentration and (b) glycerol conversion with time; evolution of (c) yield and (d) selectivity of liquid products with glycerol conversion, (e) evolution of current intensity with time. Anode: WO_3/carbon cloth; cathode: Pt (20 wt.%)/C/carbon cloth; Membrane: Nafion 117. Cell temperature: 80 ºC. Cell voltage: 1.2 V. Initial glycerol concentration in anodic solution: 0.1 M. Initial volume of anodic solution: 30 mL. UV irradiation intensity: 41 mW cm^{-2}.

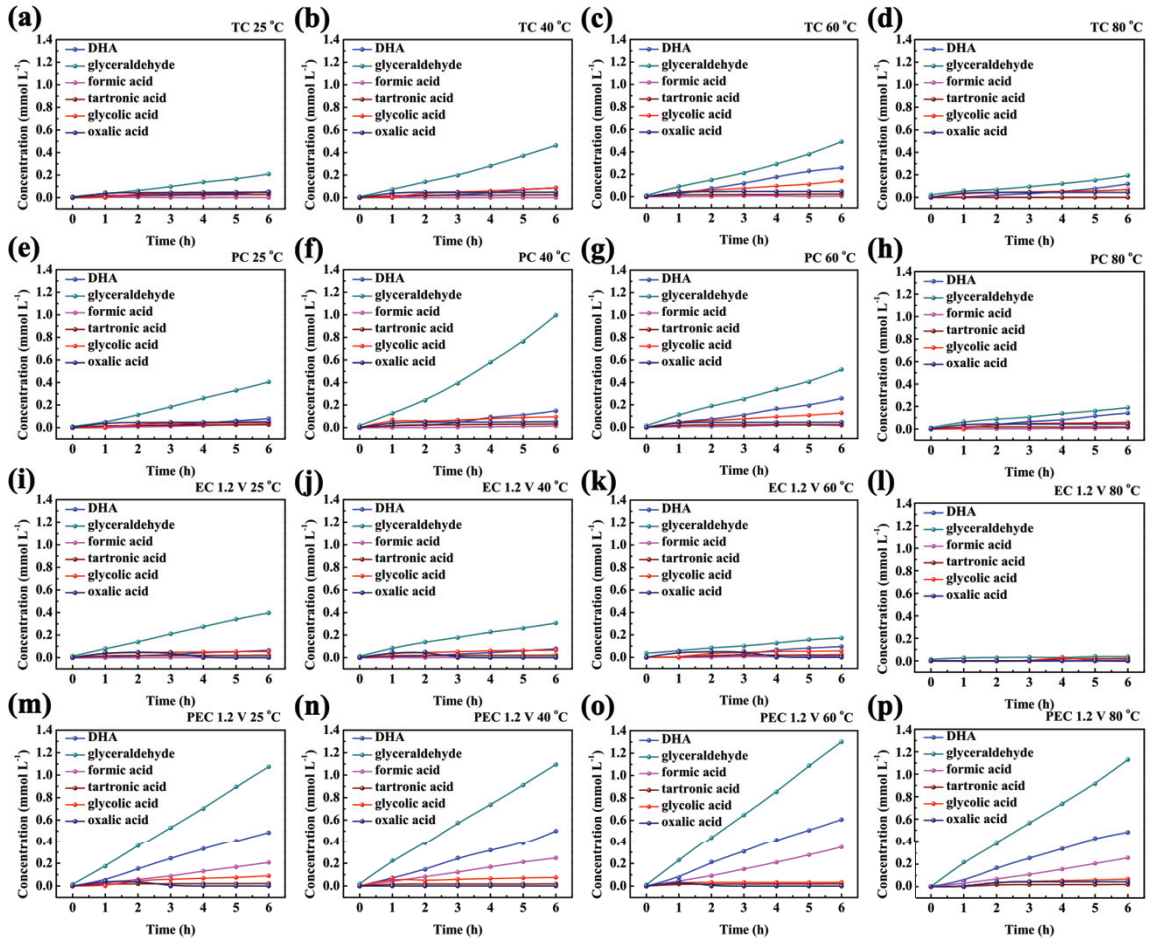

Fig. S4. 6. Evolution of products concentration in the cell with time in experiments performed at different temperatures (25-80 ºC), under (a-d) thermal catalytic (TC), (e-h) photocatalytic (PC), (i-l) electrocatalytic (EC) and (m-p) photoelectrocatalytic (PEC) conditions. EC and PEC at 1.2 V. Catalyst/anode/photoanode: WO_3/carbon cloth. Cell voltage: open circuit potential (TC, PC); 1.2 V (EC, PEC). UV irradiation intensity: 0 mW cm^{-2} (TC, EC); 41 mW cm^{-2} (PC, PEC). Initial glycerol concentration in anodic solution: 0.1 M. Initial volume of anodic solution: 30 mL.

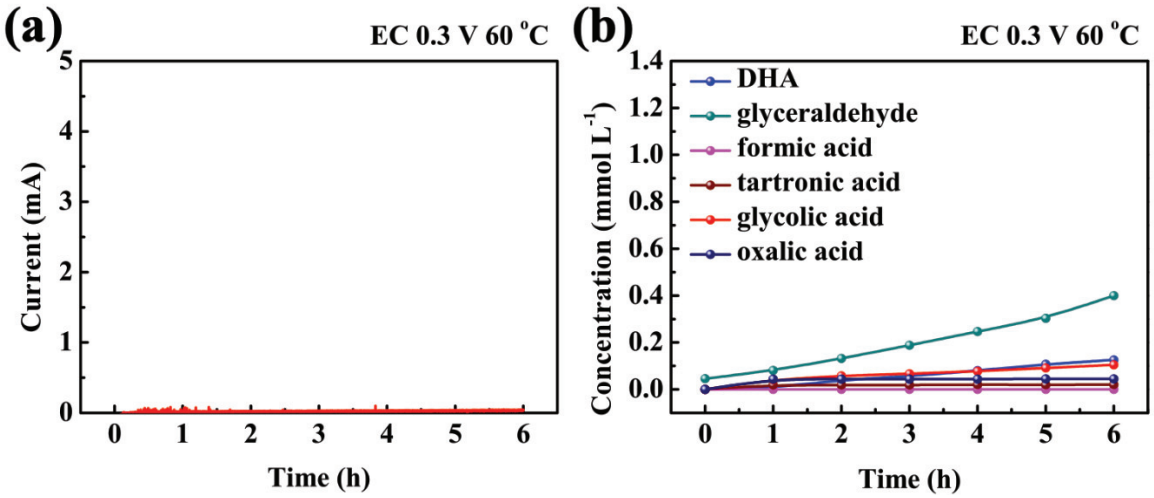

Fig. S4. 7. Evolution of (a) current intensity and (b) liquid products concentration in the cell with time in EC experiment. Anode: WO_3/carbon cloth; cathode: Pt (20 wt.%)/C/carbon cloth; Membrane: Nafion 117. Cell temperature: 60 °C. Cell voltage: 1.2 V. Initial glycerol concentration in anodic solution: 0.1 M. Initial volume of anodic solution: 30 mL.

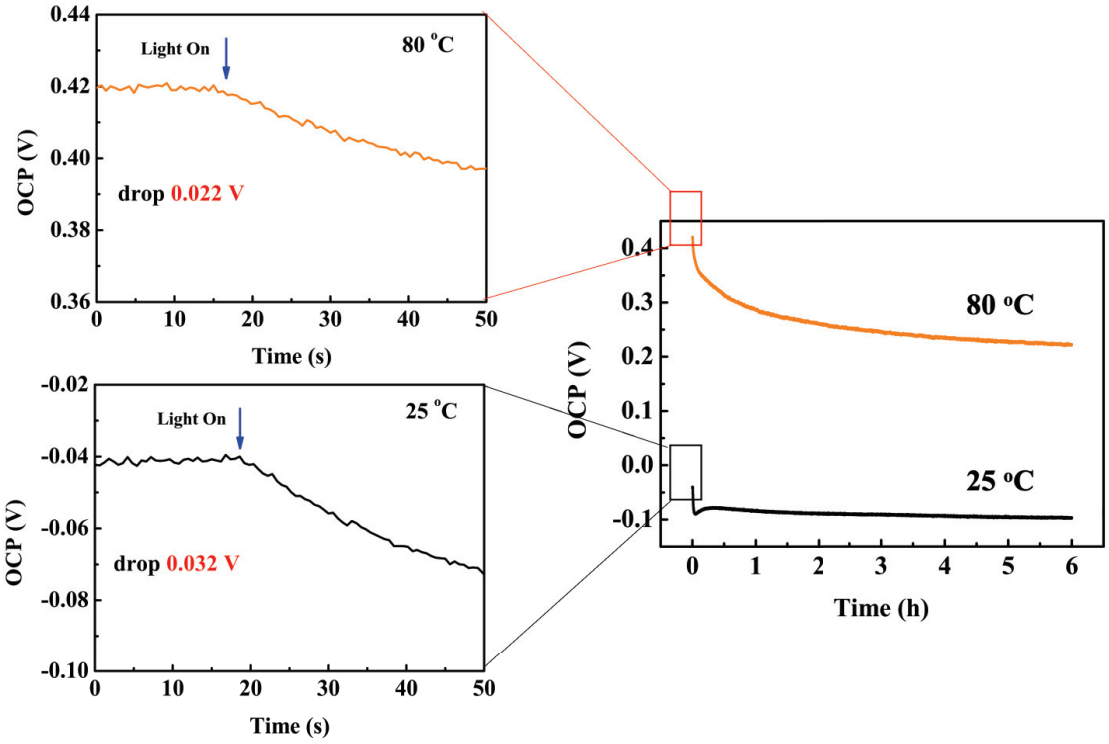

Fig. S4. 7. Open circuit potential (OCP) response with time upon light irradiation at 25 and 80 ºC. Anode: WO_3/carbon cloth; cathode: Pt (20 wt.%)/C/carbon cloth; Membrane: Nafion 117; anodic solution: 0.1 M glycerol (30 mL); cathodic solution: water (30 mL). UV light irradiation pulses: 41 mW cm^{-2}. These data are associated with those shown in Fig. S4. 7e, h.

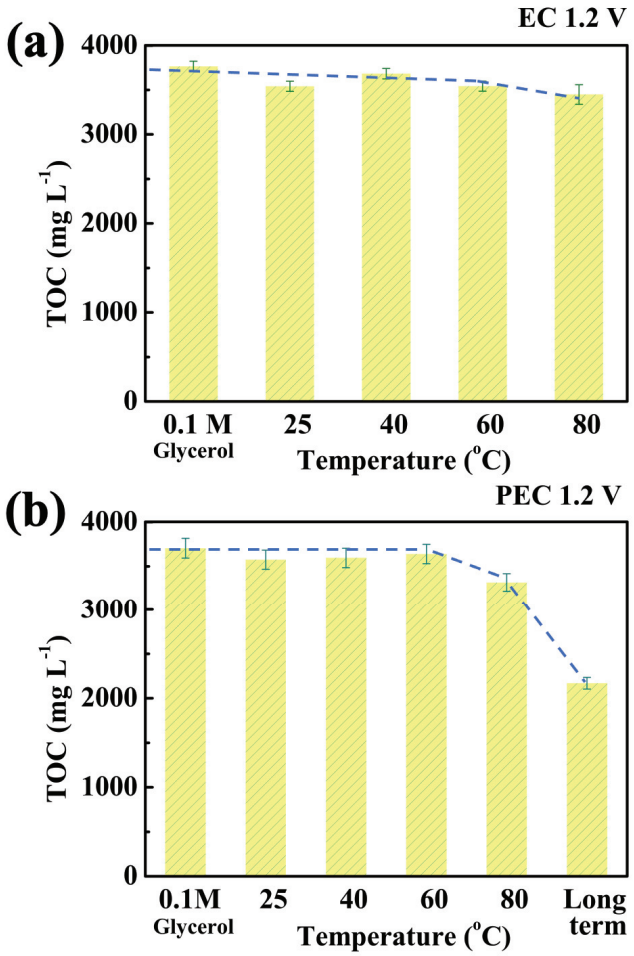

Fig. S4. 9. Total organic carbon (TOC) measured after (a) EC (in the absence of illumination) and (b) PEC experiments (UV light irradiation pulses: 41 mW cm^{-2}) at 1.2 V, including short-term experiments (6 h) at different temperatures (25-80 °C), and long-term PEC experiment (27 h) at 80 °C. Anode: WO_3/carbon cloth; cathode: Pt (20 wt.%)/C/carbon cloth; Membrane: Nafion 117; anodic solution: 0.1 M glycerol.

Conclusions

In this study, we demonstrated, the high performance of WO_3-based catalysts for the selective photo- or photoelectron-catalytic glycerol oxidation towards glyceraldehyde with simultaneous hydrogen generation.

In part I, by comparing the activity of pure TiO_2 (Anatase, Rutile and $P25_{anatase/rutile}$) and pure WO_3 (prepared by a simple hydrothermal method), we found that: i) TiO_2 catalysts allow for a higher overall conversion of glycerol, where the selectivity to glyceraldehyde is hindered by its further photooxidation, and ii) WO_3 catalysts exhibit slower kinetics for glycerol oxidation, but show an outstanding selectivity and yield of glyceraldehyde. While the activity of TiO_2 is attributed to electronic effects (better separation of photogenerated charge carriers), the high glyceraldehyde selectivity of WO_3 is linked to its enhanced acidity, which selectively activates C-O bonds in glycerol, and facilitates the desorption of glyceraldehyde (avoiding its further photooxidation). Hence, a commercial WO_3/TiO_2 material (DTW5) is proven to combine the best features of both semiconductors, with high levels of glycerol conversion and selectivity to glyceraldehyde. This study opens therefore a new field dealing with the development of advanced photocatalytic materials for an advanced valorization of glycerol into high added-value products.

In part II, we have investigated the photoelectrocatalytic (PEC) performance of a monoclinic WO_3 catalyst obtained by a post-calcination method for glycerol valorization to high value-added chemicals achieving very promising results in terms of dihydroxyacetone (DHA) and, especially, glyceraldehyde selectivity under ambient conditions and near-neutral pH. With respect to a previously tested uncalcined WO_3 catalyst, the one synthesized herein with the proper oxygen defects (~18%) shows a much higher crystallinity and much better photogenerated current densities upon light irradiation. This catalyst also shows a wider light harvesting and a higher and more stable PEC activity for glycerol oxidation, in terms of generated current density and C_3 chemicals production, than a commercial DTW5 catalyst at potentials above 0.9 V vs. Ag/AgCl. On both materials, the PEC glycerol oxidation shows to be triggered by the light irradiation and boosted by the means of an external bias, due to a more efficient charge carriers (h^+/e^-) separation, thus hindering their recombination and providing more holes available for glycerol (and water) oxidation. However, the presence of sub-stoichiometric WO_{3-x}, which in the case of DTW5 catalyst is likely limited to the outermost surface, and the corresponding amount of oxygen vacancies seem to be the key feature of the

pure tungsten oxide catalyst. The presence of proper oxygen defects probably contributes to the better light response, charge carrier separation and electrical conductivity. These characteristics are likely responsible for the better WO_3 PEC activity for glycerol oxidation and also for the water oxidation reaction. Therefore, the selectivity towards C_3 products, already favoured by the strong acidity of this catalyst, is further upgraded under PEC operation conditions by the OER influence. This can be explained by the lower availability of strongly oxidant OH species for the over-oxidation of glycerol or its derived undesired products. For instance, the commercial WO_3/TiO_2 catalyst shows a lower oxygen evolution activity and much higher formic acid selectivity. Importantly, the proposed monoclinic WO_3 catalyst (actually $WO_{2,92}$) shows a joint selectivity for glyceraldehyde/DHA of 87-95%, among liquid products, which is nearly stable (potential-independent) in the studied potential window of 0-1.5 V vs. Ag/AgCl (pH 5.5). Indeed, after carefully disclosing the quantitative liquid products obtained under purely PC conditions and those hypothetically derived from the assistance of the external polarization, we found that the additional active holes are employed for the C_3 selective production with an efficiency (50-64%) that is stable or even slightly increases with the applied potential. Thus, the obtained results show the great potential of this defect-engineered WO_3 catalyst for the PEC valorization of glycerol, especially taking into account its wide margin of improvement in terms of overall performance. For example, by enhancing its morphological and textural characteristics (such as particle size, surface area, and film thickness) or by using dopants that further improved the band edge positions, higher photocurrents and product yields could be expected, while maintaining such a high C_3 selectivity.

In part III, a bifunctional photoelectrocatalytic (PEC) cell with a proton-exchange membrane (PEM) configuration has been applied to the simultaneous glycerol valorization and pure green hydrogen generation under near-neutral conditions. For this purpose, the WO_3 catalyst with suitable properties for selective glycerol oxidation to value-added products glyceraldehyde and DHA has been employed as a photoanode. The PEC performance of the system has been evaluated under different temperatures and cell voltages, and it has been compared with that obtained under electrocatalytic (EC), photocatalytic (PC) and thermocatalytic (TC) conditions. We found that:

-An increase in either the cell voltage or the temperature leads to an enhancement of the obtained current in the PEC cell and thus the hydrogen generation rate at the cathode. The cell voltage positively affects the selective glycerol oxidation to C_3 compounds at the anode, due

to the enhanced photogenerated charge separation, but in the case of the temperature, its increase may facilitate the acceleration of charge recombination.

- Under optimum PEC operation conditions, 60 ºC and 1.2 V, stable glyceraldehyde and DHA production rates of 11.1 and 5.2 mmol m^{-2} h^{-1} are obtained, respectively, along with the simultaneous production of 44.0 mmol H_2 m^{-2} h^{-1}. Under such conditions, the selectivity of glyceraldehyde+DHA reaches 40% after the operation for 6 h, corresponding with 4.5% glycerol conversion. The system also proved a remarkable stability even at 80 ºC for 27 h. However, for its practical application at a larger scale, the targeted C_3 products should be online collected from the anode effluent to avoid their recycling and overoxidation.

- In this PEM configuration, the WO_3 photoanode shows a much higher EC activity in dark conditions than other conventional PEC systems reported in literature, which is mostly attributed to the water electrooxidation activity. In this case, the increase of either the temperature or the cell voltage specifically favours the EC hydrogen production at the cathode but hinders the glycerol valorization at the anode. However, at low applied potentials, the EC glycerol oxidation is significant and can be attributed to the purely TC reactions.

- Under purely PC conditions, the catalyst performs a high selectivity for glyceraldehyde production with an optimum operating temperature of 40 ºC. Thus, while the direct electron transfer from the anode under EC conditions favours the water electrooxidation reaction, the holes photogenerated by PC seem to be rather involved in the selective glycerol oxidation reactions.

The PEC performance is better than the sum of the individual PC and EC performances, which is likely attributed to a strong synergistic effect found between electro- and photo-catalytic effects. Thus, PEC proves to be the most promising among the explored technologies studied for the spatially separated synthesis of hydrogen at the cathodic side and glyceraldehyde/DHA at the anodic compartment in the bifunctional PEM cell and from the energy efficiency point of view, given the higher faradaic efficiency values obtained by PEC.

Appendix

Experimental

1. Material and chemicals

1.1 Organic compounds

Name	Chemical formula	Source
Glycerol	$C_3H_8O_3$	Sigma-Aldrich
Glyceraldehyde	$C_3H_6O_3$	Sigma-Aldrich
Dihydroxyacetone	$C_3H_6O_3$	Sigma-Aldrich
Oxalic acid	$H_2C_2O_4$	Sigma-Aldrich
Tartronic acid	$C_3H_4O_5$	Sigma-Aldrich
Glycolic acid	$C_2H_4O_3$	Sigma-Aldrich
Glyceric acid	$C_3H_6O_4$	Sigma-Aldrich
Formic acid	CH_2O_2	Sigma-Aldrich
Acetic acid	CH_3COOH	Sigma-Aldrich
Ethanol	C_2H_5OH	Carlo Erba Reagents
Isopropanol	$C_3H_8O_2$	Carlo Erba Reagents

1.2 Photocatalysts and materials

Several WO_3- and TiO_2-based materials were used in this study. First of all, a pure WO_3 photocatalyst was prepared by a simple hydrothermal method. Firstly, 0.6 g of WCl_6 was dissolved in 120 mL of Ethanol solution under constant stirring at room temperature for 10 min. Then, the obtained solution was transferred to a Teflon-lined stainless-steel autoclave (200 mL) and kept in an oven for 12 h (180 ^oC). Finally, after cooling down to room temperature, WO_3 powder was withdrawn, washed with Ethanol (3 × 90 mL) and deionized water (3 × 90 mL), and dried at 80 ^oC in air overnight. It was used in the first project. A calcined WO_3 catalyst used in the second and third projects was obtained by calcining the as-prepared WO_3 catalyst at 450 ^oC for 1 hour in air with a heating rate of 5 $^oC\ min^{-1}$.

In addition, a series of TiO_2-based materials were acquired commercially, including Anatase (HPX-200), Rutile (HPX-400C) and DTW5 (5 wt% WO_3/TiO_2), all of them provided by Tronox®, while P25 (a very well-known heterojunction of anatase/rutile) was supplied by Evonik®.

1.3 Elaboration of photoanodes

For the preparation of the photoanode in the second part of the work, the photoanode/working electrode was prepared by the following process: 20 g L^{-1} of the catalyst-isopropanol solution was sonicated for 10 minutes and dropped on the conductive side of the ITO substrate (20 µL× 3) and dried at room temperature until achieving 1 mg cm^{-2}.

For the preparation of the photoanode in the third part of work, a catalyst ink was prepared by mixing the obtained WO_3 catalyst powder with a 5 wt.% Nafion (Sigma-Aldrich) perfluorinated resin solution in aliphatic alcohols and water (to reach a WO_3:Nafion wt. ratio of 1:1) and 5 mL isopropanol (HPLC-isocratic grade, Carlo Erba Reagents). Then the ink was sprayed with an aerograph on a Carbon Cloth (W1S1011, FuelCellStore) electrode-support with a thickness of 410 µm and an area of 5.3 cm^2. The alcohol/water solvent was evaporated at 80 ºC, and the catalyst loading on the Carbon Cloth was controlled by weight measurement, reaching a value of 3.5 mg cm^{-2}.

2. Setups and protocols

The first part of the work was conducted in a homemade Pyrex reactor. A typical photocatalytic experiment was carried out according to the following protocol: 7.5 mg of the catalyst were introduced in the reactor containing 30 mL of glycerol (in aqueous solution concentration of 1.10 mmol L^{-1}). The photocatalytic reactions were conducted under ultraviolet light with a UV lamp (UV-A PL-L, 18 W) which delivers an irradiation intensity of 5.60 mW cm^{-2}. The reactor is open to the air without bubbling. Prior to the photocatalytic reaction, the suspension was stirred for 30 min in the dark to achieve the adsorption-desorption equilibrium of glycerol on the surface of catalysts. Every 30 min, a sample (0.5 mL) was taken from the mixture solution and immediately filtered by a Millipore 0.45 µm (hydrophilic PVDF) membrane using a plastic syringe. In the case of WO_3, the sampling interval is 2 h and its photooxidation performance is tested by two parallel experiments owing to its low kinetic.

The second part of the work was carried out in a traditional 3-electrode cell where Ag/AgCl electrode acts as the reference electrode, Pt wire serves as the counter electrode and ITO glass coated by catalysts is the working electrode. The electrochemical (EC) and photoelectrocatalytic (PEC) properties of the catalysts were investigated with an Origalys OGBO5A electrochemical station (OrigaLys ElectroChem SAS) at room temperature. The working electrode is DTW5 or WO_3 deposited on a Indium Tin Oxide (ITO) support, with a geometric area of ca. 1 cm^{-2} and a catalyst loading of ca. 1 mg cm^{-2}. The PEC reactor was filled with 15 mL of either 0.5 M Na_2SO_4 solution or the mixed solution of 0.1 M glycerol and 0.5 M Na_2SO_4 (pH 5.5). A typical photoelectrocatalytic experiment was carried out according to

the following protocol: Firstly, 30 min of dark reaction was required to achieve a steady-state. Then, different external potentials (0.3, 0.6, 0.9, 1.2, and 1.5 V vs. Ag/AgCl) were successively applied for 5 h each. During this process, 0.6 mL of solution was sampled from the glycerol/Na_2SO_4 solution in dark conditions (at a time denoted as -30 min) and every 1 h during the PEC experiments. For the evaluation of EC and PC performances, analogous measurements were carried out without any light irradiation (i.e., only driven by external polarization) and without any applied potential (i.e., only driven by illumination), respectively.

The third part of the work was taken place in an advanced proton exchange membrane (PEM) PEC cell in the same Origalys OGBO5A electrochemical station as above. The synthesized carbon cloth-supported WO_3 was used as the photoanode, and a commercial carbon cloth-supported Pt (20% wt.)/C (Fuel Cell Store) with a loading of 0.2 $mg \cdot cm^{-2}$ was used as cathode. The PEC system was fed either 30 mL of 0.1 M glycerol (or pure water) to the anodic side of the cell, and fed 30 mL of pure water to the cathodic side. The photoelectrocatalytic experiments were conducted under different applied cell voltages, between 0.3 and 1.2 V, and at different temperatures between 25 and 80 ºC. Purely PC, EC and TC experiments were also carried out at different cell temperatures in the absence of either external bias, light irradiation or both, respectively. Prior to all measurements, the anolyte and catholyte solutions were flowing through the cell for 30 min under dark and open-circuit conditions, at room temperature to achieve the adsorption-desorption equilibrium of glycerol on the surface of the catalyst. Then, the PEC/PC/EC/TC measurements were initiated and, every hour, a sample (0.6 mL) was collected from the anode solution. The reaction time was generally 6 h, except for the long-term experiment (27 h).

Some details about the PEM PEC cell are described below. The carbon cloth behaves as gas diffusion layer (GDL) with microporous layer (MPL) and a thickness of 365 μm. A NafionTM 117 membrane was used as the PEM with a thickness of 183 μm, which does not only serve as the solid electrolyte, but also as the separator for the obtained redox products. Prior to assembly, the membrane was pretreated by successive immersions in 3 different 150 mL-solutions, 3% wt. H_2O_2, 0.5 M H_2SO_4 and deionized water, in that order. The membrane electrode assembly (anodic photoelectrode/PEM/cathodic electrode) was prepared by hot-pressing under 1 metric ton at 120 ºC for 3 min.

The employed (photo)electrochemical cell was adapted from a 5 cm^2-commercial electrochemical cell (Dioxide Materials), by designing and constructing one of the two bipolar plates, i.e., the anode side, to house a suitable quartz window for the PEC measurements. The PEC was also modified to introduce heating resistance rods. The MEA was held between two

Teflon gaskets to ensure the correct sealing of the PEC cell, and it was placed so that the catalyst on the photoanode faces the cell window (3.8 cm^2), while the catalyst on the cathode faces the membrane. A temperature control system was used, and 30 mL-solutions of 0.1 M glycerol and pure water (pH 5.5 both) were continuously fed (recycled) by means of a peristaltic pump (ISMATEC SA, Switzerland) through the anode and cathode sides of the cell from the respective reservoirs at a flow rate of approximately 3 mL min^{-1} each.

3. Characterization

X-ray diffraction (XRD) was conducted with a Bruker D8 diffractometer using Cu Kα (λ= 0.15406 nm) radiation equipped with a 1-D fast multistrip detector (LynxEye, 192 channels on 2.95°) and a Ni filter. Other test conditions included a current of 100 mA, an operating voltage of 40 kV, a scanning range between 2θ = 4-80°and a scan rate of 0.02°/ s. Phase, crystallinity and average crystallite size identification were carried out using the Diffrac. Eva software (Bruker) and the ICDD-PDF4+ database. The % crystallinity which means the ratio of crystalline to non- or nano-crystalline species in a material is evaluated by careful evaluation of the baseline to peak separation in an extended scan range.

X-ray photoelectron spectra (XPS) were conducted via a Thermo Scientific ESCALAB 250 spectrometer equipped with a monochromatic Al Kα radiation source. C 1s peak at 284.6 eV was used as a reference to correct the binding energy.

Scanning electron microscopy (SEM) was conducted by FEI-XL30. Each sample was sprinkled on a conductive tape and sprayed with gold under a 15 kV work voltage. The high-resolution transmission electron microscopy (HRTEM) was performed on a JEOL-2010 microscope equipped with an EDX detector.

The Brunauer−Emmett−Teller (BET) surface area of the catalysts was measured via nitrogen adsorption at −196 °C (Micromeritics ASAP 2020). The catalysts were degassed at 160 °C for 3 h under vacuum. The porous volume and the pore size distribution were calculated via the Barrett-Joyner-Halenda (BJH) method.

UV-vis diffuse reflectance spectroscopy (UV-vis DRS) measurements were conducted using an AvaSpec-2048 Fiber Optic Spectrometer. Spectra were recorded from 200 to 600 nm using a 2048 pixel CCD detector array. Barium sulfate ($BaSO_4$) was used as a blank reference.

The electrochemical photocurrent experiments were carried out in a photoelectrochemical cell (supplied by redox.me ®) with a standard three-electrode or PEM PEC system as described above. For the first part of the work, 5 mg of the catalyst (as-prepared WO_3 or commercial samples) were dispersed in 0.5 mL ethanol. Then, 20 μL of that dispersion were impregnated over an indium-tin oxide (ITO) substrate, with an active area of ca. 1 cm^2, and dried at room

temperature. Different electrical potentials were applied with a potentiostat-galvanostat (VoltaLab PGZ402). For the second and third part of the work, the photocurrent measurements were conducted at different applied potentials from 0.3 V to 1.5 V vs. Ag/AgCl with 15 seconds of irradiation interval in the same 3-electrode using the working electrode as described in the section of setups and protocols. **Cyclic voltammetry (CV)** was recorded from 0 to 1.5 V vs. Ag/AgCl at a scan rate of 20 mV s^{-1} in dark conditions (EC) or with the light irradiation (PEC) from a LED UV lamp (350 mW cm^{-2}). For the third part of the work, the transient photocurrent tests were carried out at different applied cell voltages from 0.3 V to 1.5 V with 15 seconds of irradiation interval, using a LED UV lamp as the light source (41 mW cm^{-2}), with an incidence area of 1 cm^2. CV was recorded between 0 and 1.5 V (cell voltages) at a scan rate of 10 mV s^{-1} for 10 cycles under light irradiation.

The Electron Paramagnetic Resonance (EPR) spectra of solids were recorded on a Bruker EMX micro instrument operating at a frequency of 9.75 GHz. The acquisition parameters were as follows: the center field: 3480 G, the sweep time: 60 s, the number of points: 4200, the modulation amplitude: 4 G, the power: 0.6 mW and the field frequency modulation: 100 kHz. All the measurements were carried out at -173.25 ºC to avoid the fast recombination of electron-hole pairs. Spectra were recorded without illumination and upon illumination with a solar simulated light radiation. The Raman spectra were recorded on a Jasco NRS-5500 with an excitation wavelength of 514 nm. The scanned wavenumber range was from 1000 to 100 cm-1 and gathered 25 scans. In the case of DTW5, an additional Raman spectrum focusing on the 750-850 cm^{-1} region was performed.

Acid properties of the different samples were determined by using pyridine as a probe molecule. Pyridine adsorption was followed by Diffuse reflectance infrared Fourier transform spectroscopy (DRIFTS), which were carried out on a Fourier-transform infrared spectroscopy (FTIR) instrument (Perkin Elmer Frontier) equipped with an environmental chamber (Harrick HVC-DRM). A resolution of 4 cm^{-1} was used with 125 scans averaged to obtain a spectrum from 4000 to 400 cm^{-1}. Prior to each experiment, pyridine adsorption was carried out at 100 °C for 45 min allowing the saturation of the catalyst surface. The physically adsorbed pyridine was then removed from the surface with an air flow (50 mL·min^{-1}). Finally, the IR spectra were recorded at 100 °C. Bands at 1448 and 1537 cm^{-1} (corresponding to Lewis and Brönsted acid sites, respectively) were integrated and acidity was determined using the corresponding molar extinction coefficients.

4. Sample analysis

The concentrations of glycerol and derivate products were analysed by a Shimadzu SPD-M20A prominence ultrafast high-performance liquid chromatography (HPLC) assembled with a Transgenomic ICSep ICE-COREGEL-87H3 organic acid column. The mobile phase is 5 mmol L^{-1} of H_2SO_4 and its flow rate is 0.7 mL min^{-1}. The temperature of the oven is 30 °C. The products of glycerol oxidation could be determined by the ultraviolet detector at the wavelength of 210 nm except from glyceric acid which is identified at 240 nm and DHA which could be identified at 270 nm. Glycerol could be analyzed by the refractive index detector (RID).

In the first part of the work, the Glycerol conversion (in %) was calculated according to equation (1):

$$\text{Glycerol conversion (\%)} = \left(\frac{C_{0\ \text{glycerol}} - C_{t\ \text{glycerol}}}{C_{0\ \text{glycerol}}}\right) \times 100 \quad (1)$$

where $C_{0\ glycerol}$ and $C_{t\ glycerol}$ stand for the initial and real-time concentrations of glycerol, respectively.

The Yield (in %) of every product was calculated according to equation (2):

$$\text{Yield (\%)} = \left(\frac{C_{t\ \text{product}}}{C_{0\ \text{glycerol}}}\right) \times 100 \times n \quad (2)$$

where $C_{t\ product}$ stands for the real-time concentration of the product and n is the ratio of the carbon number present in the product divided by the number of carbon present in the glycerol.

The Selectivity (in %) of every product was calculated according to equation (3):

$$\text{Selectivity (\%)} = \left(\frac{C_{t\ \text{product}}}{C_{0\ \text{glycerol}} - C_{t\ \text{glycerol}}}\right) \times 100 \times n \quad (3)$$

where all the parameters were already defined in equations (1) and (2).

In the second and the third part of the work, due to the less volume of glycerol solution (15 mL or 30 mL) than that in the first part of the work (100 mL), glycerol conversion, yield and selectivity were calculated based on the following formula.

The Glycerol conversion (in %) at a given time was calculated according to equation (4):

$$\text{Glycerol conversion (\%)} = \frac{V_0 x C_{0\ \text{glycerol}} - N_{t\ \text{glycerol}}}{V_0 x C_{0\ \text{glycerol}}} \times 100 \quad (4)$$

Where V_0 (in L) and $C_{0,glycerol}$ (in mM) stand for the initial electrolytic solution volume and glycerol concentration, respectively, and $N_{t,glycerol}$ is the unreacted amount of glycerol at a given time, t.

The Yield (in %) and the Selectivity (in %) of every product were calculated at a given time, t, according to equations (5) and (6), respectively:

$$\text{Yield (\%)} = \frac{N_{t,i}}{V_0 x C_{0\ \text{glycerol}} x f_i} \times 100 \quad (5)$$

$$\text{Selectivity (\%)} = \frac{N_{t,i}}{(V_0 x C_{0\ \text{glycerol}} - N_{t\ \text{glycerol}}) x f_i} \times 100 \quad (6)$$

where f_i is the stoichiometric factor of the product i with respect to glycerol (i.e., according to reactions (1-5) as shown below).

The concentrations of total organic carbon (TOC) of the solutions before and after the photocatalytic tests on different materials were measured using a Shimadzu TOC-VCPN analyzer equipped with an auto-sampler.

5. Faradaic efficiency (FE)

According to the liquid products detected, the photo- (or electro-)catalytic reactions (1-5) were assumed to take place on the WO_3 catalyst surface, by considering the transfer of either holes left in the valence band (h^+_{VB}) upon illumination (under PEC or PC operation conditions) or electrons (e^-, under EC conditions).

$C_3H_8O_3 + 2h^+_{VB}(-2e^-) \rightarrow 2H^+ + C_3H_6O_3$ (glyceraldehyde/DHA) (1)

$C_3H_8O_3 + 2H_2O + 8h^+_{VB}(-8e^-) \rightarrow 8H^+ + C_3H_4O_5$ (tartronic acid) (2)

$2C_3H_8O_3 + 3H_2O + 10h^+_{VB}(-10e^-) \rightarrow 10H^+ + 3C_2H_4O_3$ (glycolic acid) (3)

$2C_3H_8O_3 + 6H_2O + 22h^+_{VB}(-22e^-) \rightarrow 22H^+ + 3C_2H_2O_4$ (oxalic acid) (4)

$C_3H_8O_3 + 3H_2O + 8h^+_{VB}(-8e^-) \rightarrow 8H^+ + 3CH_2O_2$ (formic acid) (5)

The total amount ($N_{t,i}$, in mmol) of unreacted glycerol and each produced chemical, *i*, at a given time (i.e., sampling time), *t*, was calculated from the concentration values quantified by HPLC, according to equation (7):

$$N_{t,i} = V_t \times C_{t,i} + V_s \times \sum_{t=0}^{t-1} C_{t,i} \quad (7)$$

where V_t (in L) and $C_{t,i}$ (in mM) are the solution volume and the concentration of the chemical *i* in the cell, respectively, at the time *t*, V_s is the sample volume (i.e., 6 x 10^{-4} L) and, thus, the term $[V_s \times \sum_{t=0}^{t-1} C_{t,i}]$ stands for the accumulated amount of product or unreacted glycerol collected in previous samplings.

Then, the faradaic efficiency of each target product, *FE* (in %) was calculated through equation (8).

$$FE = \frac{Ni}{N_e} \times 100 \quad (8)$$

Where N_i and N_e (in mmol) stand, respectively, for the number of electrons/holes that would be transferred for the EC/PEC production of the quantified amounts of product *i*, and those electrochemically transferred according to the measured electric charge, Q (in C), which can be calculated, at a given time, through equations (9) and (10):

$$N_i = n_{e,i} \times N_{t,i} \quad (9)$$

$$N_e = \frac{Q}{F} \times 1000 = \frac{\int_0^t I\,dt}{F} \times 3600 \quad (10)$$

Where $n_{e,i}$ is the number of mol of electrons/holes theoretically transferred for the production of each mol of target product i (i.e., according to reactions (1-5)), F is the Faraday constant (96485 C $mol_{e^-}^{-1}$) and I (in mA) is the current obtained at a given time, t (in h).

Due to the electrocatalytic performance of glycerol oxidation being negligible, to better discriminate the contribution of pure PC from the overall PEC performance, the faradaic efficiencies have also been calculated after subtracting to the quantified chemicals production from the PEC tests, that from the corresponding purely PC measurement. In this way, the modified parameters, FE*, stands for the chemicals production hypothetically only derived from the additional effect of the external polarization.

For more details, please refer to the section on experimental in chapters 2-4.

◊ Publications:

1. **J. Yu**, F. Dappozze, J. Martín-Gomez, J. Hidalgo-Carrillo, A. Marinas, P. Vernoux, A. Caravaca*, Chantal Guillard*. Glyceraldehyde production by photocatalytic oxidation of glycerol on WO_3-based materials [J]. Applied Catalysis B: Environmental, 2021, 299:120616.
2. **J. Yu**, J. González-Cobos, F. Dappozze, F. J. López-Tenllado, J. Hidalgo-Carrillo, A. Marinas, P. Vernoux, A. Caravaca *, C. Guillard*. WO_3-based materials for photoelectrocatalytic glycerol upgrading into glyceraldehyde: Unravelling the synergistic photo- and electro-catalytic effects [J]. Applied Catalysis B: Environmental, 2022 (Accepted)
3. **J. Yu**, J. González-Cobos, F. Dappozze, P. Vernoux, A. Caravaca*, C. Guillard*. Optimization of a bifunctional PEM photoelectrocatalytic system for the simultaneous selective glycerol valorization and hydrogen generation [J]. (Submitted to Energy & Environmental Science Journal)
4. **J. Yu**, J. González-Cobos, F. Dappozze, P. Vernoux, A. Caravaca*, C. Guillard*. Basic comprehension and future trends in photoelectrocatalysis: a mini-review [J]. (Submitted to Green Chemistry)

◊ Communications:

1. **J. Yu**, F. Dappozze, P. Vernoux, A. Caravaca*, C. Guillard*. Photo-electrocatalytic valorization of glycerol to glyceraldehyde by WO_3-based materials. ISGC: International symposium on green chemistry, May 2022, Rochelle, France.
2. **J. Yu**, F. Dappozze, P. Vernoux, A. Caravaca*, C. Guillard*. Selective photoelectrocatalytic oxidation of glycerol to high value-added glyceraldehyde with simultaneous hydrogen generation via WO_3-based materials in a PEM reactor. The French Research network on Hydrogen energy, May 2022, Aussois, France.
3. **J. Yu**, F. Dappozze, P. Vernoux, A. Caravaca*, C. Guillard*. Solar to chemical energy conversion viaPhotoelectrocatalytic biomass valorization. Climate Change Risks in a Changing World, April 2022, Graz, Austria.
4. **J. Yu**, F. Dappozze, P. Vernoux, A. Caravaca*, C. Guillard*. Selective photocatalytic oxidation of glycerol to high value-added glyceraldehyde via WO_3-based materials. French-Chinese Conference on Green Chemistry, October 2021, Lyon, France.
5. **J. Yu**, F. Dappozze, J. Martín-Gomez, J. Hidalgo-Carrillo, A. Marinas, P. Vernoux, A. Caravaca*, C. Guillard*. Selective photocatalytic oxidation of glycerol to high value-added glyceraldehyde via WO_3-based materials. 5th International Conference on GDR Solar Fuels, October 2021, Rennes, France.